LASER IONISATION STUDIES

- APPLICATIONS IN NUCLEAR WASTE MONITORING

Christine Margaret Houston B.Sc.

Department of Chemistry

Department of Physics and Astronomy

University of Glasgow

Presented as a thesis for the degree of Doctor of Philosophy

in the University of Glasgow.

December 1986

ProQuest LLC.
789 East Eisenhower Parkway
P.O. Box 1346
Ann Arbor, MI 48106 – 1346

ACKNOWLEDGEMENTS

I would like to thank the following people who have provided valuable assistance in the course of this work:

--- my supervisors; Dr. Kenneth W. D. Ledingham for constant help and advice over the past three years, and Prof. Murdoch S. Baxter whose research interests provided the initial impetus for the study

--- my fellow research students; Mr. Michael Towrie and Mr. Michael H. C. Smyth in whose (amiable) company much of the experimental work was carried out

--- Dr. D. T. Stewart, Dr. K. M. Smith and Mr. J. Cahill for helpful discussions and suggestions and, in particular, Dr. C. Raine for help with computing

--- Mr. T. McCanny and Mr. D. A. Seath for technical support and advice

--- Mr. G. Saunders for typing of the manuscript, and

--- Mrs. M. Waterson for annotating some of the illustrations.

Finally, I would like to acknowledge both the financial support of the S.E.R.C., and the forebearance of my mother, Mrs. Margaret Houston, during the period of this research.

PUBLICATIONS

Laser induced ionisation in proportional counters sealed with low ionisation potential vapours.

Nuclear Instruments and Methods 225, 319 (1984)

K. W. D. Ledingham, C. Raine, K. M. Smith, A. M. Campbell, M. Towrie, C. Trager and C. M. Houston.

Wavelength dependence of laser induced ionisation in proportional counters.

Nuclear Instruments and Methods A 241, 441 (1985)

K. W. D. Ledingham, C. Raine, K. M. Smith, M. H. C. Smyth, D. T. Stewart, M. Towrie and C. M. Houston.

Detection of phenol in proportional counter gas by two-photon ionisation spectroscopy.

CERN - EP/85-198 (Dec. 1985)

J. W. Cahill, C. M. Houston, K. W. D. Ledingham, C. Raine, K. M. Smith, M. H. C. Smyth, D. T. Stewart and M. Towrie.

Detection of phenol in proportional counter gas by two-photon ionisation spectroscopy.

Journal of Physics B: Atomic and Molecular Physics 19, 1989 (1986)

M. Towrie, J. W. Cahill, K. W. D. Ledingham, C. Raine, K. M. Smith, M. H. C. Smyth, D. T. Stewart and C. M. Houston.

The detection of Cs atoms by two-photon Resonance Ionisation Spectroscopy.

Proc. SPIE - Int. Soc. Opt. Eng. ("Laser Applications in Chemistry and Biophysics") 620 (1986)

K. W. D. Ledingham, C. Raine, K. M. Smith, M. H. C. Smyth, D. T. Stewart, M. Towrie and C. M. Houston.

Detection of toluene in proportional counter gas by resonant two-photon ionisation spectroscopy.

CERN - EP/86-28 (Feb. 1986)

S. L. T. Drysdale, C. M. Houston, K. W. D. Ledingham, C. Raine, K. M. Smith, M. H. C. Smyth, D. T. Stewart and M. Towrie.

Detection of toluene in proportional counter gas by resonant two-photon ionisation spectroscopy.

Nuclear Instruments and Methods (to be published)

S. L. T. Drysdale, K. W. D. Ledingham, C. Raine, K. M. Smith, M. H. C. Smyth, D. T. Stewart, M. Towrie and C. M. Houston.

Investigation of the effect of gas purification on the background laser ionisation in proportional chambers.

ALEPH 86-30 (distr. TPCC-AL) (1986)

S. L. T. Drysdale, A. P. Land, K. W. D. Ledingham, C. Raine, K. M. Smith, M. H. C. Smyth, D. T. Stewart, M. Towrie and C. M. Houston.

Applications of resonant ionisation spectroscopy to accelerator based High Energy Physics.

"R.I.S. - 86", Swansea (1986) (to be published)

K. W. D. Ledingham, J. W. Cahill, S. L. T. Drysdale, C. Raine, K. M. Smith, M. H. C. Smyth, D. T. Stewart, M. Towrie and C. M. Houston.

Multiphoton tranistions in caesium vapour.

"R.I.S. - 86", Swansea (1986) (to be published)

C. M. Houston, S. L. T. Drysdale, K. W. D. Ledingham, C. Raine, K. M. Smith, M. H. C. Smyth, D. T. Stewart and M. Towrie.

The potential of resonant ionisation mass spectroscopy for detecting environmentally important radioactive nuclides.

"R.I.S. - 86", Swansea (1986) (to be published)

M. H. C. Smyth, S. L. T. Drysdale, R. Jennings, K. W. D. Ledingham, D. T. Stewart, M. Towrie, C. M. Houston, M. S. Baxter and R. D. Scott.

CONTENTS

2-3/

CHAPTER 5/

IV/

LIST OF FIGURES

3.33/

LIST OF PLATES

LIST OF TABLES

SUMMARY

This thesis is concerned with the development of the new, laser-based analytical technique of Resonance Ionisation Spectroscopy (RIS) for monitoring of components of nuclear waste materials, in the environment, which are difficult to assay by radiometry.

Chapter one begins with a review of the literature on RIS since its inception in 1975, and concludes with a brief discussion of the theory of the technique: multiphoton ionisation is described and saturation conditions derived; the basic resonance ionisation schemes, plus variants which do not involve photons in the ionisation step, are given.

Chapter two deals with the nuclear power industry. Basic reactor design and waste management procedures are detailed, with particular emphasis on the ways in which radioactive species are generated and how they may subsequently, by accident or authorised discharge, be released to the environment. The unsuitability of counting techniques for monitoring of low energy, β^- active nuclides (particularly if present in low concentration) is noted, as is the suitability of RIS for this task. From a literature-based assessment, $^{135}_{55}Cs$ was deemed to be the low energy β^- emitter of greatest environmental significance and, consequently, a study of multiphoton transitions in caesium was undertaken.

Chapter three contains an outline of the apparatus and equipment employed in the experimental work. The laser system and caesium detection/

detection chambers are described in detail.

The study of background ionisation in proportional counter systems similar to that used for caesium comprises Chapter four. The significance of this work is that non-resonant background ionisation arising in impurities in the counter gas may swamp resonant signals, limiting the sensitivity of RIS. From the wavelength dependence of the background ionisation, phenol and toluene were identified as contaminants.

Chapter five contains the results of experimental work on the detection of caesium vapour emanating from a solid sample of the metal. Both two photon (one photon resonant) ionisation and three photon (two photons resonant via a virtual level) ionisation were used. The dependence of the observed transitions on laser fluence was studied. The efficiency of ionisation at different wavelengths and using different ionisation schemes is compared and, for analytical work, detection of caesium by resonant excitation to Rydberg levels followed by collisional ionisation is recommended. A value of the single photon ionisation cross section for caesium of 1.16×10^{-19} cm^2 is obtained as are values of the two photon resonant ionisation cross sections for the $6s_{\frac{1}{2}} - 7p_{\frac{3}{2}}$ and the $6s_{\frac{1}{2}} - 7p_{\frac{1}{2}}$ transitions.

In Chapter six, future work on RIS at Glasgow, which will principally consist of the construction and use of resonance ionisation mass spectrometers, is described. General conclusions are drawn concerning the achievable detection limit of such devices and on their future applicability, in particular to nuclear waste monitoring.

The Appendix describes a non-analytical applications of laser induced ionisation in calibration of multi-wire drift chambers for high energy physics experiments. Results are presented of a project aimed at selection of a suitable ionisable additive (seeding agent) for the time projection chamber at CERN.

CHAPTER 1 RESONANCE IONISATION SPECTROSCOPY

1-1 Introduction

Interest in laser induced ionisation in gases has arisen from two main fields of scientific endeavour. In experimental High Energy Physics the use of pulsed lasers to simulate particle tracks for calibration of large, multi-wire drift chambers has been under investigation; whilst in Chemistry the potential of the laser as the ultimate in analytical tools, capable of element- or even isotope-specific, single atom detection, has received much attention.

The analytical technique of Resonance Ionisation Spectroscopy (RIS) was developed by G. S. Hurst and co-workers at Oak Ridge National Laboratory in the U.S.A. (1-6). Independently, a group in Moscow, U.S.S.R., headed by V. S. Letokhov, were also involved in investigating analytical applications of laser ionisation (7,8).

The basis of RIS is element-specific photoionisation brought about by high power, pulsed laser radiation. Laser photons are tuned to precisely match atomic transitions within a selected target element and ionisation is brought about by a stepwise multiphoton process. In the simplest scheme - two photon resonance ionisation, shown in Figure 1.11 - a laser photon ω_1 promotes an electron in an atom from a selected quantum state A (which may be the ground state) to an excited intermediate state B lying more than half way to the continuum C. A second photon from the same laser pulse, interacting with/

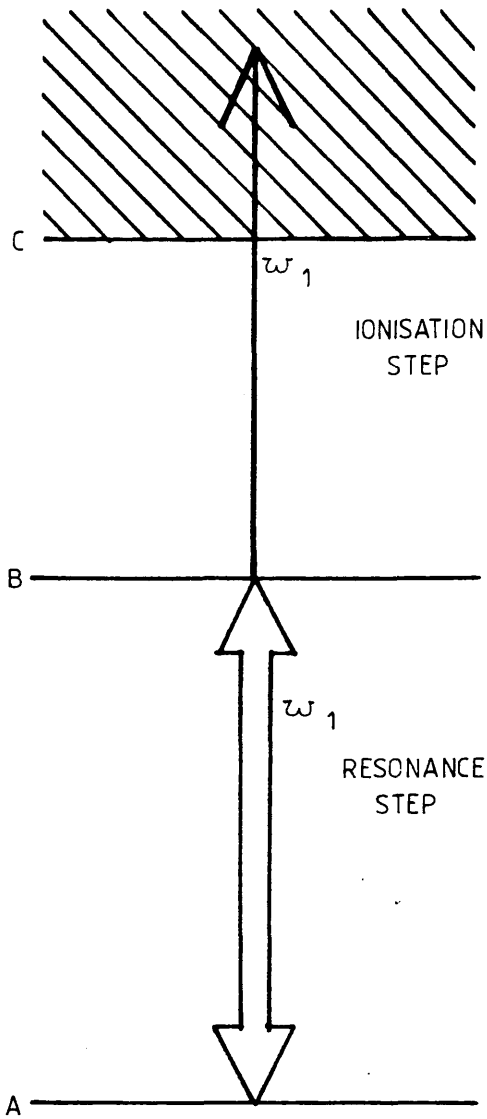

FIG. 1·11 : Two photon resonance ionisation

with the excited atom, removes the electron to the continuum. Since photons may be tuned to a transition of an element which does not coincide with the spectral line of any other element, elemental selectivity is possible. Also, with high incident laser fluence (number of photons/cm^2 of beam area) the above process may be made 100% efficient, i.e. saturated. Since detectors exist which are 100% efficient for observation of the electron (or positive fragment) generated by the laser, e.g. proportional counters, electron multipliers, it is possible to accurately and directly probe the population of any selected quantum state of an atom, including the ground state, by RIS.

1-2 A Short History of RIS

I Early Experiments

RIS was named, and first used, in 1975 (9) in an experiment to directly measure the population of the He (2^1s) metastable state generated by proton excitation. Atoms in the 2^1s level were resonantly ionised via the 3^1p intermediate state by the absorption of two photons at λ = 501.5 nm, and detected using an ionisation chamber. Laser fluence of around 1 J/cm^2 was required to saturate the process. Later, saturation was demonstrated at lower incident laser power by the use of single photon excitation to 3^1p, followed by an associative ionisation step involving collision between atoms in 3^1p and ground state He atoms (10). Although this early work utilised an excited state as the lower level of the resonance ionisation process, the possibility/

possibility of extending the technique to the ionisation of ground state atoms was apparent.

II Single Atom Detection

A sample of caesium metal was sealed into a proportional counter through which P-10 counter gas (10% CH_4 in Ar) was pumped at a pressure of 100 torr. Two photon resonance ionisation from the ground state $6^2s_{\frac{1}{2}}$ via the intermediate levels $7^2p_{\frac{3}{2}}$ and $7^2p_{\frac{1}{2}}$ was achieved. Sharp resonances were observed at the expected wavelengths of 455.5 nm and 459.3 nm, and saturation (i.e. 100% conversion of ground state Cs to the continuum) was shown to be possible. Populations of Cs atoms in the range 10^2 to 10^6 were detected (calibration being to 6.4 keV x-rays from a $^{57}_{27}Co$ source) and statistical fluctuations in the numbers of atoms in a small well-defined region of space, i.e. the laser volume, were studied. The detection of single atoms of Cs (calibrated by the exponential-like pulse height distribution generated by single photoelectrons ejected from the counter walls when exposed to a Hg lamp) was demonstrated (11,12,13).

The following year - 1978 - detection of single atoms of ytterbium was achieved (14). A three-step photo-excitation process was used to promote atoms to the 17^3p_2 Rydberg level; followed by electric-field ionisation.

III Single Molecule Detection

Molecular CsI above a heated, solid, crystalline source was photo-dissociated/

photo-dissociated by an ultraviolet laser (λ = 317.5 nm). A second, larger laser beam (λ = 459.3 nm), fired co-axially with the first but after a variable delay, served to detect Cs atoms still within the detector laser volume at an arbitrary time after their production (13,15). Since both dissociation and detection stages of the experiment could be saturated, the experiment was considered proof of the feasibility of detection of single CsI molecules by RIS.

IV Diffusion Studies

Using similar instrumentation and experimental techniques to those used to study CsI dissociation (15), the rate of diffusion of Cs atoms in Ar gas was investigated (16). At low Ar pressures, i.e. 100 torr, the rate of disappearance of Cs from the detector laser volume could be attributed virtually entirely to diffusion processes. At higher Ar pressures, reaction of Cs with impurities became significant. A value of the diffusion coefficient D for the alkali atom of 0.12 $cm^2 s^{-1}$ (at 1 atm. Ar) was obtained. Small concentrations of O_2 were added to the counter which greatly enhanced the rate at which Cs was removed from the counter volume.

By improving the experimental design to incorporate a detector laser which was not co-axial with the dissociating laser, and which could be positioned at a variable distance from it, more precise measurement of D (i.e. to an uncertainty of $\pm$ 5%) was possible (17). From this work, D = 0.217 cm^2 s^{-1} (normalized to 760 torr) for the diffusion of Cs in P-10 gas. The value for Cs in Ar is expected to be similar and the discrepancy between this value and the earlier result was attributed to uncertainties in the quality and diameter of the laser beams/

beams used in the first study (10).

V Decay-Daughter Coincidence Detection

Detection of single Cs atoms was demonstrated under the adverse conditions associated with ionisation tracks (18). Cs was produced as a radioactive species by the spontaneous fission of $^{252}_{98}Cf$. The ionisation associated with the passage of the fission product nuclide through the counting gas was swept on to a plate before the laser, tuned to either 455.5 nm or 459.3 nm, was fired. The laser linewidth was broad (0.4 nm) to encompass any isotope shift effects - and all Cs isotopes were resonantly ionised and detected in a proportional counter. Since the decay of the parent nuclide $^{252}_{98}Cf$ was used to trigger the laser apparatus, and since the decay product ^{n}Cs was detected in time coincidence with its formation, this type of experiment became known as Decay-Daughter Coincidence Counting. An experimental result suggesting $(8.5 \pm 2.2)\%$ of the $^{252}_{98}Cf$ heavy mass peak are Cs atoms was obtained; comparable with the calculated value of 7%. It was also discovered that Cs atoms stopped (thermalised) in the gas tended to be neutral and not Cs^{+1} as was previously assumed.

VI Resonance Ionisation Spectroscopy with Amplification (RISA)

RISA is a technique whereby atoms ionised or raised to Rydberg (i.e. highly excited, s-like) states by laser photons are then returned to the ground state by collisional processes and made avaliable for re-excitation (19). The cyclic photo-ionisation schemes so created enable more than one electron to be extracted and detected from each atom/

atom of the target species. Thus, signals arising from very small populations of atoms may be enhanced and their number ascertained with greater precision.

Two possible photo-ionisation cycles for RISA are shown in Figure 1.21. In the charge transfer process, atoms are ionised in the usual way by, for example, two photon resonance ionisation involving a ground state 0, an intermediate state 1, and the continuum C. Collision between the ionised species A^+ and another molecule or atom M returns species A to its ground state: i.e. A^o is regenerated.

i.e. $$A^+ + M \longrightarrow A^o + M^+$$

In the Penning ionisation scheme, the target species A is resonantly excited by two dissimilar laser photons to a Rydberg state 2. Collision with foreign bodies again de-excites the A* to the ground state species A^o. An electron is ejected from the colliding species M and may be detected in the same way as a photoionisation-produced electron.

$$A^* + M \longrightarrow A^o + M^+ + e^-$$

VII Elemental and Molecular Detection using Resonance Ionisation Spectroscopy

Following the early work which involved mainly caesium, a number of elements were detected, in the gas phase, by laser ionisation studies. Hurst and co-workers proceeded to detect atomic lithium (20) which had been photodissociated from LiI vapour in a similar way to the method used for the detection of caesium from CsI (13,15). Lithium was ionised by three photons, two of which were resonant.

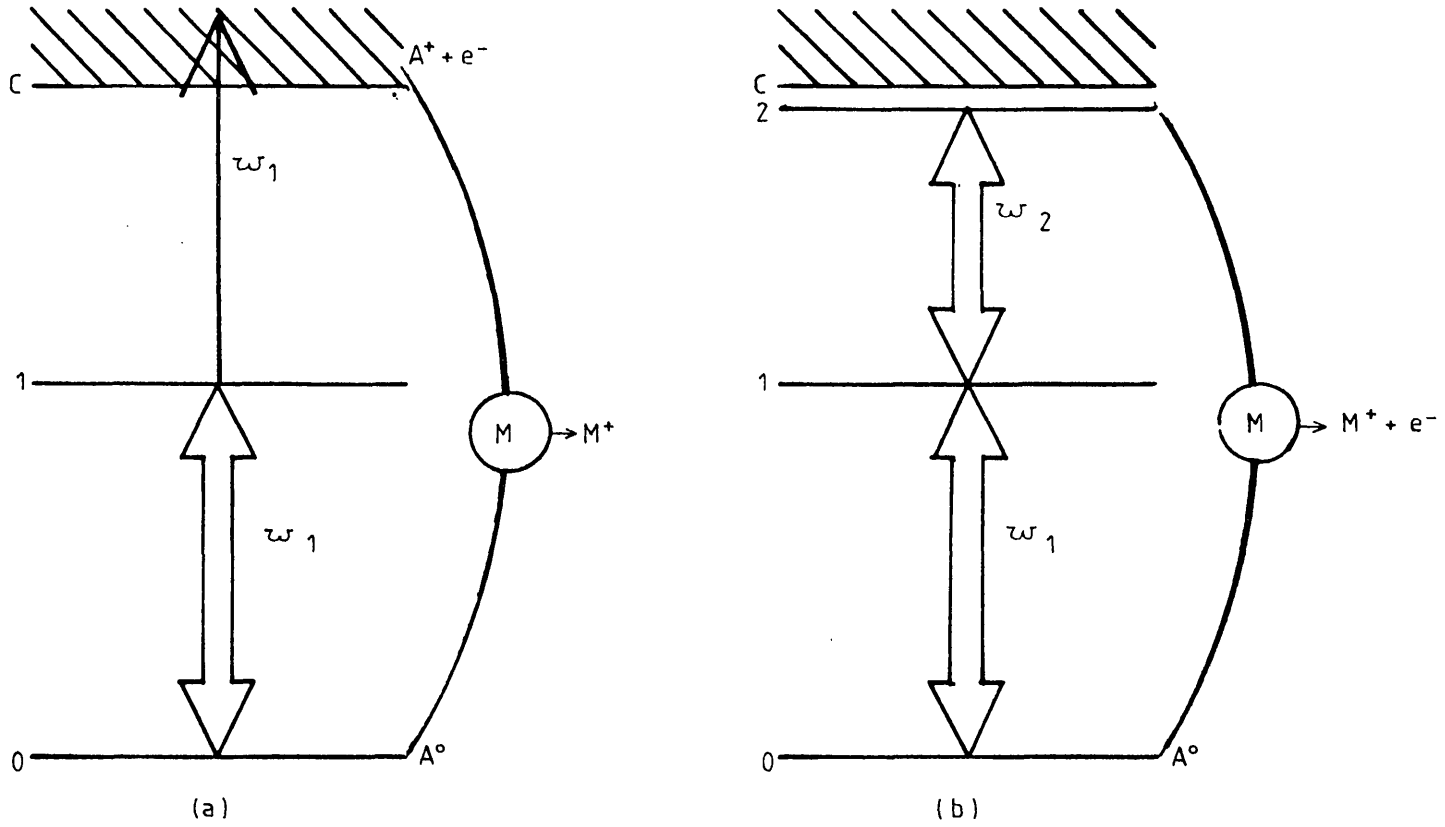

FIG. 1·21: Photoionisation cycles for RISA (a) Charge transfer
(b) Penning ionisation

Bekov and Letokhov, working in Russia, designed and developed a sophisticated laser-based technique capable of trace element determination in natural objects (7,21,22). A solid or liquid sample is placed in a collimated crucible, inside a graphite tube, under vacuum. After evaporating to dryness, the crucible is heated, in temperature increments of a few hundred degrees, and a beam of atoms emanates which may be probed with tunable laser radiation. Resonant excitation of the atomic vapour is followed by electric field ionisation of Rydberg levels. A reference atomic beam, from an oven containing the element under study, was also incorporated for fine tuning of the laser system.

Aluminium in water, e.g. river samples, surface water from the Mediterranean and pore water in Indian Ocean sediments, has been detected (21) at the μgl^{-1} level ($\equiv$ ppb). The sodium content of CdS crystals and the sodium, aluminium and boron contents of high-purity germanium were determined, as was aluminium in human blood (7). Ruthenium in natural oceanic objects e.g. sediment, seawater and fish-bones could be assayed at sub-ppm levels (22).

Rubidium has been studied and collisionally induced ionisation of Rydberg levels was observed by Bushaw and Whitaker (23), who also investigated hyperfine levels of xenon in a doppler-free environment using counterpropagating lasers (24). At the same laboratory, a device for routine analysis of mercury in air was constructed (25).

The halogens too have received attention. Both chlorine and bromine have been detected at around the 10^5 atom level by (two photon resonant)/

resonant) three photon ionisation (26,27). In this work, the ionising laser also served to pyrolyse simple, molecular precursors to produce free halogen atoms. Although the lowest excited state of fluorine at 95.5 nm is well outside the range of commercial laser systems, resonance ionisation using three 286 nm photons to achieve excitation has proved feasible (28).

Not only atomic species can be detected by RIS: molecules too are amenable to study provided they have energy levels suitable for multi-photon ionisation. For example, as early as 1979, aniline (C_6H_7N) was detected in laboratory air as a demonstration of the feasibility of monitoring atmospheric pollutants by laser two-photon ionisation (29). Since that time, a large number of molecules, ranging from simple diatomics to relatively complex organometallic species, have been studied. For an overview of the work to date in this area of laser ionisation studies, the reader is referred to El-Sayed's review article.(30).

RIS has been carried out in liquids as well, and two-photon ionisation spectra of a number of organic solutes in n-pentane have now been recorded (31). From these spectra, solvated phase ionisation potentials of the dissolved species were determined which are considerably lower than gas phase values, the difference being attributed to the influence of the liquid medium on the photoionisation process. Non-resonant detection of aromatic molecules in hexane using a N_2 laser (λ = 337 nm) has been reported (32) with a view to improving the sensitivity of the technique by incorporating a dye laser to allow resonant ionisation.

VIII Resonance Ionisation Mass Spectrometry (RIMS)

The scope of an analytical instrument combining the elemental selectivity of RIS with the mass selectivity of mass spectrometry was realised in 1980 (33). In such a device, the non-selective electron gun ioniser or thermal emission source of a conventional mass spectrometer would be replaced by a laser which could be tuned to ionise only a selected elemental or molecular species. For a chosen element, as long as the laser bandwidth is broad enough to ionise all isotopes with equal probability, the mass spectrum output will accurately reflect the isotopic composition of the species in the sample with which the laser is resonant.

RIMS (34) was first demonstrated with potassium (35). Using two photon resonance ionisation (λ = 404.4 nm) in conjunction with a quadrupole mass spectrometer tuned to alternately pass $^{39}_{19}K$ and $^{41}_{19}K$ atoms, an isotope ratio $^{39}_{19}K : ^{41}_{19}K$ of 13.6 : 1 was determined. This agrees well with the ratio expected from natural abundance data of 13.5 : 1.

It was thought that the RIMS system used for this work could be improved by the replacement of the quadrupole mass spectrometer with a time-of-flight (TOF) system. The principal advantage of the TOF device is that ions of all masses are collected at each laser pulse whereas the quadrupole is tuned to pass only a selected mass/charge ratio at each pulse. Thus, variations in ionising laser fluence are allowed for in the TOF system but may introduce errors when a quadrupole mass spectrometer is used.

Quadrupole systems, however, were successfully applied to the detection of the noble gases Xe and Kr (38,36,37). Resonantly ionised atoms were passed through a quadrupole mass filter and implanted into a target medium. When all the atoms of interest had been counted and implanted, residual gas in the spectrometer was pumped out. By heating the target, implanted atoms were then released for a second pass through the quadrupole. By such an iterative process, isotope enrichment of the gas within the chamber was possible. An atom buncher was also used to reduce counting time. 10^3 atoms of ^{81}Kr were detected in a sample containing 10^{10} - 10^{12} unlike atoms.

Donohue and Young, investigating mixtures of neodymium and samarium (which are extremely difficult to separate by chemical means), obtained 'clean', i.e. free from isobaric interference, mass spectra for each element (39). Many transitions were observed for both elements when the laser was tuned over the range 423 - 465 nm (40). Nd and Sm have isotopes associated with nuclear waste so this work demonstrated the possible suitability of RIMS for waste management and monitoring. With similar applications in view, the same workers turned their attention to the detection of plutonium (41). Isobaric interference between $^{238}_{92}U$ and $^{238}_{94}Pu$, and between $^{241}_{94}Pu$ and $^{241}_{95}Am$ was eliminated by tuning the laser to selectively ionise either uranium or plutonium in mixtures (42). Resonant ionisation spectra of several actinide elements were also obtained (43). A more detailed discussion of the applications of RIS and RIMS in nuclear waste monitoring is deferred to chapter 2.

Various/

Various molecules have been studies by resonance ionisation mass spectrometry. For example, Lubman and co-workers have distinguished many compounds by monitoring the wavelength at which their parent ions appear in the mass spectrum. Azulene and naphthalene have been distinguished ($C_{10}H_8$ isomers) in a quadrupole system, and the effect of laser fluence on fragmentation investigated (44). Using supersonic beam techniques to depopulate rotational-vibrational levels and enhance spectral purity, plus TOF mass spectrometry, the isomers of cresol were observed separately (45) as were a number of disubstituted benzenes (46). Aromatic molecules with different isotopes of chlorine and bromine as substituents could also be selectively ionised (47) and detected by RIMS.

At the National Bureau of Standards, Washington, an instrument was developed with the capacity for multielement determination: it could detect a large selection of elements without need for any alteration in the incident lasers or detection apparatus. The device incorporated a tunable ultraviolet laser system (frequency doubled, Nd:YAG pumped dye) and a magnetic sector mass spectrometer with thermal evaporation source. Preliminary work on molybdenum, rhenium and vanadium (48) was followed by the determination of eighteen, separately loaded elements within the wavelength range of a single laser dye (292 - 304 nm) (49). A mixed, multi-element sample containing seven species was also studied and resonance ionisation spectra from 282 - 286.5 nm recorded for each component. The iron content of samples of human blood serum and water was then determined (50), demonstrating the feasibility of applying RIMS to some naturally occurring or environmental samples. Modification of the thermal vaporisation source of the mass spectrometer, allowing/

allowing it to operate in a pulsed mode, was found to improve sample utilisation effficiency by a factor of thirty (51).

More recently, RIMS of carbon was demonstrated with the instrument (52). A detection limit of 10^7 atoms/cm^3 was achieved using a graphite-coated treated filament as the carbon vapour source and (two photon resonant) three photon ionisation. The possibility of improving the measurement of ^{14}C in small samples and hence the accuracy of ^{14}C dating is an exciting prospect for RIMS if it ever becomes routinely feasible.

It was shown by a group at Los Alamos, New Mexico, that lutetium could be selectively detected in ytterbium (53). These elements are very difficult to separate chemically. Tantalum was also studied and the possibility of the use of continuous wave rather than pulsed laser ionisation in RIMS suggested (54). Later, using the same spectrometer as in the earlier work, the Lu/Yb measurements were repeated with continuous wave laser radiation (55). Increased selectivity and sensitivity were claimed and calculations indicated that the larger number of atoms within the laser volume of continuous wave systems more than compensated for the lower fluence of the beam. Continuous wave RIMS of barium has since been demonstrated (56) by Bushaw, Whitaker and Cannon.

The same group have also studied strontium by photon-burst spectroscopy (58,57). This is a continuous wave laser based technique in which atoms traversing the beam oscillate between the ground and an excited state, emitting photons (via fluorescence) on each cycle and it is particularly/

particularly applicable where isotopically selective detection is required but no mass spectrometer is available.

IX Analysis of Refractory Solids by Resonance Ionisation Spectroscopy

In order to extend the applicability of RIS to the analysis of solids which are not susceptible to thermal atomisation, an alternative means of vaporising material was required. The method should produce gas phase atoms which accurately represent the composition of the solid. An established technique which fulfills this criterion - secondary-ion mass sepctrometry (SIMS) - uses an ion beam to sputter a plume from a solid surface into the vapour phase. In SIMS, the ions in the plume are then directed into a mass spectrometer for analysis. However, it has been determined that neutral atoms by far outnumber ions in the sputtered plume, i.e. by 10^2 (59). Using RIS it would be possible to analyse the neutral atom population by traversing the sputtered plume with a tunable laser. If the sputtering/ionisation apparatus were to be incorporated into a mass spectrometer, isotope sensitive, element selective analysis of refractory solids becomes feasible.

RIS of sputtered material was first demonstrated at Pennsylvania State University in 1982 (60). A pulsed beam of Ar^+ ions directed, at an angle, on to an indium surface, sputtered neutral In atoms into the path of a mixed Nd:YAG / dye laser beam at 410.1 nm where they were resonantly ionised. A quadrupole mass spectrometer detected the laser induced ions but the secondary ions produced at the In surface were excluded by time-gating the detector. Sensitivity far greater

than/

than that achievable by SIMS was predicted for the laser ionisation method.

Hurst and co-workers at Atom Sciences Inc. also developed apparatus for sputter-initiated resonance ionisation spectroscopy (SIRIS). Their device employed a pulsed Ar^+ ion source for sputtering material from sample surfaces, a tunable Nd:YAG pumped dye laser to ionise the sputtered neutrals, and a double focusing mass spectrometer to detect the laser-generated ions (61,62,63). In initial tests, 1 part in 10^4 of Ga doped into Si was detected (61). Sensitivity was later improved to the 0.5 and even 0.05 ppm level for the same type of substrate (62,63). The Al and V contents of stainless steel standards were determined to the ppm level; and In in Si was detected at even lower concentration (63,62). A sensitivity of 1 part in 10^{12} for routine analysis is prospected for the SIRIS equipment produced by Atom Sciences (63,62).

Continued work on In by Winograd and co-workers revealed a variation in neutral/ion ratio in the sputtered plume when the In surface was oxidised to In_2O_3, with In^+ increasing at the expense of In^o as oxygen was added (64). The effects of various experimental factors, including duty cycle, primary ion current, laser dimensions and positioning on measured ionisation were studied in detail (59).

An alternative method of evaporating for RIS is laser ablation. Laser ablation resonance ionisation spectroscopy (LARIS) has detected Na impurities in Si at $\sim$1 part in 10^{11} using a proportional counter, i.e. without mass filtering (65). The Si sample was vaporised by an incident/

incident focused laser beam at 590 nm and Na atoms in the ablation plume resonantly ionised. Laser ablation with resonant ionisation and (time-of-flight) mass detection has been used to investigate chromium in a stainless steel sample (66). All four stable isotopes were observed, their ratios corresponding quantitatively to relative natural abundance data. Non-selective laser ionisation of the same sample revealed considerable isobaric interference between the various isotopes of iron, vanadium, cobalt and chromium presnt in the 50 - 59 amu mass region (66). This was not apparent in the resonant ionisation spectrum.

Various other RIMS groups have also begun analysis of refractory solids by RIS. Donohue's group have modified an existing ion microprobe mass analyser (with continuous primary ion beam) and observed signals from Sm and U metal samples embedded in plastic (67). Lubman and Tembreull have used laser desorption in combination with their supersonic beam/mass spectrometer apparatus; studying organic compounds which are prone to decomposition when thermally evaporated (68). Pulsed desorption has also been used to generate Ta atoms from a pre-heated filament (69), a similar technique to that of Fassett (51), except that a laser was used to generate spurts of atoms from the filament instead of a pulsed applied current.

Surface analysis by non-resonant multiphoton ionisation has also proved viable (70). SALI (surface analysis by laser ionisation) uses a non-selective ultraviolet laser to ionise sputtered or desorbed atoms. Although the technique suffers from isobaric interference, as does conventional mass spectrometry, it does not require tunable lasers/

lasers and is suitable for rapid analyses. Impurities present in a Cu standard at the ppm level were assayed by this method (70).

X Summary

Resonance ionisation spectroscopy and its variants RIMS and SIRIS/LARIS have now been applied to a number of problems, most of them analytical. Although by no means exhaustive, the foregoing review hopes to illustrate some of the principal achievements of the technique during its first decade. A table (Table 1) summarising the elements studied (at the time of writing and to the knowledge of the author) and ionisation schemes and laser wavelengths used, follows.

TABLE 1

Elements and Suitable Ionisation Schemes

Element	Ionisation Scheme *	Wavelength(s) (nm.) ‡	Reference
Lithium	$Li\left[w_1, w_2, We^-\right]Li^+$	w_1 670·8	(20)
		w_2 610·4	
Carbon	$C\left[w_1 w_1, w_1 e^-\right]C^+$	w_1 287·0	(52)
Fluorine	$F\left[w_1 w_1 w_1, w_1 w_1 e^-\right]F^+$	w_1 286	(28)
Sodium	$Na\left[w_1, w_2, Ee^-\right]Na^+$	w_1 589·0	(8)
		w_2 418·0	
		E >10·6 kV/cm.	
	$Na\left[w_1, w_2, We^-\right]Na^+$	w_1 589·6 or 589·0	(65)
		w_2 568·8 or 568·2	

Aluminium/

TABLE 1 (cont.)

Element	Ionisation Scheme *	Wavelength(s) (nm.) ‡	Reference
Aluminium	$Al[w_1, w_2, Ee^-]Al^+$	w_1 396·15	(8)
		w_2 447·4	
		E 13 kV/cm.	
	$Al[w_1, w_2 e^-]Al^+$	w_1 309·3	(62)
		w_2 618·6	
Chlorine	$Cl[w_1 w_1, w_1 e^-]Cl^+$	230 - 245	(27)
Potassium	$K[w_1, w_1 e^-]K^+$	w_1 404·4	(35)
Titanium	$Ti[w_1, w_1 e^-]Ti^+$	292 - 304	(49)
Vanadium	$V[w_1, w_1 e^-]V^+$	292 - 304	(49)
		282 - 286·5	(49)
	$V[w_1, w_1 e^-]V^+$	w_1 294·24 or 294·32	(48)
	$V[w_1, w_1 e^-]V^+$	w_1 318·4	(62)
Chromium	$Cr[w_1, w_2 e^-]Cr^+$	w_1 425·4	(66)
		w_2 308·0	
Iron	$Fe[w_1, w_1 e^-]Fe^+$	w_1 283·6	(50)
	$Fe[w_1, w_1 e^-]Fe^+$	292 - 304	(49)
		282 - 286·5	(49)
Cobalt	$Co[w_1, w_1 e^-]Co^+$	292 - 304	(49)
		282 - 286·5	(49)
Nickel	$Ni[w_1, w_1 e^-]Ni^+$	292 - 304	(49)
		282 - 286·5	(49)
Gallium	$Ga[w_1, w_2 e^-]Ga^+$	w_1 287·5	(61)
		w_2 575·0	
Bromine	$Br[w_1 w_1, w_1 e^-]Br^+$	240 - 285	(26)
Krypton/			

TABLE 1 (cont.)

Element	Ionisation Scheme *	Wavelength(s) (nm.) ‡	Reference
Krypton	$Kr[w_1, w_2, w_3 e^-]Kr^+$	w_1 116•5	(37)
		w_2 558•1	
		w_3 1064•0	
Rubidium	$Rb[w_1, w_2, \text{collision } e^-]Rb^+$	w_1 780	(23)
		w_2 478 – 516	
	$Rb[w_1, w_2 e^-]Rb^+$	w_1 421•5 or 420•2	(71)
		w_2 694•3	
Strontium	$Sr[w_1, w_1 e^-]Sr^+$	292 – 304	(49)
Yttrium	$Y[w_1, w_1 e^-]Y^+$	292 – 304	(49)
Zirconium	$Zr[w_1, w_1 e^-]Zr^+$	292 – 304	(49)
Molybdenum	$Mo[w_1, w_1 e^-]Mo^+$	292 – 304	(49)
	$Mo[w_1, w_1 e^-]Mo^+$	w_1 313•26	(48)
Ruthenium	$Ru[w_1, w_2, w_3, Ee^-]Ru^+$	w_1 392•59	(22)
		w_2 633•05	
		w_3 567•3	
		$E \leq 10$ kV/cm.	
Indium	$In[w_1, w_1 e^-]In^+$	292 – 304	(49)
	$In[w_1, w_1 e^-]In^+$	w_1 410•1	(64)
	$In[w_1, w_2 e^-]In^+$	w_1 303•8	(60)
		w_2 607•7	
Xenon	$Xe[w_1 w_1, w_1 e^-]Xe^+$	w_1 256•02	(24)
	$Xe[w_1 w_1, w_1 e^-]Xe^+$	w_1 252•6 or 249•6	(36)
	$Xe[w_1 w_1, w_2 e^-]Xe^+$	w_1 252	(73)
		w_2 504	
Caesium	$Cs[w_1, w_1 e^-]Cs^+$	w_1 455•5	(11)
** Barium	$Ba[w_1, w_2, w_3 e^-]Ba^+$		(56)

Neodymium/

TABLE 1 (cont.)

Element	Ionisation Scheme *	Wavelength(s) (nm.) ‡	Reference
Neodymium	various	423 - 463	(40)
	$Nd[W_1, W_1e^-]Nd^+$	W_1 425•8	(39)
Samarium	various	423 - 463	(40)
	$Sm[W_1, W_1e^-]Sm^+$	W_1 429•9	(39)
	$Sm[W_1, W_1, W_1e^-]Sm^+$	580 - 607	(67)
Dysprosium	$Dy[W_1, W_1e^-]Dy^+$	292 - 304	(49)
Erbium	$Er[W_1, W_1e^-]Er^+$	292 - 304	(49)
Ytterbium	$Yb[W_1, W_2, W_3, Ee^-]Yb^+$	W_1 555•6	(14)
		W_2 679•96	
		W_3 595•0 - 577•0	
		E 14 kV/cm.	
Lutetium	$Lu[W_1, W_1e^-]Lu^+$	292 - 304	(49)
		282 - 286•5	(49)
	$Lu[W_1, W_1e^-]Lu^+$	W_1 452	(53)
Hafnium	$Hf[W_1, W_1e^-]Hf^+$	292 - 304	(49)
Tantalum	$Ta[W_1, W_1e^-]Ta^+$	292 - 304	(49)
	$Ta[W_1W_1, W_1e^-]Ta^+$	W_1 454•92	(69)
Rhenium	$Re[W_1, W_1e^-]Re^+$	292 - 304	(49)
	$Re[W_1, W_1e^-]Re^+$	W_1 299•236	(48)
Mercury	$Hg[W_1, W_2, W_2e^-]Hg^+$	W_1 253•73	(25)
		W_2 435•95	
Lead	$Pb[W_1, W_1e^-]Pb^+$	282 - 286•5	(49)
Thorium	$Th[W_1, W_1e^-]Th^+$	292 - 304	(49)
	various	580 - 607	(43)
Uranium/			

TABLE 1 (cont.)

Element	Ionisation Scheme *	Wavelength(s) (nm.) ‡	Reference
Uranium	$U[W_1, W_1 e^-]U^+$	292 - 304	(49)
		282 - 286·5	(49)
	various	580 - 607	(43)
	$U[W_1, W_1, W_1 e^-]U^+$	W_1 591·54 or 596·92	(67)
	$U[W_1, W_1, W_1 e^-]U^+$	W_1 591·54	(42)
	$U[W_1, W_1, W_1 e^-]U^+$	W_1 591·5	(72)
	$U[W_1 W_1, W_1 e^-]U^+$	W_1 585	(73)
Neptunium	various	580 - 607	(43)
Plutonium	$Pu[W_1, W_1 e^-]Pu^+$	W_1 431·1	(41)
		430 - 450	(41)
	$Pu[W_1, W_1, W_1 e^-]Pu^+$	W_1 588·04	(42)
	$Pu[W_1 W_1, W_1 e^-]Pu^+$	W_1 595	(73)
	$Pu[W_1, W_2, W_3 e^-]Pu^+$	W_1 586	(74)
		W_2 688	
		W_3 578	
	various	580 - 607	(43)
Americium	various	580 - 607	(43)

* for an explanation of the notation used see reference (75).

‡ where a range is given, several multiphoton transitions were observed within the quoted region.

** CW lasers used.

In concluding this section, it is interesting to compare the sensitivity of RIS with those of existing, currently used analytical techniques. This is presented in Table 2 (which is taken from references 7 and 8).

TABLE 2

Comparison of Various Analytical Techniques

Method	Detection Limit % *(Calibrated Solutions)	Detection Limit % *(Real Samples)	Selectivity for Elements
Atomic Absorption Spectrometry	10^{-4} - 10^{-9}	10^{-4} - 10^{-7}	moderate
Neutron Activation Analysis	10^{-5} - 10^{-9}	10^{-5} - 10^{-9}	moderate
Spark Mass Spectrometry	10^{-6} - 10^{-8}	10^{-5} - 10^{-7}	high
Laser Fluorescence Spectrometry	10^{-6} - 10^{-11}	10^{-5} - 10^{-8}	high
Laser Stepwise Photo-ionisation Spectrometry (RIS)	10^{-11} - 10^{-14}	10^{-8} - 10^{-11}	ultrahigh

* detection limits achieved for calibrated solutions are measurements carried out under near-ideal conditions. Measurements in real samples may suffer from a variety of matrix effects or from interference, reducing sensitivity.

The detection limits of RIS are up to three orders of magnitude lower than those of any other analytical technique, and it has the greatest elemental selectivity. Thus, RIS is amenable to widespread application wherever extreme sensitivity and selectivity is required.

1-3 Theory

I Multiphoton Ionisation

The simplest form of multiphoton ionisation - two photon ionisation - involves the absorption of two quanta of light by a single atom, promoting it from a ground state to the continuum. Two photon resonant ionisation is shown in Figure 1.31 and described below.

A photon from an intense light source, i.e. a pulsed laser beam, is tuned to exactly the correct wavelength to raise an atom from an initial state 0 to an excited state 1: i.e.

$$h\omega = E_1 - E_0 \qquad \text{---- 1}$$

where h is Planck's constant,

ω is the frequency of the laser,

E_1 is the energy of state 1, and

E_0 is the energy of state 0.

A second photon from the same laser pulse can photoionise the atom in state 1 since

$$h\omega > E_c - E_1 \qquad \text{---- 2}$$

where E_c is the energy of the ionisation threshold

i.e. the ionisation potential of the atom in the laser beam.

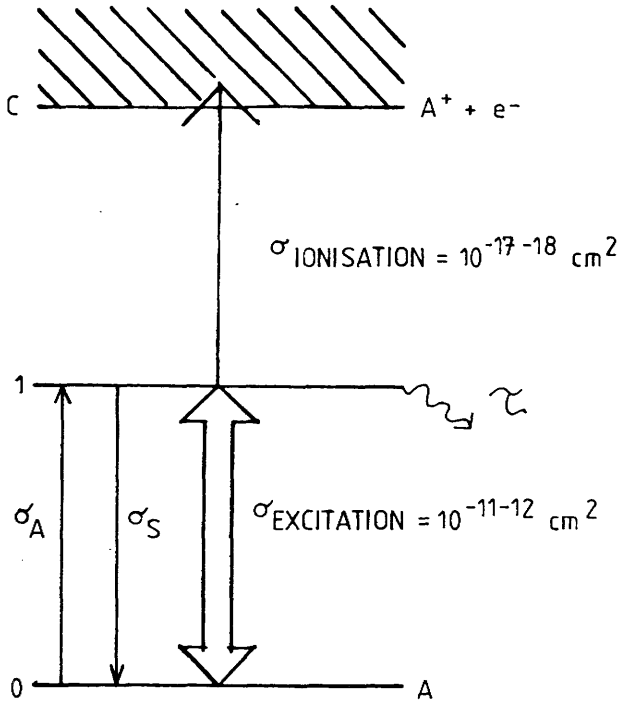

FIG. 1·31: TWO PHOTON RESONANCE IONISATION.

During the laser pulse an equilibrium is set up in which the rate of stimulated emission from state 1 to state 0 σ_S equals the rate of production of state 1 by absorption σ_A . (In actuality, only a quasi-equilibrium is established because the population of state 2 is continuously depleted by ionisation.) Ionisation of state 1 occurs more slowly than transitions between states 0 and 1. Typical cross sections are, for excitation, $\sigma_{EXCITATION} = 10^{-11} - 10^{-12}$ cm^2, and for ionisation, $\sigma_{IONISATION} = 10^{-17} - 10^{-18}$ cm^2 (7).

Saturation is a term given to the condition where all atoms within the laser beam of the correct type to energy match with the laser photons are converted to ion pairs during the light pulse. Since the cross section for ionisation is much smaller than that for excitation, more incident laser power is required to saturate the ionising transition than the bound-bound transition. However, with commercially available pulsed lasers, both excitation and ionisation stages of the resonance ionisation process may be saturated.

II Saturation Conditions

To resonantly ionise all state 0 atoms within the laser volume, the laser power and the atomic cross sections for excitation and ionisation must fulfill a number of criteria.

Firstly, the laser fluence, i.e. no. of photons per unit area of beam multiplied by the ionisation cross section, must be substantially greater than unity, i.e. the fluence condition is

$$\phi \sigma_{IONISATION} \gg 1 \qquad \text{---- 3}$$

where ϕ is the fluence.

Secondly, the laser flux, i.e. number of photons per unit area of beam per unit time, must be large enough to compensate for the rate at which the intermediate level 1 can be destroyed by processes such as collisions, which de-excite atoms in state 1 to non-photo-ionisable species.

The flux condition is

$$\sigma_{EXCITATION} \bar{\Phi} \gg \frac{1}{\tau} \qquad \text{—— 4}$$

where $\bar{\Phi}$ is the flux, and

τ is the mean lifetime of state 1.

From equation 4 it is obvious that the flux condition is easier to satisfy if the intermediate level chosen for resonance ionisation is of long lifetime. Therefore, resonance ionisation through a real excited state ($\tau \sim 10^{-8}$ s) is generally easier to saturate than resonance ionisation via a virtual state ($\tau \sim 10^{-15}$ s).

It can be shown that the flux and fluence conditions must be fulfilled for saturation to occur, as follows:-

For the scheme shown in Figure 1.31, the rates of change of the populations of states 0, 1 and C are given by

$$\frac{dN_0}{dt} = -N_0\sigma_A\bar{\Phi} + \frac{N_1}{\tau} + N_1\sigma_A\bar{\Phi} \qquad \text{—— 5}$$

$$\frac{dN_1}{dt} = N_0\sigma_A\bar{\Phi} - \frac{N_1}{\tau} - N_1\sigma_A\bar{\Phi} - N_1\sigma_I\bar{\Phi} \qquad \text{—— 6}$$

$$\frac{dN_I}{dt} = N_1\sigma_I\bar{\Phi} \qquad \text{—— 7}$$

where/

where N_0, N_1 and N_I are the numbers of atoms in states 0, 1 and C respectively,

Φ is the flux,

σ_A is the stimulated absorption cross section (state 0 $\longrightarrow$ state 1),

σ_I is the ionisation cross section (state 1 $\longrightarrow$ continuum),

τ is the spontaneous emission cross section of state 1;

and assuming i) $\sigma_A = \sigma_S$

where σ_S is the stimulated emission cross section (state 1 $\longrightarrow$ state 0),

ii) deactivation of state 1 leads only to state 0;

adding equations 5 and 6,

$$\frac{dN_0}{dt} = -\frac{dN_1}{dt} - N_1\sigma_I\Phi \qquad \text{—— 8}$$

differentiating equation 6 w.r.t. time, and using equation 8,

$$\frac{d^2N_1}{dt^2} = \sigma_A\Phi\frac{dN_0}{dt} - \frac{1}{\tau}\frac{dN_1}{dt} - \sigma_A\Phi\frac{dN_1}{dt} - \sigma_I\Phi\frac{dN_1}{dt}$$

$$= -\sigma_A\Phi\frac{dN_1}{dt} - \sigma_A\sigma_I\Phi^2N_1 - \frac{1}{\tau}\frac{dN_1}{dt} - \sigma_A\Phi\frac{dN_1}{dt}$$

$$- \sigma_I\Phi\frac{dN_1}{dt}$$

$$= \frac{dN_1}{dt}\left[-\sigma_A\Phi - \frac{1}{\tau} - \sigma_A\Phi - \sigma_I\Phi\right] - \sigma_A\sigma_I\Phi^2N_1$$

So $$\frac{d^2N_1}{dt^2} + \left[(2\sigma_A + \sigma_I)\,\underline{\Phi} + \frac{1}{\tau}\right]\frac{dN_1}{dt} + \sigma_A\sigma_I\,\underline{\Phi}^2 N_1 = 0$$

Let $$(2\sigma_A + \sigma_I)\,\underline{\Phi} + \frac{1}{\tau} = 2b \qquad \text{—— 9}$$

and $$\sigma_A\sigma_I\,\underline{\Phi}^2 = w^2 \qquad \text{—— 10}$$

$$\frac{d^2N_1}{dt^2} + 2b\frac{dN_1}{dt} + w^2N_1 = 0 \qquad \text{—— 11}$$

If N_1 is of the form $e^{-\lambda t}$, then $\dot{N}_1 = -\lambda e^{-\lambda t}$ and $\ddot{N}_1 = \lambda^2 e^{-\lambda t}$ and equation 11 becomes

$$\lambda^2 - 2b\lambda + w^2 = 0$$

This is a quadratic in λ, and the roots are given by

$$\lambda = \frac{2b \pm \sqrt{4b^2 - 4w^2}}{2}$$

$$\lambda_1 = b - \sqrt{b^2 - w^2} \qquad \lambda_2 = b + \sqrt{b^2 - w^2} \qquad \text{—— 12 (a,b)}$$

$$N_1 = Ae^{-(b + \sqrt{b^2 - w^2})t} + Be^{-(b - \sqrt{b^2 - w^2})t}$$

where A and B are constants

$A = -B$ since $N_1 = 0$ at $t = 0$

so $$N_1 = A\left[e^{-\lambda_1 t} - e^{-\lambda_2 t}\right] \qquad \text{—— 13}$$

Putting equation 13 into equation 6 (to find A)

$$A\left[-\lambda_1 e^{-\lambda_1 t} + \lambda_2 e^{-\lambda_2 t}\right] = N_0\,\sigma_A\,\underline{\Phi} + N_1\left[-\frac{1}{\tau} - \sigma_A\,\underline{\Phi} - \sigma_I\,\underline{\Phi}\right]$$

when $t = 0$, $e^{-\lambda t} = 1$ and $N_1 = 0$

$$N_0(0) = \frac{A\left[\lambda_2 - \lambda_1\right]}{\sigma_A \bar{\Phi}}$$

where $N_0(0)$ is the population of state 0 at $t = 0$

$$A = \frac{N_0(0)\, \sigma_A \bar{\Phi}}{\left[\lambda_2 - \lambda_1\right]}$$

and equation 13 becomes

$$N_1 = \frac{N_0(0)\, \sigma_A \bar{\Phi}}{\left[\lambda_2 - \lambda_1\right]} \left[e^{-\lambda_1 t} - e^{-\lambda_2 t}\right] \quad \text{—— 14}$$

Now, assuming state 1 is real, and that the laser is tuned to resonance with it,

$$\sigma_A \gg \sigma_I$$

Equation 9 may be simplified to

$$2b = 2\sigma_A \bar{\Phi} + \frac{1}{\tau}$$

$\Rightarrow$ $b^2 \gg w^2$ $\Rightarrow$ $\lambda_2 \gg \lambda_1$ from equations 9, 10, 12a and 12b

So equation 14 simplifies to

$$N_1 = \frac{N_0(0)\, \sigma_A \bar{\Phi}}{\lambda_2} \left[e^{-\lambda_1 t}\right] \quad \text{—— 15}$$

Since $\lambda_2 \approx 2b \approx 2\,\sigma_A \bar{\Phi} + \frac{1}{\tau}$

$$N_1 = \frac{N_0(0)\, \sigma_A \bar{\Phi}}{2\,\sigma_A \bar{\Phi} + \frac{1}{\tau}} \left[e^{-\lambda_1 t}\right] \quad \text{—— 16}$$

To test whether the flux and fluence conditions (equations 4 and 3) are necessary for saturation, they will be used to calculate $N_I(T)$, the number of atoms ionised within the duration of a rectangular laser pulse of duration T. Assuming the flux condition, equation 16 becomes

$$N_1 = \frac{N_0(0)}{2}\left[e^{-\lambda_1 t}\right] \qquad \text{---- 17}$$

From equation 12a

$$\lambda_1 = b - b\left(1 - \frac{w^2}{b^2}\right)^{\frac{1}{2}}$$

$$= b - b\left(1 - \tfrac{1}{2}\frac{w^2}{b^2}\right) \qquad \text{assuming } b^2 \gg w^2$$

$$= \tfrac{1}{2}\frac{w^2}{b} \qquad = \frac{\sigma_A \sigma_I \bar{\Phi}^2}{2\sigma_A \bar{\Phi} + \frac{1}{\tau}}$$

$$\therefore \quad \lambda_1 = \frac{\sigma_I \bar{\Phi}}{2} \qquad \text{again assuming the flux condition.}$$

From equation 7

$$N_I = \sigma_I \bar{\Phi} \int_0^T N_1$$

$$= \sigma_I \bar{\Phi} \int_0^T \frac{N_0(0)}{2}\left[e^{-\lambda_1 t}\right] \qquad \text{from equation 17}$$

$$= \sigma_I \bar{\Phi} \frac{N_0(0)}{2}\left[-\frac{1}{\lambda_1} e^{-\lambda_1 t}\right]_0^T$$

$$= \sigma_I \bar{\Phi} \frac{N_0(0)}{2}\left[-\frac{1}{\lambda_1} e^{-\lambda_1 T} + \frac{1}{\lambda_1} e^{-\lambda_1 0}\right]$$

$$= \sigma_I \bar{\Phi} \frac{N_0(0)}{2}\left[-\frac{1}{\lambda_1} e^{-\lambda_1 T} + \frac{1}{\lambda_1}\right]$$

Assuming the fluence condition

$$\lambda_1 T \gg 1 \qquad \text{---- 18 *}$$

$$N_I = \frac{\sigma_I \bar{\phi} N_0(0)}{2\lambda_1}$$

$$= \frac{2\,\sigma_I \bar{\phi} N_0(0)}{2\,\sigma_I \bar{\phi}}$$

$$= N_0(0)$$

i.e. where equations 3 and 4 are valid, all atoms in the beam are ionised during the laser pulse, which is the definition of saturation.

Taking typical values of $\sigma_I = 10^{-17} - 10^{-18}$ cm^2

$\sigma_1 = 10^{-11} - 10^{-12}$ cm^2

$\tau = 10^{-8}$ s

$T = 10^{-8}$ s

From the flux condition $\bar{\phi}\,\sigma_1 \gg \frac{1}{\tau}$

The onset of saturation of the excitation step of two photon resonance ionisation occurs when $\phi \gg 10^{11} - 10^{12}$ photons/cm^2

Since the number of photons in 1 J = $5 \times 10^{15} \times \lambda$ (in nm),

saturation occurs when $\phi \gg 4.4 - 0.44$ nJ/mm^2 .

---

* N.B. Equation 18 is a form of the fluence condition, since:

$$\lambda_1 T \gg 1$$

$$\tfrac{1}{2}\,\sigma_I \bar{\phi} T \gg 1$$

$\sigma_I \phi \gg 1$ (the more usual form of the fluence condition)

where ϕ is the fluence

and $\phi = \bar{\phi} T$

From the fluence condition $\phi \sigma_I \gg 1$

The onset of saturation of the ionisation step occurs when

$$\phi \gg 10^{17} - 10^{18} \text{ photons/cm}^2$$

<u>i.e.</u> when $\phi \gg 4.4 - 0.44 \text{ mJ/mm}^2$.

III Resonance Ionisation Spectroscopy of the Elements

Two photon resonance ionisation is not the only possible way in which laser photons may be tuned to detect atoms. Due to the spacing of their atomic levels many ground state elements are not amenable to detection with this scheme; the energy of two photons from within the wavelength range of currently available dye lasers being insufficient to achieve ionisation, or the intermediate level being beyond that which would be accessible with a single photon. Five basic RIS schemes are envisaged by Hurst (2). By the use of these, all of the elements in the periodic table except helium and neon may be resonantly ionised. The notation used to describe the schemes (75) is as follows:

$$\text{———} \quad \left[\text{———} \;,\; \text{———} \;,\; \text{———} \right] \quad \text{———}$$

ATOM — EXCITATION STEP(S) — IONISATION STEP — POSITIVE ATOM

e.g. for the caesium experiments discussed earlier (11,12,13,15,16,17, 18) the element was ionised using a $Cs\left[\omega_1, \omega_1 e^-\right] Cs^+$ process, i.e. caesium atoms were excited by a resonant photon of frequency ω_1 and ionised by a second ω_1 photon generating a free electron e^- and a positive Cs^+ ion.

The five RIS schemes are shown in Figure 1.32. Scheme one is two photon resonance ionisation as already discussed and illustrated in Figures 1.11 and 1.31. In scheme two, in order to reach the excited state, ω_1 is frequency doubled (76) to $2\omega_1$. Ionisation is completed by photons of the fundamental beam at frequency ω_1 . Scheme three is

three/

1 : $A[w_1, w_1 e^-]A^+$

2 : $A[2w_1, w_1 e^-]A^+$

3 : $A[w_1, w_2, we^-]A^+$

4 : $A[2w_1, w_2, we^-]A^+$

5 : $A[w_1 w_1, we^-]A^+$

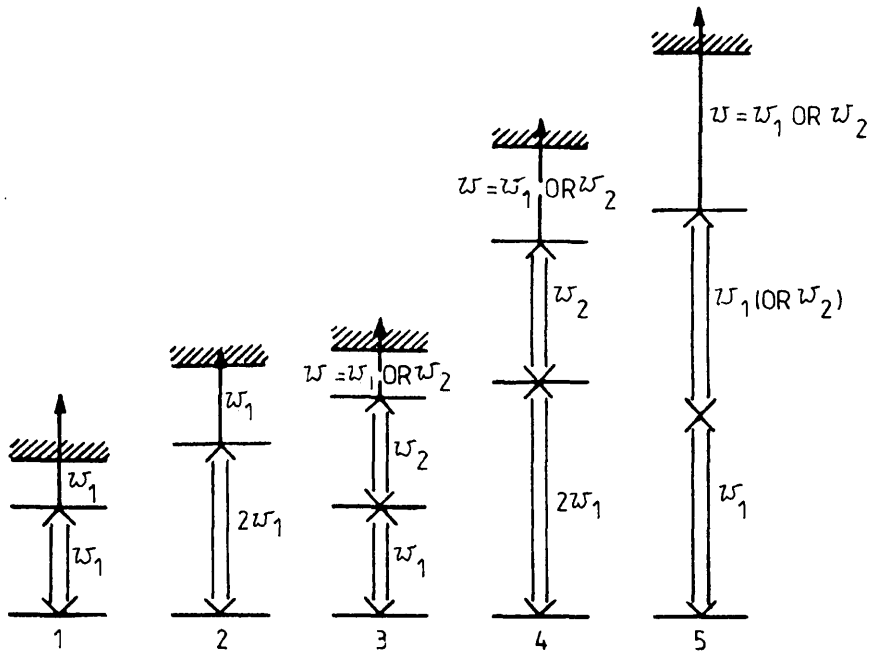

FIG. 1·32 : RIS SCHEMES

three photon ionisation (two photon resonant, one photon ionisation). The first laser, ω_1 , promotes the atom to an excited state where it is then raised to a second, higher-lying excited state by absorption of a photon from a different coloured laser ω_2 . Ionisation is completed by a third photon which may be of either frequency ω_1 or ω_2 . Scheme four is much like scheme three with the exception of the transition to the first excited state which requires a frequency-doubled laser. In schemes one and two time coincidence of the photons required for the various transitions is guaranteed automatically. However, for schemes three and four, space and time synchronisation of more than one laser may lead to experimental difficulties. Scheme five is unique in that the excited level is reached by means of a two photon transition via a virtual intermediate state. Although saturation is more difficult to achieve due to the short lifetime of the virtual level, ionisation via such a level is useful in that it is possible to reach real states for which single-photon transition from the ground state are forbidden, by two photon processes.

Hurst has proposed suitable ionisation schemes for nearly all of the elements (2). These were selected on the basis of the spacing of the element's energy levels, on which type of transitions (one or two photon) are allowed between them, and on the energies of the first excited state and the continuum. The preferred schemes are shown in Figure 1.33, with the symbol for the element in the upper left and the RIS scheme in the lower right. Where uncertainty in the positions of the atomic levels exists, a possible scheme is denoted with a question mark. Twenty three elements are amenable to scheme one resonance/

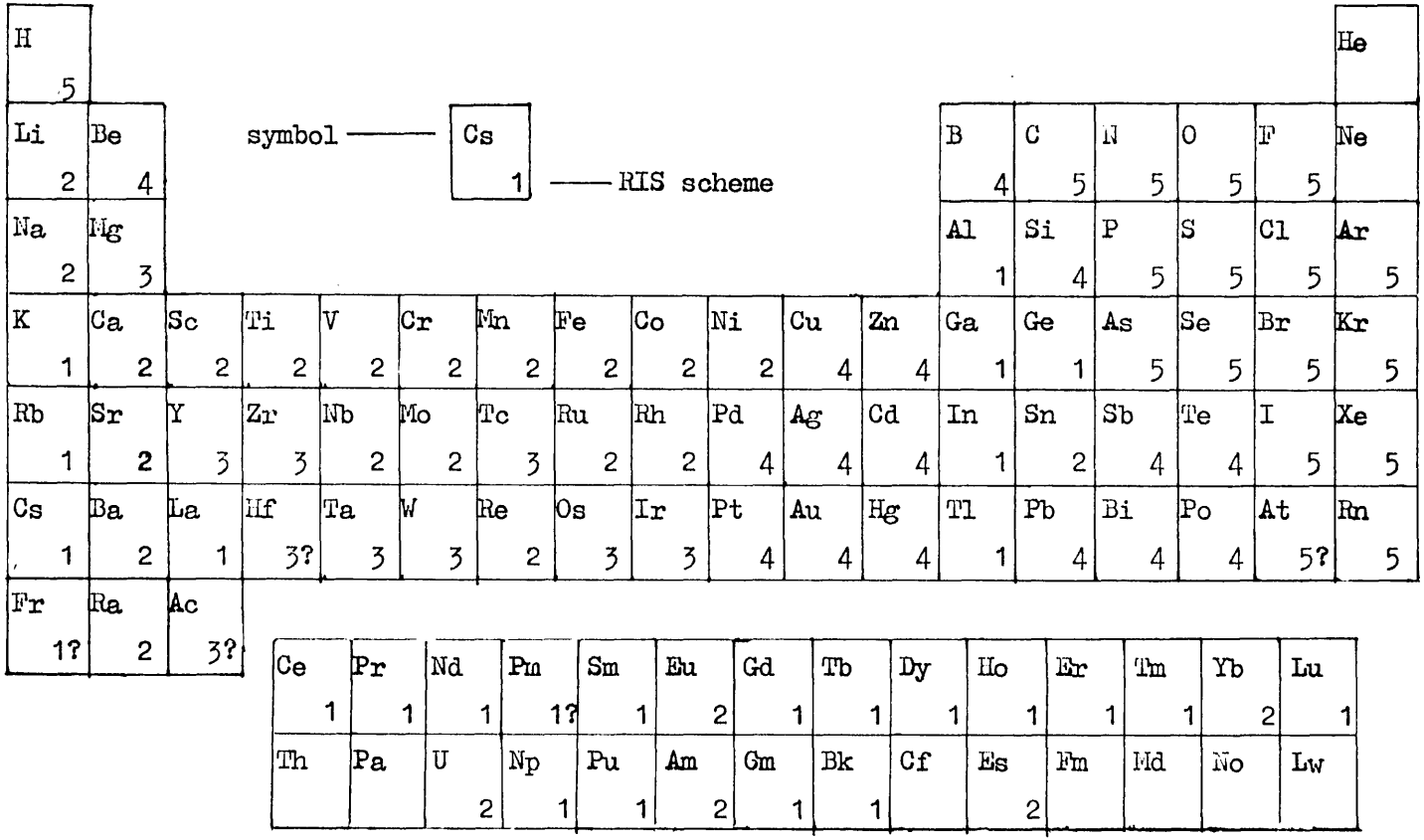

Figure 1.33 RIS schemes for the elements

resonance ionisation and twenty five to scheme two. With two-laser schemes (three to five), most other elements may be ionised.

IV Non-Laser Ionisation-Step Schemes

The use of high laser fluence, such as is necessary to saturate resonance ionisation processes has its associated problems. Firstly, spectral transitions studied may be broadened and resolution lost and, more importantly, background ionisation resulting from low ionisation potential impurities within the detector system may be enhanced, limiting sensitivity. Since it is normally the bound-continuum transition which requires, by orders of magnitude, the highest laser fluence for saturation; the replacement of the laser for the ionisation step by a process which does not involve photons would be desirable. The laser would still be used to excite the atom, but, as saturation of bound-bound transitions can be achieved at lower fluence, background enhancement would thus be minimised. Suitable methods for non-laser ionisation-step RIS are shown in Figure 1.34.

The atom is promoted to a high lying excited level i.e. a Rydberg state R by the usual means. Ionisation is then induced either by an electric field E of $\sim$ 10 - 14 kV/cm (as in method a), or by various collisional processes. Associative ionisation involving either another similar atom A (method b) or a dissimilar, counter gas atom B (method c) produces molecular ions A^+_2 and AB^+ respectively. Counter gas may also act as a catalyst, as shown in method d.

Penning ionisation, as proposed for RISA (19), could also be used (method e)/

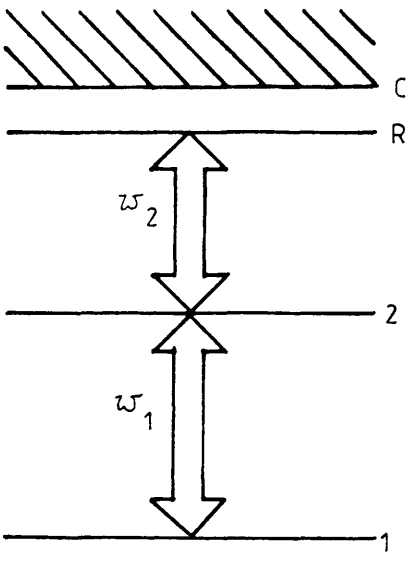

a) $A[\omega_1, \omega_2, Ee^-]A^+$

b) $A[\omega_1, \omega_2, Ae^-]A_2^+$

c) $A[\omega_1, \omega_2, Be^-]AB^+$

d) $A[\omega_1, \omega_2, Be^-]A^+$

e) $A[\omega_1, \omega_2, Me^-]M^+$

f) $A[\omega_1, \omega_2, MM^-]A^+$

FIG. 1·34 : IONISATION OF RYDBERG STATES BY PROCESSES THAT DO NOT INVOLVE PHOTONS.

(method e) with molecular additives M (which may be counter gas) generating electrons for detection and returning the excited atom to its ground state. Where M has high electron affinity chemi-ionisation (method f) is possible. On collision an electron is transferred from the excited atom to the molecular additive, generating A^+ and M^-. Both methods a and b were successfully exploited in the early years of RIS (14,10), and a collisional method (possibly c or d) was used for the ionisation of rubidium by Whitaker and Bushaw (23).

CHAPTER 2 AN APPLICATION OF RESONANCE IONISATION SPECTROSCOPY IN NUCLEAR GEOCHEMISTRY

2-1 Introduction

The generation of electricity from nuclear reactors is increasing (77) and with it concern both within the nuclear industry and amongst the general public over the problems of radioactive waste management and disposal. The recent incident at the Chernobyl nuclear power reactor in the U.S.S.R., has further highlighted the need for swift, isotope-selective and quantitative analysis of environmental samples in order to accurately assess the magnitude of reactor accidents.

Resonance ionisation spectroscopy is relevant to these problems as it represents a swift and extremely sensitive method of counting atoms. Hence, potentially, it offers both rapid accident assessment and, during normal reactor operation, a means for environmental monitoring of those isotopes eluted by nuclear establishments which are difficult to detect by conventional radiometric techniques, e.g. the low-energy β^- emitting nuclides.

2-2 Nuclear Reactor Technology

In any commercial power station, whether oil-, coal- or nuclear-fired, heat is used to generate steam which turns turbines generating electricity. In a nuclear reactor, the source of heat is the thermal fission of $^{235}_{92}U$. The reaction may be expressed as follows/

follows:-

$$\underline{e.g.}\quad {}^{1}_{0}n_{\text{thermal}} + {}^{235}_{92}U \longrightarrow {}^{141}_{56}Ba + {}^{92}_{36}Kr + 3\,{}^{1}_{0}n_{\text{fast}} \qquad \text{---- 19}$$

A neutron at thermal energies (i.e. with the same order of magnitude of energy as atoms at room temperature) collides with a uranium nucleus which flies apart to produce fission products, releasing heat and more, higher energy, neutrons. The fast neutrons may induce a variety of further reactions, as is discussed in section 2-3 of this chapter, but, for a stable chain reaction to be maintained, one neutron from each fission must be slowed to thermal energies and collide with another fissile actinide nucleus.

A schematic diagram of a thermal reactor is shown in Figure 2.21. A detail of the core appears as Figure 2.22. Fuel pellets stacked into rods are packed together and surrounded by a cladding material which prevents escape of fission products from the fuel to the primary coolant which is circulated through the core and carries heat to external heat exchangers. The fuel assemblies are suspended within the moderator - a low atomic mass material, often graphite, which can interact with fast neutrons to produce thermal neutrons. Control rods are also suspended within the core. These are composed of materials such as Cd or B which have high neutron affinity (thermal neutron capture cross section). The rods are movable, can be pushed further into or withdrawn from the core, and serve two main purposes. In normal operation, they regulate and maintain a stable level of criticality within the reactor and, should an emergency shutdown be necessary, they can be dropped into the core

- quenching/

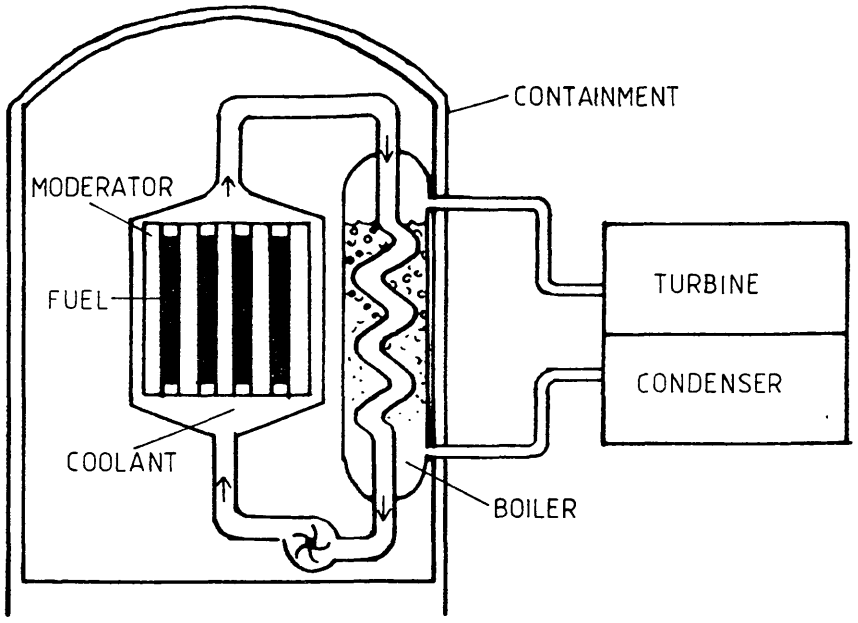

FIG. 2·21 : Schematic diagram of a thermal nuclear reactor

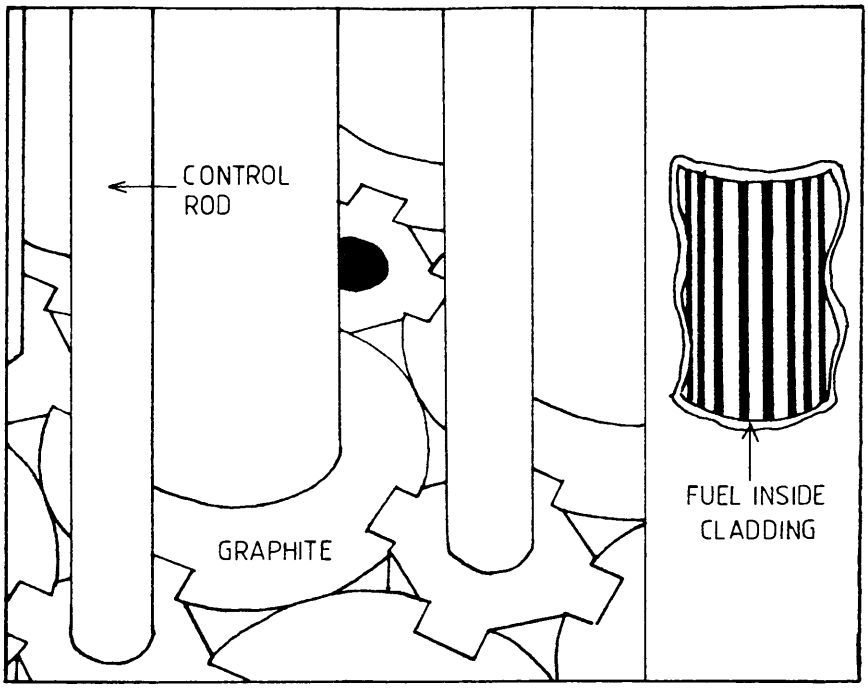

FIG 2·22: Detail of a thermal reactor core.

- quenching the fission chain reaction. The heat exchanger or boiler may be within or outside the reactor containment shield. The primary coolant transfers heat to a secondary coolant (often H_2O) which drives the turbines, generating electricity. The secondary coolant may be recondensed and allowed to recirculate through the boiler or may be discharged into rivers or the sea - a process facilitated by the tendency of power stations to be situated in coastal sites.

In the United Kingdom the majority of currently operating power reactors are of two types - the Magnox type and the Advanced Gas-cooled Reactor (AGR). See Figure 2.23 for a map of their distribution. The sites at Hunterston, Hinkley Point and Dungeness have both types of reactor. The Dounreay and Winfrith sites house prototype reactors: the prototype fast reactor, which uses plutonium fuel, is at Dounreay, and a steam-generating heavy water reactor, which has been connected to the national grid, is situated at Winfrith.

Schematic diagrams of both Magnox and AGR are shown in Figure 2.24. Both are graphite moderated and use CO_2 as the primary and H_2O as the secondary coolant. In the Magnox reactor uranium metal ($^{235}_{92}U$ 0.7% natural abundance) serves as fuel and this is clad in a magnesium alloy (Magnox) which has low affinity for neutrons. The steam generator is situated outside the confinement shield of the reactor. In the AGR, the fuel is enriched ($^{235}_{92}U$ 2.5%) uranium dioxide UO_2 and the cladding is stainless steel. This type of core arrangement allows the reactor to operate at higher temperature, with increased coolant pressure and with increased efficiency. The core is also physically smaller than in the Magnox reactor. The design parameters are compared in Table 3, below.

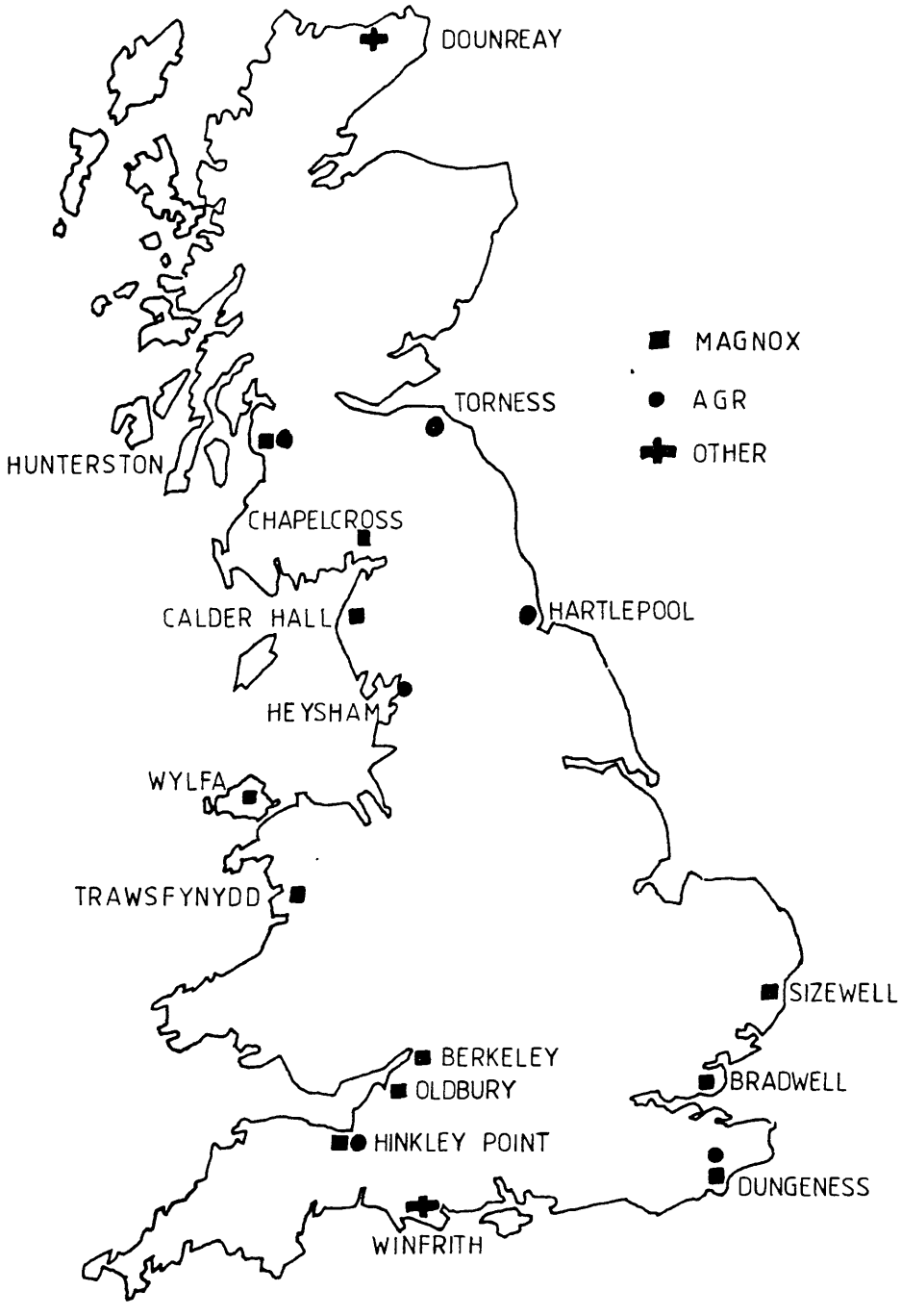

FIG. 2·23: Distribution of Nuclear Power Stations in Britain.
(N.B. The Torness AGR is not yet fully operational)

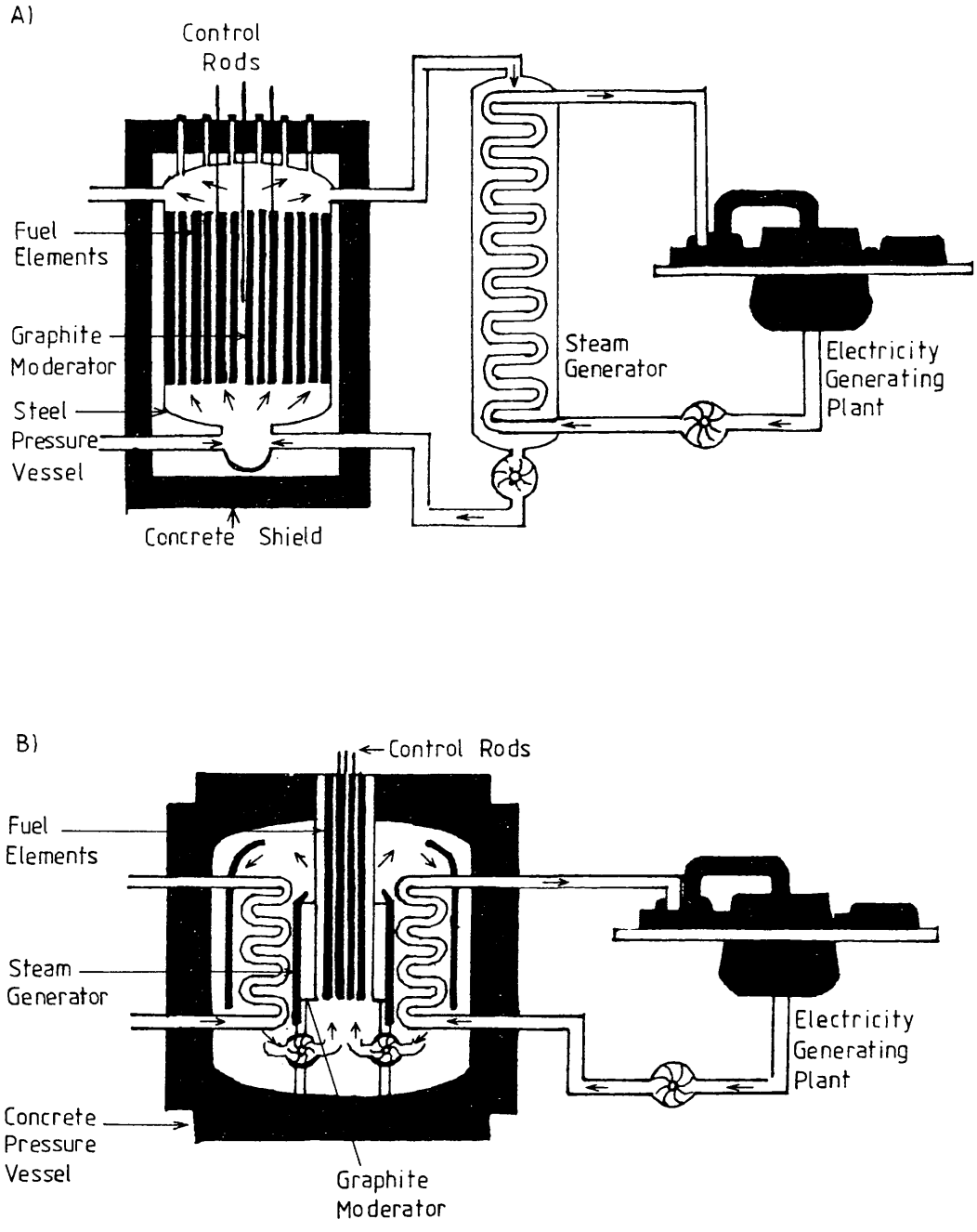

Fig. 2·24: A) The Magnox and B) The AGR Thermal Reactors

TABLE 3

Reactor Characteristics (77)

	MAGNOX	AGR
FUEL	Uranium Metal (0.7% $^{235}_{92}U$)	UO_2 (2.5% $^{235}_{92}U$)
CLADDING	Magnox alloy	Stainless Steel
MODERATOR	Graphite	Graphite
PRIMARY COOLANT	CO_2	CO_2
COOLANT OUTLET TEMPERATURE *	$400^{\circ}C$	$650^{\circ}C$
COOLANT PRESSURE *	300 psi	600 psi
STEAM CYCLE EFFICIENCY *	31%	42%
CORE DIMENSIONS *	14 m. diam. x 8 m. high	9.1 m. diam. x 8.5 m. high

* Data for a reactor of 600 MW size

2-3 Nuclear Waste and Waste Management

Radioactive waste materials, although created principally at the site of a nuclear power reactor, are not necessarily released to the environment in that location. Radionuclides may escape or be released in various physical forms - as solids, liquids or gases - both on site and at reprocessing. It is convenient to consider the production of radionuclides in a reactor as occurring via two processes - fission and neutron activation.

Fission products include both the nuclides formed directly during fission and their decay daughters. Being neutron rich, fission products tend to decay by β^- emission. Typically, they undergo a number of radioactive β^- decays - a decay chain - ending with the formation of stable isotopes. Not all pairs of fission products occur with equal probability: the formation of unequal masses is more likely than the formation of equal masses. The most probable products from the fission of a $^{235}_{92}U$ nucleus are of atomic mass around 95 and 135 amu (78). See Figure 2.31.

Neutron activation occurs when a stable atom absorbs a neutron. The product is (usually) a radioactive atom of the same element and a gamma ray is also emitted.

$$\underline{e.g.}\quad {}^{1}_{0}n_{\text{thermal}} + {}^{59}_{27}Co \longrightarrow {}^{60}_{27}Co + \gamma \qquad \text{---- 20}$$

Neutron activation products are manifold since any part of the reactor exposed to neutron flux may activate, and since chemical elements present only as impurities in the reactor materials may have/

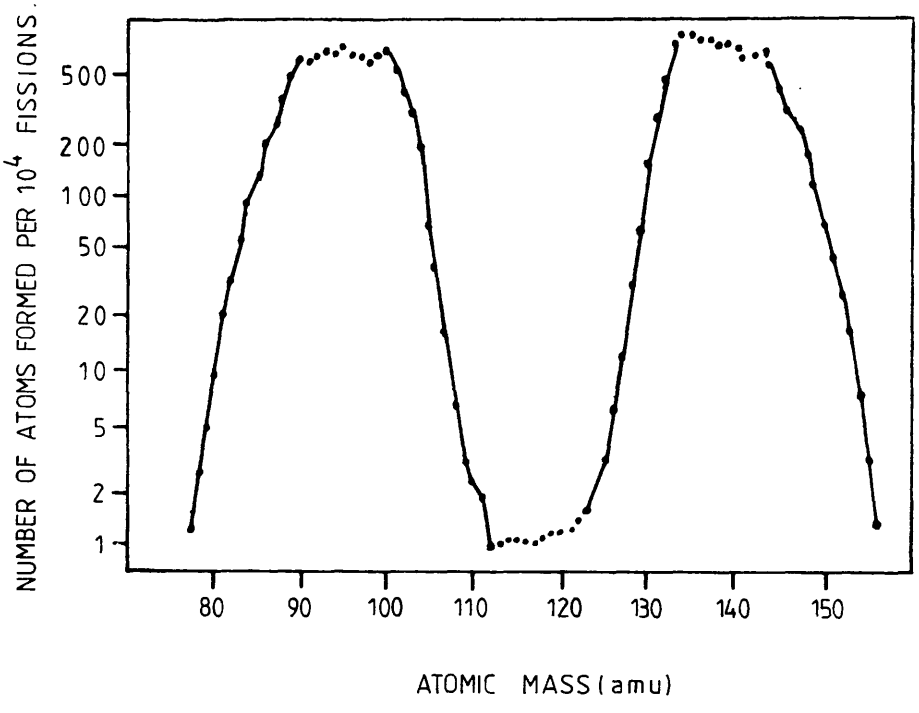

FIG. 2·31: Fission product yields for the thermal fission of $^{235}_{92}U$

have large neutron capture cross sections.

Figure 2.32 is a diagram showing how neutrons are distributed in a thermal reactor. One hundred fission events generate around two hundred and sixty neutrons. One hundred of these (38.6%) are absorbed by fuel but do not bring about fission. These neutron activations lead to higher actinides and their decay products, of particular importance being $^{239}_{94}Pu$, a fissile material generated from the fertile $^{238}_{92}U$ nuclei by a process known as breeding:

$$^{238}_{92}U + {}^{1}_{0}n_{\text{thermal}} \longrightarrow {}^{239}_{92}U \xrightarrow[23.5\ \text{min}]{\beta^-} {}^{239}_{93}Np \xrightarrow[2.35\ \text{d}]{\beta^-} {}^{239}_{94}Pu \qquad (21)$$

A further 22.8% of the neutrons are absorbed by fission products or by the structural components of the reactor. The remaining hundred neutrons give rise to a further round of fission events. The majority of fissioning nuclei are $^{235}_{92}U$ but a significant number are the $^{239}_{94}Pu$ nuclei produced by neutron activation. A small number of $^{238}_{92}U$ nuclei also undergo fission due to interaction with fast, unmoderated neutrons.

To explain the modes and locations of discharge of the nuclides formed in reactors it is necessary to refer to the nuclear fuel cycle shown in Figure 2.33 (79). Uranium ore is processed, enriched (if necessary) and fabricated into fuel elements. Waste arising in these stages of the cycle is principally composed of naturally occurring uranium isotopes and their natural series decay products (80). The waste is buried if solid and diluted and dispersed into seawater if liquid.

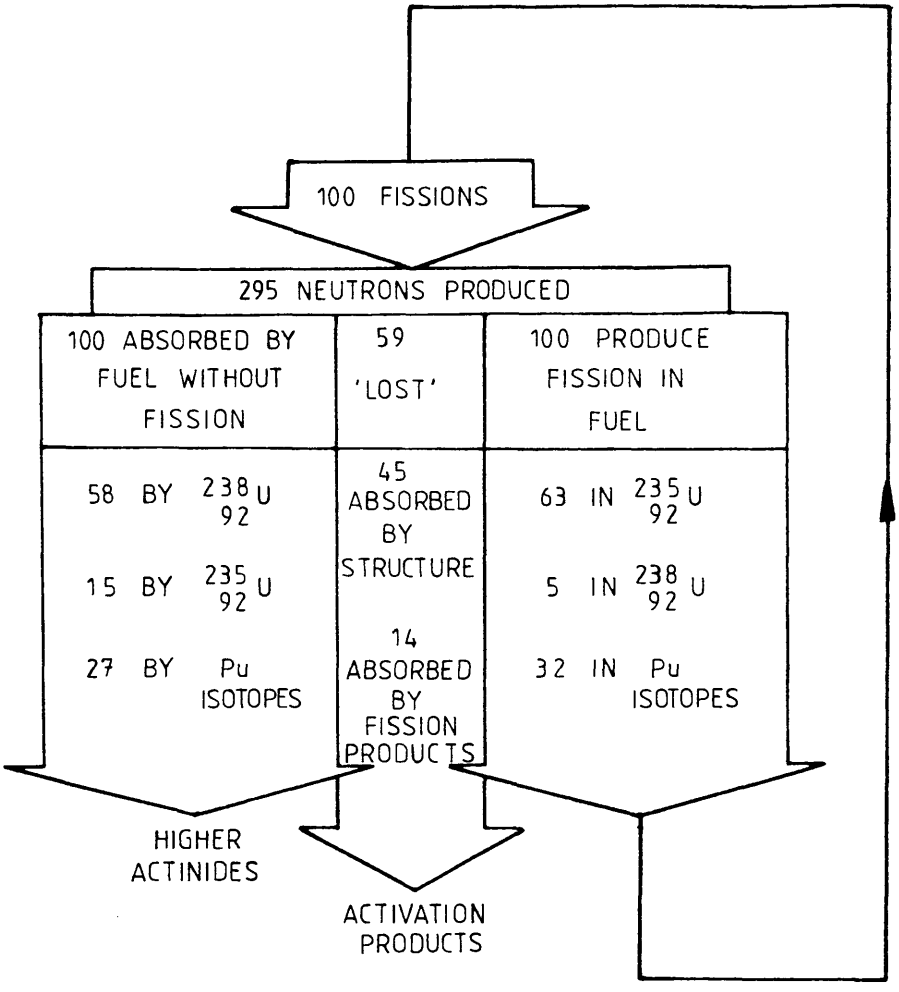

FIG. 2·32: Neutron utilization in a Thermal Reactor

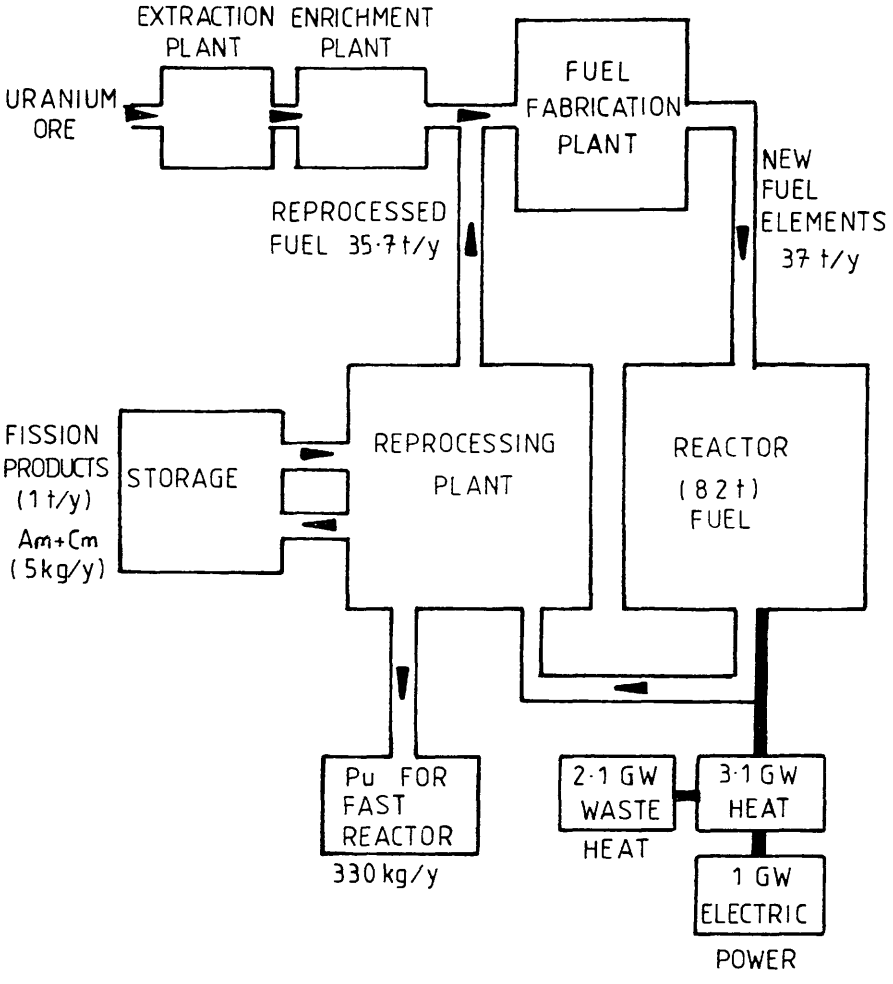

FIG. 2·33: Fuel Cycle for a Thermal Reactor of 1GW capacity.

During reactor operation, fission products and higher actinides are produced within the fuel. Minor quantities of these escape, through defects in the cladding, to the primary coolant. The constituents of the reactor core (including coolant) also become radioactive by neutron activation. Small amounts of primary coolant activity may then pass to the secondary coolant (i.e. seawater or fresh water) if there are defects in the heat exchanger. However, the majority of the radioactivity produced in the structure of the reactor, excluding fuel elements which are reprocessed, does not constitute a waste management problem until decommissioning.

Spent fuel elements withdrawn from the core are stored in large tanks of water for several months to allow short-lived nuclides present to decay before transportation to the reprocessing site. The water in these ponds becomes contaminated with radioactivity due to cladding defects.

At the reprocessing plant, cladding is stripped or dissolved from the fuel element and the fuel itself dissolved in nitric acid (HNO_3). Gaseous radionuclides may be liberated from both materials during this phase of processing. Uranium and plutonium are next extracted, leaving a highly radioactive liquid containing fission products and transuranics other than plutonium. Purification of the extracted actinides leads to further liquid waste - some contaminated with plutonium which is hazardous both due to its radioactivity and to its extreme toxicity. Reclaimed uranium is fabricated into new fuel elements and the plutonium may be used to fuel fast reactors. Figure

2.33/

2.33 also shows the volumes of these materials relevant to one year's operation of a thermal reactor of 1 GW capacity.

Nuclear waste is designated as low, intermediate or high level depending on the activity present. These definitions are somewhat arbitrary, however, and should be considered approximate only.

Low level solid waste, e.g. miscellaneous scraps of paper, cloth or metal from laboratories, is either buried in designated disposal sites such as that at Drigg near Windscale, or is cast in cement inside steel drums and dumped on the ocean floor.

Intermediate level solid waste is, where possible, treated so that the bulk of the material becomes low level waste. The concentrated remainder is compacted and packaged for storage until a disposal method for this level of waste is agreed between the government and the nuclear authorities. Fuel cladding is also compacted and embedded for storage in an inert matrix such as glass or concrete.

Low level liquid waste consists mainly of low activity effluent streams from reprocessing plants, water from fuel storage ponds, and contaminated secondary coolant from nuclear power stations. The waste is normally treated by e.g. filtration or ion exchange before discharge. It is discharged to the sea or to estuaries by power stations, except for the Trawsfynydd reactor which releases effluent into a freshwater lake. The Sellafield (previously known as Windscale) reprocessing plant in Cumbria discharges waste 2 km. off-

shore/

shore via a pipeline.

High activity liquid waste (the solution remaining after extraction of uranium and plutonium from spent fuel), like the intermediate level solid waste, is consigned to storage since no agreement over the best mode of disposal has been reached. A particular difficulty in dealing with high level waste is its associated high heat output. Current proposals for disposal of this material involve a phase of liquid storage during which some nuclides will decay and the heat output will drop, followed by packaging in solid form. The solid waste may require a further cooling period, possibly in an underground repository, before final disposal either by deep burial within stable geological formations on land, on the ocean floor, or within deep ocean sediments (81).

Strict government control is exerted over the amount of radioactivity released by the nuclear industry. Discharge limits are set in order that the exposure of critical groups (sections of the population most at risk from the radiation released) be well below the dose limits recommended by the International Commission on Radiological Protection (ICRP) (82). Emphasis is also given to the principle that all exposures should be kept As Low As Reasonably Achievable (ALARA). No level of radiation exposure is considered to carry zero risk.

Monitoring is carried out by nuclear installations as a condition of their obtaining a licence (an Authorisation) to release radioactive wastes. Discharges are also kept under review by the Ministry of Agriculture/

Agriculture, Fisheries and Food (Directorate of Fisheries Research) which publishes independent surveys of activity in the aquatic environment arising from all sources of radioactive waste within the United Kingdom (83).

Evidence exists, however, which suggests that improvements in waste monitoring would be advantageous. For example, over sixty nuclides were identified in work carried out in 1959 on low level reactor effluent (84), but significantly fewer are subject to individual limits or separately assayed by nuclear installations. The most extensive effluent monitoring carried out by a British nuclear installation occurs at Sellafield reprocessing plant in Cumbria, where around thirty nuclides are assayed and reported (85). The remaining nuclides are discharged under "umbrella" headings of gross α and gross β^- activity. Gross beta counting (86) of solid samples precipitated from waste streams is an unreliable technique since the detection efficiency varies with the energy of the emitted β^- particle. In particular, the low energy β^- emitters (whose activity is mostly absorbed within the thickness of the sample) are poorly assayed by this method. Consequently little is known of the volumes of these nuclides discharged or of their behaviour once in the environment, and possible critical pathways (i.e. ways of returning to man).

A further criticism of current waste management philosophy is that it makes no allowance for the formation of new nuclides, via radioactive decay, once the waste is discharged. Particularly hazardous is/

is the possibility of forming, in the environment, a highly radiotoxic daughter from a relatively innocuous parent. For example, discharge of alpha activity from the Sellafield reprocessing plant is highly restricted, but discharge of $^{241}_{94}Pu$, a low-energy beta emitter, is unrestricted despite the fact that $^{241}_{94}Pu$ produces the alpha emitters $^{241}_{95}Am$ and $^{237}_{93}Np$, as shown below:

$$^{241}_{94}Pu \xrightarrow[14.7\ y.]{\beta^-} {}^{241}_{95}Am \xrightarrow[433\ y.]{\alpha} {}^{237}_{93}Np \xrightarrow[10^6\ y.]{\alpha} \qquad \text{---- 22}$$

In 1981 it was calculated that a $^{241}_{95}Am$ activity of ~ 22.2 TBq resulting from decay of plutonium was present in the Irish Sea close to the Sellafield pipeline. This value is three times the $^{241}_{95}Am$ activity reported for that year's effluent (87). The same workers also suggested that all americium and a significant proportion of the plutonium discharged was retained in sediment close to the release site and not dispersed in the ocean. Thus americium levels were not only enhanced (by $^{241}_{94}Pu$ decay), but were also localised. $^{241}_{95}Am$ detected in the dispersal plume from the Sellafield plant was attributed to decay of the soluble, i.e. conserved fraction of $^{241}_{94}Pu$.

Under the terms of the Authorisation for radioactive waste discharge from Sellafield, only three nuclides are required to be measured individually - $^{90}_{38}Sr$, $^{106}_{44}Ru$, and $^{144}_{58}Ce$. However, over the years, the number of nuclides reported by British Nuclear Fuels in their annual report on the plant's releases has increased as methods for assaying nuclides "not subject to separate limits within the terms of the Pipeline Authorisation" have been developed. It is interesting to speculate both on how much of the nuclides now assayable have been/

been discharged in the past, undetected, and on how much of those isotopes for which reliable monitoring techniques do not, yet, exist are currently discharged. At the Hanford reactor in the U.S.A., nuclide specific monitoring techniques were introduced in 1960, replacing gross β^- analysis. In that year, prediction of the total β^- discharge based on gross β^- counting methods was 3440 TBq/y. However, individual nuclide assessment measured 11,800 TBq/y. of $^{51}_{24}Cr$, 962 TBq/y. of $^{239}_{93}Np$, 518 TBq/y. of $^{65}_{30}Zn$ and 2,290 TBq/y. of $^{32}_{15}P$ (88).

A further area of concern is the correct identification of critical groups and critical pathways by which radioactivity discharged to the environment may return to man's environs and pose a radiological hazard. Just as $^{241}_{95}Am$ was retained on sediment close to the Windscale pipeline and not dispersed in the ocean as predicted (87), so other environmental materials may, via selective uptake or expected transfer processes, constitute unpredictable hazards to mankind. Examples of critical pathways of this type include the ingestion of $^{106}_{44}Ru$ from the Sellafield plant via seaweed consumption and external irradiation sustained by fishermen working near Dounreay caused by radioisotopes adhering to fishing nets (89).

It is evident, then, that more reliable means to assay nuclides present in low level waste and study of their behaviour in the environment is extremely important if radiological hazards associated with the Nuclear Industry are to be accurately assessed. Nuclide assay by resonance ionisation spectroscopy is proposed as a way of overcoming/

overcoming the inherent difficulty of detecting low-energy radionuclides - both in waste and in the environment - by conventional radiometric means.

2-4 The Application of RIS to Waste Management

Conventional types of radiation detectors may be subdivided into three main categories - gas-ionisation detectors, e.g. ionisation chambers, proportional counters, and Geiger-Müller counters; semiconductor devices, e.g. Ge(Li) and Si(Li); and scintillation counters, e.g. NaI(Tl) (90). A common feature of all these devices is that their operation is based on the observation of radioactive decay events, and their sensitivity is limited by the efficiency with which particles or photons emitted during these events can be detected. The number of atoms present of the isotope of interest is not measured directly but is inferred from the relationship

$$A = N\lambda \qquad \text{---- 23}$$

where A = activity (in Bq),

N = the number of parent atoms,

and λ = the decay constant.

Decay constant and half life ($t_{\frac{1}{2}}$) of a nuclide are related by

$$\lambda = \frac{0.693}{t_{\frac{1}{2}}} \qquad \text{---- 24}$$

For nuclides of long half life activity is low and long counting times are required to assay such species by conventional methods.

Low/

Low activity nuclides which are also of the type whose decay energy is difficult to detect, e.g. low-energy β^- emitters, cannot be assessed with any certainty even with long counting times.

A number of resonance ionisation spectroscopy based techniques have been proposed for radionuclide assay which do not rely on the detection of decay events alone. These include decay-daughter coincidence counting (33), direct counting of parent atoms, and delayed counting of the daughter atoms as they accumulate (5). The processes are illustrated in Figure 2.41 as is conventional decay counting.

Direct parent atom counting is particularly applicable to measurements on very low activity samples. An element-specific laser pulse ionises all atoms of the chosen radioactive parent present in the sample and the pulse of electrons or positive ions is measured in a suitable detector. In decay-daughter coincidence counting, the detection of a radioactive decay by a conventional technique triggers a laser pre-tuned to resonantly ionise atoms of the daughter species. Only real i.e. non-background events produce a response from both the radiation detector and the laser-based apparatus, and background count rate may be reduced by, at least, a factor of 10^{-4} (33). The technique was demonstrated in 1978 (18) when caesium atoms were detected in coincidence with their production by the spontaneous fission of $^{252}_{98}Cf$. Delayed daughter counting also involved laser-ionisation of daughter isotopes, but not in time coincidence with their production. The daughter species is allowed to accumulate and its/

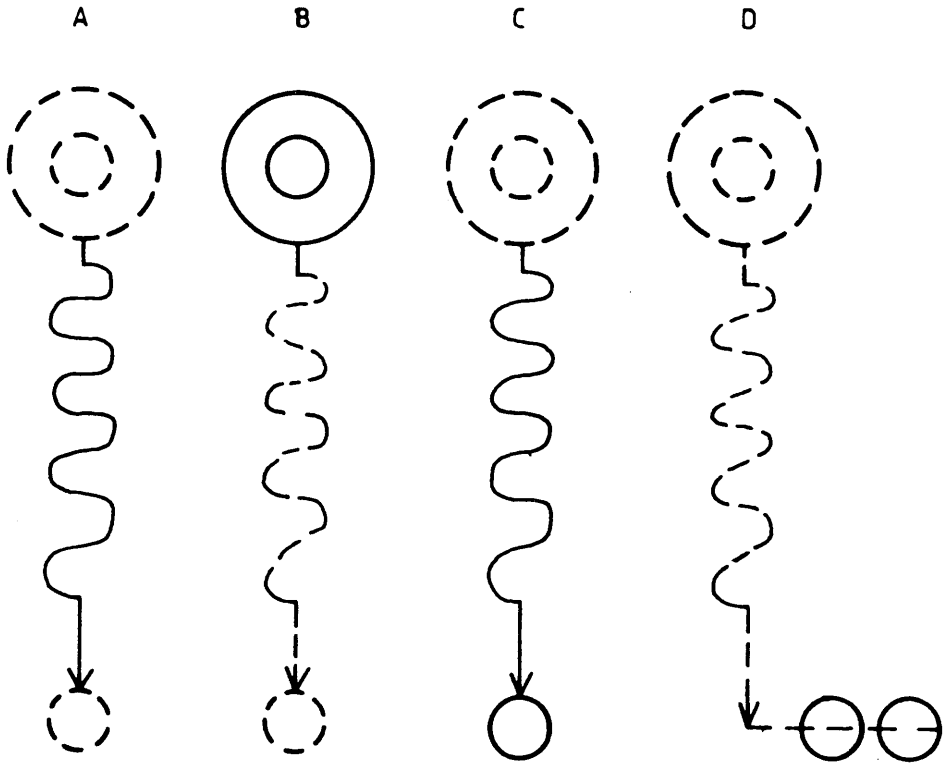

FIG. 2·41: B,C,D ways in which RIS may be used to count radioactive atoms compared with conventional counting (A)

its population monitored by periodically firing (or sweeping) the laser beam through the detection chamber. The experiment can be arranged either a) so that each atom is only registered once and then implanted on to the surface of the detector, or b) so that, once ionised the atom is neutralised and allowed to re-enter the laser volume. The latter method - resonance ionisation spectroscopy with amplification (RISA) (19) is particularly attractive for detection or study of small populations of atoms, e.g. the small number of daughter species produced by a long half life parent.

The combination of the single atom detection capability of RIS type techniques (11,14) with mass spectrometry presents the possibility of an isotopically selective, extremely sensitive analytical technique (33). Although, in practice, the ultimate sensitivity of resonance ionisation spectroscopy as a general technique may be limited by the so-called "background" ionisation present in detection chambers (see Chapter 4) it is likely, in the future, that the detection capability of resonance ionisation mass spectrometry (RIMS) systems will exceed that obtainable by conventional radiometric means, at least for nuclides with long half lives.

A particularly relevant group of nuclides is the low-energy β^- emitters mentioned earlier, which are difficult to detect conventionally at specific activities of around 1 pCi per gram of sample (3.7×10^{-2} Bq/g) (91). If the sample is of a typical geological or environmental material, it contains $\sim 10^{22}$ atoms per gram, some of which are the radioactive species of interest. Based on a specific activity/

activity of 3.7×10^{-2} Bq/g, the concentrations of a variety of important β^- emitters in a typical sample were calculated, and are presented in Table 4. (N.B. for each nuclide it was assumed that it alone gave rise to the activity of the sample.)

TABLE 4

Concentrations of β^- emitters in environmental samples to give 3.7×10^{-2} Bq/g activity

Z	A	ELEMENT	HALF LIFE	NO. OF ATOMS	CONCENTRATION
38	90	Strontium	28 y	4.9×10^{7}	4.9×10^{-15}
43	99	Technetium	2.13×10^{5} y	3.6×10^{11}	3.6×10^{-11}
48	113	Cadmium	14.6 y	2.5×10^{7}	2.5×10^{-15}
53	129	Iodine	1.57×10^{7} y	2.6×10^{13}	2.6×10^{-9}
55	135	Caesium	2.06×10^{6} y	5.1×10^{12}	5.1×10^{-10}
55	137	Caesium	30.17 y	5.0×10^{7}	5.0×10^{-15}
61	147	Promethium	2.62 y	4.4×10^{6}	4.6×10^{-16}

Estimating the current sensitivity achievable by RIMS as 0.1 ppb (1 part in 10^{10}), it can be seen from Table 4 that only $^{135}_{55}Cs$ and $^{129}_{53}I$ could be detected (92). If the SIRIS system (61,62,63) achieves the 1 part in 10^{12} sensitivity prospected by its manufacturers, $^{99}_{43}Tc$ would also be amenable to monitoring at the pCi/g level.

Curently, therefore, nuclides of half life $< \sim 10^6$ years cannot be assayed at pCi/g levels by RIS unless some chemical procedure is used to enrich the sample in the nuclide(s) of interest. A promising tool to aid in isotope enrichment chemistry is the recently reported rapid microwave dissolution of rocks and sediments (93). Exactly how this technique may best be combined with RIMS remains a problem for the future.

Studies aimed at environmental monitoring of nuclides associated with the Nuclear Industry have already been undertaken by various RIMS groups. Most have concentrated on detection not of β^- emitters but of the transuranic nuclides associated with reactor fuel.

Assay of transuranics by RIS of neutron or photon induced, noble gas fission products (Xe and Kr) has been proposed (94). Spectral studies on plutonium using a N_2-pumped dye laser revealed a large number of transitions in the region 431-451 nm, and demonstrated the feasibility of RIS detection of the element (41,42). A Nd:YAG pumped dye laser system, in conjunction with a time-of-flight mass spectrometer achieved a detection limit of 2×10^{11} $^{239}_{94}Pu$ atoms with a single-wavelength ionisation scheme (73). $^{239}_{94}PuO$ and $^{239}_{94}PuO_2$ were also observed (73). The same workers, using an upgraded system consisting of three dye lasers pumped by a single, copper vapour laser (74), improved their sensitivity to $\sim 10^8$ plutonium atoms. Uranium could also be detected with this system, and plutonium auto-ionisation levels were investigated. Uranium has also been detected using intra-cavity laser radiation (72). Spectral lines suitable for resonance ionisation/

ionisation of various actinides have recently been located in the 580 - 607 nm region (43).

The use of RIS to detect low-energy β^- emitters discharged by the Nuclear Industry represents a previously unexplored application of the technique; although β^- decay products have previously been considered for RIS studies on ocean water circulation (95). However, it is also a particularly important application in view of the lack of knowledge concerning the behaviour of such nuclides in the environment and the inefficiency with which they are assayed by conventional means.

2-5 Literature-Based Nuclide Assessment

Before commencing preliminary experiments to develop RIS techniques for application to nuclear waste monitoring, a literature-based assessment was undertaken, the aim of which was to determine the likely constituents i.e. the nuclide composition of nuclear waste materials reaching the environment. In particular, it was hoped to identify nuclides (such as low-energy β^- emitters) potentially assayable by RIS but difficult to detect by conventional counting, which have high probabilities of being released in relatively large amounts. The choice of nuclide(s) was further constrained by the type of laser system available, to being of an element amenable to scheme 1 or scheme 2 (2) resonance ionisation.

The assessment was subdivided into two parts: a) fission products and/

and b) neutron activation products. Fission products were classed under the actinide element from which they arose and activation products subdivided according to the part of the reactor where activation occurred.

I Fission Products

Fission product nuclides and their yields from the thermal neutron induced fission of $^{235}_{92}U$ and $^{239}_{94}Pu$ (96) were tabulated. For each nuclide, the half life (96), decay mode and energy (97), and allowed limits of intake (82) were tabulated, as was the resonance ionisation scheme for the element recommended by Hurst (2). Decay chains from the fission products to stable nuclides were drawn out based on data in references 97 and 78, in order that important daughter isotopes of the direct fission products could be considered.

II Neutron Activation Products

Since neither a review article on which to base this section of the assessment nor data on the number of atoms of each element present in the reactor were available, only qualitative information (based on the assumption that the chemical elements present have their natural isotopic compostion) could be deduced.

A number of elements present or potentially present as impurities in reactor materials were tabulated and decay (97) / neutron activation (98) schemes constructed for each isotope to determine which other nuclides they produce.

Activation of fuel nuclides generated higher actinides, principally by combinations of neutron absorption and β^- decay reactions. Although many of the nuclides in this section are also α active, the long half lives for these α processes ($> \sim 20$ y) renders them relatively insignificant as the useful life of a fuel rod is only 1 or 2 years. Principal links in the so-called 'Heavy Atom Burn-Up Chain' are shown in Figure 2.51 (77). The amounts of some representative actinides produced in this way are shown in Table 5. The values given are for a 1000 MW pressurised water reactor (77).

TABLE 5

Production rates and associated activity for some important actinides

ISOTOPE	PRODUCTION RATE	
	kg/year	Ci/year
^{241}Am	2	6×10^3
^{242}Cm	0.1	3×10^5
^{244}Cm	0.8	7×10^4

Isotopes of the natural decay series (80) were also considered as they may be present in fuel due to inadequate chemical separation during ore processing and fuel fabrication.

Activation of fission products was treated similarly, i.e. decay chain and daughters were included, but only the fission products with large/

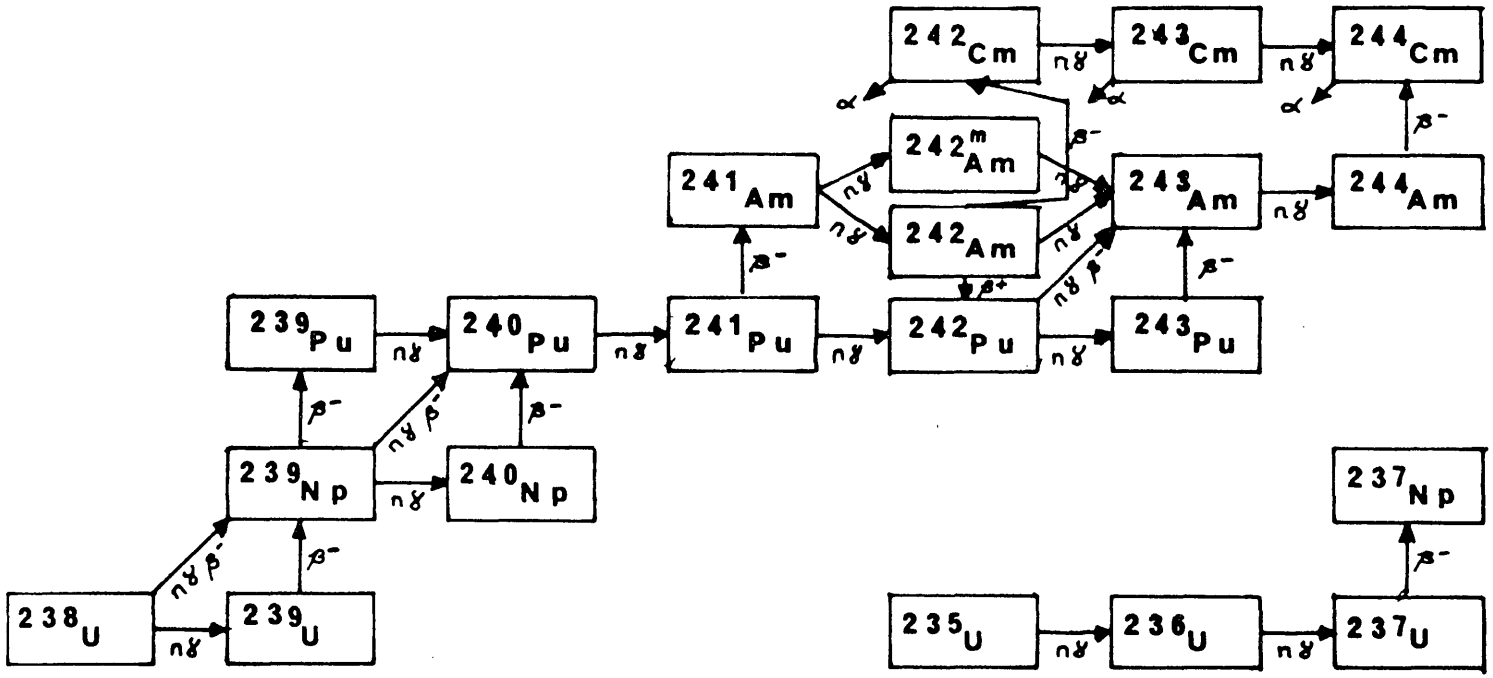

FIG. 2.51: PRINCIPAL LINKS IN THE HEAVY-ATOM BURN UP CHAIN

large thermal neutron capture cross section (>25 barns) were considered. These are listed in Table 6. Data is for a typical thermal reactor (77).

TABLE 6

Neutron Capture in Fission Products

ISOTOPE	% OF TOTAL f.p. CAPTURES	THERMAL NEUTRON CAPTURE CROSS SECTION (barns) (98)	PRODUCT
^{135}Xe	25	$(2.65 \pm 0.2) \times 10^6$	^{136}Xe
^{149}Sm	10	$41,000 \pm 2,000$	^{150}Sm
^{143}Nd	8	3.25 ± 10	^{144}Nd
^{103}Rh	7	150 ± 5	^{104}Rh m+g
^{147}Pm	6	85 ± 5	^{148m}Pm
		96 ± 1.8	^{148}Pm
^{131}Xe	5	90 ± 10	^{132}Xe
^{133}Cs	5	29 ± 1.5	^{134}Cs m+g

m = metastable m+g = metastable + ground state

Finally, activation of fuel cladding and other reactor core materials was/

is the possibility of forming, in the environment, a highly radiotoxic daughter from a relatively innocuous parent. For example, discharge of alpha activity from the Sellafield reprocessing plant is highly restricted, but discharge of $^{241}_{94}Pu$, a low-energy beta emitter, is unrestricted despite the fact that $^{241}_{94}Pu$ produces the alpha emitters $^{241}_{95}Am$ and $^{237}_{93}Np$, as shown below:

$$^{241}_{94}Pu \xrightarrow[14.7\ y.]{\beta^-} {}^{241}_{95}Am \xrightarrow[433\ y.]{\alpha} {}^{237}_{93}Np \xrightarrow[10^6\ y.]{\alpha} \qquad \text{---- 22}$$

In 1981 it was calculated that a $^{241}_{95}Am$ activity of $\sim$ 22.2 TBq resulting from decay of plutonium was present in the Irish Sea close to the Sellafield pipeline. This value is three times the $^{241}_{95}Am$ activity reported for that year's effluent (87). The same workers also suggested that all americium and a significant proportion of the plutonium discharged was retained in sediment close to the release site and not dispersed in the ocean. Thus americium levels were not only enhanced (by $^{241}_{94}Pu$ decay), but were also localised. $^{241}_{95}Am$ detected in the dispersal plume from the Sellafield plant was attributed to decay of the soluble, i.e. conserved fraction of $^{241}_{94}Pu$.

Under the terms of the Authorisation for radioactive waste discharge from Sellafield, only three nuclides are required to be measured individually - $^{90}_{38}Sr$, $^{106}_{44}Ru$, and $^{144}_{58}Ce$. However, over the years, the number of nuclides reported by British Nuclear Fuels in their annual report on the plant's releases has increased as methods for assaying nuclides "not subject to separate limits within the terms of the Pipeline Authorisation" have been developed. It is interesting to speculate both on how much of the nuclides now assayable have been/

been discharged in the past, undetected, and on how much of those isotopes for which reliable monitoring techniques do not, yet, exist are currently discharged. At the Hanford reactor in the U.S.A., nuclide specific monitoring techniques were introduced in 1960, replacing gross β^- analysis. In that year, prediction of the total β^- discharge based on gross β^- counting methods was 3440 TBq/y. However, individual nuclide assessment measured 11,800 TBq/y. of $^{51}_{24}Cr$, 962 TBq/y. of $^{239}_{93}Np$, 518 TBq/y. of $^{65}_{30}Zn$ and 2,290 TBq/y. of $^{32}_{15}P$ (88).

A further area of concern is the correct identification of critical groups and critical pathways by which radioactivity discharged to the environment may return to man's environs and pose a radiological hazard. Just as $^{241}_{95}Am$ was retained on sediment close to the Windscale pipeline and not dispersed in the ocean as predicted (87), so other environmental materials may, via selective uptake or expected transfer processes, constitute unpredictable hazards to mankind. Examples of critical pathways of this type include the ingestion of $^{106}_{44}Ru$ from the Sellafield plant via seaweed consumption and external irradiation sustained by fishermen working near Dounreay caused by radioisotopes adhering to fishing nets (89).

It is evident, then, that more reliable means to assay nuclides present in low level waste and study of their behaviour in the environment is extremely important if radiological hazards associated with the Nuclear Industry are to be accurately assessed. Nuclide assay by resonance ionisation spectroscopy is proposed as a way of overcoming/

overcoming the inherent difficulty of detecting low-energy radionuclides - both in waste and in the environment - by conventional radiometric means.

2-4 The Application of RIS to Waste Management

Conventional types of radiation detectors may be subdivided into three main categories - gas-ionisation detectors, e.g. ionisation chambers, proportional counters, and Geiger-Müller counters; semiconductor devices, e.g. Ge(Li) and Si(Li); and scintillation counters, e.g. NaI(Tl) (90). A common feature of all these devices is that their operation is based on the observation of radioactive decay events, and their sensitivity is limited by the efficiency with which particles or photons emitted during these events can be detected. The number of atoms present of the isotope of interest is not measured directly but is inferred from the relationship

$$A = N\lambda \qquad \text{---- 23}$$

where A = activity (in Bq),

N = the number of parent atoms,

and λ = the decay constant.

Decay constant and half life ($t_{\frac{1}{2}}$) of a nuclide are related by

$$\lambda = \frac{0.693}{t_{\frac{1}{2}}} \qquad \text{---- 24}$$

For nuclides of long half life activity is low and long counting times are required to assay such species by conventional methods.

Low/

Low activity nuclides which are also of the type whose decay energy is difficult to detect, e.g. low-energy β^- emitters, cannot be assessed with any certainty even with long counting times.

A number of resonance ionisation spectroscopy based techniques have been proposed for radionuclide assay which do not rely on the detection of decay events alone. These include decay-daughter coincidence counting (33), direct counting of parent atoms, and delayed counting of the daughter atoms as they accumulate (5). The processes are illustrated in Figure 2.41 as is conventional decay counting.

Direct parent atom counting is particularly applicable to measurements on very low activity samples. An element-specific laser pulse ionises all atoms of the chosen radioactive parent present in the sample and the pulse of electrons or positive ions is measured in a suitable detector. In decay-daughter coincidence counting, the detection of a radioactive decay by a conventional technique triggers a laser pre-tuned to resonantly ionise atoms of the daughter species. Only real i.e. non-background events produce a response from both the radiation detector and the laser-based apparatus, and background count rate may be reduced by, at least, a factor of 10^{-4} (33). The technique was demonstrated in 1978 (18) when caesium atoms were detected in coincidence with their production by the spontaneous fission of $^{252}_{98}Cf$. Delayed daughter counting also involved laser-ionisation of daughter isotopes, but not in time coincidence with their production. The daughter species is allowed to accumulate and its/

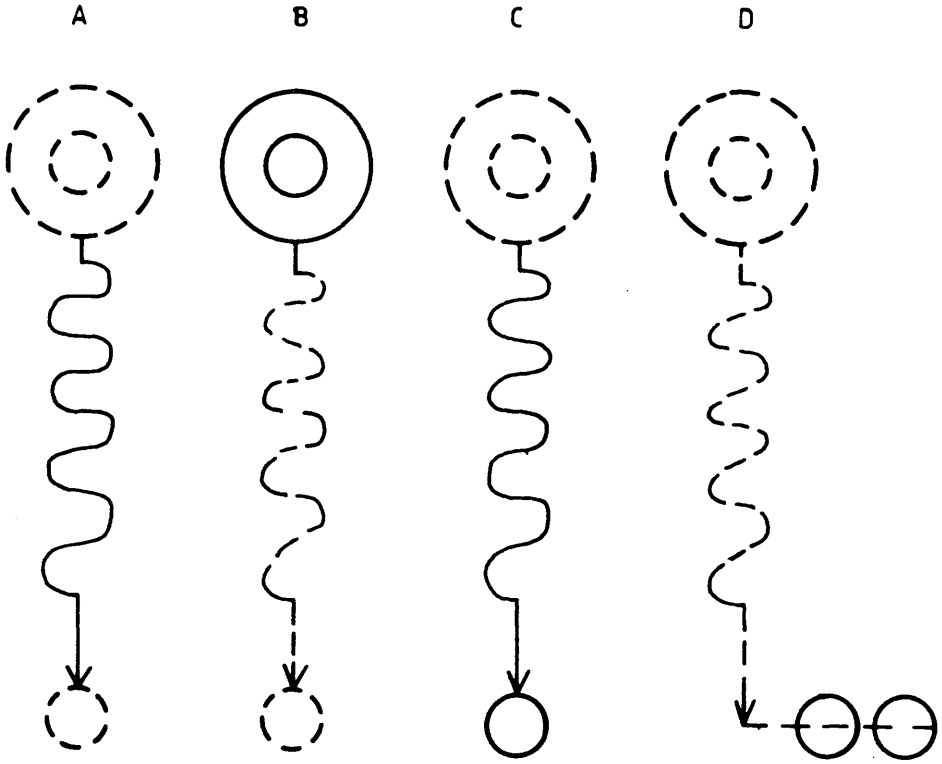

FIG. 2·41: B,C,D ways in which RIS may be used to count radioactive atoms compared with conventional counting (A)

its population monitored by periodically firing (or sweeping) the laser beam through the detection chamber. The experiment can be arranged either a) so that each atom is only registered once and then implanted on to the surface of the detector, or b) so that, once ionised the atom is neutralised and allowed to re-enter the laser volume. The latter method - resonance ionisation spectroscopy with amplification (RISA) (19) is particularly attractive for detection or study of small populations of atoms, e.g. the small number of daughter species produced by a long half life parent.

The combination of the single atom detection capability of RIS type techniques (11,14) with mass spectrometry presents the possibility of an isotopically selective, extremely sensitive analytical technique (33). Although, in practice, the ultimate sensitivity of resonance ionisation spectroscopy as a general technique may be limited by the so-called "background" ionisation present in detection chambers (see Chapter 4) it is likely, in the future, that the detection capability of resonance ionisation mass spectrometry (RIMS) systems will exceed that obtainable by conventional radiometric means, at least for nuclides with long half lives.

A particularly relevant group of nuclides is the low-energy β^- emitters mentioned earlier, which are difficult to detect conventionally at specific activities of around 1 pCi per gram of sample (3.7×10^{-2} Bq/g) (91). If the sample is of a typical geological or environmental material, it contains $\sim 10^{22}$ atoms per gram, some of which are the radioactive species of interest. Based on a specific activity/

activity of 3.7×10^{-2} Bq/g, the concentrations of a variety of important β^- emitters in a typical sample were calculated, and are presented in Table 4. (N.B. for each nuclide it was assumed that it alone gave rise to the activity of the sample.)

TABLE 4

Concentrations of β^- emitters in environmental samples to give 3.7×10^{-2} Bq/g activity

Z	A	ELEMENT	HALF LIFE	NO. OF ATOMS	CONCENTRATION
38	90	Strontium	28 y	4.9×10^{7}	4.9×10^{-15}
43	99	Technetium	2.13×10^{5} y	3.6×10^{11}	3.6×10^{-11}
48	113	Cadmium	14.6 y	2.5×10^{7}	2.5×10^{-15}
53	129	Iodine	1.57×10^{7} y	2.6×10^{13}	2.6×10^{-9}
55	135	Caesium	2.06×10^{6} y	5.1×10^{12}	5.1×10^{-10}
55	137	Caesium	30.17 y	5.0×10^{7}	5.0×10^{-15}
61	147	Promethium	2.62 y	4.4×10^{6}	4.6×10^{-16}

Estimating the current sensitivity achievable by RIMS as 0.1 ppb (1 part in 10^{10}), it can be seen from Table 4 that only $^{135}_{55}Cs$ and $^{129}_{53}I$ could be detected (92). If the SIRIS system (61,62,63) achieves the 1 part in 10^{12} sensitivity prospected by its manufacturers, $^{99}_{43}Tc$ would also be amenable to monitoring at the pCi/g level.

Curently, therefore, nuclides of half life $< \sim 10^6$ years cannot be assayed at pCi/g levels by RIS unless some chemical procedure is used to enrich the sample in the nuclide(s) of interest. A promising tool to aid in isotope enrichment chemistry is the recently reported rapid microwave dissolution of rocks and sediments (93). Exactly how this technique may best be combined with RIMS remains a problem for the future.

Studies aimed at environmental monitoring of nuclides associated with the Nuclear Industry have already been undertaken by various RIMS groups. Most have concentrated on detection not of β^- emitters but of the transuranic nuclides associated with reactor fuel.

Assay of transuranics by RIS of neutron or photon induced, noble gas fission products (Xe and Kr) has been proposed (94). Spectral studies on plutonium using a N_2-pumped dye laser revealed a large number of transitions in the region 431-451 nm, and demonstrated the feasibility of RIS detection of the element (41,42). A Nd:YAG pumped dye laser system, in conjunction with a time-of-flight mass spectrometer achieved a detection limit of 2×10^{11} $^{239}_{94}Pu$ atoms with a single-wavelength ionisation scheme (73). $^{239}_{94}PuO$ and $^{239}_{94}PuO_2$ were also observed (73). The same workers, using an upgraded system consisting of three dye lasers pumped by a single, copper vapour laser (74), improved their sensitivity to $\sim 10^8$ plutonium atoms. Uranium could also be detected with this system, and plutonium auto-ionisation levels were investigated. Uranium has also been detected using intra-cavity laser radiation (72). Spectral lines suitable for resonance ionisation/

ionisation of various actinides have recently been located in the 580 - 607 nm region (43).

The use of RIS to detect low-energy β^- emitters discharged by the Nuclear Industry represents a previously unexplored application of the technique; although β^- decay products have previously been considered for RIS studies on ocean water circulation (95). However, it is also a particularly important application in view of the lack of knowledge concerning the behaviour of such nuclides in the environment and the inefficiency with which they are assayed by conventional means.

2-5 Literature-Based Nuclide Assessment

Before commencing preliminary experiments to develop RIS techniques for application to nuclear waste monitoring, a literature-based assessment was undertaken, the aim of which was to determine the likely constituents i.e. the nuclide composition of nuclear waste materials reaching the environment. In particular, it was hoped to identify nuclides (such as low-energy β^- emitters) potentially assayable by RIS but difficult to detect by conventional counting, which have high probabilities of being released in relatively large amounts. The choice of nuclide(s) was further constrained by the type of laser system available, to being of an element amenable to scheme 1 or scheme 2 (2) resonance ionisation.

The assessment was subdivided into two parts: a) fission products and/

and b) neutron activation products. Fission products were classed under the actinide element from which they arose and activation products subdivided according to the part of the reactor where activation occurred.

I Fission Products

Fission product nuclides and their yields from the thermal neutron induced fission of $^{235}_{92}U$ and $^{239}_{94}Pu$ (96) were tabulated. For each nuclide, the half life (96), decay mode and energy (97), and allowed limits of intake (82) were tabulated, as was the resonance ionisation scheme for the element recommended by Hurst (2). Decay chains from the fission products to stable nuclides were drawn out based on data in references 97 and 78, in order that important daughter isotopes of the direct fission products could be considered.

II Neutron Activation Products

Since neither a review article on which to base this section of the assessment nor data on the number of atoms of each element present in the reactor were available, only qualitative information (based on the assumption that the chemical elements present have their natural isotopic compostion) could be deduced.

A number of elements present or potentially present as impurities in reactor materials were tabulated and decay (97) / neutron activation (98) schemes constructed for each isotope to determine which other nuclides they produce.

Activation/

Activation of fuel nuclides generated higher actinides, principally by combinations of neutron absorption and β^- decay reactions. Although many of the nuclides in this section are also α active, the long half lives for these α processes ($> \sim 20$ y) renders them relatively insignificant as the useful life of a fuel rod is only 1 or 2 years. Principal links in the so-called 'Heavy Atom Burn-Up Chain' are shown in Figure 2.51 (77). The amounts of some representative actinides produced in this way are shown in Table 5. The values given are for a 1000 MW pressurised water reactor (77).

TABLE 5

Production rates and associated activity for some important actinides

ISOTOPE	PRODUCTION RATE	
	kg/year	Ci/year
^{241}Am	2	6×10^3
^{242}Cm	0.1	3×10^5
^{244}Cm	0.8	7×10^4

Isotopes of the natural decay series (80) were also considered as they may be present in fuel due to inadequate chemical separation during ore processing and fuel fabrication.

Activation of fission products was treated similarly, i.e. decay chain and daughters were included, but only the fission products with large/

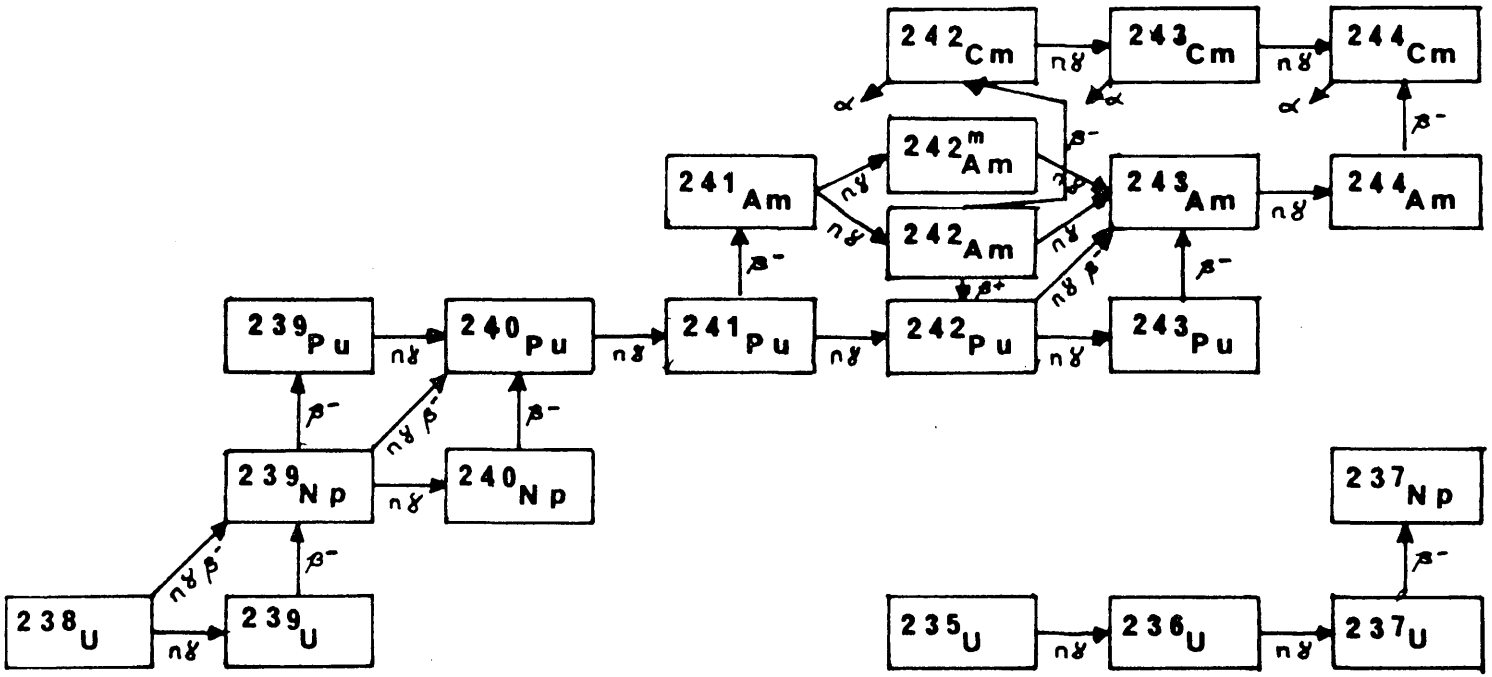

FIG. 2.51: PRINCIPAL LINKS IN THE HEAVY-ATOM BURN UP CHAIN

large thermal neutron capture cross section (>25 barns) were considered. These are listed in Table 6. Data is for a typical thermal reactor (77).

TABLE 6

Neutron Capture in Fission Products

ISOTOPE	% OF TOTAL f.p. CAPTURES	THERMAL NEUTRON CAPTURE CROSS SECTION (barns) (98)	PRODUCT
^{135}Xe	25	$(2.65 \pm 0.2) \times 10^6$	^{136}Xe
^{149}Sm	10	$41{,}000 \pm 2{,}000$	^{150}Sm
^{143}Nd	8	3.25 ± 10	^{144}Nd
^{103}Rh	7	150 ± 5	^{104}Rh m+g
^{147}Pm	6	85 ± 5	^{148m}Pm
		96 ± 1.8	^{148}Pm
^{131}Xe	5	90 ± 10	^{132}Xe
^{133}Cs	5	29 ± 1.5	^{134}Cs m+g

m = metastable m+g = metastable + ground state

Finally, activation of fuel cladding and other reactor core materials was/

was considered. Possible daughter species from radioactive decay and/or neutron activation of isotopes of the following elements were listed:

Cr, Mn, Fe, Co, Ni, Zr, Nb, Sb, Mg	(metal cladding, coolant pipes, steel etc.)
B, Cd	(control rods)
C, O	(graphite moderator, CO_2 coolant)
Si	(concrete pressure vessel)
P, S, As, Ca, Sr, Ag, Cu, Zn, Sn, Sc, Y	(possible trace impurities in alloys or concrete)

To reduce the resulting list of isotopes to more manageable proportions, two criteria were applied. All nuclides of short $t_{\frac{1}{2}}$ (< 5 d) were eliminated as their rate of decay both in storage prior to release and in the environment would be rapid. All non resonance ionisation scheme 1 or 2 (2) elements were eliminated since, although many were of interest, they could not be efficiently ionised by a single excimer-dye laser system.

From the remaining shortlist of elements, caesium was chosen. The reasons for this selection were as follows. Several isotopes of the element are associated with the Nuclear Industry, most of which are fission products. Thus some semi-quantitative information on the amounts produced may be deduced. $^{137}_{55}Cs$ is the principal reported component of low level liquid waste. In 1982 2,000 TBq of the isotope were eluted by the Sellafield reprocessing plant (85), a value/

value almost an order of magnitude greater than that attributed to any other, separately assayed nuclide, and constituting more than half the total β^- activity discharged. $^{134}_{55}Cs$ is also currently assayed separately. However, of more interest from the RIS viewpoint is $^{135}_{55}Cs$. It is a low-energy β^- emitter produced in high yield (i.e. $\sim$ 6%) from the thermal fission of the principal fuel nuclides (96), but is subject to no discharge restriction apart from the gross β^- activity limit. It is also, as was shown in Table 4, assayable (at levels where conventional radiometry becomes unreliable) with existing RIMS technology. Since discharges of $^{137}_{55}Cs$ and $^{134}_{55}Cs$ are high, it is likely that considerable amounts of $^{135}_{55}Cs$ are also present in low level waste but remain largely undetected. Finally, caesium has already proved itself amenable to RIS - as shown by the early work of Hurst et al. (11,12,13,15,16,17,18).

Table 7 shows the isotopes of caesium associated with the Nuclear Industry. Their decay modes and energies (97) and annual limits for intake (both oral and by inhalation) appropriate to members of the general public (82) are also tabulated.

Before progressing to isotopically selective Cs detection, or to environmental material, detection at an elementally selective level was required. To demonstrate the capacity of the experimental system to perform this task, a sample of caesium metal (100% $^{133}_{55}Cs$) was obtained from Aldrich Chemical Co. The metal appeared yellow-tinged and melted readily at just above room temperature. Cs is the most electropositive and most alkali of metals. As well as spontaneously igniting/

TABLE 7

The isotopes of Cs associated with nuclear waste

ISOTOPE	HALF LIFE (97)	DECAY MODE (97)	DECAY ENERGY MeV (97)	A.L.I. (PUBLIC) MBq (82)	
				oral	inhal.
$^{132}_{55}Cs$	6.5 d	β^+, EC	2.09	10	10
$^{134}_{55}Cs$	2.05 y	β^-	2.062	0.3	0.4
$^{135}_{55}Cs$	3×10^6 y	β^-	0.210	3	4
$^{136}_{55}Cs$	13 d	β^-	2.54	2	2
$^{137}_{55}Cs$	30.23 $\pm$ 0.16 y	β^-	1.176	0.4	0.6

igniting in air, it was found to be highly reactive towards many substances including plastics, glasses and (especially) organic solvents. It reacted explosively with water. Techniques employed for handling the metal are discussed in Chapter three, along with the apparatus used. Some basic properties of caesium are presented in Table 8.

Results of Cs experimental work appear in Chapter five.

TABLE 8

Basic Properties of Caesium (97)

Atomic weight	132.9054
Atomic number	55
Melting point (^{o}C)	28.40 $\pm$ 0.01
Boiling point (^{o}C)	669.3
Valence	1

CHAPTER 3 INSTRUMENTATION

3-1 Introduction

An excimer-dye laser system was used for the detection of gas-phase atoms above a Cs metal source at room temperature. For clarity, an overview of the complete apparatus used is presented at the beginning of this chapter, followed by detailed descriptions of the component parts. See Figure 3.11 for the overview.

An excimer laser [LUMONICS TE-860-3M] operating at 308 nm (XeCl filling) was used to pump a dye laser [LUMONICS EPD-330], generating tunable, visible or near ultraviolet output. The dye laser was automatically positioned by a scan control system [LUMONICS EPD-60 "Compuscan"] operating through a motor drive [LUMONICS EPD-50]. The dye beam was, optionally, passed through harmonic generating crystals to produce tunable ultraviolet output. Both manual and automatic operation of the frequency doubler [INRAD HARMONIC GENERATOR MODEL 562-126 and SERVO ELECTRONICS MODEL 5-12] was possible. When tunable ultraviolet laser light alone was required, a blue filter was inserted after the doubling crystals to eliminate the fundamental. A collimating aperture (usually 1 mm x 1 mm) was positioned before the experimental chamber and a lens of focal length = 20 cm could be inserted to focus the beam to 0.13 mm x 0.13 mm at the centre of the Cs detection apparatus (as/

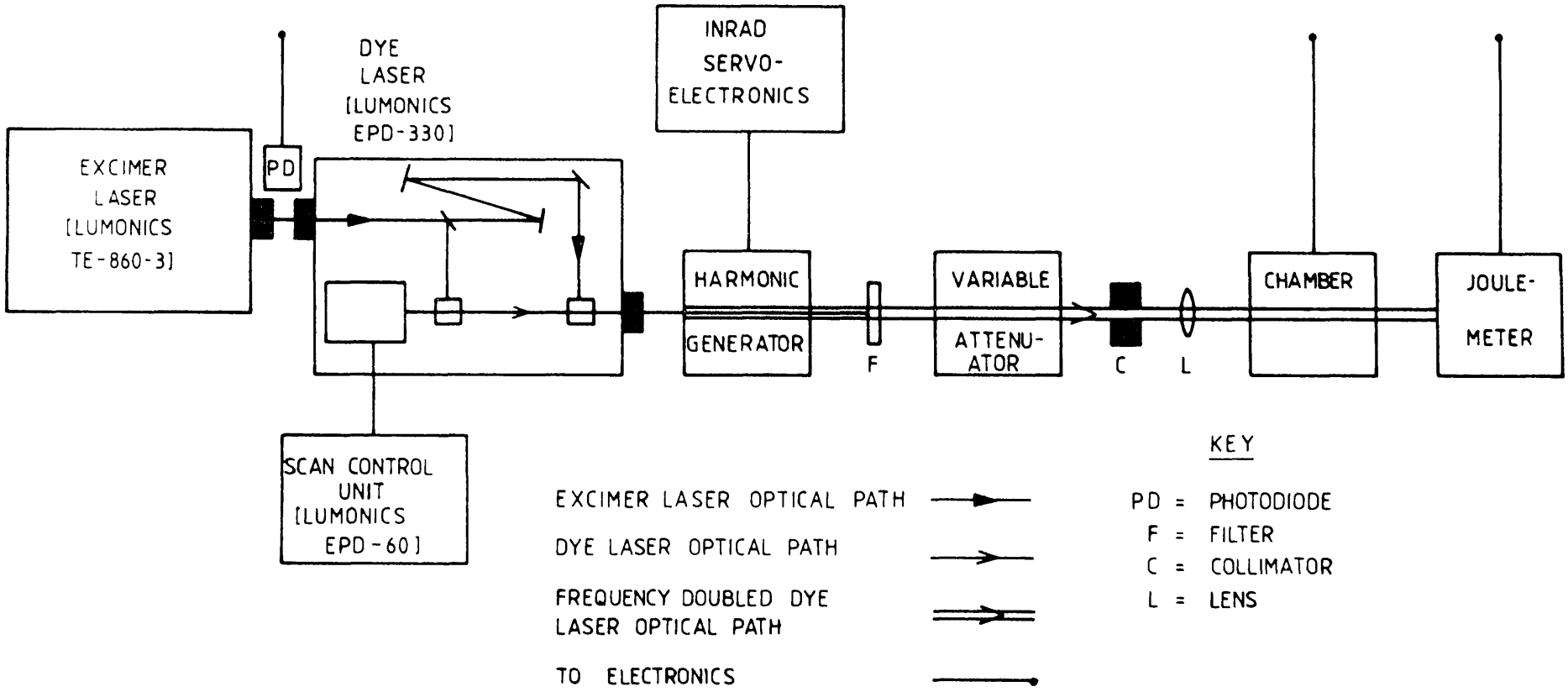

FIG. 3.11: INSTRUMENTATION FOR CAESIUM DETECTION

(as measured by a Spiricon photodiode array). Laser fluence was monitored at the end of the experimental line by a pyroelectric joulemeter [MOLECTRON J3-09] and could be controlled by a variable attenuator [NRC 935-5].

The laser induced ionisation signal from the proportional counter passed to a preamplifier [ORTEC 142] which also carried volts from the power supply [NUCLEAR ENTERPRISE 4519] to the chamber. Signals from both chamber and joulemeter were amplified and delayed to time coincidence with the gate of a peak-sensing ADC. A photo diode, positioned close to the excimer output, served as a timing signal for the electronics. Data collection was governed by an LSI-11 micro-computer and raw data was stored (event by event) on floppy disc prior to transference to an IBM mainframe computer for processing and analysis.

3-2 The Excimer Laser

Excimer lasers are high powered, pulsed, molecular lasers. Output wavelengths range from the vacuum ultraviolet ($\lambda < 200$ nm) to the visible (400 - 700 nm) depending on the molecular species involved, i.e. on the nature of the operating gas mixture (99). In excimer molecular systems, some electronically excited states formed by one ground state atom and one electronically excited atom are bound whereas the molecular ground state is not, i.e. the constituents of the gas mixture repel each other, at the atomic level, unless some of the atoms are excited. See Figure 3.21. Excitation is usually brought/

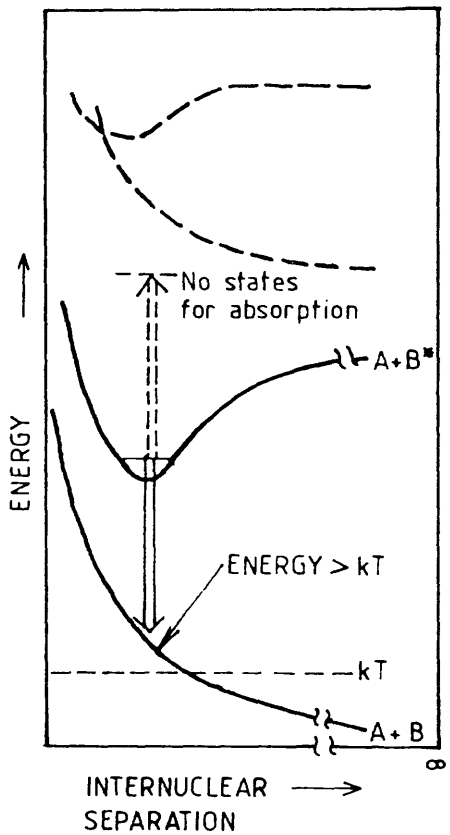

FIG. 3·21: SCHEMATIC ENERGY LEVEL DIAGRAM FOR AN EXCIMER LASER

brought about by an intense electron beam or a fast electrical discharge and lasing arises as the excimer molecule, composed of two atoms A and B, in the bound, excited state A+B* , returns to the ground state and dissociates.

Excimer laser systems are unusual in that, as long as the A+B* state (the upper state of the laser transition) is populated, a population inversion automatically exists. This is due to the speed with which the ground state molecule dissociates, i.e. $\sim 10^{-13}$ s (100). Thus, every excited molecule contributes a photon to the laser beam instead of only sufficient photons being emitted to equalise upper and lower state populations.

Not all excimer molecular systems are suited for lasing action: the principal disadvantage of most being that bound states exist at higher energy than A+B* and, if these are accessible from A+B* by absorption of a photon they will reduce the effective population inversion and may quench the lasing action. Loss of efficiency may also occur due to intermolecular collisions dissociating the molecular species before stimulated emission can occur.

Suitable active media for excimer lasers include rare gas dimers e.g. Xe^*_2 , rare gas oxides e.g. XeO^* , and rare gas halides e.g. $XeCl^*$.

The laser used in this study [LUMONICS TE-860-3M] had a filling gas mixture of the composition shown in Table 9:

TABLE 9

Excimer Gas Mixture

TYPE OF GAS	CONSTITUENTS	PRESSURE
BOC Research Grade	Xe	39 torr
BOC Special Mix	H_2 0.95% HCl 4.73% He balance	31 torr
BOC Standard Grade	He	to 50 psi

Lasing action arose from $XeCl^*$ excimers produced by a fast electrical discharge of ~ 32 kV. The wavelength of the laser was 308 nm in the ultraviolet. When fitted with stable resonator optics, the output energy was ~ 80 mJ/pulse, with a pulse to pulse reproducibility of ± 3% (at 35 Hz). The power and reproducibility deteriorated after a few days operation and it was found necessary to recharge the laser once power dropped below ~ 50 mJ/pulse. The beam was rectangular with cross section 8 mm x 12 mm and full angle beam divergence of 2.4 mR x 6 mR. Pulse width was typically in the range 8 ns - 12 ns (FWHM). The laser appears in Plate 1.

3-3 The Excimer-Pumped Dye Laser

Dye lasers are sources of tunable radiation within the approximate/

to follow Page 63

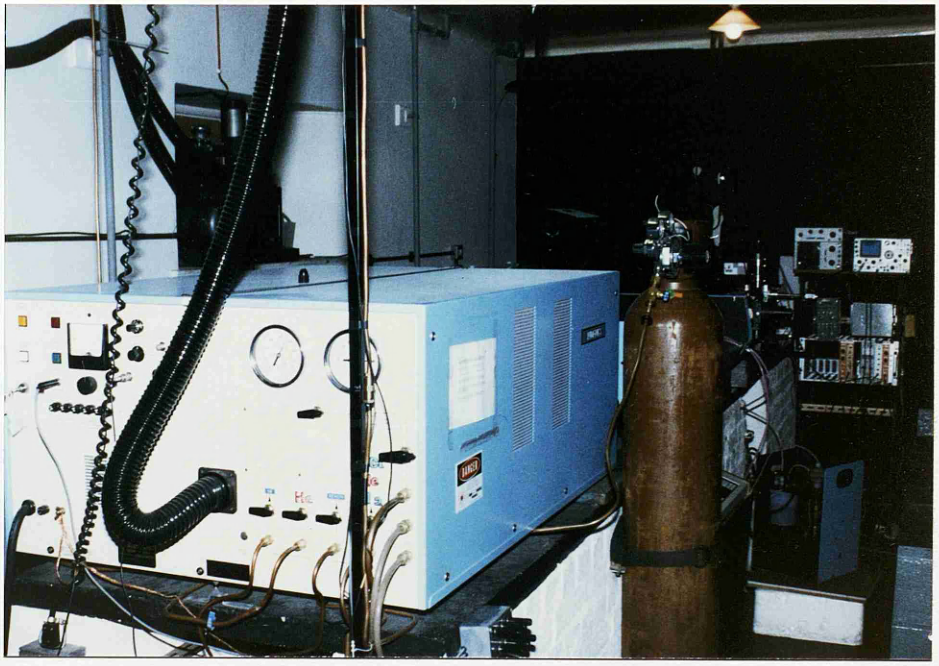

PLATE 1

LUMONICS EXCIMER LASER

approximate range of 315 nm - 1200 nm, i.e. from the ultraviolet to the infrared regions of the spectrum. The active medium was discovered in 1966 by Sorokin and Lankard (101), and is a solution containing a fluorescent organic dye. Suitable dyes include the xanthenes and coumarins (102). The first narrow bandwidth dye laser (i.e. bandwidth $< \sim$ 0.1 nm) was reported in 1972 by Hansch (103). Dye lasers require to be optically pumped by either another laser (e.g. the excimer, Nd:YAG or N_2 laser) or by a flashlamp.

Figure 3.31 is a schematic energy level diagram illustrating lasing action in a dye laser (100). Since dye molecules are large and complex, precise calculation of the wavefunctions and energies of all the permitted molecular states is not possible. Instead, the energy level diagram is derived by analogy with that of a simple diatomic molecule with the horizontal axis of the diagram representing a configuration coordinate analogous to the internuclear separation in the diatomic system. For clarity, the origin of the configuration coordinate for the triplet states of the molecule has been shifted to the position of the dashed line. At room temperature, only the lower vibrational-rotational levels of an electronic state are populated. It should be noted that the configuration coordinate corresponding to minimum energy is different for each electronic level.

During the pump pulse, dye molecules are excited from $S_0 \rightarrow S_1$ by absorption of photons. This is represented by a vertical line on the diagram due to the Franck-Condon Principle, which states that the/

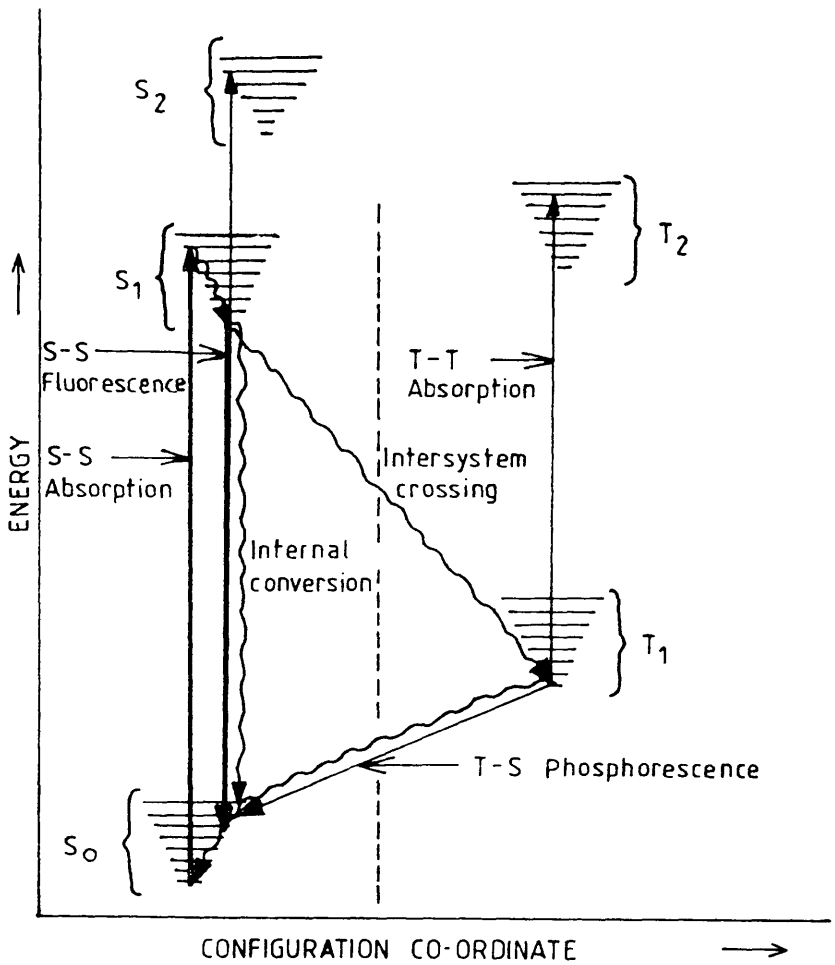

FIG. 3·31: SCHEMATIC ENERGY LEVEL DIAGRAM FOR A DYE MOLECULE

the molecular configuration cannot change during an electronic process. Having achieved the S_1 state, the molecule may re-emit the photon and return to the ground state. More probable, however, is a non-radiative transition to lower energy states in S_1 (taking $\sim 10^{-12}$ s) (100) - with the excess energy being taken up by solvent molecules - followed by fluorescence. It is the fluorescence transition, which has a radiative lifetime of $\sim 10^{-9}$ s (100), which is responsible for laser action. The emitted photon is of lower energy than the absorbed, i.e. the fluorescnece band of the dye is shifted to longer wavelength than its associated absorption band - the so-called Stokes Shift. The fluorescence band is also broad (typically $\sim$ 50 nm) as it involves transitions from all the thermally populated vibrational-rotational levels of S_1 to the many, high level, vibrational-rotational states of S_0 . Following fluorescence, further non-radiative transitions in S_0 occur to return the population to its thermal distribution.

Fluorescence quantum efficiency is the ratio of the number of photons emitted by the dye to the number absorbed. If all molecules excited to S_1 de-excite by fluorescence the value is unity. However, a number of competing processes deplete the S_1 population and thus affect the gain of dye lasers. Transitions from $S_1 \rightarrow S_n$ (where $n \neq 0$) occur as do non-radiative $S_1 \rightarrow S_0$ transitions (internal conversions). The triplet states, although not directly involved in laser action, influence the fluorescence quantum efficiency since non-radiative transitions between states of different multiplicity, although formally forbidden, can and in fact do occur due to the small amounts of admixing/

admixing between pure triplet and pure singlet states which arise from spin-orbit interactions. Fluorescence quantum efficiency is thus further reduced by intersystem crossing $S_1 \longrightarrow T_1$ which takes $\sim 10^{-5}$ s (100). Worse still, population of T_1 leads to triplet absorptions $T_1 \longrightarrow T_2$ which often occur at similar frequencies to $S_1 \longrightarrow S_0$ radiative transtions and can severely limit or quench laser action by absorbing the fluorescence emission. Other possible transitions of a molecule in T_1 are intersystem crossing $T_1 \longrightarrow S_0$ and a radiative transition (phosphorescence) between the two states. These processes are forbidden also, and phosphorescence has a much slower radiative decay rate than fluorescence (i.e. phosphorescent lifetime is $\sim$ ms), limiting the rate at which molecules crossing to triplet states can return to the S_0 ground state for re-excitation.

To reduce the number of molecules in triplet states most dye lasers are operated in pulsed mode with pulsewidth shorter than the time necessary for T_1 to achieve significant population.

The laser used in this study was a Lumonics EPD-330, pumped by the XeCl excimer described above. The output power was 3 - 14% of the pump power depending on the dye used. The beam size also varied from dye to dye but was, typically, 1 mm x 2 mm with full angle beam divergence of less than 1 mR. Pulsewidth was 2 ns less than that of the excimer, i.e. 6 - 10 ns (FWHM), and the linewidth was 0.05 nm without and 0.003 nm with the prism beam expander inserted in the laser cavity. The dye laser beam was polarised (> 95%) in the vertical plane.

The following dyes, listed in Table 10 and shown in Figure 3.32, have been used to fill the Lumonics dye laser used.

An optical schematic of the dye laser is shown in Figure 3.33, and a photograph showing it operating on a DCM dye fill comprises Plate 2. The pump beam enters 7.6 cm above and parallel to the optical baseplate. It is divided by a partially reflecting mirror [M1] and one portion is focused into the oscillator cell [DC1] whilst the remainder is steered via a system of mirrors [M2 - M4] and focused more tightly into the amplifier cell [DC2] . The output coupler, a quartz flat with a 1° wedge, serves to align the dye laser beam with the gain region of the oscillator cell. The output is tuned by movement of a holographic grating [GR] (2400 lines/mm): this may be operated manually or, as in this study, controlled by an external electronic unit. The Lumonics "Compuscan" [EPD-60] was used for automatic scanning and wavelength positioning of the laser. A prism beam expander, which improves laser linewidth by increasing the number of lines on the grating with which the beam is incident, was also installed. However, for most of the Cs study, this was demounted since it reduced laser fluence considerably. The dye solution was circulated in a single, water cooled, closed loop system passing through first the oscillator and then the amplifier cell. The laser was also fitted with a standard gravity interlock and with a fibre optic cable which emerged from the rear of the cavity. When coupled to a photodiode this generated a timing signal for the data collection system and when passed into a monochromator [HILGER & WATTS] the light from the fibre optic served as/

to follow Page 67

PLATE 2

EXCIMER-PUMPED DYE LASER

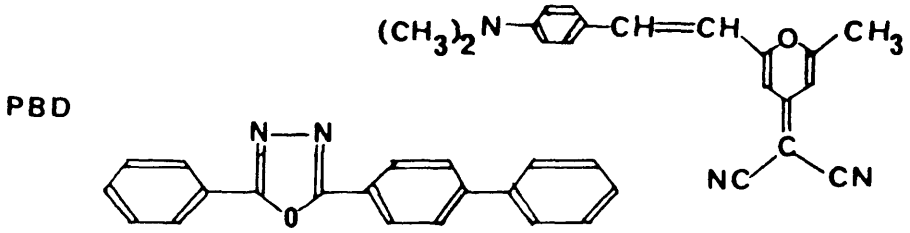

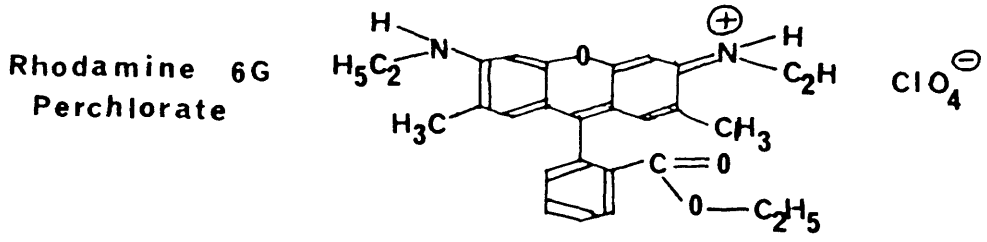

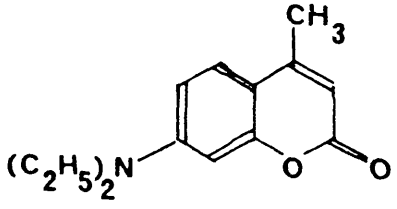

Coumarin 47

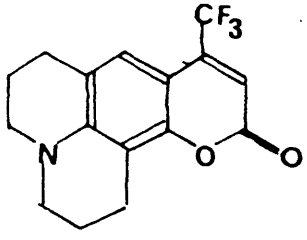

Coumarin 153

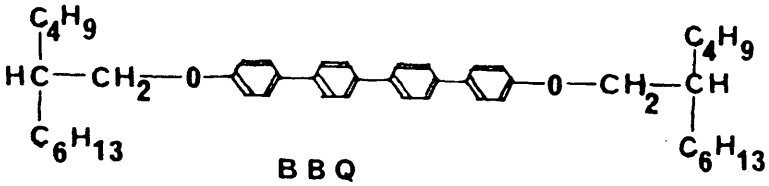

BBQ

FIG.3.32: CHEMICAL STRUCTURES OF LASER DYES

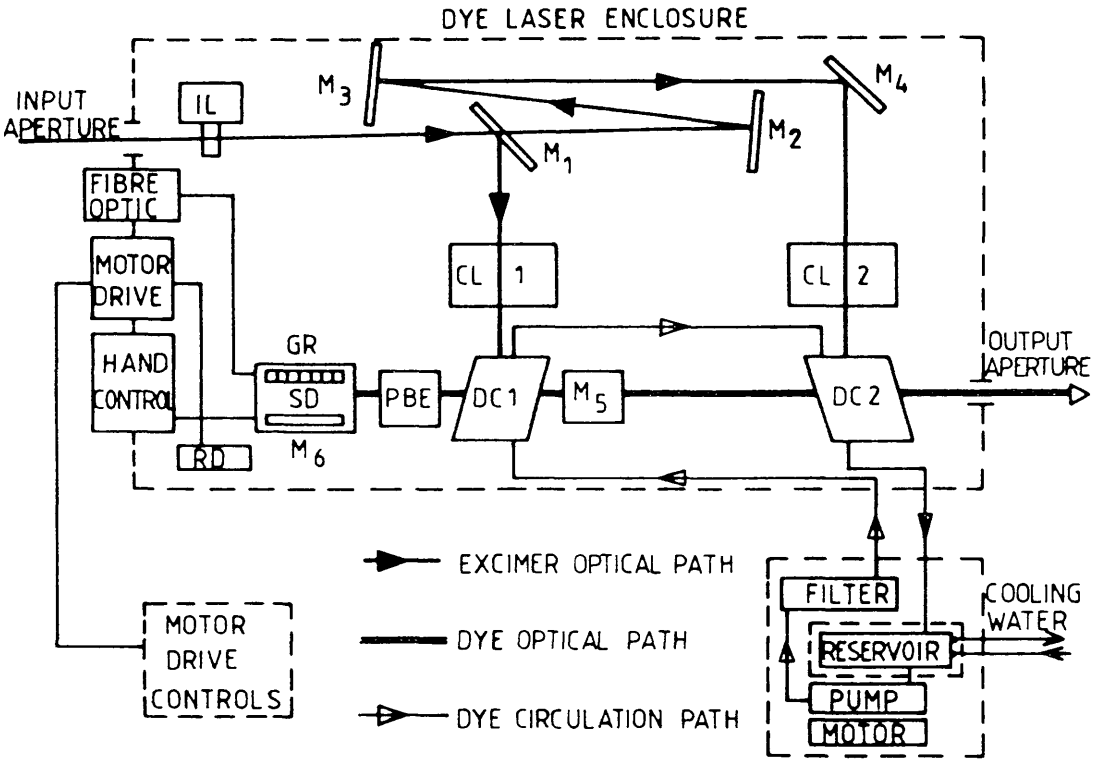

KEY : CL 1, 2 CYLINDRICAL LENSES
DC1, 2 DYE CELLS
GR GRATING
IL INTERLOCK
$M_1 - M_4 - M_6$ REFLECTORS
M_5 OUTPUT COUPLER
PBE PRISM BEAM EXPANDER
RD READOUT
SD SINE DRIVE

FIG. 3·33: OPTICAL SCHEMATIC OF THE LUMONICS EPD – 330 DYE LASER

TABLE 10 - Laser Dye Properties

DYE NAME (alternative names)	CHEMICAL NAME (102)	TUNING RANGE (nm) *	PEAK (nm)	SOLVENT	THEORETICAL EFFICIENCY (%)
PBD	2-Phenyl-5-(4-biphenylyl)-1,3,4-oxadiazole	353 - 381	360	Ethanol / Toluene (1:1)	5.2
BBQ	4,4"'-Bisbutyl octyloxy-p-quaterphenyl	366 - 400	385	Ethanol / Toluene (6:4)	7.1
Coumarin 47 (Coumarin 1)	7-Diethylamino-4-methyl coumarin	439 - 486	458	Ethanol	12.7
Rhodamine 6G	Rhodamine 6G	569 - 608	581	Methanol	9.6
Coumarin 153	2,3,5,6-1H,4H-Tetrahydro-8-trifluoro-methylquinolizino 9,9a,1-gh coumarin	521 - 594 (260 - 297)	540	Methanol	9.3
DCM	4-Dicyanomethylene-2-methyl-6-p-dimethylaminostyryl-4H-pyran	602 - 686 (301 - 343)	637	Methanol	8.3

* ( ) denotes tuning range after frequency doubling

as a check on laser wavelength.

3-4 The Harmonic Generator

Optical harmonics were first observed in 1961 (104) when the light from the newly discovered pulsed ruby laser (wavelength 694.3 nm) was focused into a quartz crystal and the second harmonic at 347.2 nm observed. Considerable interest in non-linear optical effects resulted (105), and, over a few years, the dependence of harmonic output on the properties and orientation of the crystalline medium was much studied. Continuous wave harmonic generation from the He-Ne laser followed in 1963 (106). A notable review article, giving a simplistic and readable introduction to the subject, was published by Giordmaine in 1964 (76).

Although it had long been known that strong magnetic and electrical fields could affect the propagation of light in materials, until the development of the laser these fields were always applied externally by experimenters using magnets or electrical coils. In the laser, however, the beam is so intense that the magnetic and electrical fields associated with it can themselves alter the properties (e.g. refractive index) of the material in which the light is travelling. Thus the laser affects its own propagation by modifying the propagating medium, leading to interesting, non-linear optical effects such as harmonic generation (described below) and frequency mixing.

Second/

Second harmonic generation may be explained in simple mathematical terms as follows:-

For high values of electric field E (such as those associated with a laser beam) the polarisation P is given by the series

$$P = \alpha_1 E + \alpha_2 E^2 + \alpha_3 E^3 + \ldots\ldots \qquad \text{---- (25)}$$

where α_1, α_2 and α_3 are constants

For a laser, the electric field can be expressed as

$$E = E_0 \sin \omega t \qquad \text{---- (26)}$$

where E_0, t are constants,

and ω is the laser frequency

Substituting (26) in (25)

$$P = \alpha_1 E_0 \sin \omega t + \alpha_2 E_0^2 \sin^2 \omega t + \ldots\ldots \qquad \text{---- (27)}$$

Taking only the first two terms of the series, and using the standard formula

$$\sin^2 \theta = \tfrac{1}{2} (1 - \cos 2\theta)$$

equation (27) becomes

$$P = \alpha_1 E_0 \sin \omega t + \tfrac{1}{2}\alpha_2 E_0^2 - \tfrac{1}{2}\alpha_2 E_0^2 \cos 2\omega t \qquad \text{---- (28)}$$

where the first term represents the polarisation of a laser of frequency ω, and the third term represents a contribution to P from a laser with frequency 2ω, i.e. half the wavelength of the fundamental laser beam.

A more intuitive description, which may aid in visualising the origins of harmonic generation, is also given:-

When/

When the alternating electric field of a laser beam passes through a crystalline medium, the valence electrons of the atoms in the crystal redistribute themselves in step with the field. This displacement or oscillatory motion of negative charge is known as the polarisation wave. It travels through the medium with the same velocity as the laser light wave. In a non-centrosymmetric medium such as quartz, the polarisation wave is distorted since it is easier to move electron density in one direction than in the other. The distorted polarisation wave can be shown to be the sum of three components: a wave at the fundamental frequency, a wave at twice the fundamental frequency, and a steady polarisation. See Figure 3.41. The second harmonic polarisation wave travels in step with the fundamental light wave and radiates light at the second harmonic frequency. The velocity of the second harmonic light is slower (in most media) than that of the fundamental since the refractive indices for the two frequencies are different. Since the second harmonic polarisation wave travels at the same velocity as the fundamental, the second harmonic light it radiates at any instant will not be in phase with the light it radiated a fraction of a second earlier. The distance required for the second harmonic polarisation wave and the second harmonic radiated wave to become completely out of phase is the coherence length. This is typically $\sim 10^{-3}$ cm for most crystalline media and, for crystals of thickness $\geqslant$ the coherence length, interference effects reduce harmonic output to unobservable levels.

This difficulty can be overcome by the use of doubly refracting crystals/

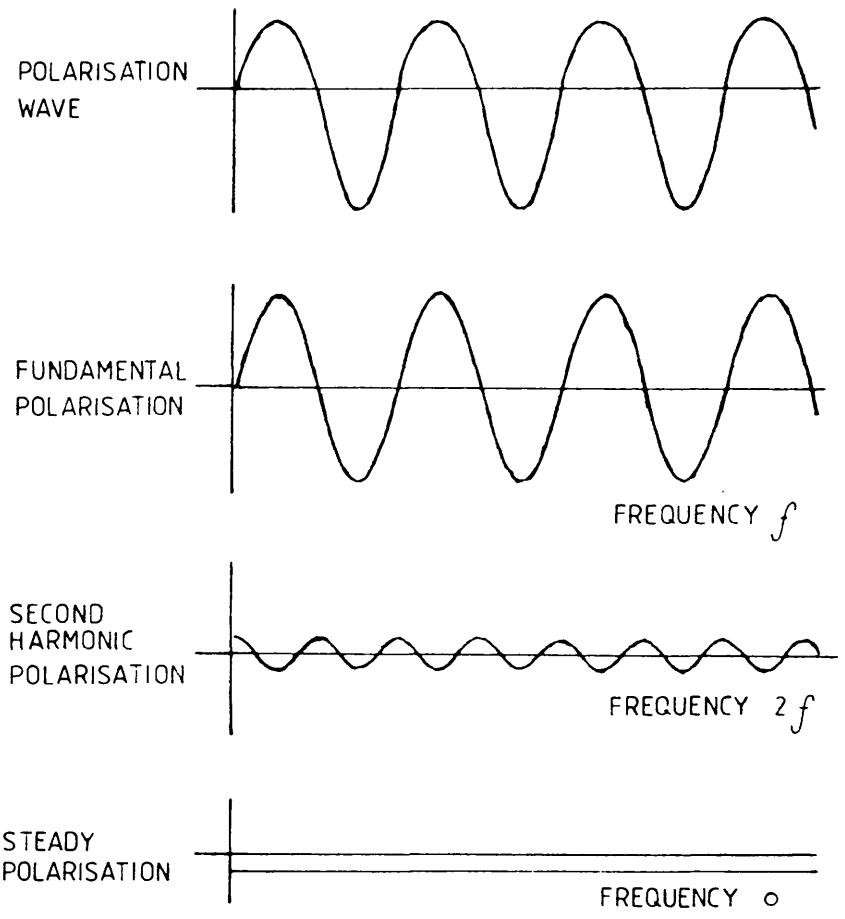

FIG. 3·41: SECOND HARMONIC GENERATION

the upper trace is the distorted polarisation wave and

the traces below are the components into which it may be resolved

crystals in which light at one wavelength can propagate at two different velocities, described as ordinary and extraordinary, which vary with the propagation direction relative to the crystallographic axes. Crystals which have this property and which have been found suitable for second harmonic generation (105) are KDP (potassium dihydrogen phosphate) and ADP (ammonium dihydrogen phosphate). With the laser beam incident at an angle of 50° to the optical axis, a crystal of KDP passes ordinary light from the ruby laser at the same velocity as extraordinary second harmonic light at 347.2 nm (107). Coherence length is thus increased and harmonic generation greatly enhanced over what was possible with other types of crystal.

In the present study four second harmonic generating crystals were mounted in a dry nitrogen purged, hermetically sealed cell [INRAD MODEL 562-126]. The wavelength ranges of the crystals are shown in table 11, and the harmonic generator itself in Plate 3.

TABLE 11

Harmonic Generating Crystals Wavelength Ranges

CRYSTAL	FUNDAMENTAL WAVELENGTH (nm)	HARMONIC WAVELENGTH (nm)
KPB "B"	443 - 469	221 - 235
KPB "C"	469 - 518	234 - 259
KDP "B1"	525 - 565	262 - 283
KDP "R6G"	565 - 660	282 - 330

to follow Page 72

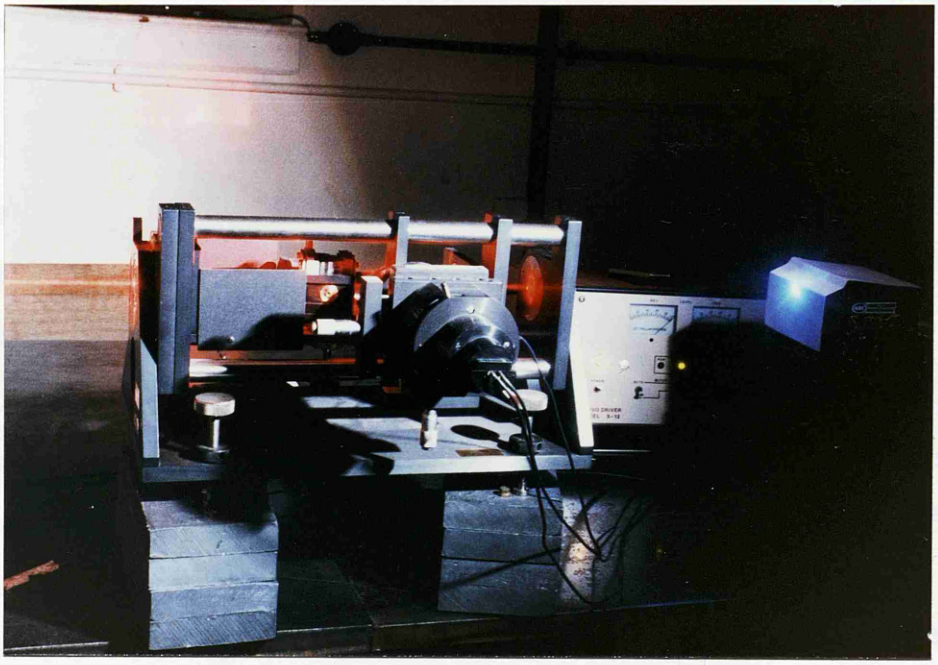

PLATE 3

INRAD HARMONIC GENERATOR

The cell containing the crystals was mounted in an Inrad Model 5-12 Autotracking System. In principle, this device was capable of sampling the beam, detecting any UV output present, and adjusting the assembly to maximise this output by orientating the second harmonic generating crystals to exactly the phase match angle. Thus, the autotracking system should be able to follow the dye laser in scanning mode - maintaining stable, ultraviolet output as the visible wavelength changed. In practice, however, the operation of the equipment was such that it was found difficult to scan in the ultraviolet region of the spectrum by varying dye laser wavelength. Extreme difficulty was encountered in keeping the autotracker in step with the dye laser as it varied in wavelength and, for almost all measurements described here, manual override of the autotracker was employed, and the crystals adjusted by hand. Most data from experiments requiring frequency doubled light were obtained, not by continuous scanning, but by incrementing the dye laser wavelength and, at each point, maximising the second harmonic output of the crystal manually.

3-5 Experimental Chambers

The chamber for caesium detection developed through three major phases.

I Caesium Chamber Mark 1 - Copper Plate Design

See Figure 3.51. The initial design of the caesium detector was a parallel plate drift chamber comprising copper plates separated/

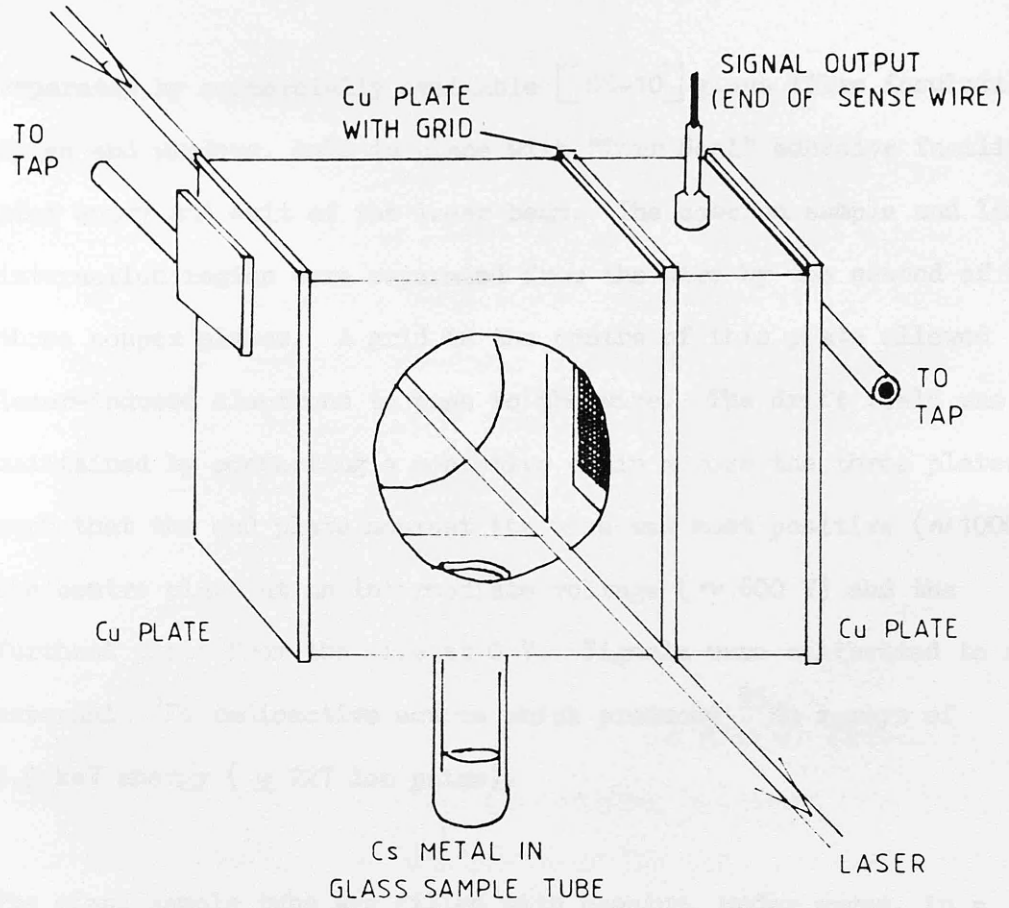

FIG. 3·51: CAESIUM DETECTION CHAMBER MARK 1

separated by commercially available [GS-10] glass fibre insulation. Glass end windows, held in place with "Torr Seal" adhesive facilitated entry and exit of the laser beam. The caesium sample and laser interaction region were separated from the wire by the second of the three copper plates. A grid in the centre of this plate allowed laser-induced electrons to pass to the wire. The drift field was maintained by connecting a resistive chain across the three plates such that the end plate nearest the wire was most positive ($\sim$1000 V), the centre plate at an intermediate voltage ($\sim$ 600 V) and the furthest plate from the wire at 0 V. Signals were calibrated to an external ^{55}Fe radioactive source which produced ^{55}Mn x-rays of 5.9 keV energy ($\equiv$ 227 ion pairs).

The glass sample tube was filled with caesium, under argon, in a glove box: the breakseal vial in which the metal is supplied was cracked, the caesium was warmed until melting (hand-heat being sufficient), and the liquid transferred with a glass pipette. The sample tube was sealed into the chamber, with araldite adhesive, whilst still under Ar. The chamber was filled with standard P-10 counting gas (90% Ar : 10% CH_4) for static operation, or connected to the gas bottle and to a flowmeter for operation in a gas-flow mode. Over a number of trials, it was found impossible to maintain the caesium in an unreacted condition for sufficient time to allow data to be taken. After only a few minutes outside the inert atmosphere of the glove box the sample showed visible signs of surface discolouration. Caesium detection was not achieved in the copper plate chambers.

II Caesium Chamber Mark 2 - Glass Design

See Figure 3.52. A glass counter was constructed from cylindrical, 5 cm (outside diameter), pyrex tubing and circular end windows - also of pyrex glass. A stainless steel proportional counter of the type used routinely in Glasgow (107) (i.e. the central part of the ionisation detector in the T-shaped chambers described in Chapter 4) was mounted inside the tubing, with electrical feedthroughs from the central wire and enclosure leading to the exterior. A positive voltage (typically ~ 750 V) was applied to the wire whilst the enclosure remained at earth potential. The calibration source (^{55}Fe) was affixed to the rear of the counter with a small aperture to allow the ionising radiation into the sensitive region close to the centre of the wire. A metal plate 3 cm x 4 cm was fixed opposite the counter. A negative voltage applied to this encouraged electrons to drift towards the wire. Caesium was introduced by vacuum distillation: heat was applied to a reservoir containing the metal and the sample holder cooled to encourage condensation in that region. The sample holder was then sealed off from the reservoir with a glass seal. The counter was filled with P-10 gas to 100 torr and isolated from the vacuum system with a further glass seal.

Detection of caesium vapour was achieved in the glass chambers and some results will be discussed in Chapter 5. However, a number of difficulties associated with the design were encountered. The chambers were easily broken and non-reusable. Having a glass outer casing, they were poorly electrically shielded and "pick-up" severely/

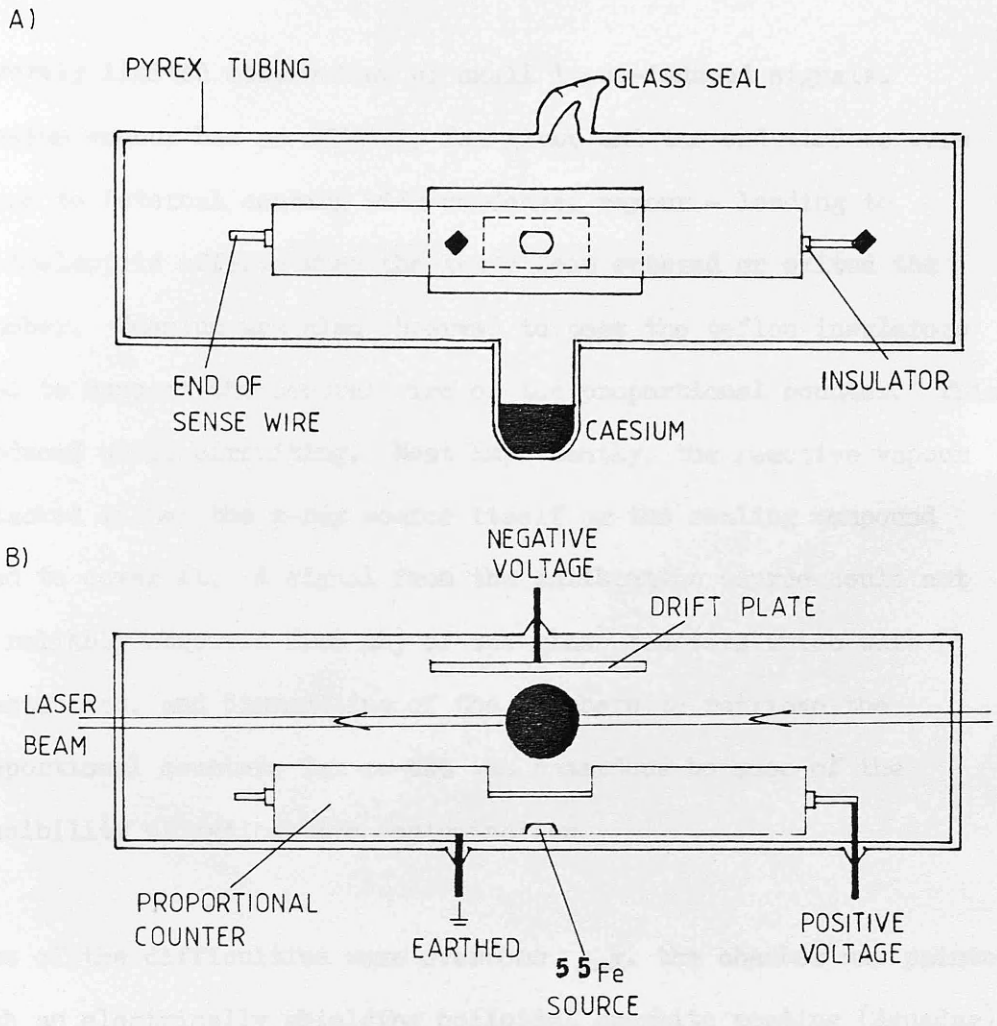

FIG. 3·52 : CAESIUM CHAMBER MARK 2
GLASS DESIGN

A) Viewed from the side.
B) Viewed from above.

severely limited observation of small laser-induced signals. Caesium vapour has an affinity for glass and the end-windows were prone to internal coating with condensed vapour - leading to photoelectric effects when the laser beam entered or exited the chamber. Caesium was also observed to coat the teflon insulators used to support the central wire of the proportional counter. This produced short circuiting. Most importantly, the reactive vapour attacked either the x-ray source itself or the sealing compound used to cover it. A signal from the calibration source could not be reliably observed from any of the glass counters which were constructed, and dismantling of the chambers to retrieve the proportional counters for re-use was hazardous because of the possibility of radioactive contamination.

Some of the difficulties were overcome e.g. the chamber was painted with an electrically shielding colloidal graphite coating (Aquadag) and the connecting cables shielded with foil. This reduced the radio frequency noise detected considerably. However, it was apparent that considerable improvement in the design of the experimental chamber was necessary if the reliable detection of small numbers of atoms of caesium was to be realised.

III Caesium Chamber Mark 3 - Stainless Steel Design

Ultra-high vacuum, stainless steel fittings were obtained from Vacuum Generators Ltd., and a third design of chamber constructed. This is shown schematically in Figure 3.53 and in use in Plate 4.

to follow Page 76

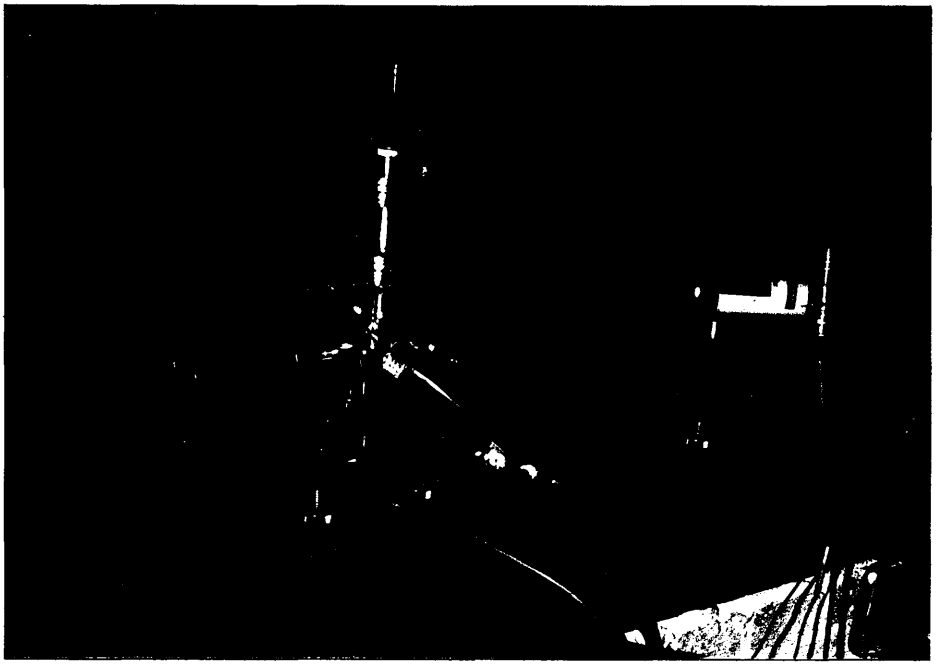

PLATE 4

CAESIUM EXPERIMENTAL CHAMBER

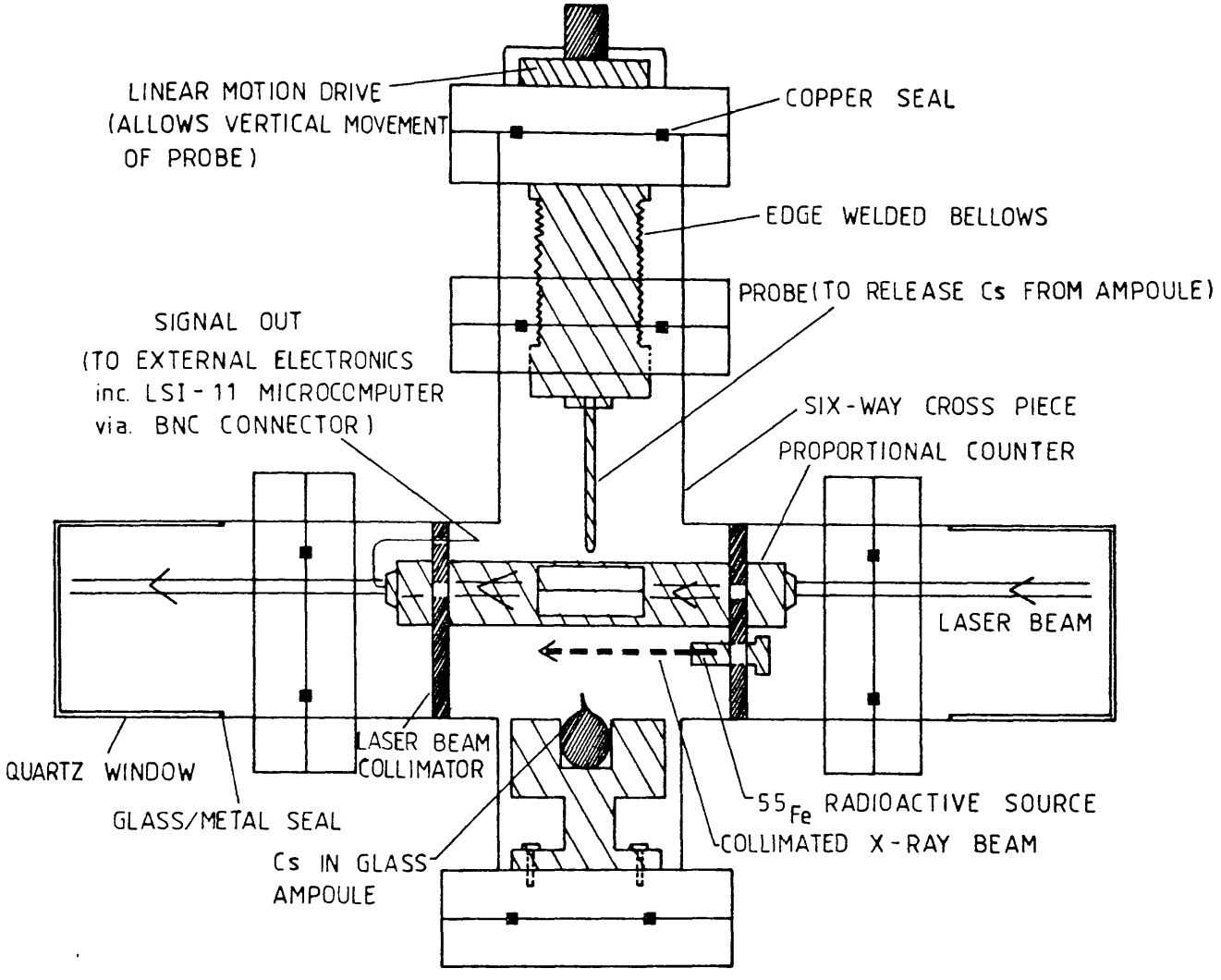

FIG. 3·53: CAESIUM CHAMBER MARK 3 STAINLESS STEEL DESIGN

A six-way cross piece was fitted with two windows to serve as laser entrance and exit ports. The windows were of quartz and were mounted, via graduated glass seals, on standard 70 mm flanges. A stainless steel proportional counter threaded with 0.025 mm stainless steel wire was push fit inside two stainless steel collimators which were themselves push fit to opposite limbs of the cross. The wire was supported in glass insulators and one end was crimped to a thicker Ni wire, whilst the tension was maintained at the other end with a small spring. The Ni wire, insulated from the collimator by glass and by ceramic beads passed into the rear (as viewed) limb of the cross where it was crimped into a few centimetres of stainless steel tubing. This tubing was push fit over the central pin of a BNC high vacuum feedthrough connected via a preamplifier [ORTEC 142] to the electronics and data acquisition system. High voltage to the central wire also passed via the pre-amplifier. Typically, 800 - 900 V were applied and the enclosure was at earth potential as was the remainder of the experimental chamber.

The aperture in the outer tube of the proportional counter was 2 cm in length x 1.4 cm wide, defining the sensitive region for detection of ionisation. Field lines extended from the anode wire to the walls of the six-way cross and thus any ionisation generated in the volume close to the counter - whether produced by the laser or the x-ray source - could be detected.

The beam collimators had knife edged apertures of 5 mm diameter to allow/

allow the laser to pass through the chamber. The apertures were widened to 10 mm diameter for experiments involving single photon ionisation of caesium since, otherwise, frequent realignment of the counter to the incident, frequency doubled laser was necessary to avoid the beam striking the knife edge at the extremes of the wavelength region investigated. One collimator also served as the mount for the ^{55}Fe calibration source.

A well was drilled from the tip of an 0-BA screw to a depth of $\sim$ 5 mm. A solution containing the source was deposited in the bottom of the well, taking care not to contaminate the tip, and the solvent allowed to evaporate. A hole was drilled and tapped in the collimator and the screw positioned in it so that the x-ray beam, collimated by the sides of the well, was parallel to the path of the laser and traversed the sensitive volume close to the proportional counter. This geometry was thought preferable to that employed in the glass counters as the relative orientation of the x-ray beam to the counter was the same as that of the laser to the counter.

The caesium metal sample, sealed in a thin-walled glass vial, was placed in a stainless steel well positioned so that evaporating caesium vapour would enter the laser interaction region close to the counter. Both an open caesium source as shown in Figure 3.53 and a collimated source - Figure 3.54A - were tested. In either case, caesium was released from the ampoule by a probe affixed to a linear motion drive. The room temperature vapour pressure of caesium is $\sim 1.5 \times 10^{-6}$ torr (108).

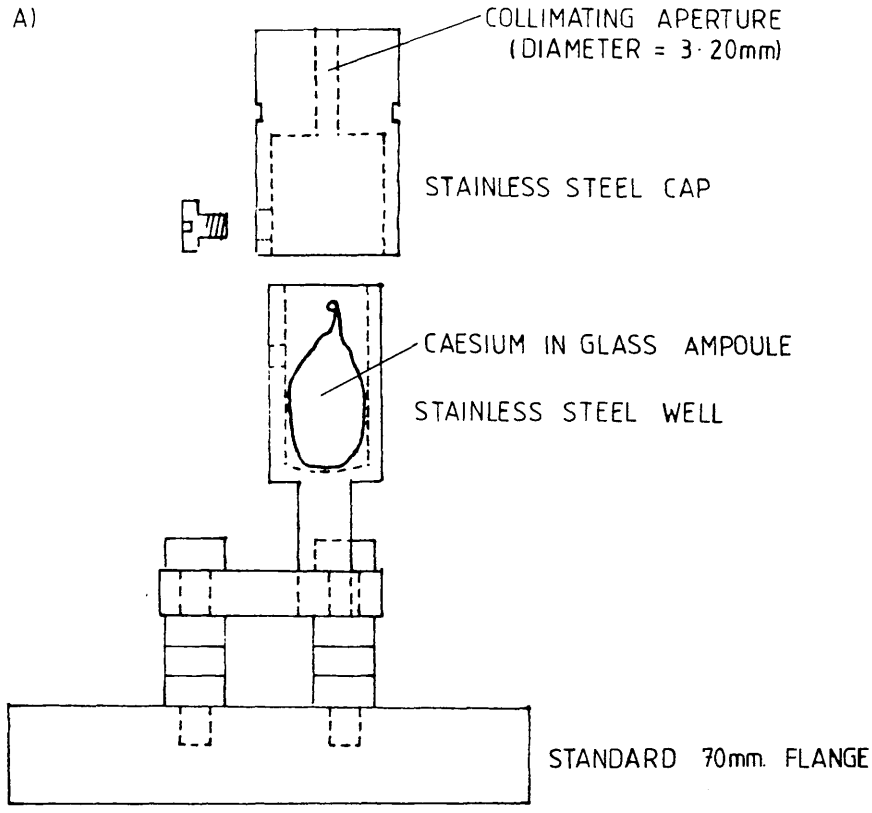

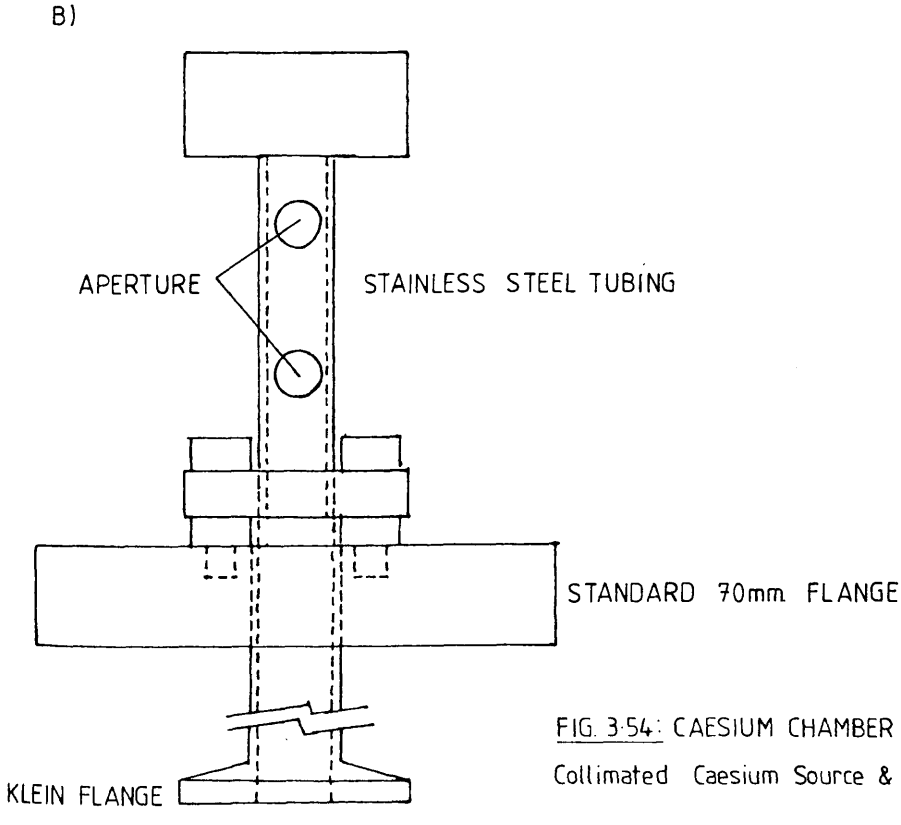

FIG. 3·54: CAESIUM CHAMBER MARK 3
Collimated Caesium Source & Gas Inlet

The final (front - as viewed) limb of the cross mounted the gas inlet pipe which connected to a standard "speedivac" tap by a Klein flange. See Figure 3.54B. The flat-topped design was necessitated by the requirement that there be an earthed cathode directly opposite the proportional counter aperture.

The chamber was normally operated with 30 torr of counter gas inside. Before filling to low pressure the counter was always flushed three times with counter gas at 760 torr, and then pumped out to, typically, $\sim 1 \times 10^{-5}$ torr. Low pressure operation was chosen for a number of reasons.

The widths of the caesium two-photon transitions are collisionally line broadened, an effect which is reduced at low gas pressure. Also, photons scattered from the laser beam on to the chamber walls produced photo-electrons which led to a background ionisation signal observable at all wavelengths. This scattering is attributed to gas molecules and, since background could limit the sensitivity of the apparatus for caesium detection, it was desirable to reduce the number of molecules of gas present by reducing the total gas pressure. Finally, assuming that some of the impurities responsible for caesium sample degradation are introduced with the filling gas, low pressure operation should prolong the lifetime of the free metal. In practice, over a period of a day or two, the number of caesium atoms detected at a constant laser fluence fell appreciably. This was attributed to surface reaction of the sample since, by re-extending the probe to puncture the caesium surface, the original counting/

counting rate could easily be restored.

A pressure of 30 torr standard P-10 (90% Ar : 10% CH_4) is close to the minimum at which a proportional counter may operate before gas multiplication becomes unstable due to there being insufficient quenching gas present. To avoid such instability, but maintain the advantages of low pressure operation, a different counter gas was used for most of the caesium experiments - Matheson high purity 70% Ar : 30% CH_4.

The use of standard vacuum fittings in the construction of the chamber facilitated rapid dismantling and reassembly for cleaning or repair. The counter could also be refilled with gas if this were required. Plastics and other organic materials were all but excluded from the design, the exception being the viton 'o' ring in the tap. Since these materials are the principal sources of "background" ionisable impurities in proportional counter systems (see Chapter 4 for a more full discussion of this), their exclusion reduced background to extremely low levels. The counter was bakeable, it could be tested for leakage, and it was possible to obtain spectra of any impurities present before the caesium was released from the ampoule. The steel casing provided the counter with good electrical shielding from radio frequency signals.

3-6 The Vacuum System

Due to the difficulty encountered in handling caesium, and to the ease/

ease with which it reacts with many materials, dedicated vacuum equipment was obtained for filling and pumping the Mark 3 caesium detector. See Figure 3.61. An oil filled diffusion pump [METROVAC] with liquid nitrogen cold trap was backed by a two stage rotary pump [EDWARDS]. The rotary pump was fitted with a foreline trap containing a molecular sieve absorber, which prevented pump oil from contaminating the upper part of the vacuum system. Also connected to the rotary pump was an automatic air admittance valve [EDWARDS MODEL PVA10EK] which allowed air to enter the pump when the mains supply failed or was switched off. All of the taps in the system, except for the one which opened and closed the diffusion pump, were speedivalves and all connections comprised viton 'o' rings between Klein flanges. Long connecting pipes were of flexible, corrugated stainless steel.

Three gauge heads were fitted close to the experimental chamber. An Edwards penning gauge (range 10^{-3} - 10^{-8} torr) and an Edwards pirani gauge (range 10^{3} - 10^{-3} torr) measured pressures below atomspheric, whilst a Leybold-Heraeus piezovac head (range 2000 - 0 mbar) was used for higher pressure and for filling the chamber. The piezovac gauge replaced a mechanical gauge with similar range which was discarded when it proved impossible to seal adequately.

Since it was of vital importance that caesium be exposed to as few reactive impurities as possible, the components of the vacuum system were rigorously baked and cleaned in ultrasonic baths prior to assembly. It was hoped that this cleaning programme would substantially/

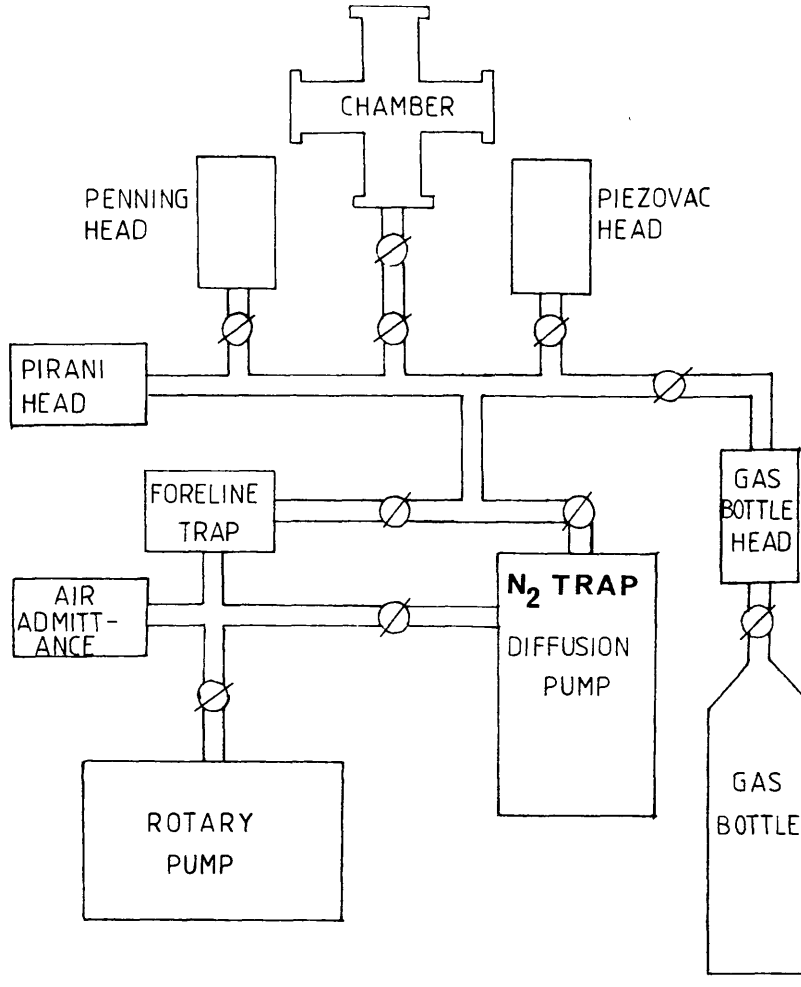

FIG. 3·61: VACUUM SYSTEM

substantially reduce impurities outgassing from the walls of the system. Once intact, the system was baked again (this time under vacuum) and tested for leaks with a He mass spectrometer. Only when the system was leak tight and clean was the caesium chamber connected to it.

3-7 Electronics and Data Acquisition System

Data collection was controlled by a LSI-11 computer. The Caty program DAQQ was used.

Laser induced ionisation signals, detected at the central wire of a proportional counter, were amplified, delayed by 2.0 μs, and passed to one input of a peak-sensitive analogue-to-digital converter [ORTEC AD 811]. The wire was maintained at a few hundred volts (positive) by a high voltage power supply. See Figure 3.71. Laser fluence was monitored by a Molectron joulemeter: the signal from this was also amplified, delayed (by 2.5 μs) and passed to a second input of the ADC. Both the chamber and the joulemeter output were usually monitored on the screen of a Tektronics 465B oscilloscope. The power supply, amplifiers and delay amplifiers were contained in a Ortec type 401A crate. The remainder of the system was powered from two Nuclear Enterprises crates, one of which also housed control units for the disc drive and for a Tektronics type 611 storage and display unit.

A photodiode positioned close to the excimer-dye laser system provided/

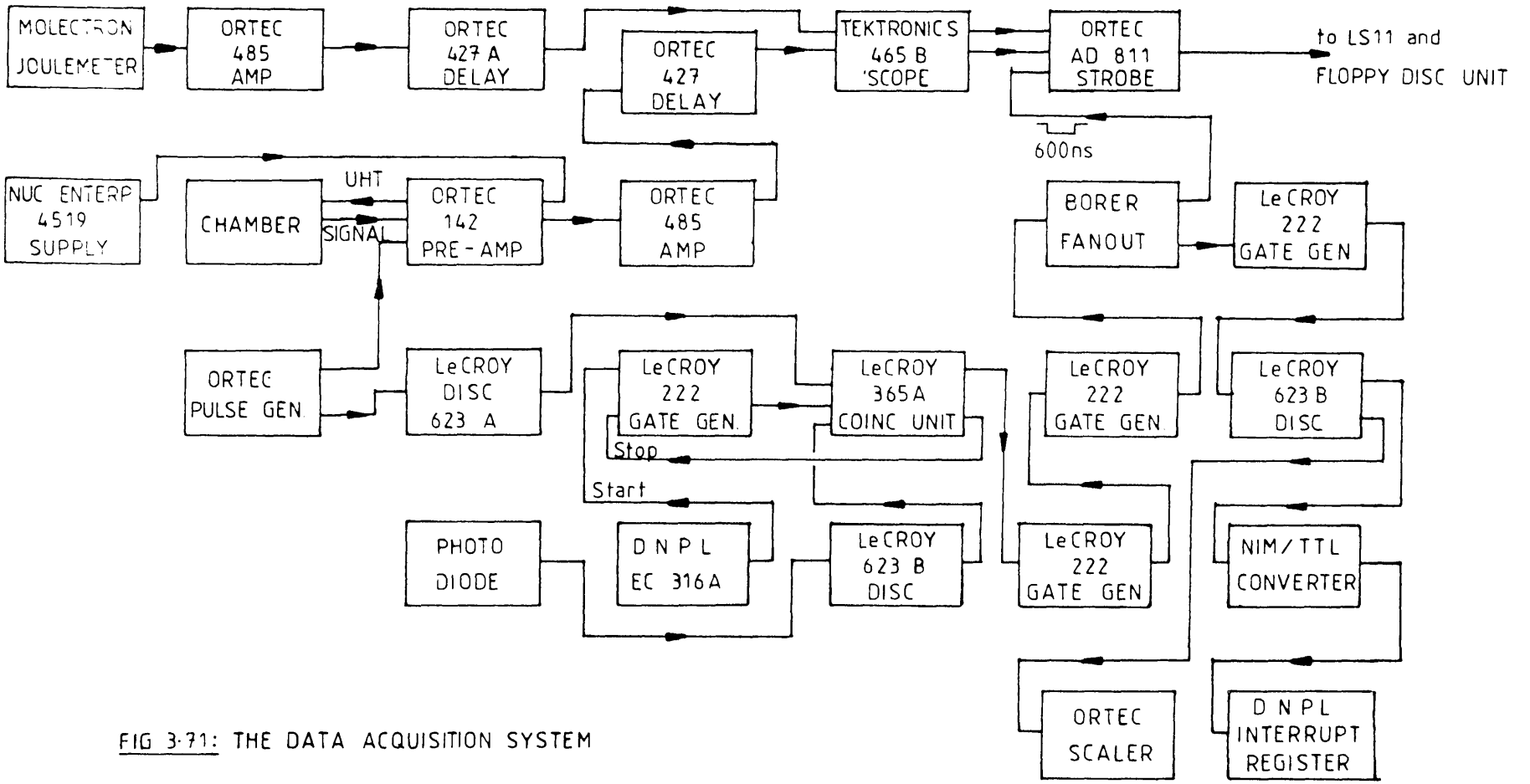

FIG 3·71: THE DATA ACQUISITION SYSTEM

provided the timing signal for the electronics. The pulse from the diode triggered an array of gate generators [LeCROY 222] and discriminators [LeCROY 623A and 623B] to strobe the ADC such that the 600 ns wide ADC gate was coincident with the maxima of the chamber and joulemeter signals. A 4-fold coincidence unit [LeCROY 365A] ensured that only when a signal was received from the photodiode, i.e. only when the laser was fired, would the ADC be triggered to pass incoming signals to the disc. Thus, only laser induced events were recorded. The timing of the various pulses is shown in Figure 3.72.

A pulse generator was included in the system as it could be used to check the linearity of the electronics without need of a laser or chamber.

Raw experimental data were stored on floppy disc and displayed, event by event, on the type 611 display unit. Plots of chamber signal versus time; joulemeter signal versus time; chamber versus joulemeter; joulemeter versus channel number; and chamber versus channel number were produced simultaneously. Of these, the first was often the most informative since, when scanning the dye laser wavelength through caesium resonances, it was possible to clearly view the transitions as they were encountered.

It was also found useful to manipulate incoming data on-line and display the results at the terminal. The data acquisition program encompassed this facility: data could be normalised linearly or quadratically/

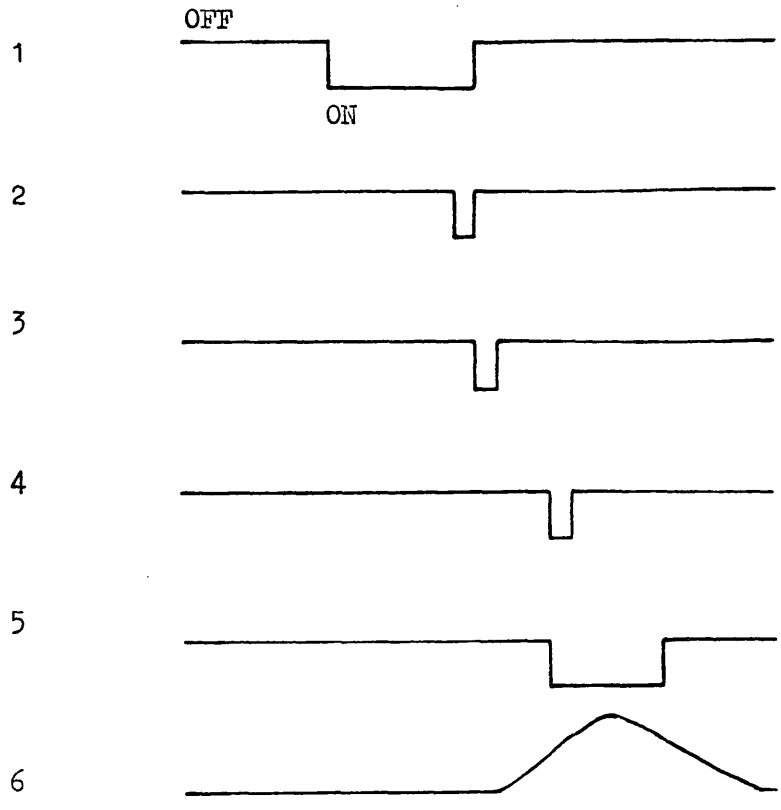

1. The LSI-11 Computer signifies readiness to accept data.
2. The photodiode pulse.
3. If one and two are coincident, the 4-fold coincidence unit emits a pulse.
4. The pulse is delayed to coincide with the incoming signals.
5. The pulse is widened from 10 ns to 600 ns, the width of the ADC gate.
6. Incoming signals from chamber or joulemeter.

FIG. 3.72: SIGNAL TIMING

quadratically to a set laser fluence and could be averaged over a number of events.

Spectra from the ^{55}Fe calibration source were recorded using a pulse height analyser with output to either an oscilloscope or an X-Y plotter. The analyser was connected to the output of the Ortec 485 amplifier.

CHAPTER 4 BACKGROUND LASER INDUCED IONISATION IN PROPORTIONAL COUNTERS

4-1 Introduction

A major problem, which may limit the use of resonance ionisation spectroscopy in conjunction with proportional counter systems, is the existence of so-called "background" ionisation. This is not the cosmic ray or natural radioactivity induced background encountered in conventional radiometry, but results from the ionisation of low ionisation potential, gaseous impurities present in the counter.

The impurities may arise from a number of sources. They may be present at trace levels in the commercially available filling gas and introduced from the gas bottle. Alternatively, they may be due to outgassing from some part of the proportional counter or from the vacuum system with which it was filled; or may represent the egression of pump oil from rotary or diffusion pumps into the filling system.

Due to the extreme sensitivity of the RIS technique (2), minute quantities of contaminant may lead to large amounts of background ionisation and may conceivably swamp small, resonant signals from species of interest. The exclusion of ionisable impurities and the reduction or elimination of background is thus of paramount importance to resonance ionisation spectroscopy in proportional counters. With this aim in view, attempts have been made/

made at Glasgow to identify the impurity species spectroscopically, to elucidate their possible sources and, where possible, to remove them.

4-2 Wavelength Dependence of Laser Induced Ionisation in Proportional Counters

The first investigation of the variation in background ionisation with laser wavelength used nitrogen, excimer and Nd:glass lasers and a proportional counter of the design shown in Figure 4.21 (109). The body of the counter is of aluminium with perspex end plates incorporating quartz windows for entry and exit of the laser beam. A thin wire is mounted along the central axis , and is sheathed at both ends by field correcting tubes which define the sensitive length of the counter to be 2 cm. The normal operating pressure was one atmosphere commercial grade 90% Ar : 10% CH_4. Calibration of laser induced signals was carried out using external radioactive sources placed over a thin aluminium foil window (^{55}Fe (5.9 keV) and Tb (44.2 keV)).

The characteristics of the lasers used are presented in Table 12.

The ionisation obtained at the various laser wavelengths is presented in Table 13.

The overall trend observed is for increased ionisation at shorter wavelengths. In the data of Table 13, an $\sim 10^3$ increase in/

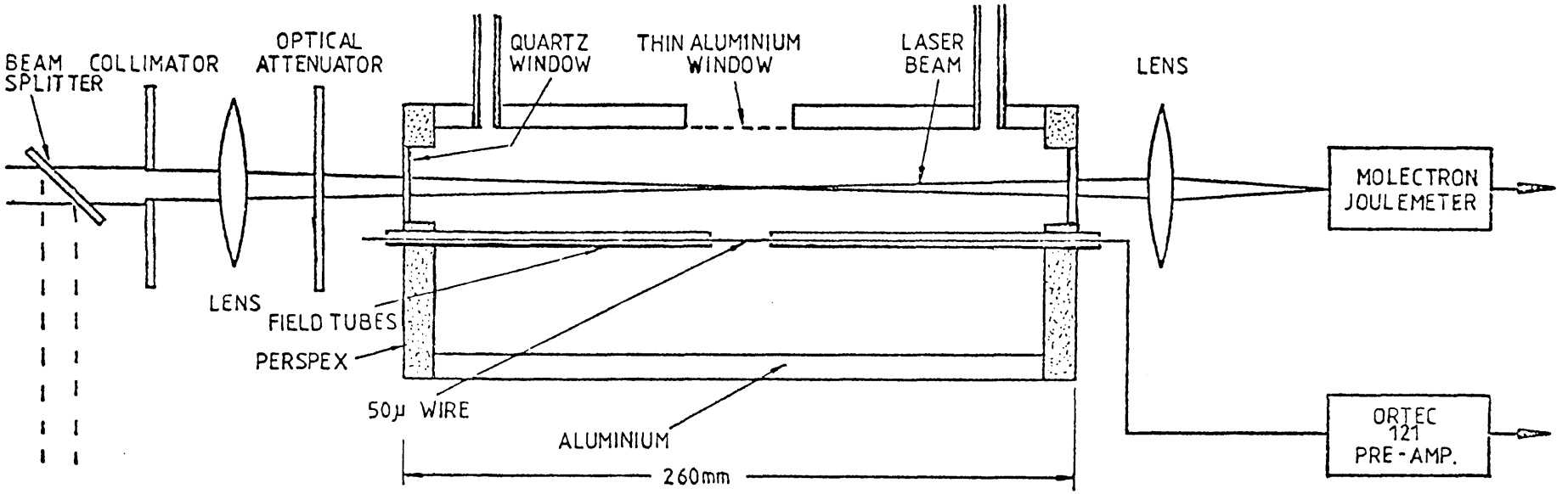

FIG. 4.21: PROPORTIONAL COUNTER TYPE 1

TABLE 12

Laser data

Type of Laser	Wavelength (nm)	Pulselength (ns)
Nitrogen [PRA IN 100]	337	0.3
Excimer [Lambda Physik EMG201]		
XeF filling	351	14
KrF filling	249	16
Nd:glass [JK Systems 2000]		25
fundamental	1060	
doubled	530	
tripled	354	
quadrupled	265	

TABLE 13

Variation of Ionisation with Wavelength

Wavelength (nm)	Fluence (/mm^2)	Ionisation (ion pairs/cm)	Photon Energy (eV)
249	50 μJ	8.5×10^5	4.98
265	50 μJ	1.2×10^5	4.68
337	140 μJ	5×10^3	3.68
351	20 mJ	6.5×10^5	3.53
354	20 mJ	3×10^4	3.5
530	150 mJ	1.5×10^4	2.34
1060	7.5 J	1.1×10^3	1.17

in ionisation between 1060 and 249 nm is apparent. However, the longer wavelength data was recorded at considerably higher incident fluence than the shorter wavelength data and the actual difference in no. of ion pairs created by a laser (of constant fluence) at wavelengths of 1060 and 249 nm would be considerably greater than 10^3 . Power dependence curves obtained showed a quadratic dependence of ionisation on laser fluence (at low power) at all wavelengths used below 530 nm. This is indicative of a two-photon ionisation process and suggests that principal components of the background in the wavelength range covered have ionisation potentials between $\sim$ 4 and 10 eV. Fivefold and $\sim$ tenfold power dependences at 530 and 1060 nm respectively indicate/

indicate the presence of another background component of ionisation potential around 11.7 eV.

At a single wavelength (337 nm) the size of the ionisation signal measured was independent of total Ar/CH_4 pressure in the range 0.3 - 2 atmospheres. This result suggested that it was unlikely that the background ionisation was due to contaminants coming from the gas bottle.

The acquisition of a dye laser allowed the background to be scanned continuously in wavelength rather than studied at only a few points corresponding to the output of available, fixed frequency, lasers. The use of a single, tunable beam also reduces any variations in ionisation due, not to wavelength dependence, but to the different beam profiles and mode structures of the different types of laser.

A new counter was constructed for use with the dye laser and is shown in Figure 4.22 . The cathode (body) is of 10 cm diameter steel pipe and was carefully internally polished (using sandpaper and alumina polish) and cleaned (using methanol) before use. The end plates, of aluminium, were also cleaned with methanol. It was hoped that background ionisation could be reduced by ensuring the materials from which the counter was built were clean. Indium 'o' rings sealed the body to the end plates. These were chosen in preference to rubber 'o' rings to minimise outgassing of potentially ionisable contaminants. The laser beam/

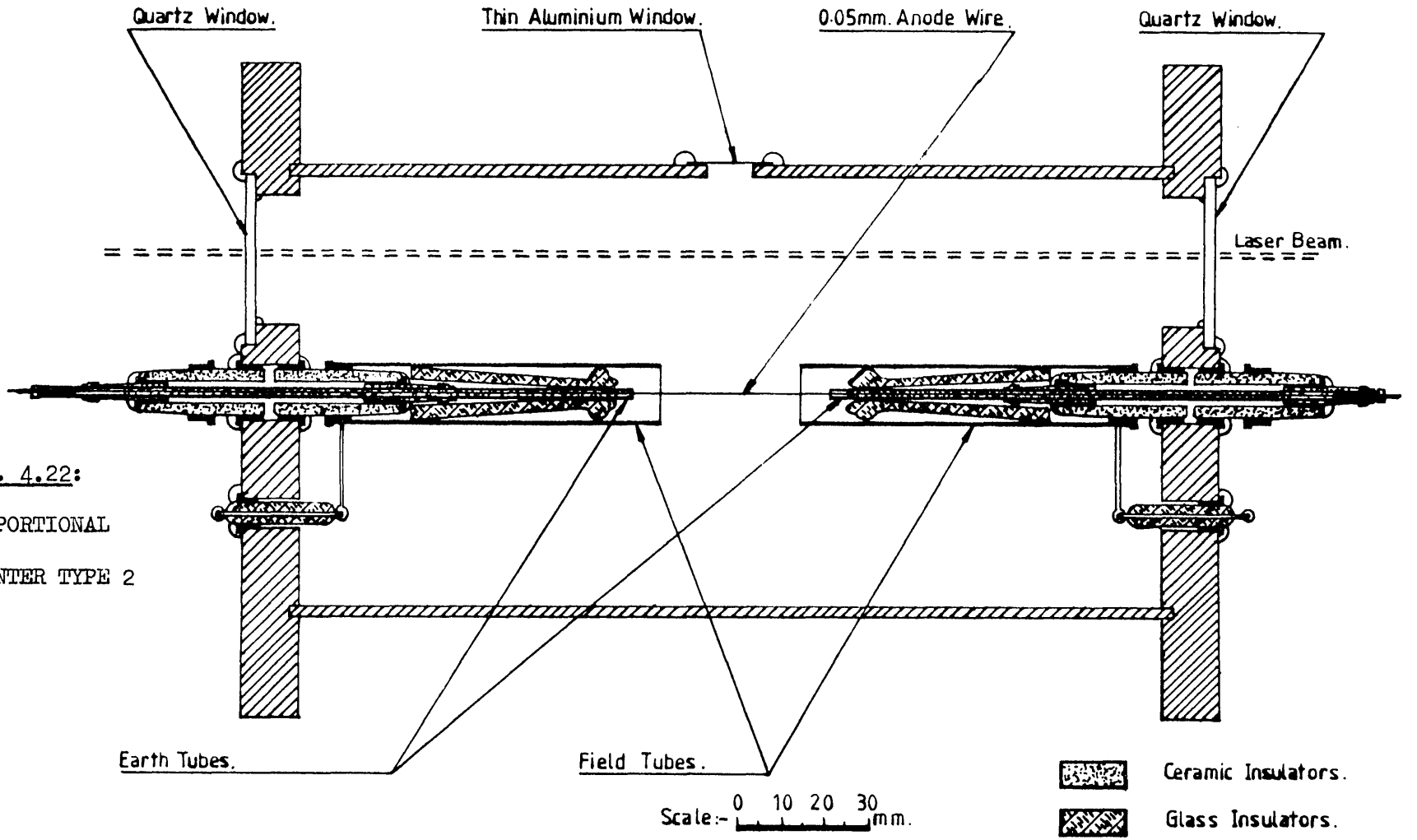

FIG. 4.22:

PROPORTIONAL

COUNTER TYPE 2

beam entrance and exit windows, electrical feedthroughs and aluminium x-ray window were all mounted using "Torr Seal" sealant. The electrical arrangement around the ends of the central wire was quite complex. The wire (0.002 inch nickel) was surrounded by earth tubes of stainless steel (with ceramic insulators between) and the earth tubes surrounded by field tubes of nickel alloy (with glass insulators intervening) The sensitive length of the counter was 3.2 cm. Laser induced electrons drifted towards the wire under the influence of a negative voltage applied to the outer casing. Signals were calibrated to an external ^{55}Fe x-ray source.

The variation in background ionisation, with 1 atmosphere P-10 filling gas, as the frequency doubled laser was tuned from 260 - 335 nm is shown in Figure 4.23 (107). The laser was stepped in ~ 1 nm increments and 500 events were collected at each wavelength setting. The fluence was 8.1 $\mu J/mm^2$, although in this and subsequent figures data is presented which have been normalised to 1 $\mu J/mm^2$ for ease of comparison with the work of other authors. Three dyes were required to cover the spectral region shown. Where a dye change was necessary, data at the same wavelength setting was, if possible, obtained with both dyes to facilitate normalisation. An increase in ionisation of four orders of magnitude is visible between 335 and 310 nm. This spectrum suggests that seeding agents previously introduced to the counter (see Appendix I) were still present. The counter was dismantled and baked in an oven for a few hours. The spectrum

was/

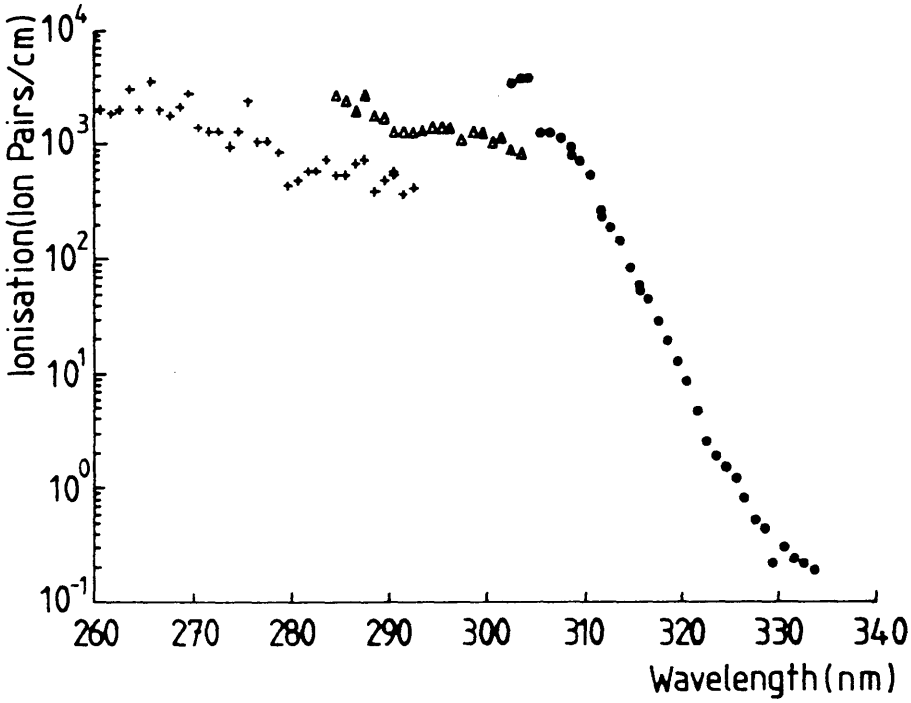

FIG. 4.23: BACKGROUND IONISATION IN A TYPE 2 COUNTER

was redetermined as above and is shown in Figure 4.24 (107,110,111). Much of the ionisation in the 290 - 310 nm region was removed by the bake-out.

At various, arbitrarily selected wavelength settings within the range of Figure 4.24, a plot of laser induced ionisation versus laser fluence showed a quadratic dependence, i.e. two-photon ionisation was responsible for the background. It can be seen from the Figure that the background ionisation still increases by around four orders of magnitude in the baked counter, but over a much longer wavelength range (325 - 278 nm). The increase is not smooth but shows two relatively flat regions around 290 - 300 nm and between 270 and 278 nm. In these two regions the ionisation is 5 ion pairs cm^{-1} and 2 x 10^3 ion pairs cm^{-1} respectively. Of particular interest is the structure apparent in the 270 - 278 nm region. This was found to be very reproducible and was investigated further as is described below.

Yet another design of counter was conceived and constructed. It is shown in Figure 4.25. To distinguish counters of this type, they were somewhat arbitrarily named after rivers. The principal advantages of this design over the previous two were a) it could be rapidly dismantled for cleaning and easily reassembled, and b) it could be operated with the outer, T-piece earthed, eliminating the hazards associated with having a high voltage on the (easily accessible) outer casing of the counter.

In/

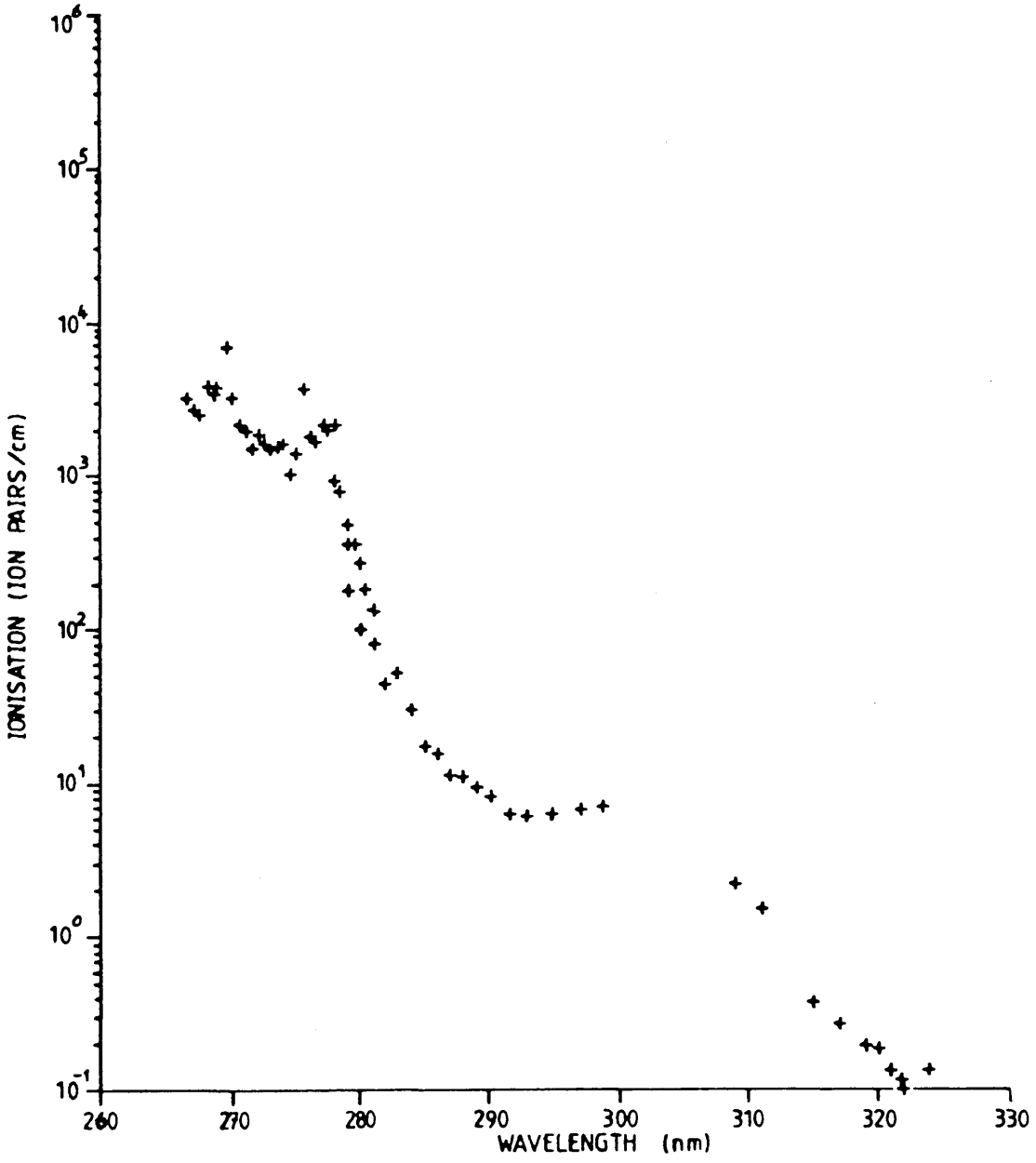

FIG. 4.24: BACKGROUND IONISATION IN A CLEAN TYPE 2 COUNTER

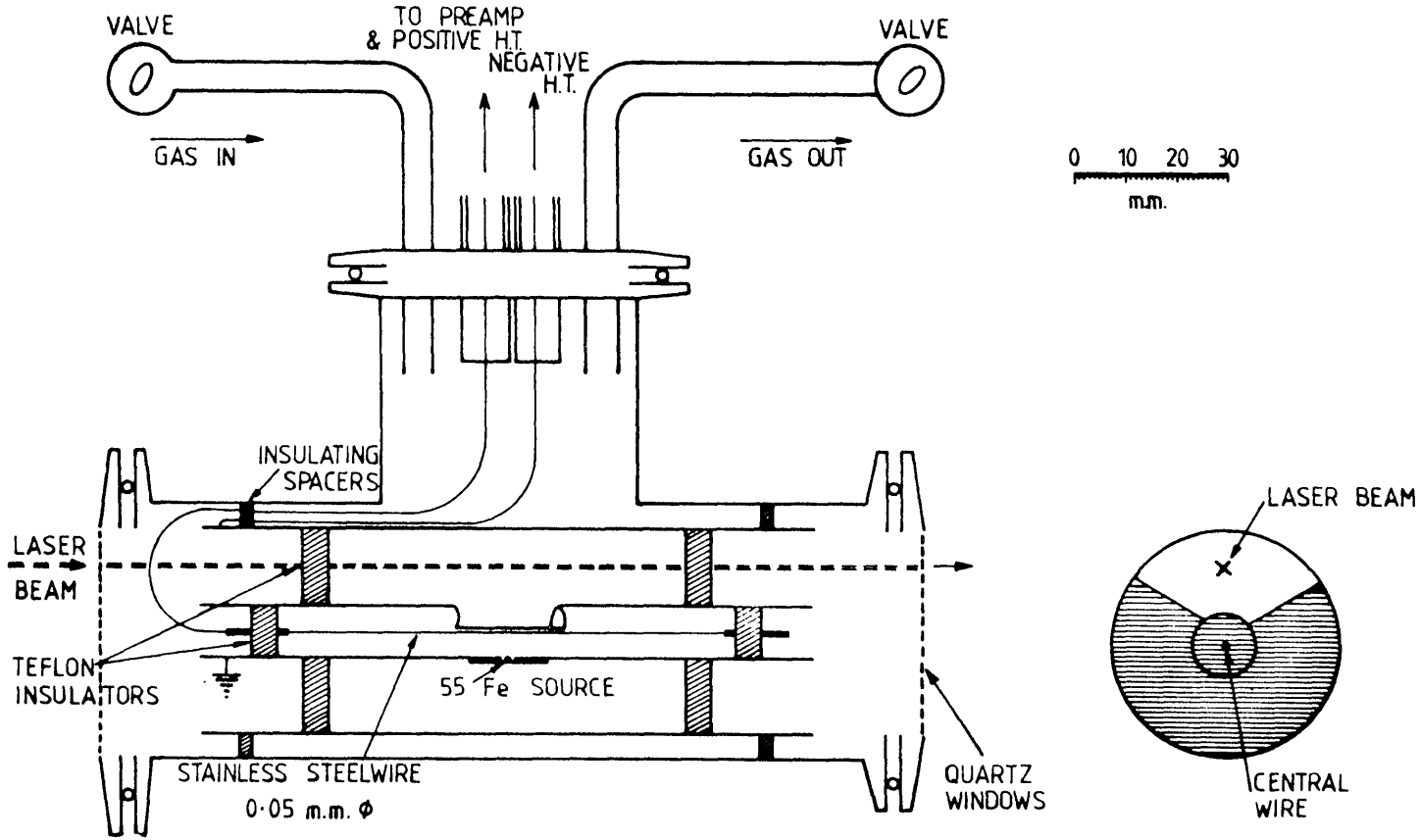

FIG. 4.25: PROPORTIONAL COUNTER TYPE 3

In the new, type 3 chamber, the proportional counter was mounted inside a standard vacuum fitting - a DURAL T-piece. "Torr Seal" sealant was used to mount quartz windows in standard flanges which were attached to the T-piece with viton 'o' rings and quick-release clamps. On the third limb of the 'T', a flange drilled to accommodate both gas inlet and outlet and electrical feedthroughs, was similarly attached. The proportional counter was constructed from concentric stainless steel tubes, with a central anode wire. The outer tube, which served as the cathode, was of length 12 cm and diameter 4 cm. It was insulated both from the T-shaped casing and from the inner tube by teflon spacers. The inner tube, maintained at earth potential and insulated from the central wire also by teflon, was of diameter 1 cm and length 12 cm. A 2 cm x 1 cm hole cut into this tube defined the sensitive length of the counter. The earthed tube also prevented stray photo-electrons from the quartz windows from reaching the wire and served as a convenient mount for a small ^{55}Fe source. In use, the counter was normally filled to one atmosphere with P-10 gas and closed off (static mode operation). It was also possible, however, to flow the gas through the counter (flowing mode operation). More detail of these two modes of operation is given in Appendix I.

A background wavelength scan, normalised to 1 $\mu J/mm^2$ laser fluence, for a counter of this design - the "Avon" - is shown in Figure 4.26 (107). This was obtained in flowing operation (flow rate 25 ml/min) after the counter had been carefully cleaned out using organic/

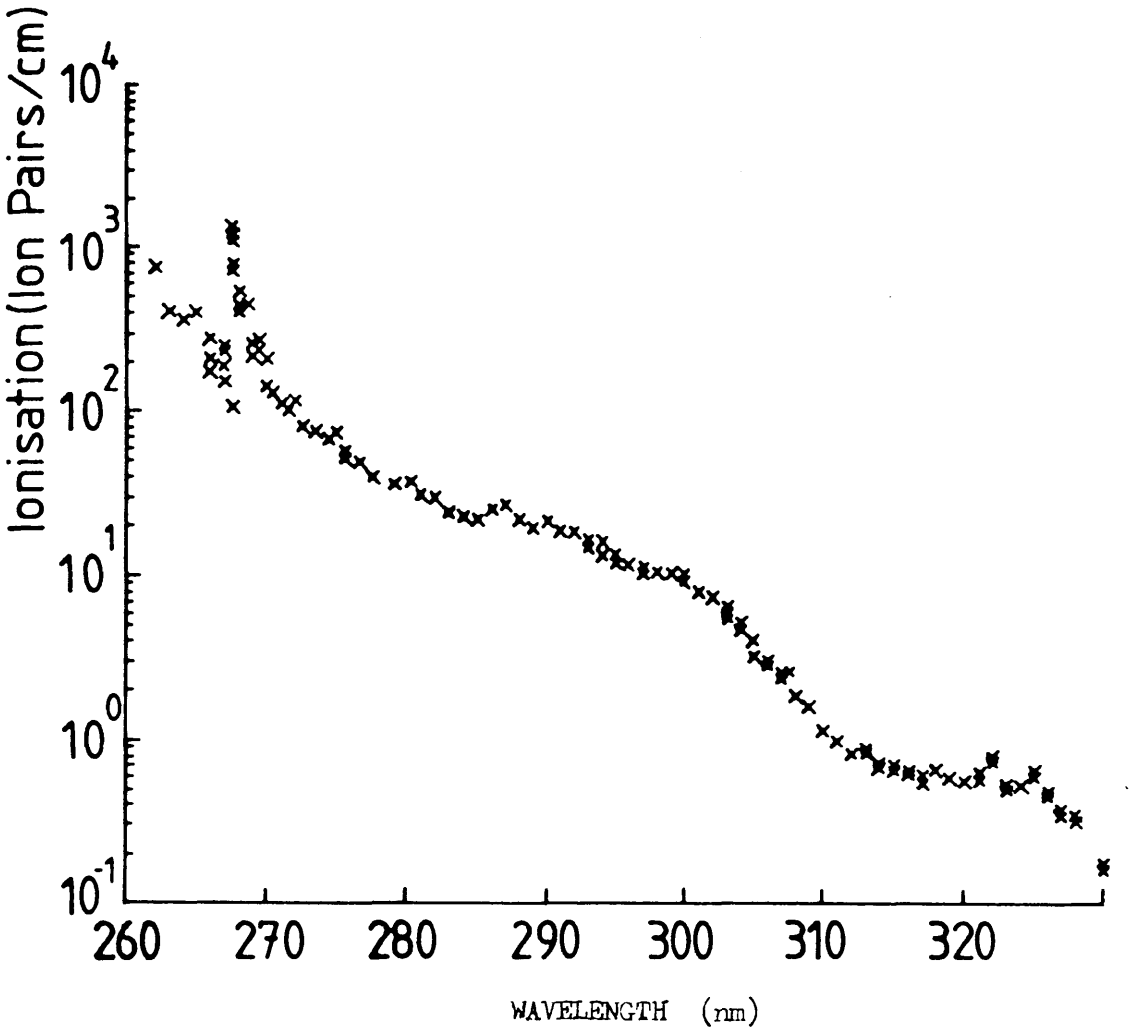

FIG. 4.26: BACKGROUND IONISATION IN A TYPE 3 COUNTER

organic solvents (methanol and ethanol), and baked to $\sim$ 70°C for several hours. It can be seen that the background ionisation at wavelengths shorter than $\sim$ 280 nm is reduced by almost one order of magnitude compared with the type 2 counter spectrum (Figure 4.24). The structure observed between 270 and 278 nm in Figure 4.24 is absent in the type 3 counter spectrum, although a peak at 268 nm is apparent (which did not appear in Figure 4.24). From these two spectra it appears that the impurity giving rise to the structure seen in Figure 4.24 was absent from, or present at a much lower concentration in, the type 3 counter. The impurity giving the structure seen in Figure 4.26 may be present in both the type 2 and the type 3 counters, but its structure would be swamped by transitions arising from the other impurity in the type 2 counter spectrum if it were present in the same concentration in both counters.

Other authors have also observed ionisation to rise as wavelength is decreased in this region of the spectrum (112). Hubricht and co-workers (112), however, observed a smaller rise of around 60 times (between 357 and 266 nm) as compared to the $\sim 10^4$ reported here. The variance may be attributed to dissimilar background impurities in the Glasgow and Dortmund chambers due to the different methods of construction and utilisation.

Various attempts were made to isolate the background-producing impurities and to concentrate them sufficiently for them to be detectable by some conventional analytical technique, e.g. mass spectrometry, gas liquid chromatography, or nuclear magnetic resonance/

resonance spectroscopy. This work concentrated on cold trapping impurities flowing through a typical experimental line, i.e. gas bottle, counter and connecting pipes. Different temperatures of trap were used but little success was achieved in any experiment of this type even when the counter gas was flowed through the traps continuously for several days.

4-3 The Identification of Phenol as an Impurity

The structure in Figure 4.24 was studied in greater detail. A wavelength scan in the 278 - 266 nm region, again using the type 2 counter and normalising to 1 $\mu J/mm^2$ fluence, was obtained, with the laser wavelength stepped in 0.025 nm increments. This is shown in Figure 4.31. A number of sharp resonances were apparent, the most intense being at 268.2 nm, 269.4 nm and 275.0 nm. A power dependence plot of ionisation versus fluence was obtained at 275.0 nm and is shown in Figure 4.32. The gradient of the line is $\sim$ 2 (the axes are somewhat distorted in the figure) and indicates that a two photon process is responsible for the signal observed. Quadratic power dependence was apparent in all ionisation versus fluence plots obtained in this spectral region. Thus, the impurity giving rise to the signal must have an ionisation potential smaller than the energy of two incident photons in this spectral range, i.e. $<$ 9.32 eV (where 4.66 eV is the energy of a single photon of wavelength 266 nm).

The spectrum of the impurity is fairly complex, which suggests that a molecule rather than an atomic species or simple inorganic compound is/

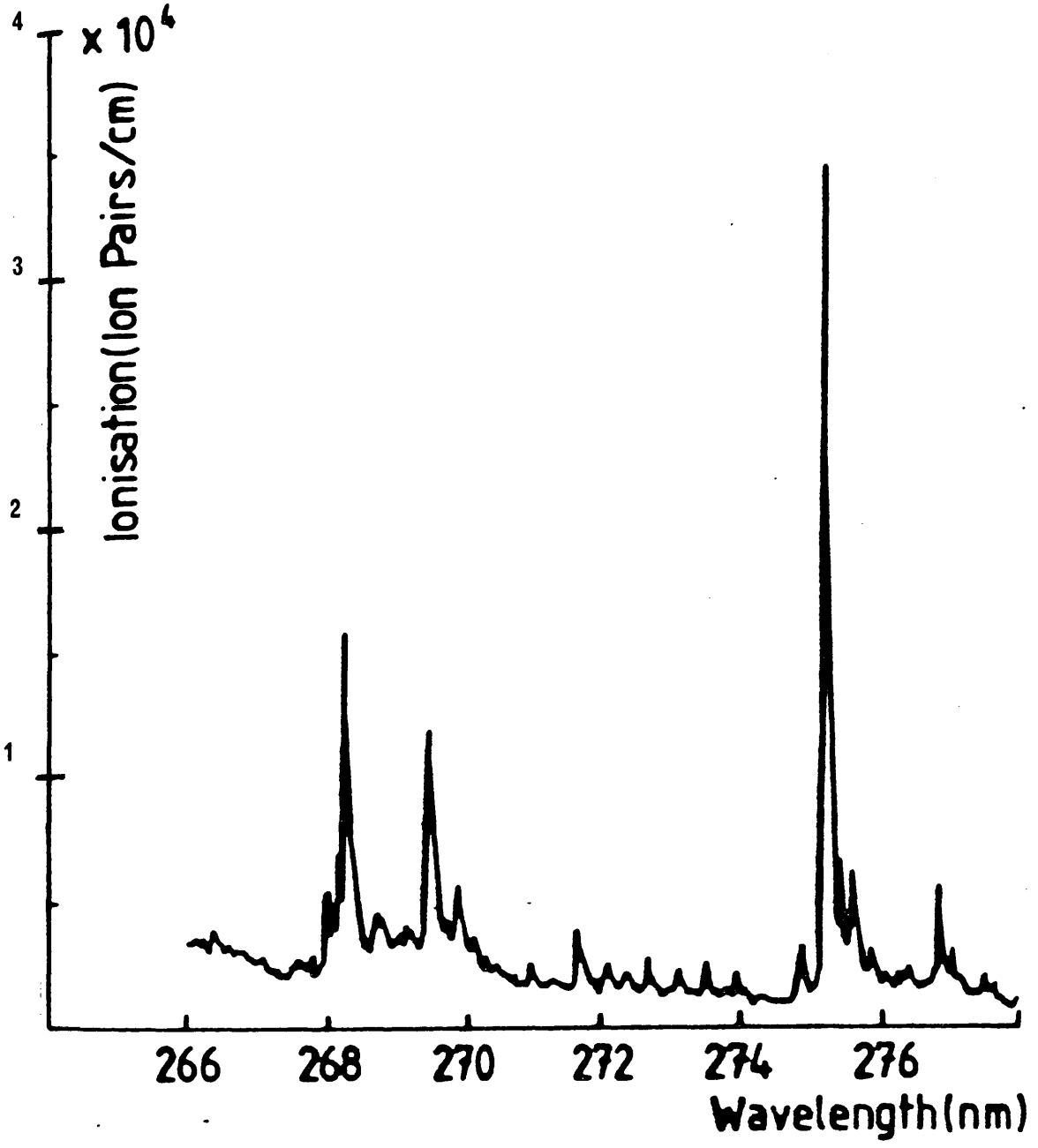

FIG. 4.31: DETAIL OF THE BACKGROUND IN A TYPE 2 COUNTER

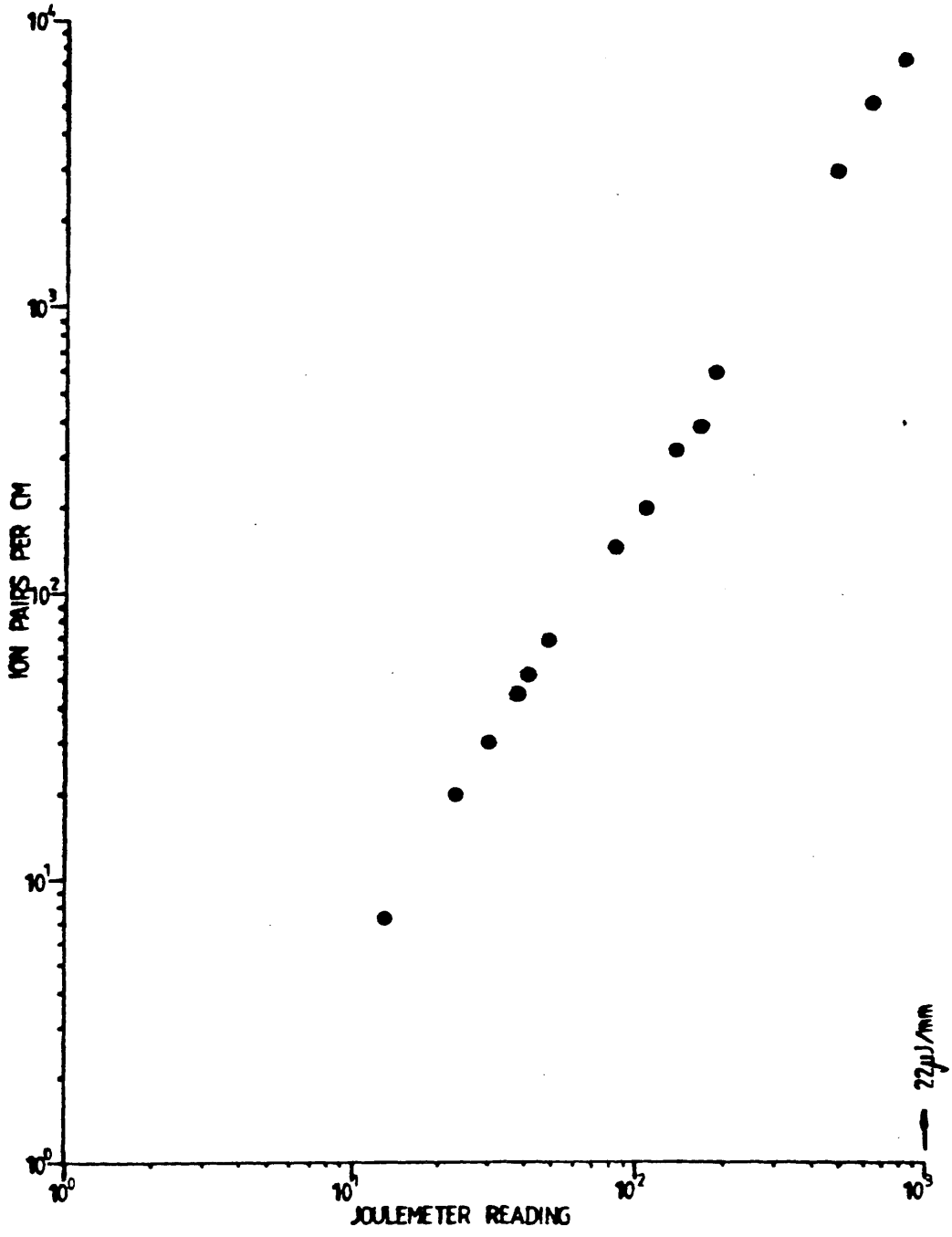

FIG. 4.32: POWER DEPENDENCE CURVE AT 275.0 nm

is responsible for the structure. Ideally, the impurity could be identified by comparison of its spectrum with two-photon ionisation spectra published in the literature. However, few of these have yet been reported and neither atlases nor databases of two-photon spectra (analogous with those available in other branches of spectroscopy) yet exist; although this will, hopefully, change in the future.

In attempting to discover the identity of the impurity the literature of single photon absorption spectroscopy, however, proved invaluable. It is expected that the vapour-phase two-photon ionisation spectrum of a molecule will closely resemble its vapour-phase electronic absorption spectrum, since the excitation steps of two-photon resonant ionisation processes involve precisely the transitions which give rise to single-photon absorption spectra. The second (ionising) step in the two-photon process has been shown to have little wavelength dependence (113).

The electronic absorption spectra of molecules are well documented, (particularly the spectra of organic molecules) and various atlases and reviews of such spectra were consulted in order to identify the impurity present in the type 2 counter, <u>e.g.</u> (114). Many compounds were found to have structure in the 266 - 278 nm range. In particular, organic molecules possessing a chromophore containing an atom with a lone pair (<u>e.g.</u> ), and conjugated organic molecules absorb in this region. It was noted, however, that benzene and some of its derivatives had spectral structure in methanol which was particularly similar to that shown in Figure 4.31. Also, they have ionisation potentials/

potentials of, typically, around 9 eV.

To supplement the literature spectra and provide vapour phase data, a number of simple benzene derivatives and other compounds were obtained, e.g. benzene, xylene, p-chlorotoluene, phenol, 2-acetylfuran, DMA and TMA, and their electronic absorption spectra recorded using a spectrophotometer [Beckman UV 5270]. These spectra were obtained by putting samples (usually liquid) of the chemicals into clean quartz cells and taking the spectra of the vapour above the liquid surface. The resolution of the Beckman spectrophotometer was 0.05 nm in this region of the spectrum, similar to the 0.05 nm linewidth of the dye laser. The best match of single-photon spectra to the background two-photon structure of the type 2 counter was obtained with hydroxybenzene (phenol). The electronic absorption spectra obtained for phenol is shown in Figure 4.33. It is very similar to the background observed, having most intense peaks at 268.1 nm, 269.4 nm and 275.0 nm. (N.B. The peak at 265.7 nm in the UV absorption spectrum is outside the range of the background scan.)

A type 3 counter - the "Avon" - whose background two-photon ionisation scan lacked the resonance structure associated with phenol (see Figure 4.26) was taken and deliberately seeded with (i.e. contaminated with) phenol so that its (phenol's) two-photon spectrum could be obtained. Phenol is a solid at room temperature (melting point = 43°C (115)) and could readily be introduced to a counter operating in flowing mode by passing the P-10 gas through a few crystals of the compound before it entered the chamber. The phenol evaporated into the gas stream and was carried into the counter with it.

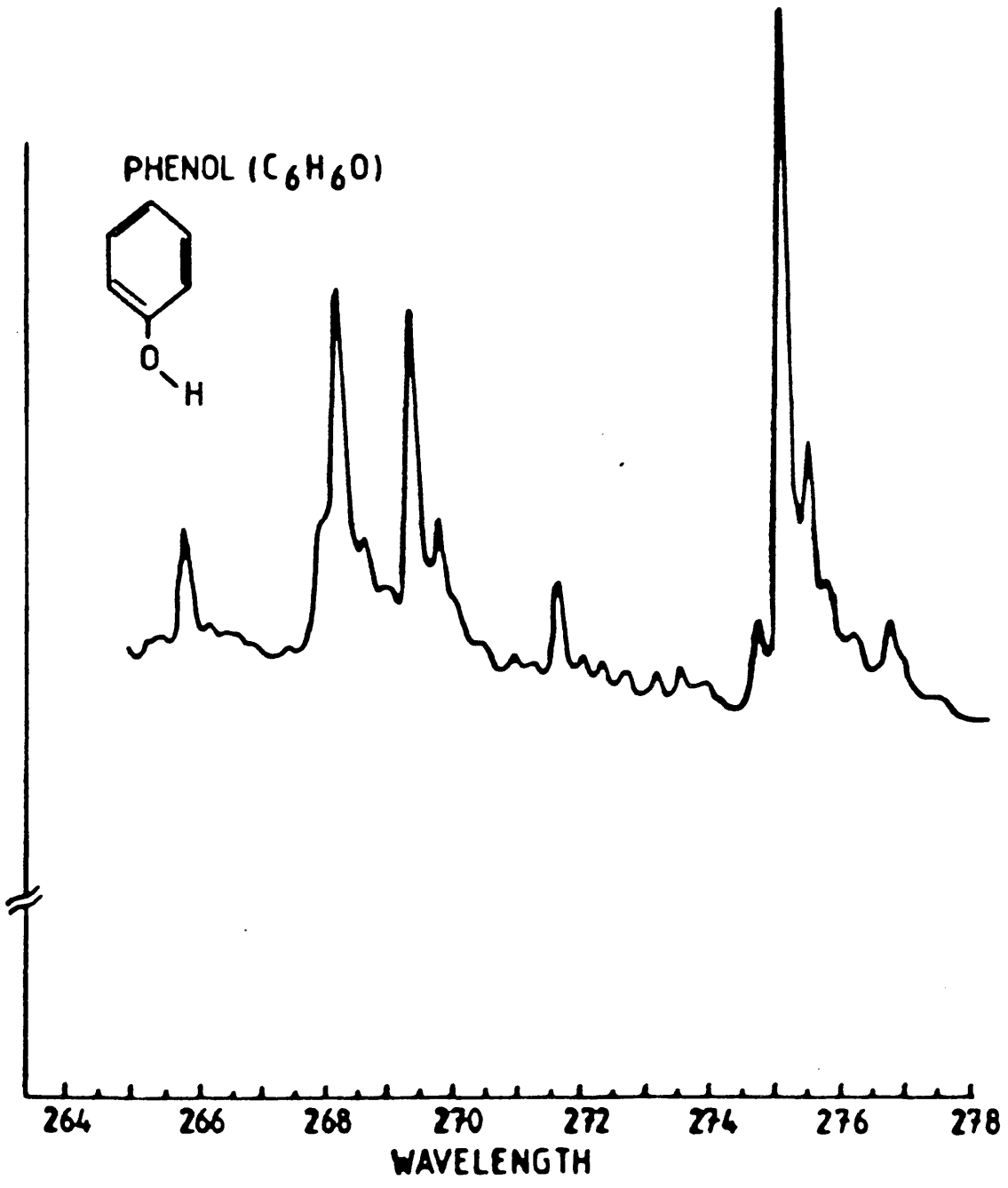

FIG. 4.33: ELECTRONIC ABSORPTION SPECTRUM OF PHENOL

Figure 4.34 shows the ionisation in the counter seeded with phenol at $-10^{o}C$ in the 265 - 310 nm region, normalised to a fluence of 1 $\mu J/mm^2$. To aid comparison, the background in the same counter before seeding is also shown. The phenol ionisation rises smoothly above the background at wavelengths shorter than around 300 nm. There is evidence of structure on the spectrum but it has not been resolved well with the laser incremented in 0.5 nm steps. A finer laser scan (increment 0.025 nm) of the phenol-doped counter ionisation in the range 266 - 278 nm was obtained and is shown in Figure 4.35. This too has been normalised to 1$\mu J/mm^2$ laser fluence. Excellent correlation is apparent between the peaks of the background fine structure (Figure 4.31) and the peaks resulting from seeding with phenol. The single photon absorption spectra, Figure 4.33, are also extremely similar, justifying the assumption of only a very weak wavelength dependence in the ionisation step of the two-photon resonant ionisation process.

Thus, phenol has been identified as a component of the background ionisable impurities present in the type 2 counter. The ionisation potential 8.5 eV (116) is of acceptable energy for a two-photon ionisation scheme, with wavelength 260 - 330 nm photons, to be feasible.

Calculation of the amount of phenol introduced to the counter in any experiment was not straightforward. In flowing mode the actual pressure in the counter was not reliably known partly because of the possibility of depression of vapour pressure by flowing gas over the liquid surface and partly because phenol tended to remain in the counter/

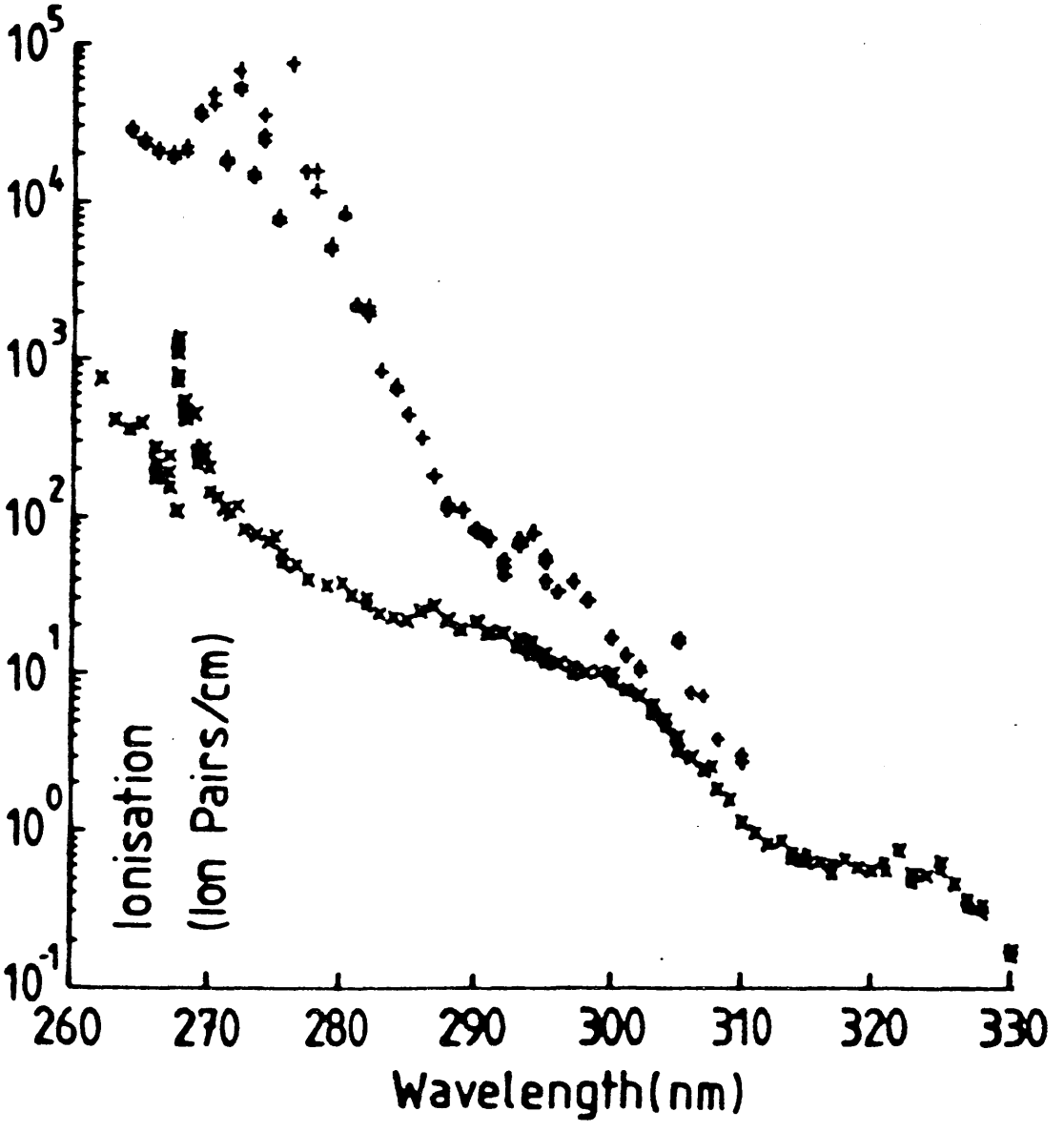

FIG. 4.34: IONISATION IN A TYPE 3 COUNTER SEEDED WITH PHENOL

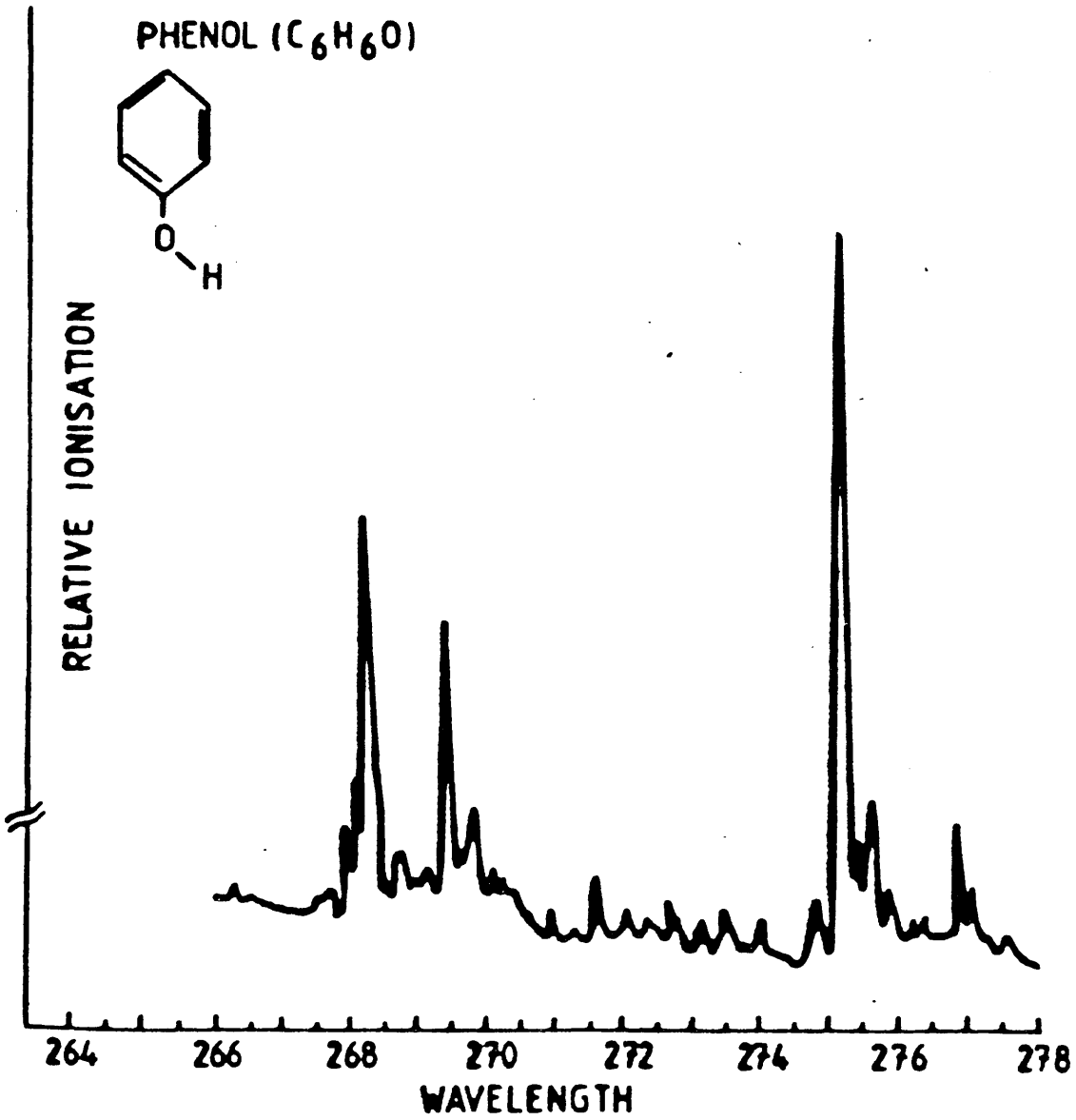

FIG. 4.35: DETAIL OF IONISATION IN A TYPE 3 COUNTER SEEDED WITH PHENOL

counter once introduced. Static tests, in which phenol at a measured pressure (the saturated room temp. vapour pressure) was introduced to a clean counter led, on extrapolation, to a detection limit of less than 0.01 ppm for phenol in type 3 proportional counters. The "background" concentration of phenol was estimated, by similar means, to be of the order of ppm.

The source of the phenol impurity was, eventually, found to be reinforced plastic tubing which had been used to fill (or flow gas through) the type 2 counter. Type 3 counters were filled using flexible, stainless steel tubing, and this avoided contamination with phenol. Following the discovery of the source of the phenol contamination, the use of plastic tubing in gas flow systems was discontinued and stainless steel used instead. In a clean, type 3 counter (the "Tweed") it was shown that the intensity of the phenol resonances, i.e. the phenol concentration, was directly proportional to the length of plastic pipe through which the counter was filled. Two metres of plastic pipe gave rise to $\sim$ 0.4 ppm of phenol in the counter. Once contaminated with phenol a counter had to be dismantled i.e. phenol could not be readily flushed, pumped or baked out of a counter.

4-4 The Identification of Toluene as an Impurity

Although phenol was not present in clean type 3 counters, the peak at 268 nm in the type 3 counter background ionisation spectrum/

spectrum indicated the presence of another impurity. This too was identified by comparison of literature UV absorption spectra and vapour-phase absorption spectra (obtained using the Beckman spectrophotometer) with the observed background structure.

A fine scan of the background ionisation in a clean type 3 counter - the "Forth" - shown in Figure 4.41 for the wavelength region 262 - 268.5 nm. The spectrum is normalised to 1 $\mu J/mm^2$ laser fluence. The laser wavelength was stepped by 0.1 nm increments. A quadratic power dependence was apparent at selected wavelengths within the region, again indicating that the impurity producing ions has ionisation potential less than around 9.4 eV.

The UV absorption spectrum of the benzene derivative toluene is shown in Figure 4.42. It resembles closely the structure of the background in general shape. Both spectra have intense peaks at around 263.5 nm, 264 nm, 267.1 nm and 267.6 nm, with similar relative intensities (117,118). The ionisation potential of toluene is 8.82 eV (116).

As was done in the case of phenol, toluene was seeded into a clean type 3 counter - the "Clyde" - so that its two-photon resonance ionisation spectrum would be obtained for comparison with the background two-photon structure. Flowing mode operation was chosen and P-10 counter gas, passing at 50 ml/min over a sample of toluene held at $-80^{\circ}C$ in a dry ice/alcohol bath, carried the toluene vapour into the counter. At this temperature the saturated vapour pressure of toluene/

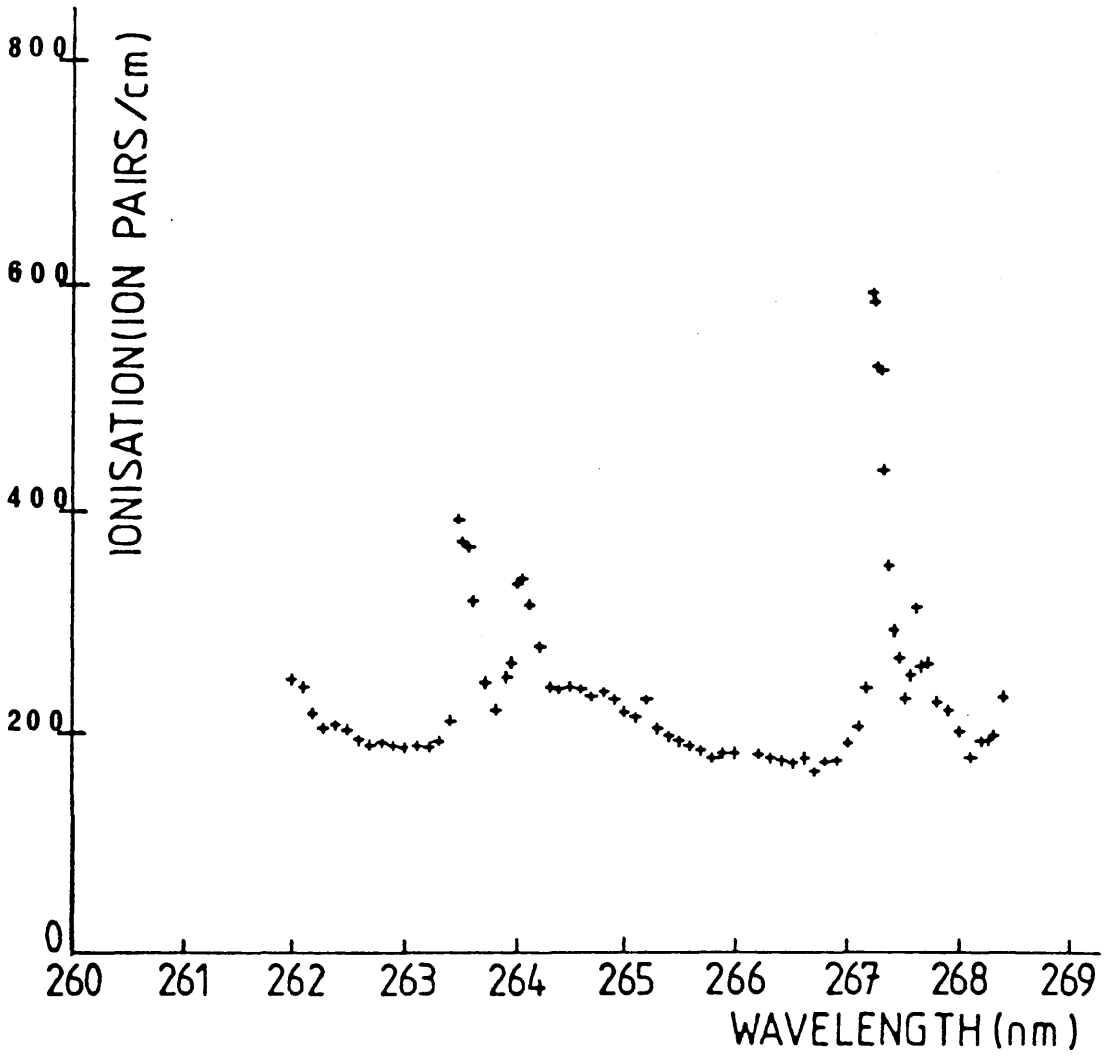

FIG. 4.41: DETAIL OF THE BACKGROUND IN A TYPE 3 COUNTER

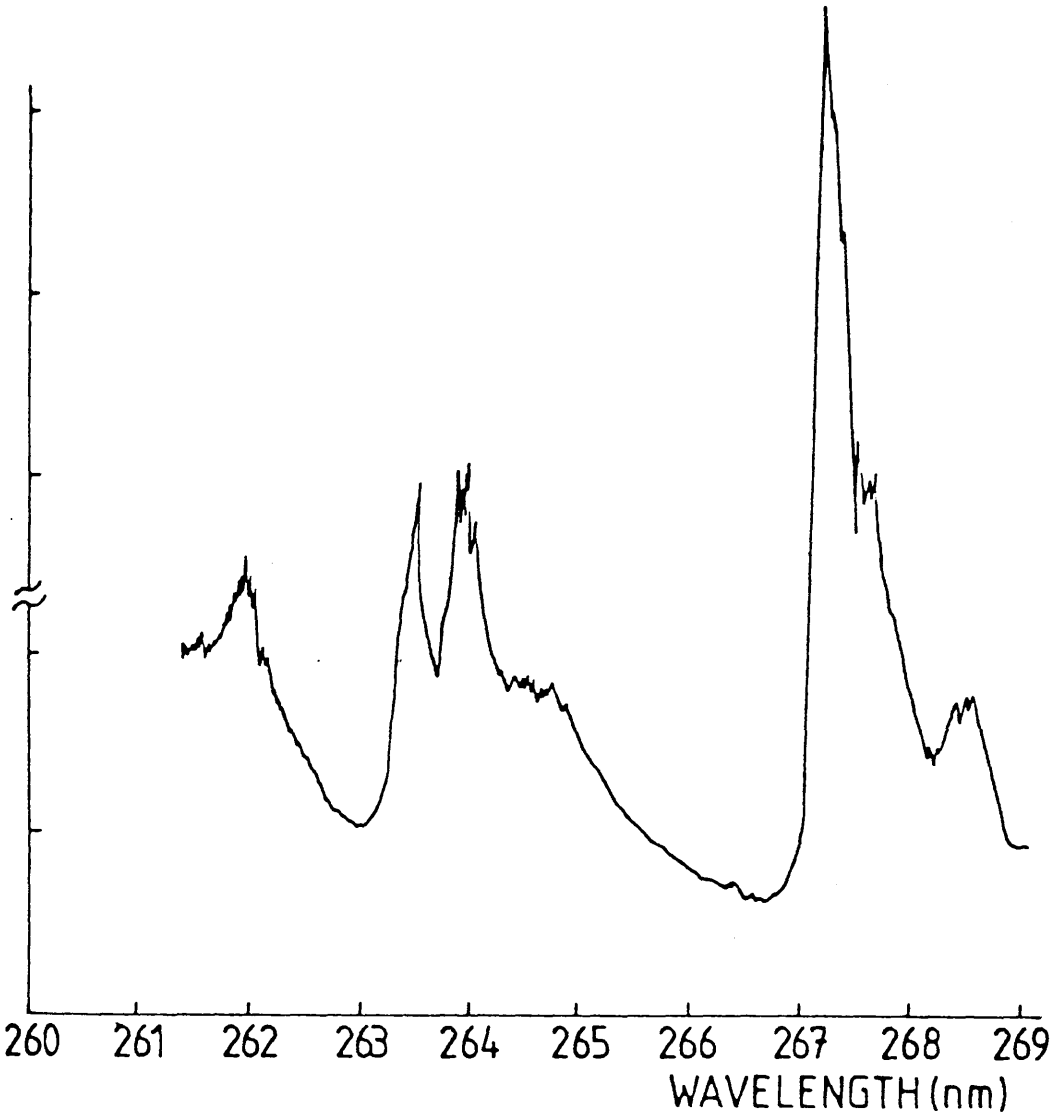

FIG. 4.42: ELECTRONIC ABSORPTION SPECTRUM OF TOLUENE

toluene is 5×10^{-3} torr (119), which corresponds to a concentration in the counter gas of, at most, 6.5 ppm. This figure was calculated assuming that the saturated toluene vapour pressure is maintained when the seed is introduced in flowing mode. In separate experiments using other organic compounds it was found that flowing mode operation depressed the seed vapour pressure considerably (see Appendix I). The two-photon resonance ionisation spectrum obtained (normalised to 1 $\mu J/mm^2$) is shown in Figure 4.43. The background structure (Figure 4.41), which has been attributed to toluene, may be overlain for ease of comparison. Excellent correlation between the two spectra is apparent, confirming that toluene is responsible for the background ionisation in the clean type 3 counter. It can also be calculated, from the relative intensities of the transitions in Figures 4.41 and 4.43, that the background concentration of toluene in the clean counter was, at most, 49 ppb.

To investigate the possibility of reducing the toluene concentration and hence the background ionisation in clean counters, further, one counter (the one later used for caesium work) was subjected to very rigorous cleaning both by baking and by periods of immersion in an ultrasonic bath. Once assembled, a process which was carried out wearing clean "Triflex" gloves, the counter was baked under vacuum for several hours. Following this procedure, the background ionisation spectrum was recorded. It is shown in Figure 4.44, which also shows the background in a type 3 counter which had not undergone the extensive cleaning process. In the "ultraclean" counter spectrum ionisation is consistently lower than before cleaning although a small/

TO FOLLOW PAGE 100

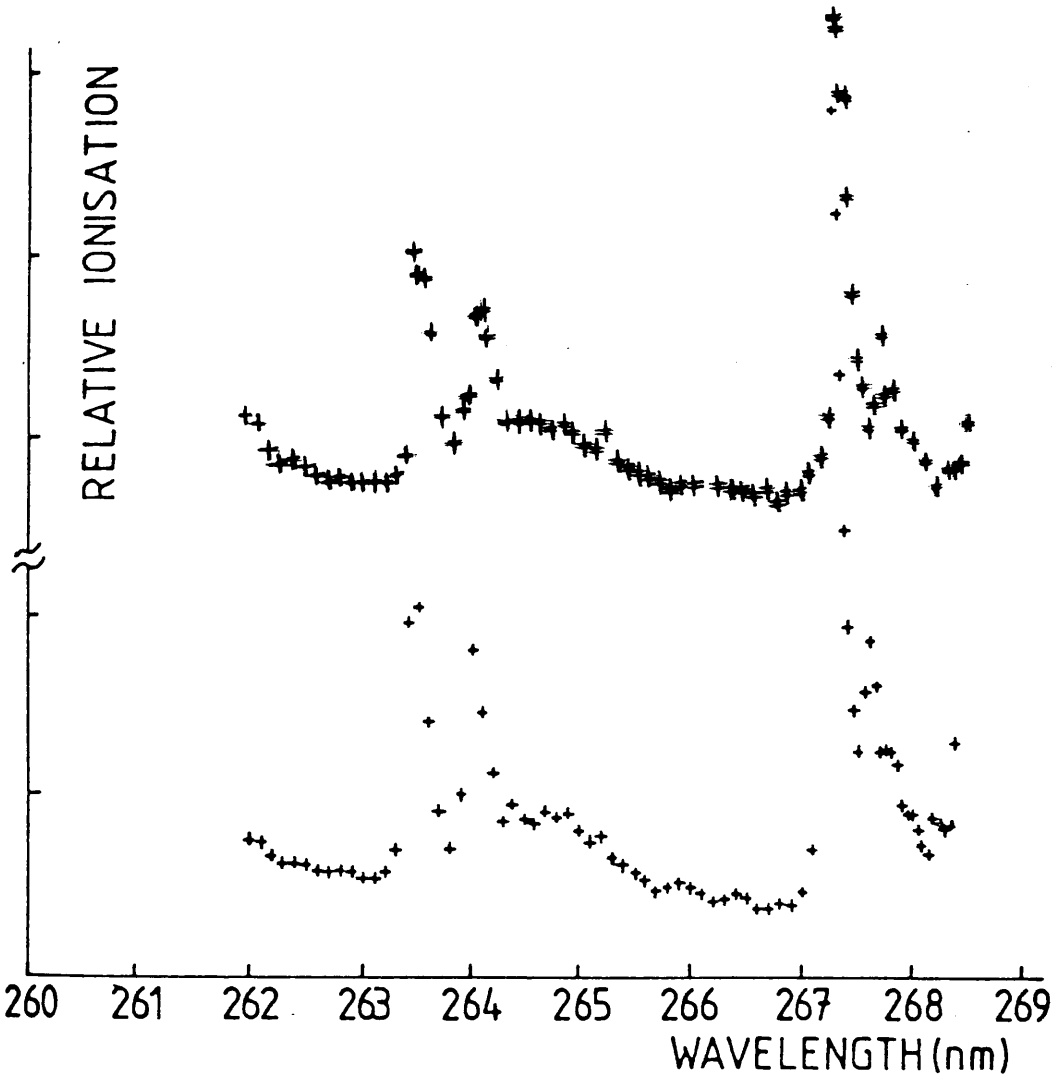

FIG. 4.43: DETAIL OF IONISATION IN A TYPE 3 COUNTER SEEDED WITH TOLUENE

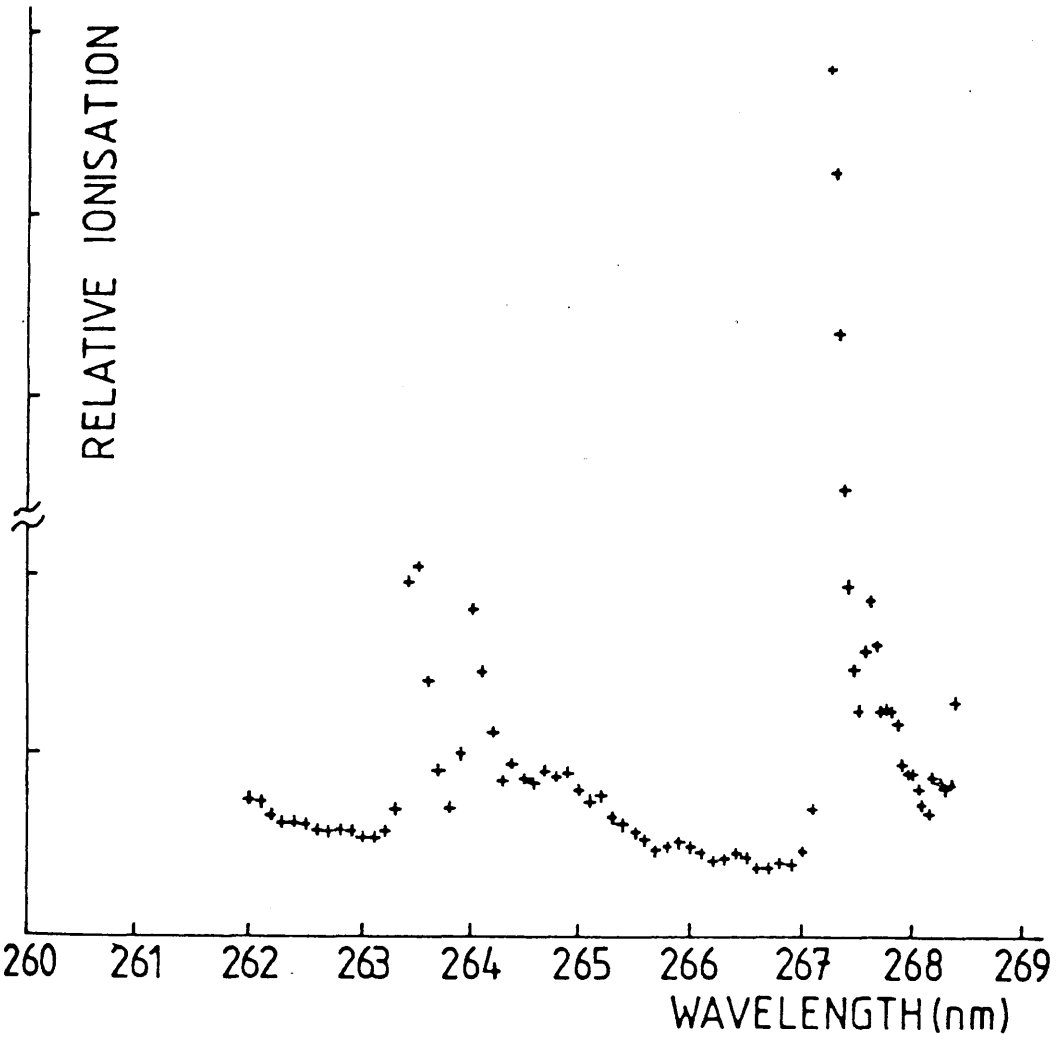

FIG. 4.43: DETAIL OF IONISATION IN A TYPE 3 COUNTER SEEDED WITH TOLUENE

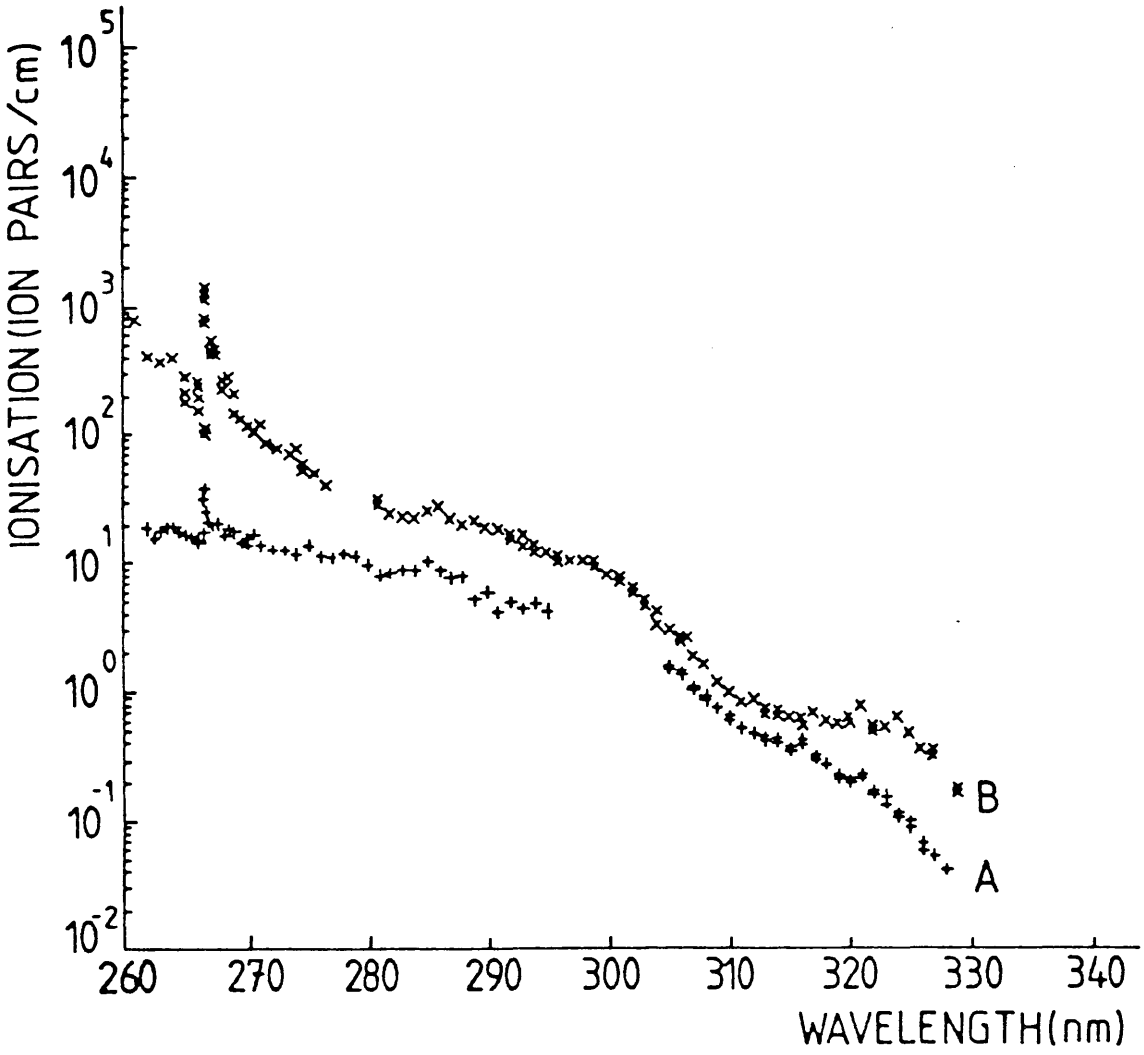

FIG. 4.44: BACKGROUND IONISATION IN AN ULTRACLEAN COUNTER

small peak, attributable to toluene, is still present at 268 nm. The concentration of toluene in the ultraclean counter, by comparison with the background spectrum Figure 4.41, is just over 1 ppb.

Unlike phenol, toluene which has been deliberately seeded into a counter is fairly easy to remove. It can be flushed out simply by flowing clean (unseeded) P-10 gas through the counter. Figure 4.45 shows the result of an experiment to demonstrate this. Toluene in P-10 counter gas was first flowed through a counter for several hours. Next the toluene sample was bypassed and clean gas flushed through (maintaining the same flow rate). The laser induced ionisation was monitored at a wavelength of 267.2 nm after the sample was bypassed and could be seen to fall rapidly, reaching levels close to background within a few minutes.

The source of toluene contamination in proportional counters is not so obvious or easy to deduce as the plastic tubing which produced phenol. It is tentatively suggested that it may be a trace impurity in the solvents, i.e. methanol and ethanol, which are used in the cleaning of parts of the counter prior to assembly. Another possibility, that it is a contaminant of the P-10 gas in the gas bottle, has been suggested by some workers at CERN (120).

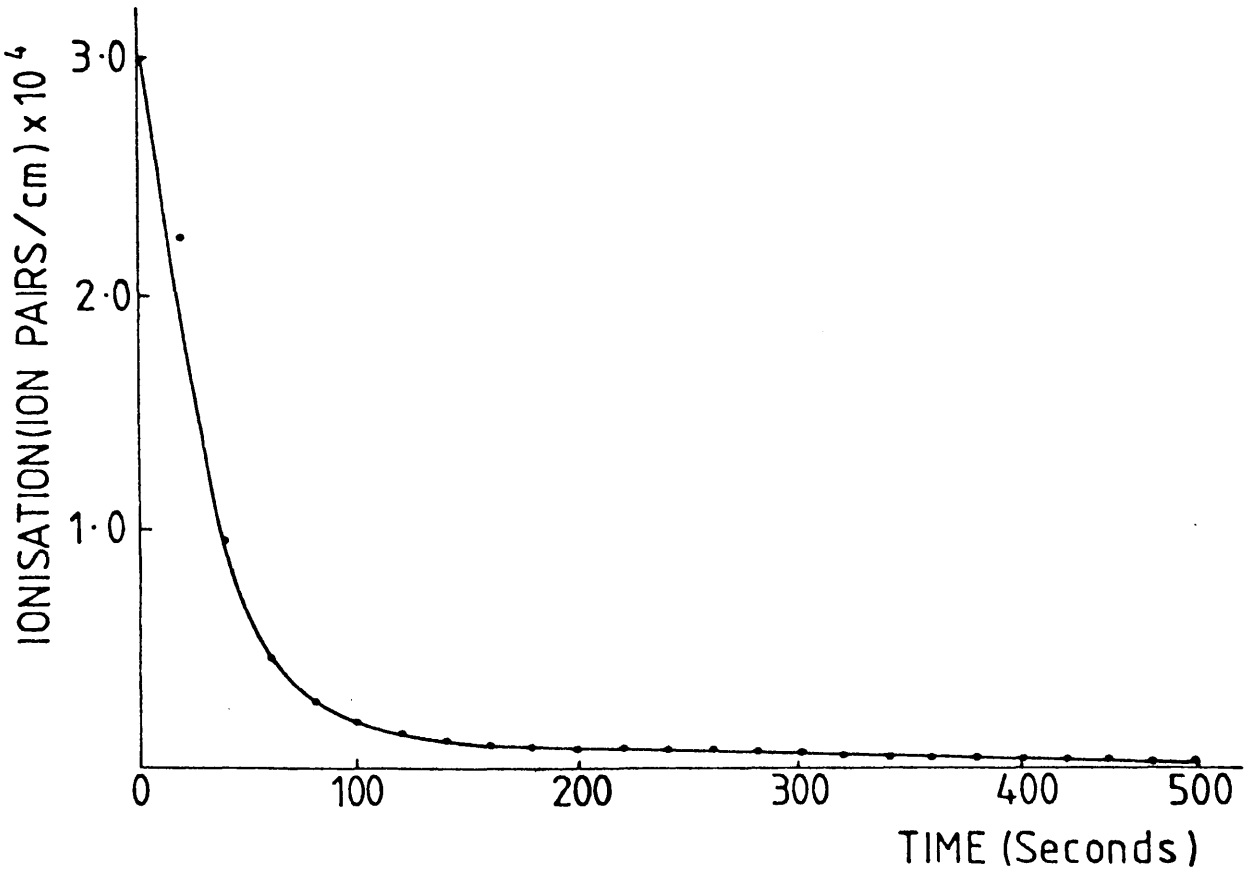

FIG. 4.45: THE REMOVAL OF TOLUENE FROM A TYPE 3 COUNTER BY FLUSHING

4-5 The Effect of Gas Purification

Preliminary attempts at reduction of background ionisation by use of a gas purification system were undertaken prior to the work on phenol and toluene, using a N_2 laser [PRA 100] and the apparatus shown in Figure 4.51. A type 2 counter was connected to two purification towers by means of copper and plastic piping; the system was evacuated and filled to one atmosphere with standard P-10 gas which could then be circulated using a peristaltic pump. One tower contained molecular sieve type 3A and the other was filled with a freshly reduced, copper based catalyst [BASF R3-11] chosen because of its affinity for oxygen. Laser induced ionisation in the counter was monitored as the gas circulated. With this system no reduction in ionisation with time was observed. Indeed, ionisation was often observed to increase as the gas circulated due to outgassing from the plastic tubing and to egression of dust from the towers into the counter.

A later, and more successful, gas purification system is shown in Figure 4.52 (121). The purpose of this system was not, however, principally to reduce background but to remove oxygen and water vapour whose gradual accumulation within a detector system due e.g. to small amounts of leakage would significantly impair the detector's operation. It was constructed from stainless steel vacuum components and incorporated a clean type 3 proportional counter. Ionisation was generated by a pulsed Nd:YAG laser [Spectron Laser Systems] which will be described in more detail in Chapter 6. A commercially available gas purification/

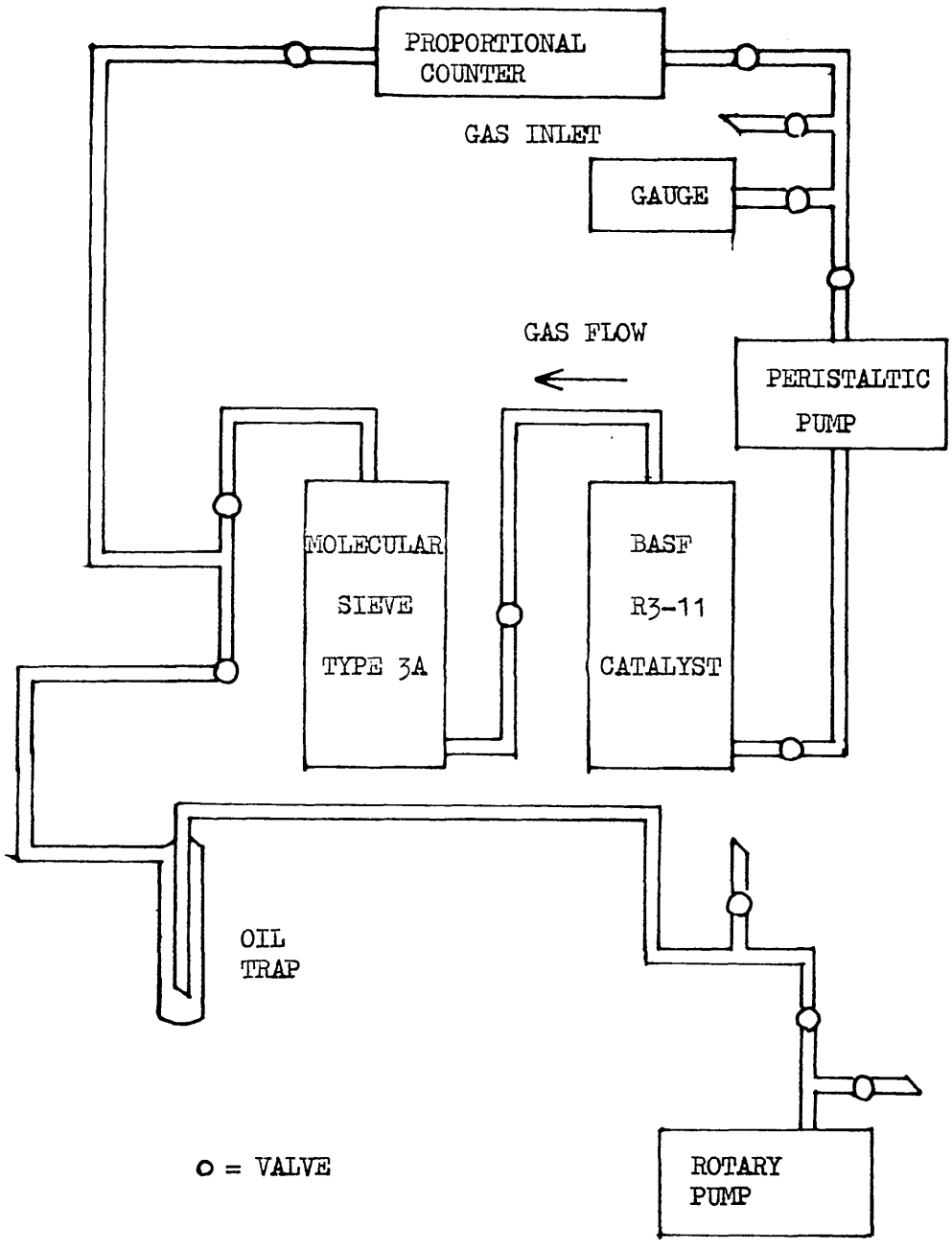

FIG. 4.51: EARLY GAS PURIFICATION SYSTEM

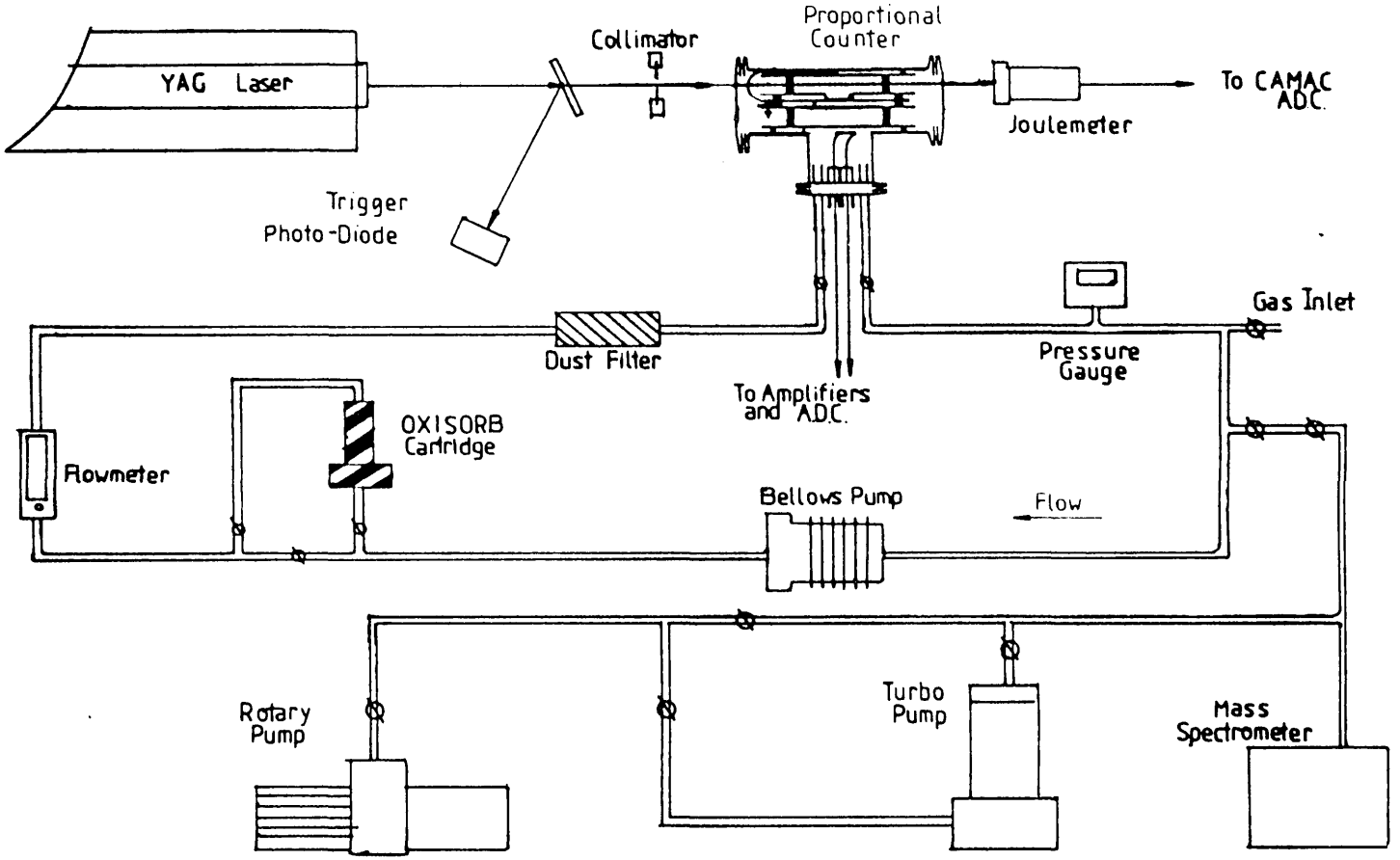

FIG. 4.52: GAS PURIFICATION SYSTEM

purification cartridge ['Oxisorb', manufactured by Messer Griesheim] was used. This contains both a reduced chromium oxide catalyst (to absorb oxygen) and a type 3A molecular sieve which will remove, from the counter gas stream, species of diameter less than about 0.3 nm. To ensure that particulate matter was not carried into the counter, a dust filter was inserted in the counter inlet pipe. A small quadrupole mass spectrometer [Edwards - 'Anavac'] was included which allowed the gas to be mass analysed. The system was tested both by monitoring total ionisation as the gas circulated and by investigating the variation in concentrations of the various components of the mixture with time (using the mass spectrometer).

Fifty millibars ($\sim$ 38 torr) of laboratory air were introduced to the system which was then filled to a total pressure of 1200 mb ($\sim$ 910 torr) with P-10 gas. With the Oxisorb cartridge bypassed, the gas mixture was circulated for twelve hours at a flow rate of 150 ml/min (equivalent to one complete circuit in 15 minutes). At the end of this period the ^{55}Fe spectrum in the counter was recorded, and is shown in Figure 4.53. The resolution is poor at 45%, compared with the 20-25% resolution typical of the type 3 counters. A mass spectrum, recorded at the same time, shows the presence of oxygen and water vapour as well as the normal P-10 gas constituents. See Figure 4.54.

The gas was now allowed to flow through the Oxisorb cartridge and, after an hour, both mass and ^{55}Fe spectra were again recorded. The/

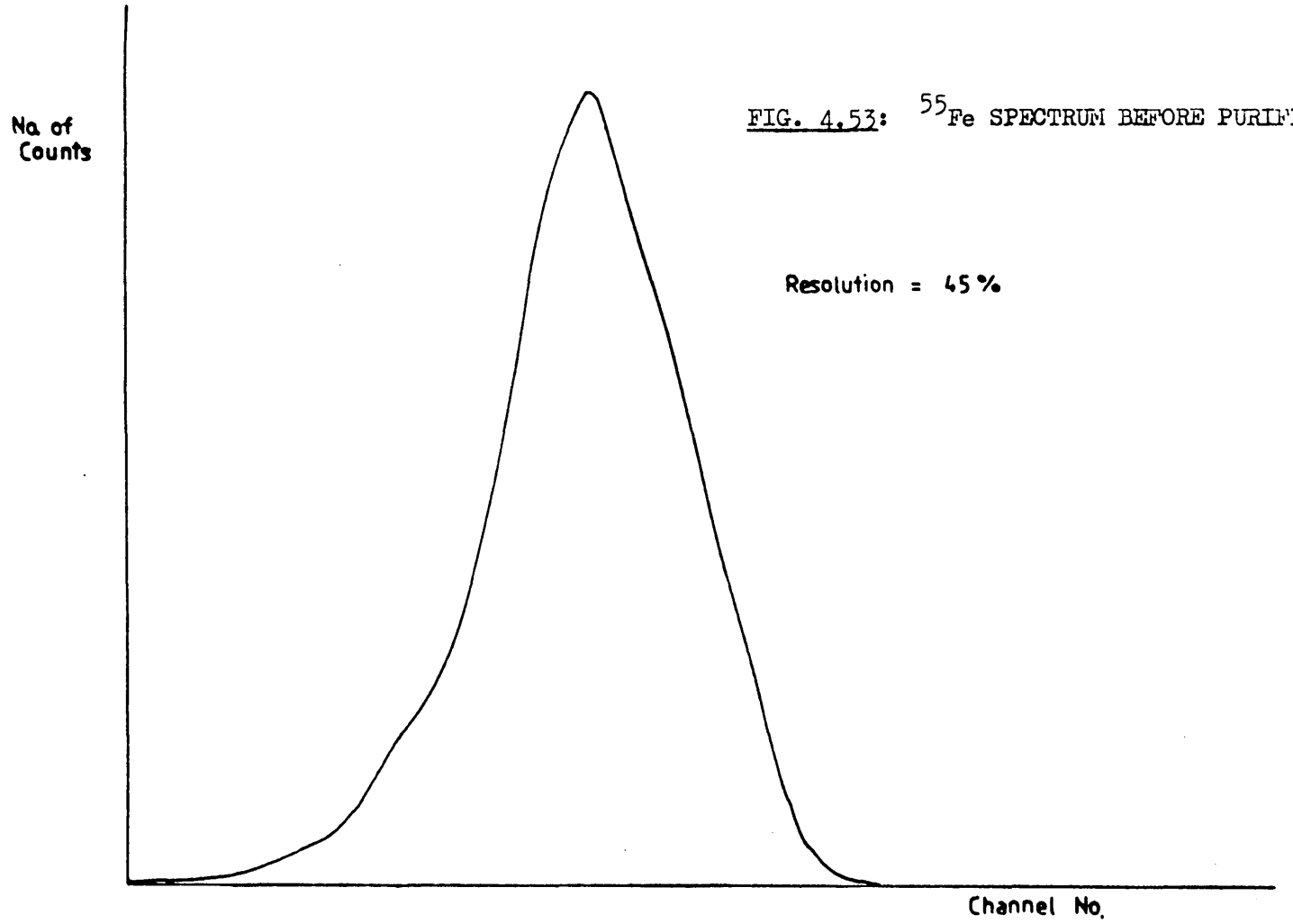

FIG. 4.53: ^{55}Fe SPECTRUM BEFORE PURIFICATION

Resolution = 45 %

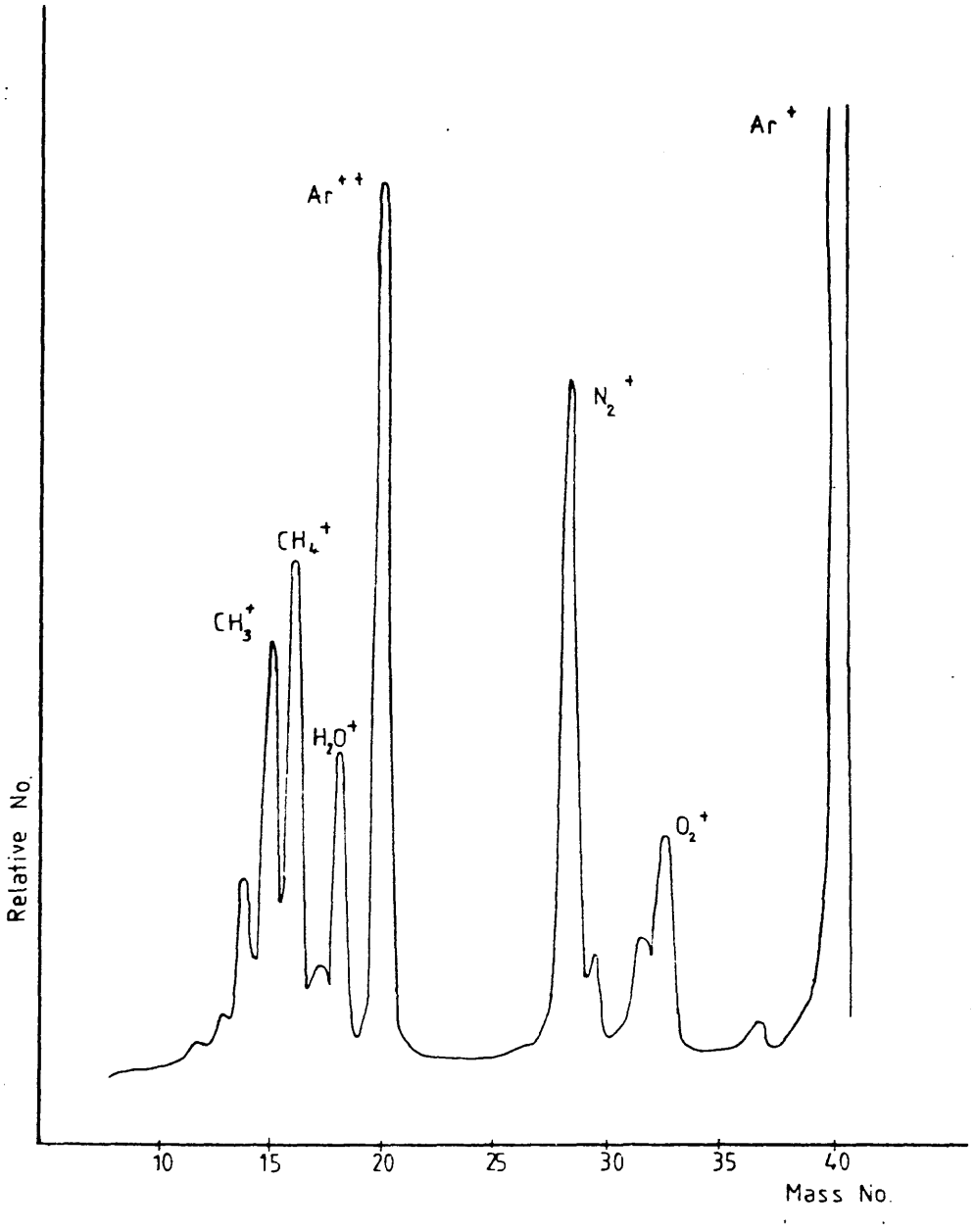

FIG. 4.54: MASS SPECTRUM BEFORE PURIFICATION

The ^{55}Fe spectrum resolution has improved markedly to 22%, as is shown in Figure 4.55, and the argon escape peak is well resolved. In the mass spectrum - Figure 4.56 - signals from O_2^+ and H_2O^+ are absent showing the efficiency of the Oxisorb cartridge for removal of these contaminants.

Gas circulation was continued for around 80 hours and the total ionisation in the counter monitored at intervals. Average values of ionisation, normalised to 1 $\mu J/mm^2$, after different circulation times are shown in Figure 4.57. At each point, a power dependence curve showed the ionisation to be a quadratic function of laser fluence. After 20 hours of flowing, ionisation in the gas had dropped by 50%, after which it remained fairly constant. This may indicate either that the Oxisorb cartridge is saturated, i.e. full, or that it has absorbed, from the gas, all species which it is able to and that the remaining ionisation is due to species which are not taken up by this type of cartridge.

Hubricht et al. have also studied the effects of gas purification on laser induced ionisation in proportional counters (113). Using an activated carbon filter only, they were able to decrease observed ionisation by a factor of 5. When a titanium getter pump was also used a total reduction in ionisation of a factor of 10 was observed. When circulation was stopped after cleaning, ionisation in the gas rose slowly to its initial, unpurified level over 3 - 5 days. The Dortmund group also observed a dramatic increase in ionisation when heat was applied to the walls of their chamber/

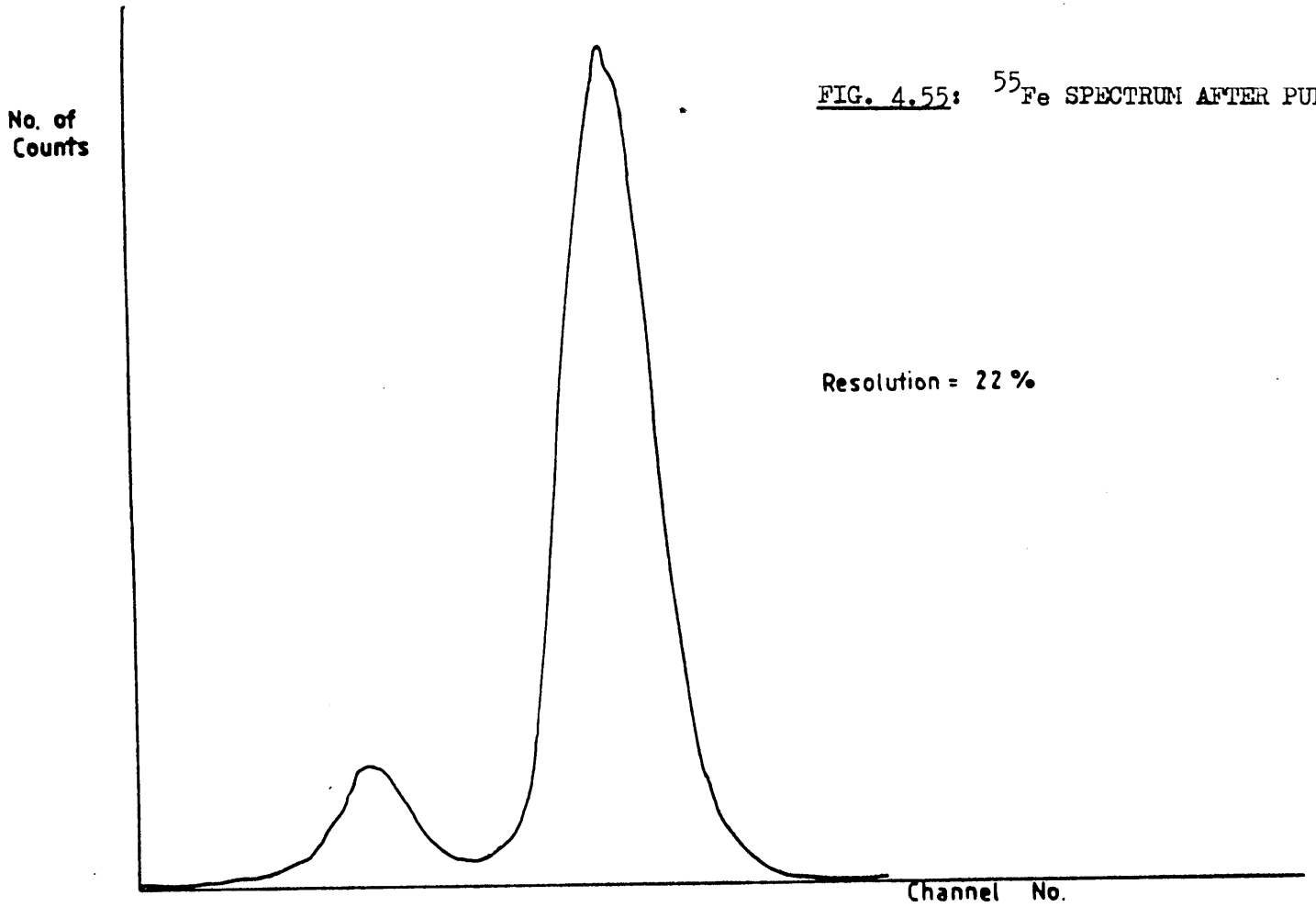

FIG. 4.55: ^{55}Fe SPECTRUM AFTER PURIFICATION

Resolution = 22 %

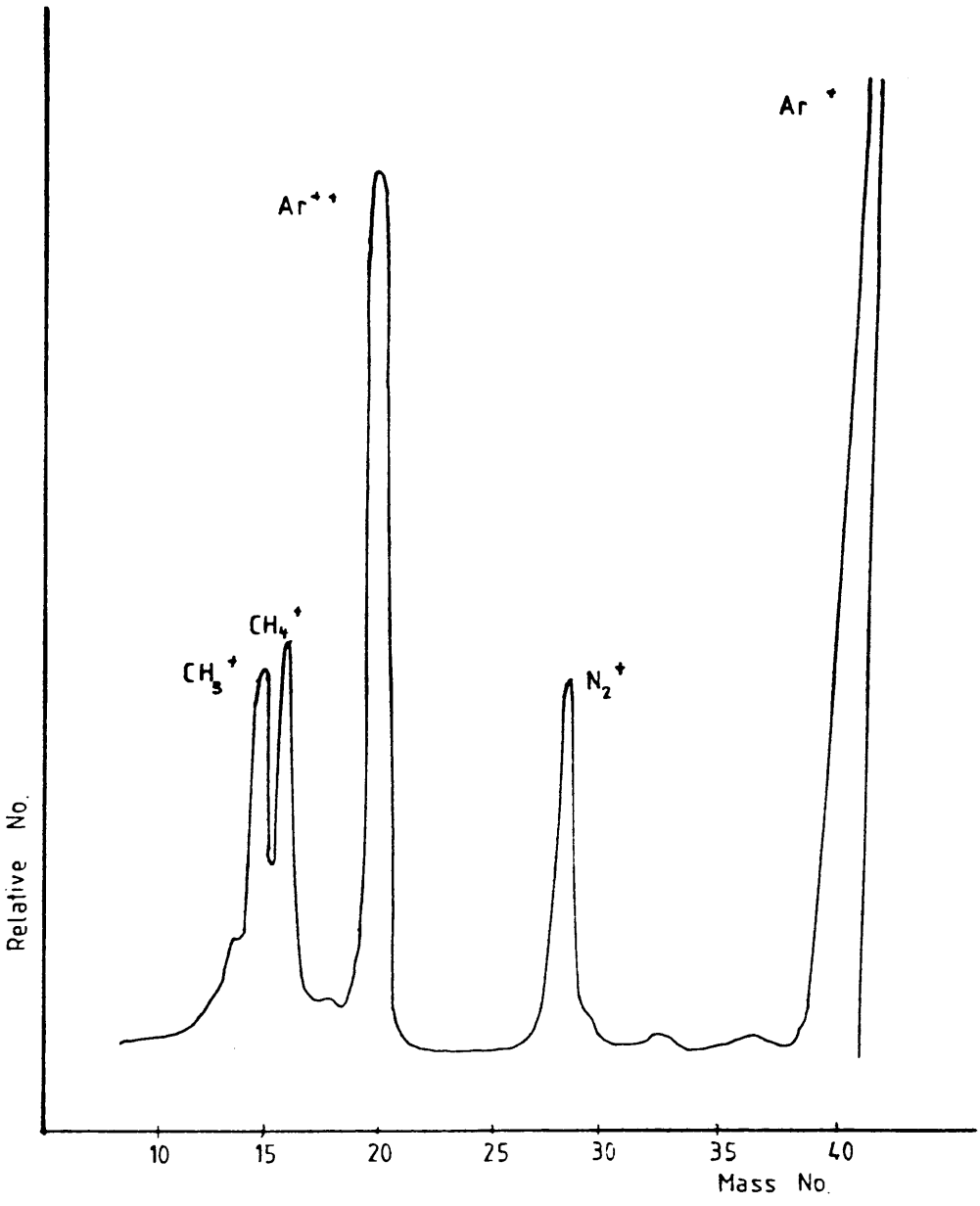

FIG. 4.56: MASS SPECTRUM AFTER PURIFICATION

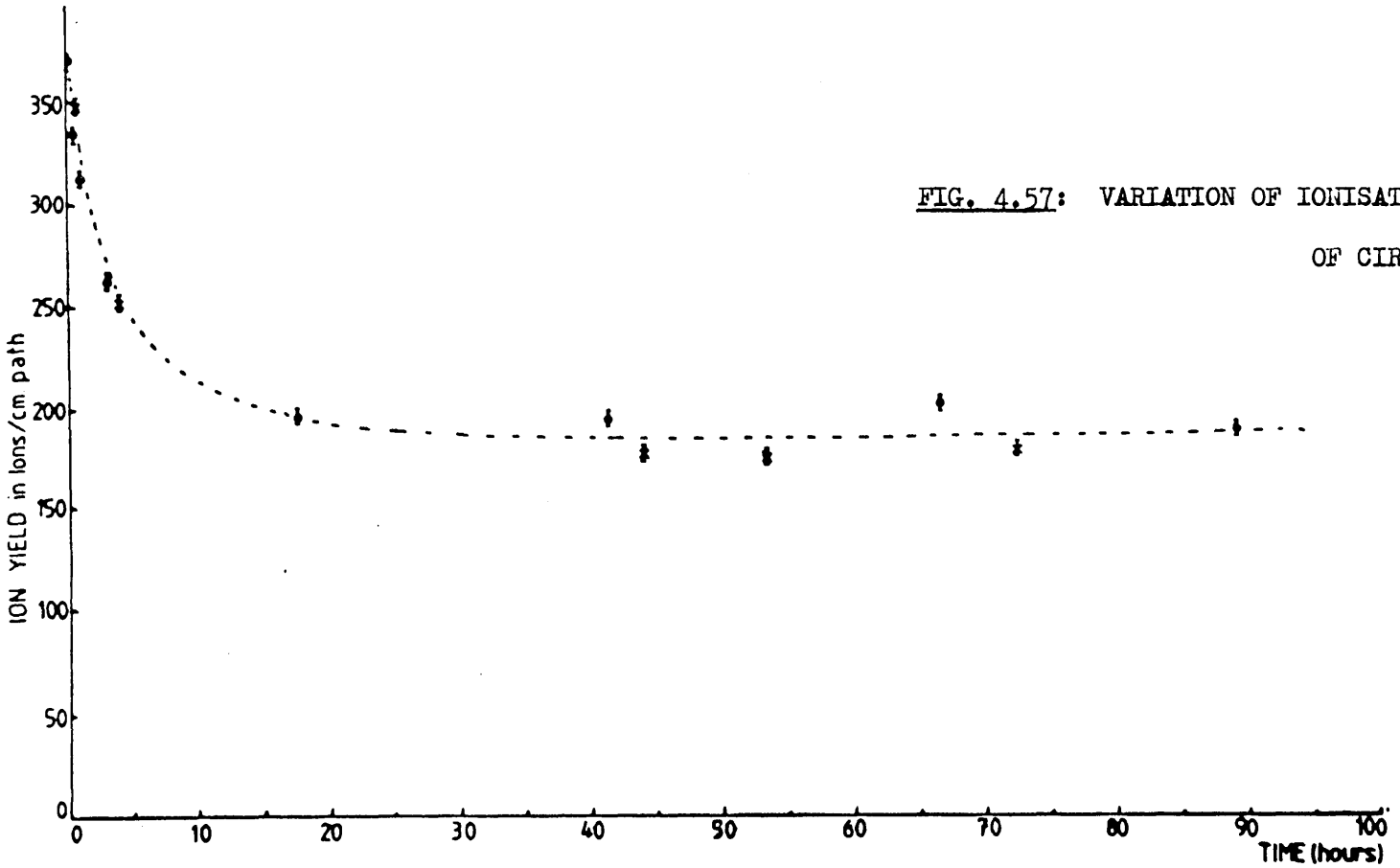

FIG. 4.57: VARIATION OF IONISATION WITH TIME OF CIRCULATION

chamber, demonstrating that impurities from chamber walls may contribute very significantly to observed background ionisation signals. This effect has also been studied in Glasgow. Figure 4.58 shows the variation in background ionisation in the chamber subsequently used for caesium detection (see Chapters 3 and 5) when heat was applied to the outer casing. A rise of approximately a factor of 7 is apparent, followed by a slow reduction to pre-heating levels after the heat source was removed. Since heat was applied to a localised area of the chamber using a "heat gun" [RS 546-994] no accurate measurement of heating temperature was possible. The estimated temperature rise was $100^{\circ}C \pm 25^{\circ}C$.

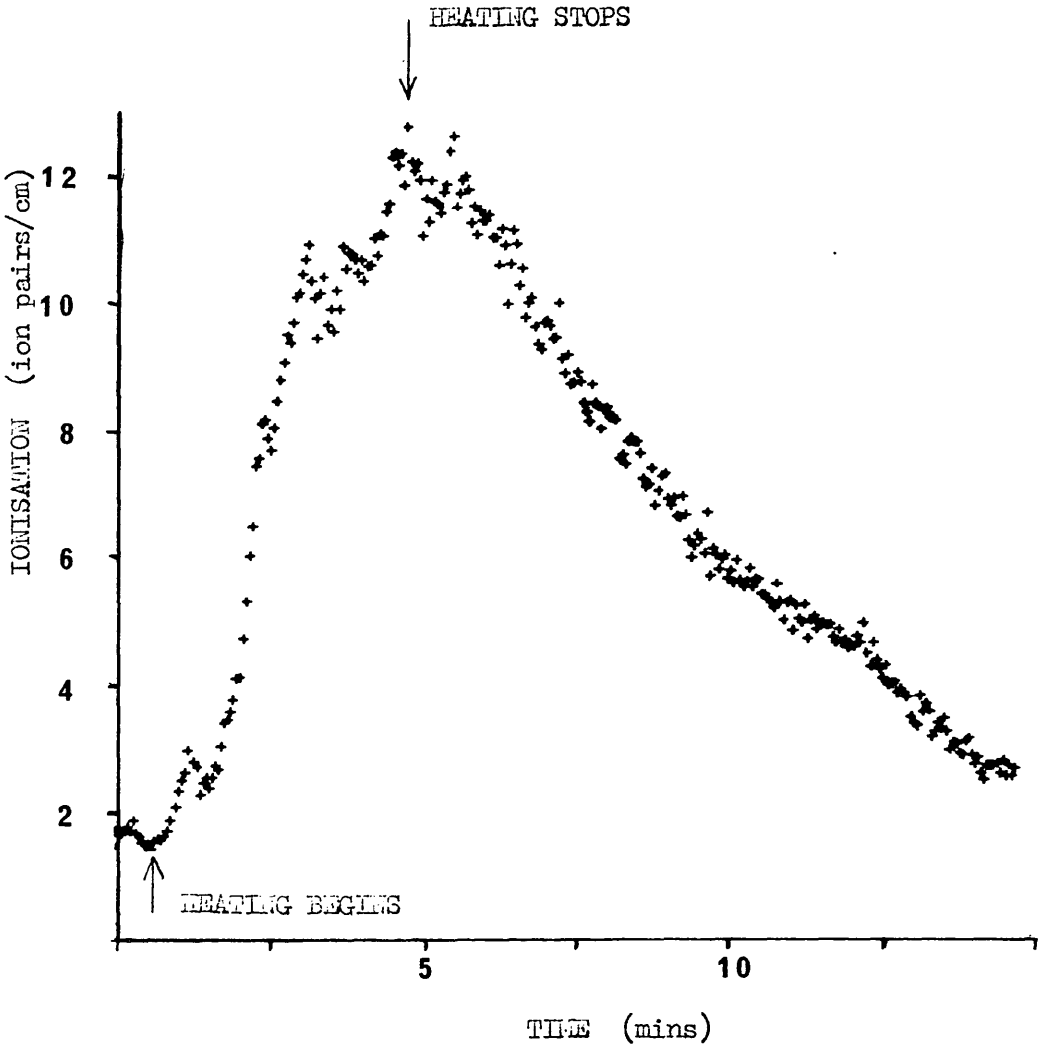

FIG. 4.58: THE EFFECT OF HEATING

CHAPTER 5 MULTIPHOTON TRANSITIONS IN CAESIUM

5-1 Introduction

In this study, a variety of multiphoton transitions in caesium vapour were investigated. Both two photon (i.e. one photon resonant, one photon ionisation) and three photon (i.e. two photon resonant via a virtual state, one photon ionisation) processes were observed. These correspond to Hurst's resonance ionisation schemes 1 and 5 respectively (2). A partial energy level diagram for caesium (adapted from reference 2) - Figure 5.11 - illustrates examples of the transitions described below.

In the glass chamber (Figure 3.52) two photon ionisation was observed when the $6^2s_{\frac{1}{2}} \rightarrow 7^2p_{\frac{3}{2}}$ and $6^2s_{\frac{1}{2}} \rightarrow 7^2p_{\frac{1}{2}}$ transitions were resonantly excited by a laser tuned to 455.5 nm or 459.3 nm (transitions c on the Figure).

In the stainless steel chamber (Figure 3.53) the $6s\text{-}8p_{\frac{1}{2},\frac{3}{2}}$ and $6s\text{-}9p_{\frac{1}{2},\frac{3}{2}}$ transitions were also observed. Repeated attempts to observe the caesium single photon absorption edge by stepping the dye laser wavelength through the region 315-332 nm were not successful. However, once the frequency doubler had been modified to allow continuous scanning in the ultraviolet region of the spectrum, large numbers of two photon, 6s-Rydberg level transitions (b on the Figure) were visible, as was the expected edge. Using the red fundamental output of the laser, a number of three photon ionisation processes were observed. Two photon excitation from the ground state $6^2s_{\frac{1}{2}}$ to

either/

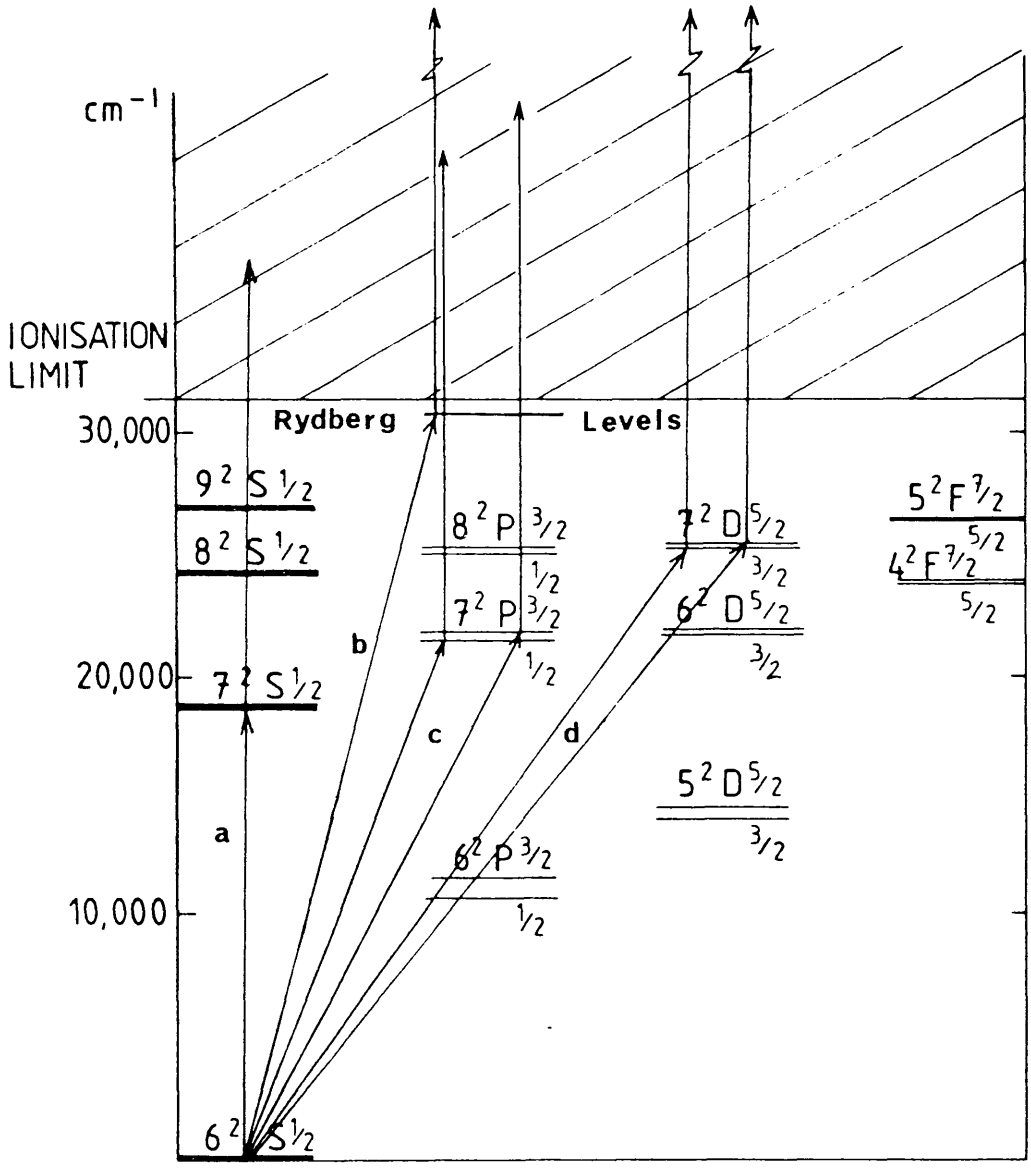

FIG. 5.11: PARTIAL ENERGY LEVEL DIAGRAM FOR CAESIUM

either d or higher s levels (d and a on the Figure), followed by ionisation by a third photon, gave rise to two series of peaks (one due to s → d transitions and the other to s → s transitions). $6^2S_{\frac{1}{2}} \rightarrow$ p transitions were not observed with the red laser as two photon excitation from s to p levels is 1-forbidden.

5-2 Glass Chamber Results

Although the glass chambers suffered from various drawbacks (as described in Chapter 3) it was possible, with care, to obtain caesium spectra from them. An example is shown in Figure 5.21. This is a scan from 455 - 460 nm, taken using a Coumarin 47 laser dye, and shows well resolved 6s → 7p transitions at the expected wavelengths (122). The 455.5 nm peak ($6s_{\frac{1}{2}} \rightarrow 7p_{\frac{3}{2}}$ resonant transition) has an intensity of ~ 17 times the non-resonant background between the two peaks and the 459.3 nm peak ($6s_{\frac{1}{2}} \rightarrow 7p_{\frac{1}{2}}$) has intensity ~ 4.5 times backgound. The ratio of the peak intensities is 3.3:1. The significance of this result will be discussed later in section 5-3 (IV). The laser fluence used to obtain Figure 5.21 was 7.2 $\mu J/mm^2$ a power level at which, from the rough calculations of Chapter 1, some degree of saturation might be expected. Power dependence graphs were obtained from both peaks and from the background. A linear power dependence was found for the background and, for the 455.5 and 459.3 nm peaks, the gradients of the ionisation versus fluence plots were 1.49 and 1.87 respectively, suggesting that the onset of saturation occurs at lower fluence for the 455.5 nm transition than for the 459.3 nm transition.

The/

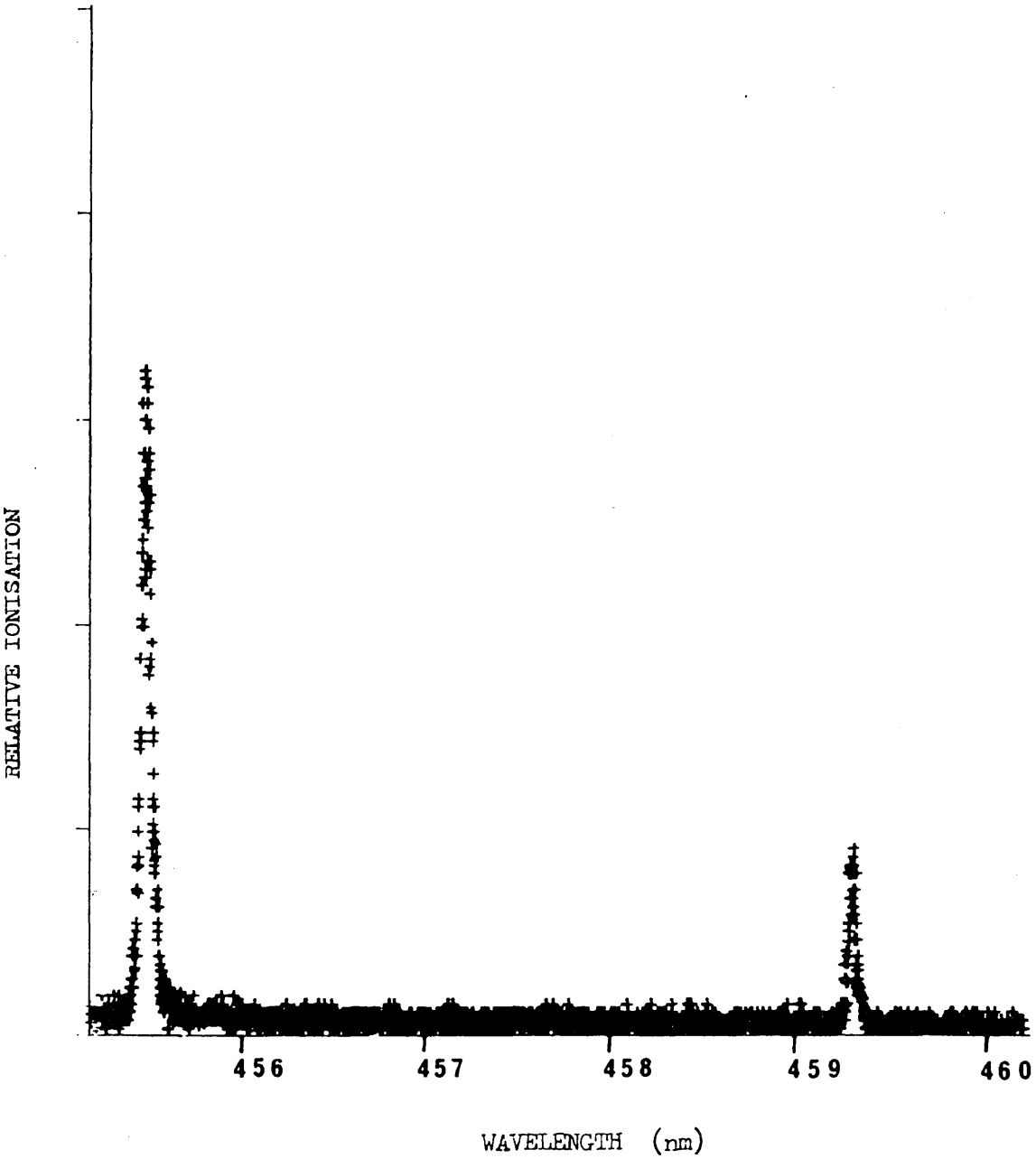

FIG. 5.21: 6s - 7p TRANSITIONS IN THE GLASS CHAMBER AT A FLUENCE OF 7.2 $\mu J/mm^2$

The linear background ionisation was attributed to photo-electrons produced when single photons from the laser beam were scattered and struck the internal surfaces of the counter.

In the glass chambers, the effect known as power broadening could be observed, i.e. an increase in linewidth of a multiphoton transition with increased laser fluence. Power broadening is a saturation effect in which the intense photon flux of a (usually) focused laser causes a decrease in absorption coefficient at the line centre of a transition. The effect is progressively less pronounced further from the line centre, and thus leads to a relative increase in the intensity of the wings of a peak (123).

Figure 5.22 shows a scan in the 455.5 nm region taken at incident laser fluences of 7.2 $\mu J/mm^2$, A; 8.9 $\mu J/mm^2$, B: and 520 $\mu J/mm^2$, C. Plots B and C have been displaced for clarity. The linewidths (Full Width at Half the Maximum height) are 0.06, 0.07 and 0.1 nm respectively. Mayfeh, who has also studied the caesium 6s $\rightarrow$ 7p transitions, reported a width of $\sim$ 0.5 nm for the 455.5 nm peak at an incident laser fluence of 11 mJ/mm^2 (124). This result may not, however, be a valid comparison with the present work due to the different laser system used.

Even at low fluences where power broadening is slight, observed caesium peak widths are considerably greater than natural linewidths due to a combination of Doppler and collisional broadening effects, and to the influence of laser bandwidth.

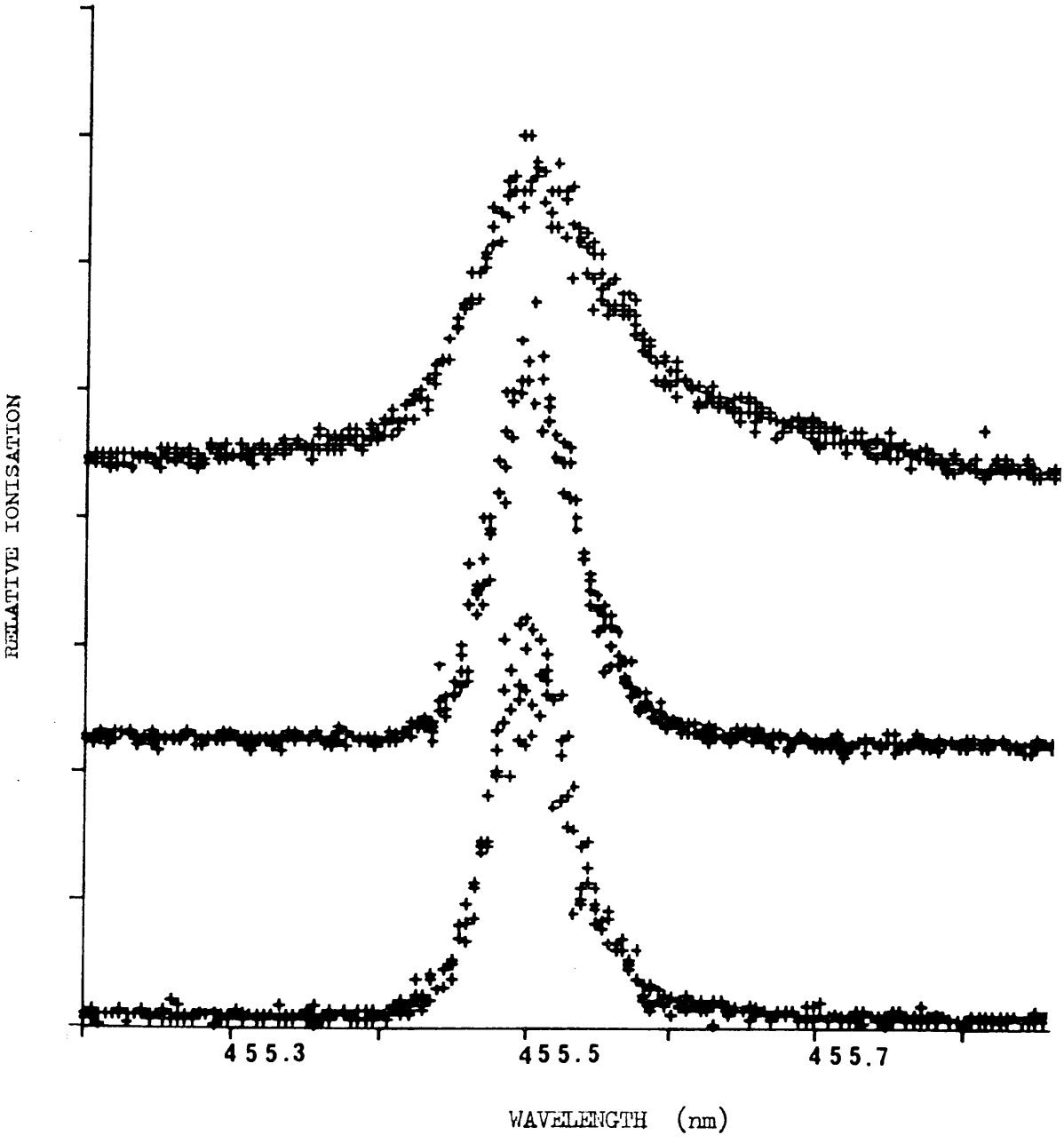

FIG. 5.22: POWER BROADENING IN THE GLASS CHAMBER

Doppler linewidth may be calculated from the formula (99):

$$\Delta E_{HM} = 2.35 \sqrt{\frac{kT}{Mc^2}} \; E \qquad \text{---- 29}$$

where ΔE_{HM} is the Doppler width (FWHM)

k is the Boltzmann constant

T is the absolute temperature

M is the mass of the caesium atom

c is the velocity of light

and E is the energy of the transition

For the 455.5 nm transition, $\Delta E = 1.49 \times 10^{-26}$ J, which may be converted to the more familiar units of nanometers by use of the relationship below:

$$\frac{\Delta E}{E} = \frac{\Delta \lambda}{\lambda} \qquad \text{---- 30}$$

Doppler broadening is thus estimated at 1.55×10^{-5} nm.

Collisional linewidth was estimated in the following way. Measured collision frequencies for gases at room temperature are typically in the region of $f = 4 \times 10^{9}$ /s (125). Assuming all caesium atoms in the laser volume are in the $^{2}7p\,\frac{3}{2}$ state and that all collisions taking place depopulate this level, i.e. either further excite or de-excite the caesium atoms, then the effective (collisional) lifetime of the state is 1/f, i.e. 2.5×10^{-10} s.

The/

The linewidth associated with a state of the above lifetime is given by the uncertainty principle:

$$\Delta E \Delta t = \hbar \qquad \text{---- 31}$$

where Δt is the state lifetime

and $\hbar = h/2$ (where h is Planck's constant)

Substituting the value of ΔE obtained, 4.22×10^{-25} J, into equation 30, collisional broadening of the $7p\,\frac{3}{2}$ state of caesium is estimated at $\Delta\lambda = 4.41 \times 10^{-4}$ nm.

Since both Doppler and collisional broadening effects are relatively small, the principal contribution to the $\geq$ 0.05 nm linewidths observed for the resonant caesium transitions is the relatively large laser bandwidth of $\sim$ 0.05 nm.

5-3 Stainless Steel Chamber Results

I Background

As discussed in Chapter 4, the background in the stainless steel chamber when, following extensive cleaning and baking, it was first assembled was the smallest encountered in a counter at Glasgow. A plot of background ionisation appeared as Figure 4.44, along with a comparative plot from one of the type 3 (Scottish Rivers) counters.

II ^{55}Fe Resolution

The resolution of the x-ray spectrum from the ^{55}Fe source, when the counter was filled to 760 torr with standard Ar/CH_4 counter gas was $\sim$ 23% ($\pm$ 2%), comparable with results obtained in the Type 3 counters/

counters and indicating that the different geometry of the source used in the Cs counter does not adversely affect resolution.

In normal operation, the Cs counter was filled to only $\sim$ 30 torr with counter gas. At this pressure, typical ^{55}Fe resolution was $\sim$ 28%. X-ray spectra from the counter are shown in Figures 5.31A and B.

III Cs Source Geometry

As originally envisaged, the source of caesium atoms in the chamber was to be the collimated sample holder. However, it became apparent during operation that atoms ionised by the laser did not originate there. Ionisation was instead taking place in the Cs vapour emanating from the tip of the probe on the linear motion drive (which had become contaminated with Cs metal when used to crack open the sample vial). If the probe was withdrawn fully into the upper part of the chamber the resonant Cs signals disappeared. When the probe was repositioned close to the beam the signals returned. To ensure the laser beam did not actually strike the probe the beam exiting from the chamber was visually checked.

It was found that, over a period of $\sim$ 24 hours, the Cs signals from the chamber decreased markedly as the Cs on the probe was used up or oxidised. To restore ionisation to its former levels, the sample reservoir was heated (to liquefy the metal) and the probe dipped and withdrawn to its original position.

IV/

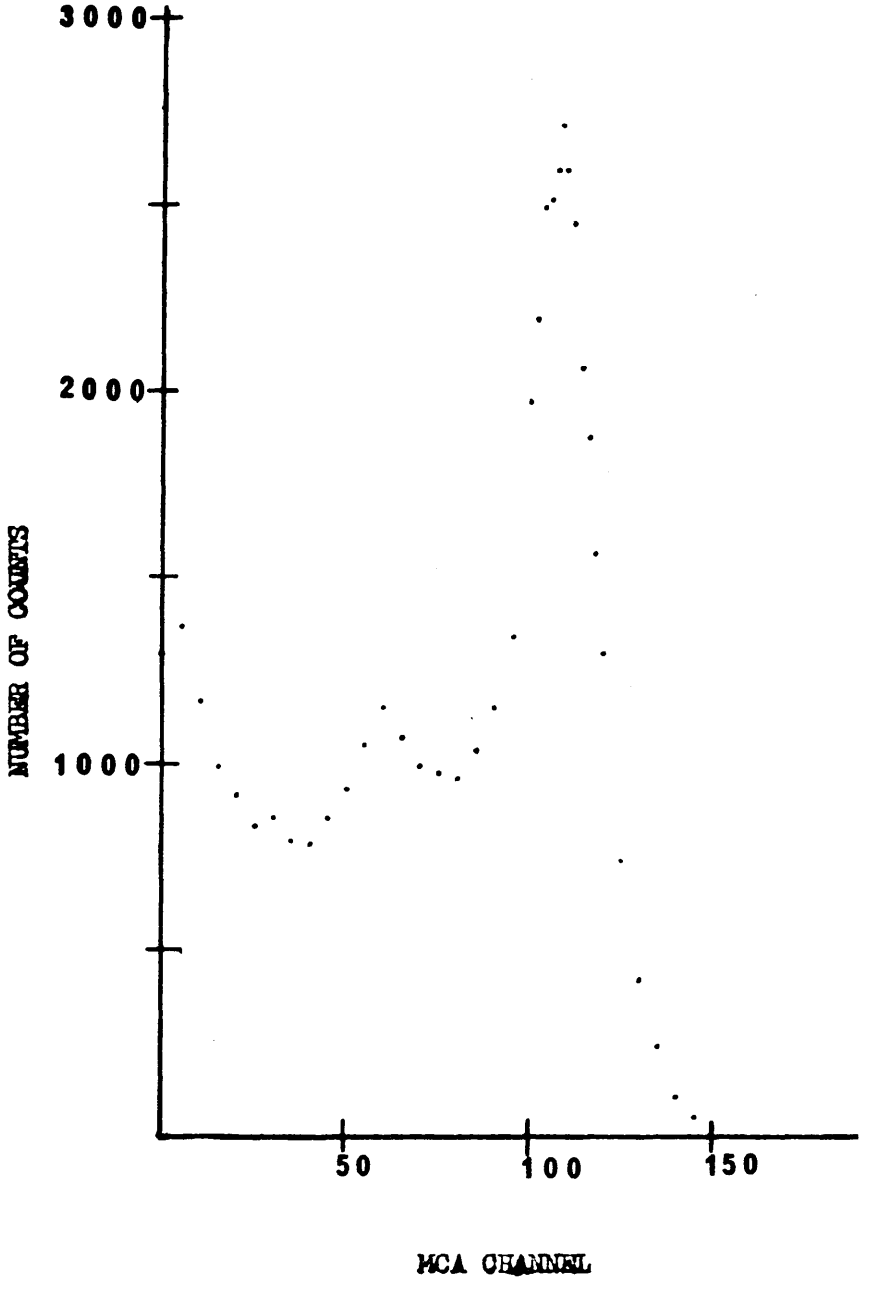

FIG. 5.31 A: ^{55}Fe SPECTRUM (760 torr)

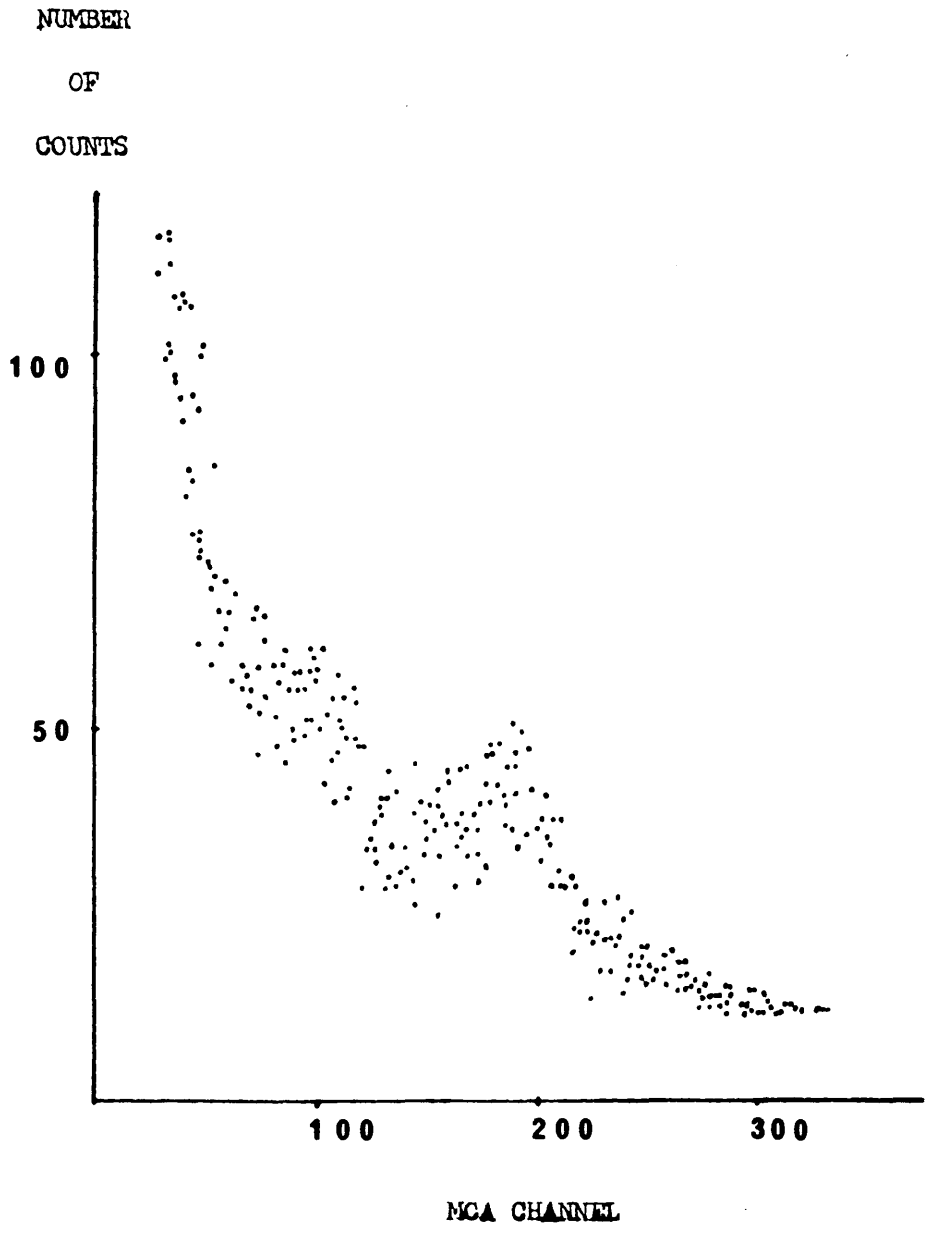

FIG. 5.31 B: ^{55}Fe SPECTRUM (30 torr)

IV 6s - 7p Transitions (126)

Two photon resonance ionisation spectra were recorded which were similar to those obtained from the glass chambers. An example, recorded at low incident laser fluence (0.8 $\mu J/mm^2$) is shown in Figure 5.32. The ratio of the peak intensities 455.5:459.3 nm is 3.1:1.

By a similar treatment to that used to derive saturation conditions in Chapter 1, it can be shown that (as long as the laser pulselength is much shorter than the intermediate state lifetime) the intensity of a two photon resonant transition is described by the following equation (127):

$$I \propto N_I = N_0 \sigma_1 \sigma_I \frac{\phi^2}{2} \qquad \text{---- 32}$$

where I is the intensity and the other symbols are as defined earlier.

Thus the intensity ratio of two, two-photon transitions observed within a single, continuous low fluence scan (i.e. at constant fluence, laser dimensions and target atom density) is given by the general relationship:

$$\frac{I_{(1)}}{I_{(2)}} = \frac{(\sigma_1 \sigma_I)_{(1)}}{(\sigma_1 \sigma_I)_{(2)}} \qquad \text{---- 33}$$

and, for caesium,

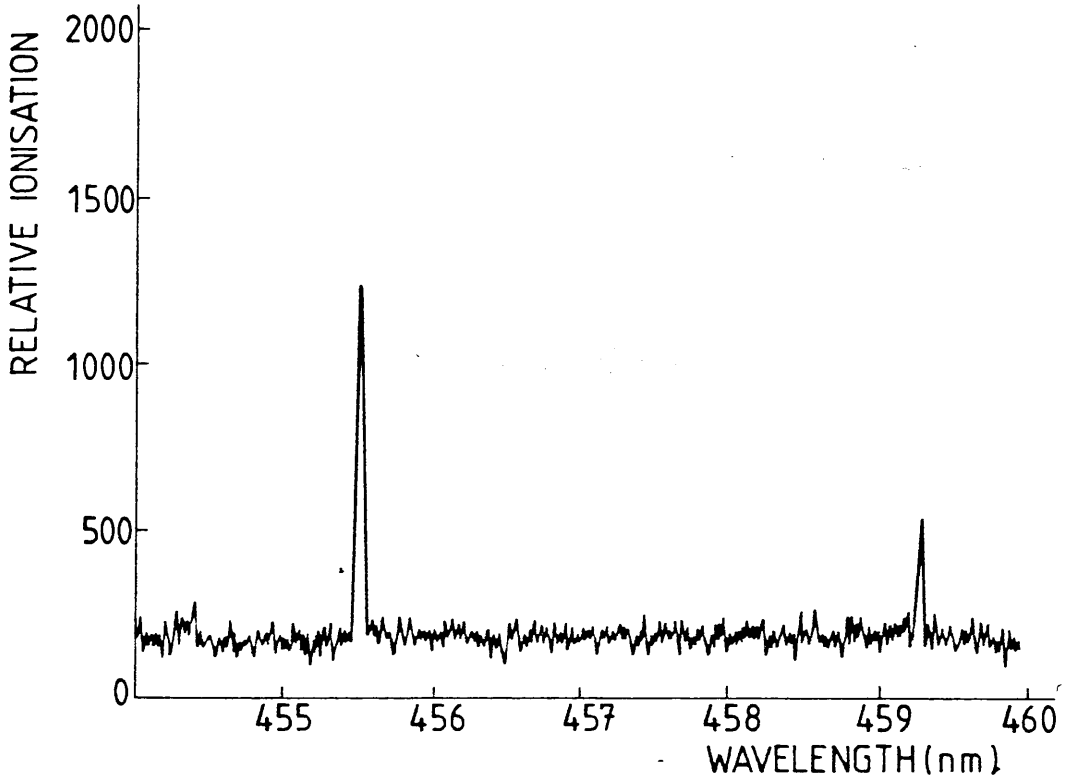

FIG. 5.32: 6s - 7p TRANSITIONS AT A FLUENCE OF 0.8 $\mu J/mm^2$

$$\frac{I_{455.5\ nm}}{I_{459.3\ nm}} = \frac{\sigma(6s_{\frac{1}{2}} - 7p_{3/2})\ \sigma(7p_{3/2} - \text{continuum})}{\sigma(6s_{\frac{1}{2}} - 7p_{\frac{1}{2}})\ \sigma(7p_{\frac{1}{2}} - \text{continuum})} \quad \text{---- 34}$$

From the cross sections and transition rates quoted by Hurst (12) the right hand side of the above relationship is equal to 3.4 ± 0.2. Estimating the error appropriate to the intensity ratio derived from Figure 5.32 as $\sim 10\%$, the left hand side of the equation is 3.1 ± 0.3, close to the literature value.

As the fluence of the laser is increased, two effects are apparent: a) the peak intensity ratio decreases and b) power broadening occurs. At a fluence of 8 $\mu J/mm^2$ - Figure 5.33 - the 455.5 nm transition is only 50% more intense than the 459.3 nm peak. At a fluence of 1.18 mJ/mm^2 - Figure 5.34 - the transitions are of similar intensity, indicating that saturation has been achieved. This value of saturation fluence is concordant with that of Hurst *et al.*, who claimed 90% saturation of the resonant two-photon ionisation process via the 7p levels of caesium with an incident fluence of 1.0 mJ/mm^2 (2). It is also in reasonable agreement with the rough calculations of Chapter 1.

From the ^{55}Fe calibration source, the saturation spectrum corresponds to 6×10^4 ion pairs, *i.e.* 6×10^4 Cs atoms in the focused laser volume of $0.13 \times 0.13 \times 10\ mm^3$. This value is around two orders of magnitude smaller than the number of caesium atoms (8.9×10^6) which would be expected to occupy the laser volume on the basis of the saturated/

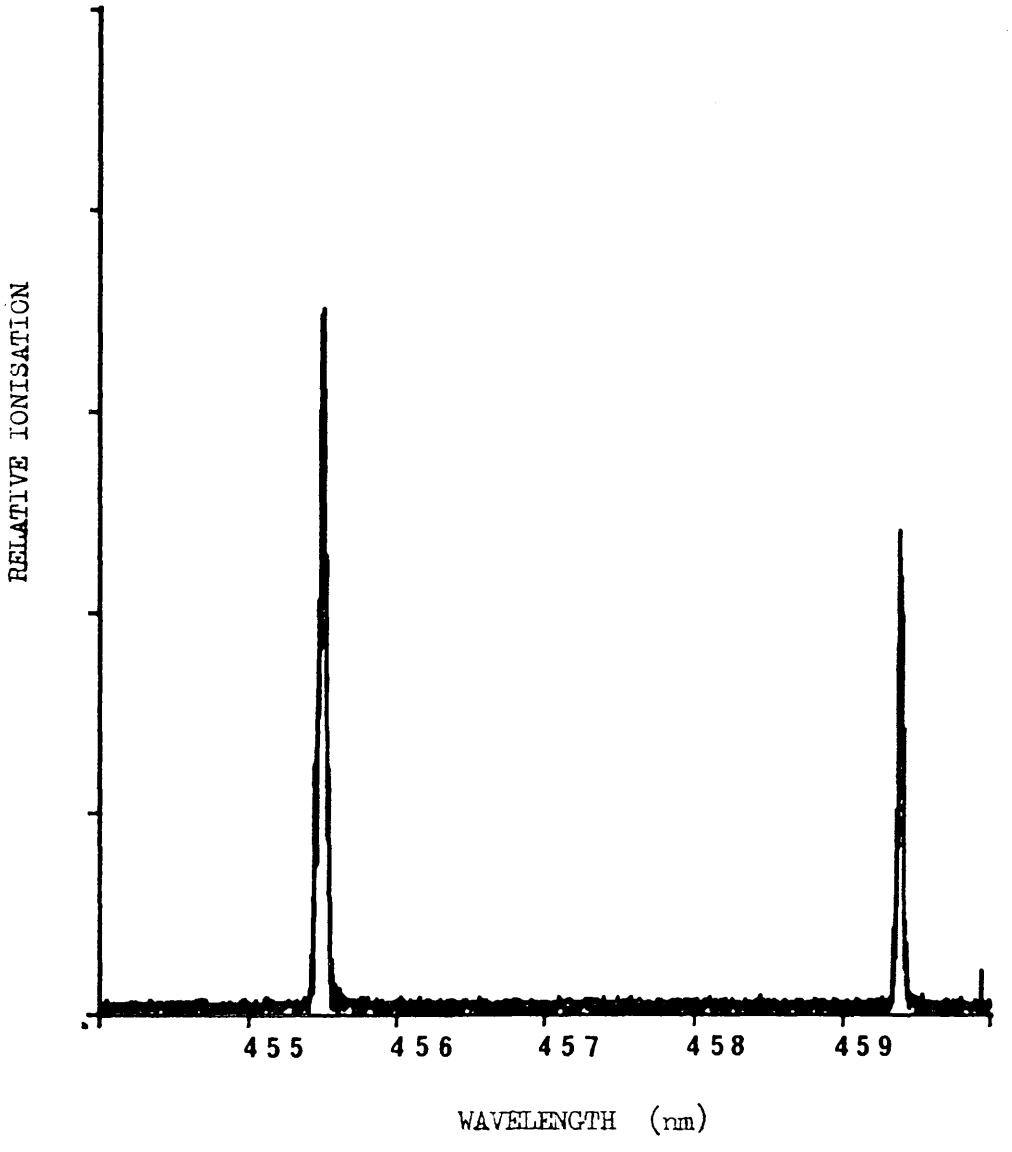

FIG. 5.33: 6s - 7p TRANSITIONS AT A FLUENCE OF 8 $\mu J/mm^2$

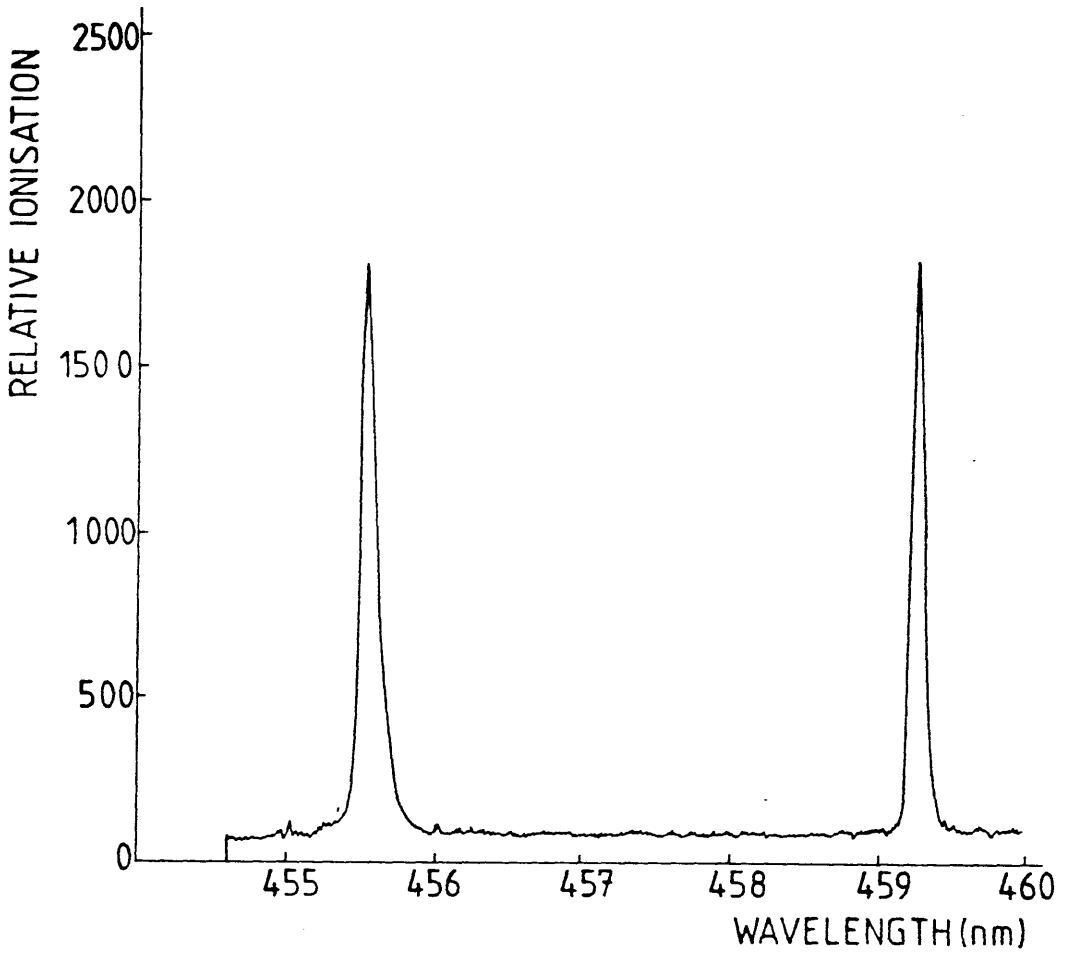

FIG. 5.34: 6s - 7p TRANSITIONS AT A FLUENCE OF 1.18 mJ/mm^2

saturated caesium vapour pressure of 1.5×10^{-6} torr (108), and demonstrates the strong tendency of caesium to be removed from the gas phase either by reaction or condensation. The ^{55}Fe calibration of the low fluence spectrum, Figure 5.32, showed the 455.5 nm peak to arise from only $\sim$ 150 atoms. However, based on the caesium vapour pressure calculated from the saturation spectrum of 1×10^{-8} torr, and on the unfocused laser volume of $1 \times 1 \times 20$ mm^3, it may readily be deduced that the actual number of caesium atoms irradiated by the beam was 7.1×10^6. Thus at low fluence, the efficiency of resonant ionisation is low (in this case $\sim$ 0.002%).

Power dependence graphs were also obtained from the 455.5 nm peak and from the background. At low fluence (0.8 $\mu J/mm^2$) the gradient of the plot - Figure 5.35 - is 1.95, indicating that the transition is far from saturation. At higher power - Figure 5.36 - ionisation becomes linearly dependent on laser fluence and, at the power levels of Figure 5.34, the dependence is sub-linear and is flattening off. (See Figure 5.37.) The ionisation never quite becomes fluence-independent, however, but continues to rise slowly. This may result from lack of saturation in the wings of the, non-rectangular, laser beam spatial profile; or from a contribution to the resonant ionisation signal arising in the background. Background ionisation is of linear power dependence in the 455 nm region, as is shown in Figure 5.38, and is (as in the glass chambers) attributed to the photo-electric effect.

The minimum number of caesium atoms which could be distinguished in the/

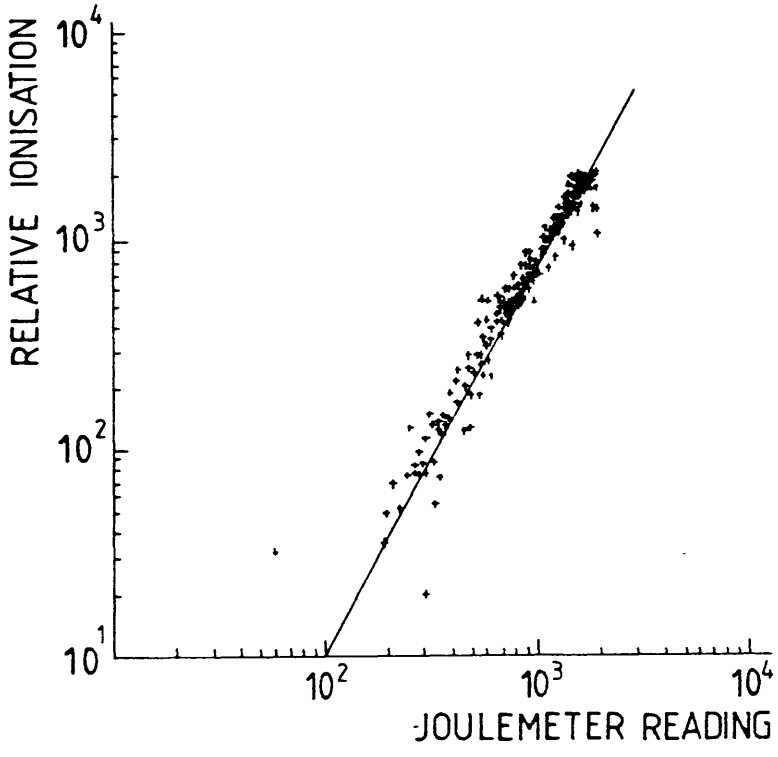

FIG. 5.35: POWER DEPENDENCE GRAPH AT LOW FLUENCE,

455.5 nm

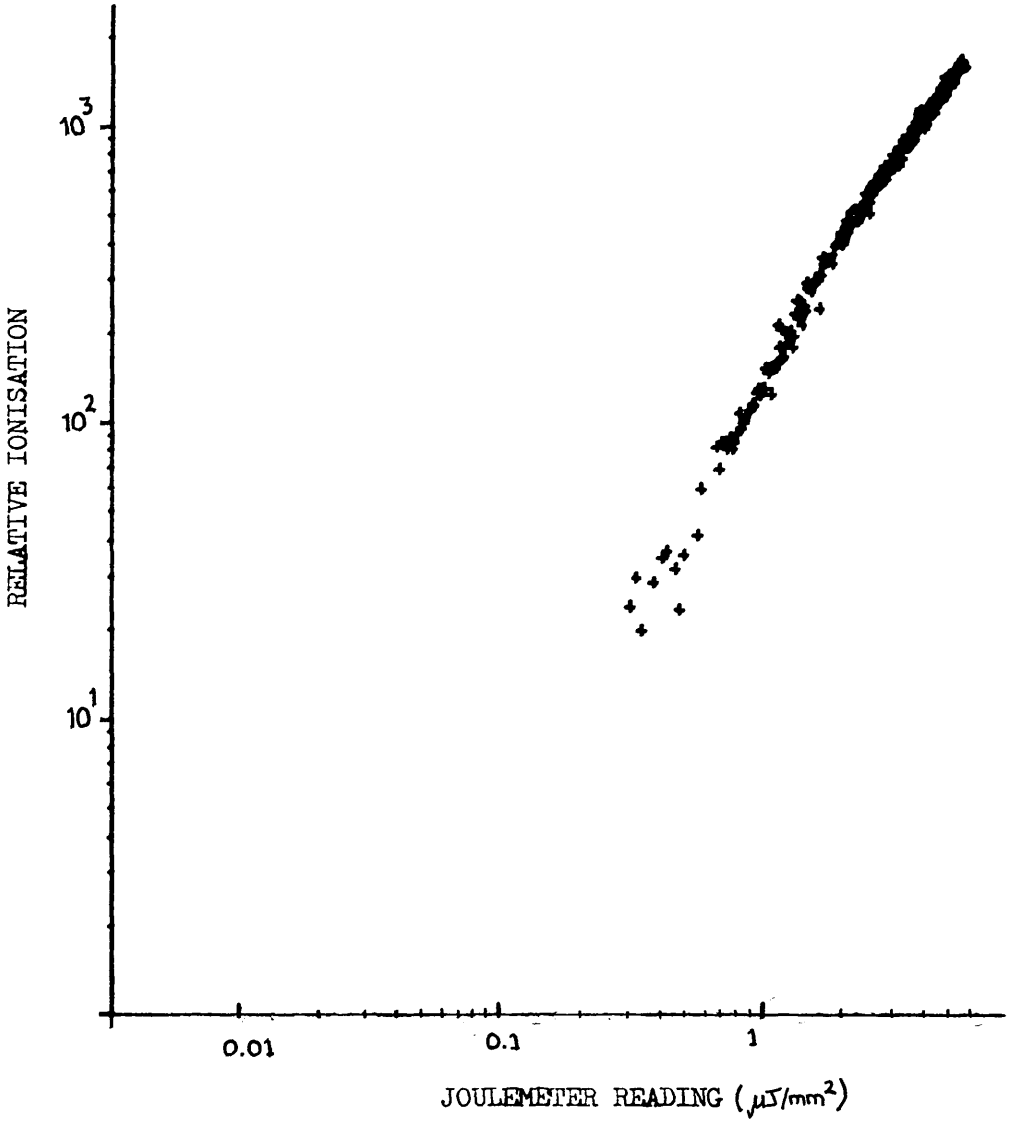

FIG. 5.36: POWER DEPENDENCE GRAPH AT INTERMEDIATE FLUENCE, 455.5 nm

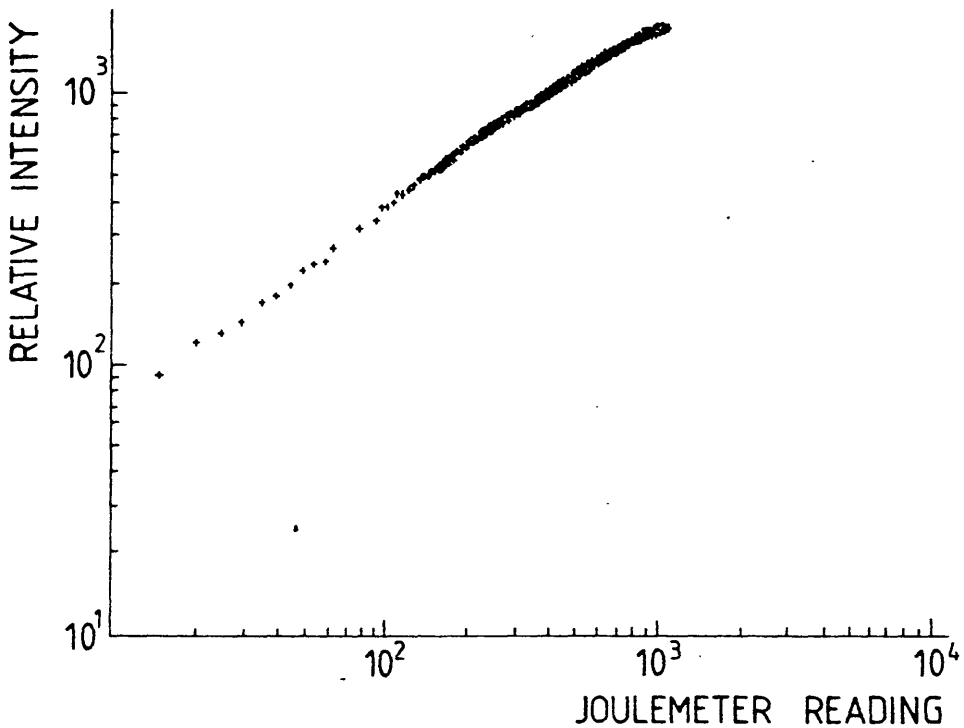

FIG. 5.37: POWER DEPENDENCE GRAPH AT SATURATION, 455.5 nm

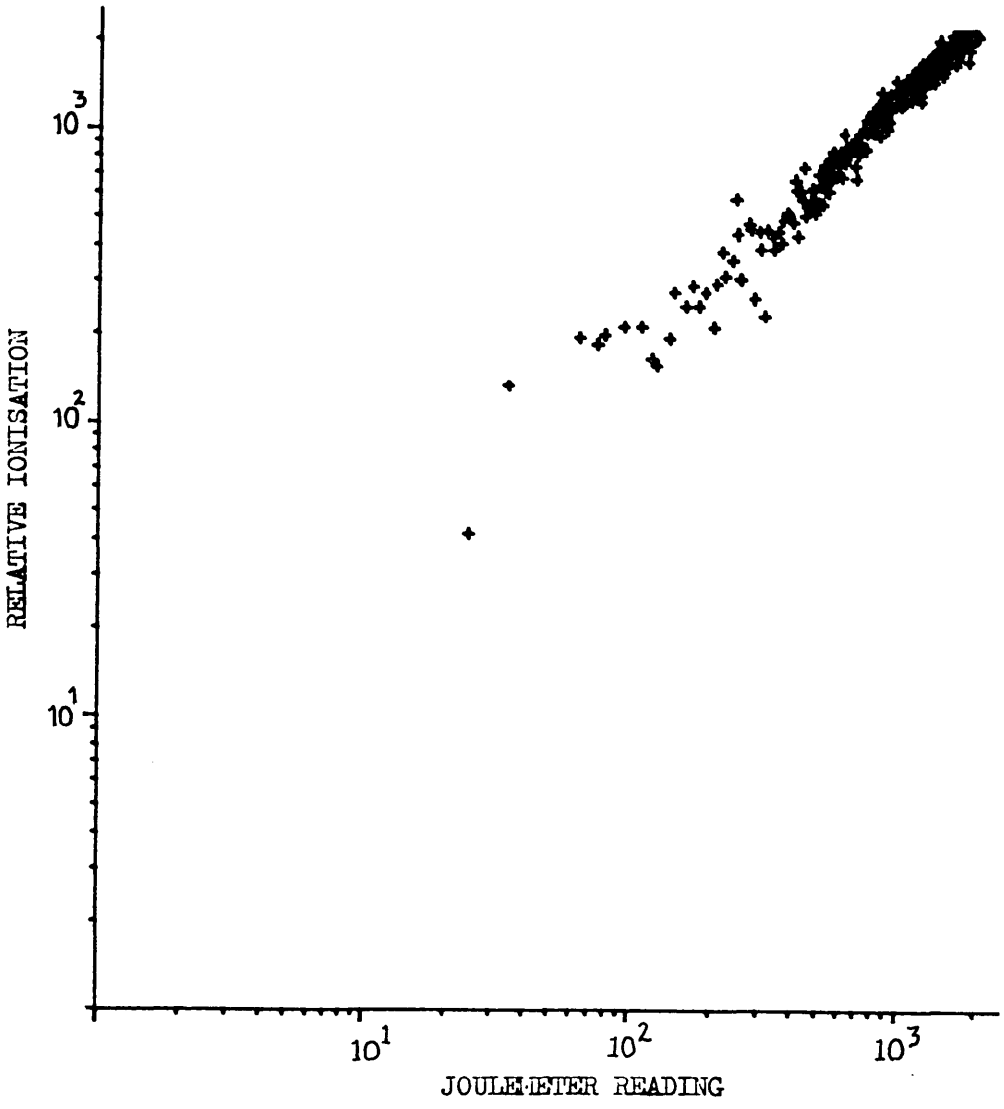

FIG. 5.38: POWER DEPENDENCE GRAPH, BACKGROUND 454.0 nm

the chamber before the resonant signal was swamped by background was ~ 35 ion pairs/$\mu J/mm^2$. This was observed at an incident fluence of 0.4 $\mu J/mm^2$ and the signal to noise (S/N) ratio of the 455.5 nm peak was 2.5:1. It should be stressed that this does not infer a detection limit of $\sim$ 35 caesium atoms since the actual number in the laser volume was $\sim 7 \times 10^6$.

To detect caesium with high efficiency, i.e. approaching 100%, saturation fluence is required. Assuming that power levels necessary for saturation will reproducibly give a background of the magnitude shown in Figure 5.34 and that a resonant signal with S/N of 2:1 can be distinguished, the minimum number of caesium atoms detectable within the focused laser volume at saturation is 7.2×10^3. Although far from the single atom sensitivity of Hurst's early work, this does represent a detection limit of 0.04 ppb (since the number of Ar/CH_4 species within the same volume, from the 30 torr fill pressure, is 1.8×10^{14}). Further, if, as we have observed, the background is in some (at present not well defined) way associated with caesium, reduction of the aomount of caesium present may reduce not only resonant but also non-resonant ionisation, allowing resonant signals from smaller numbers of atoms to be distinguished.

Power broadening is illustrated in Figure 5.39. The three traces of the 455.5 nm peak were recorded at laser fluences of 8 $\mu J/mm^2$, A; 32 $\mu J/mm^2$, B; and 400 $\mu J/mm^2$, C. The observed widths (FWHM) were 0.05, 0.1 and 0.13 nm respectively. A shoulder is apparent in the blue wing of the 455.5 nm peak at around 455.43 nm. This may be a satellite/

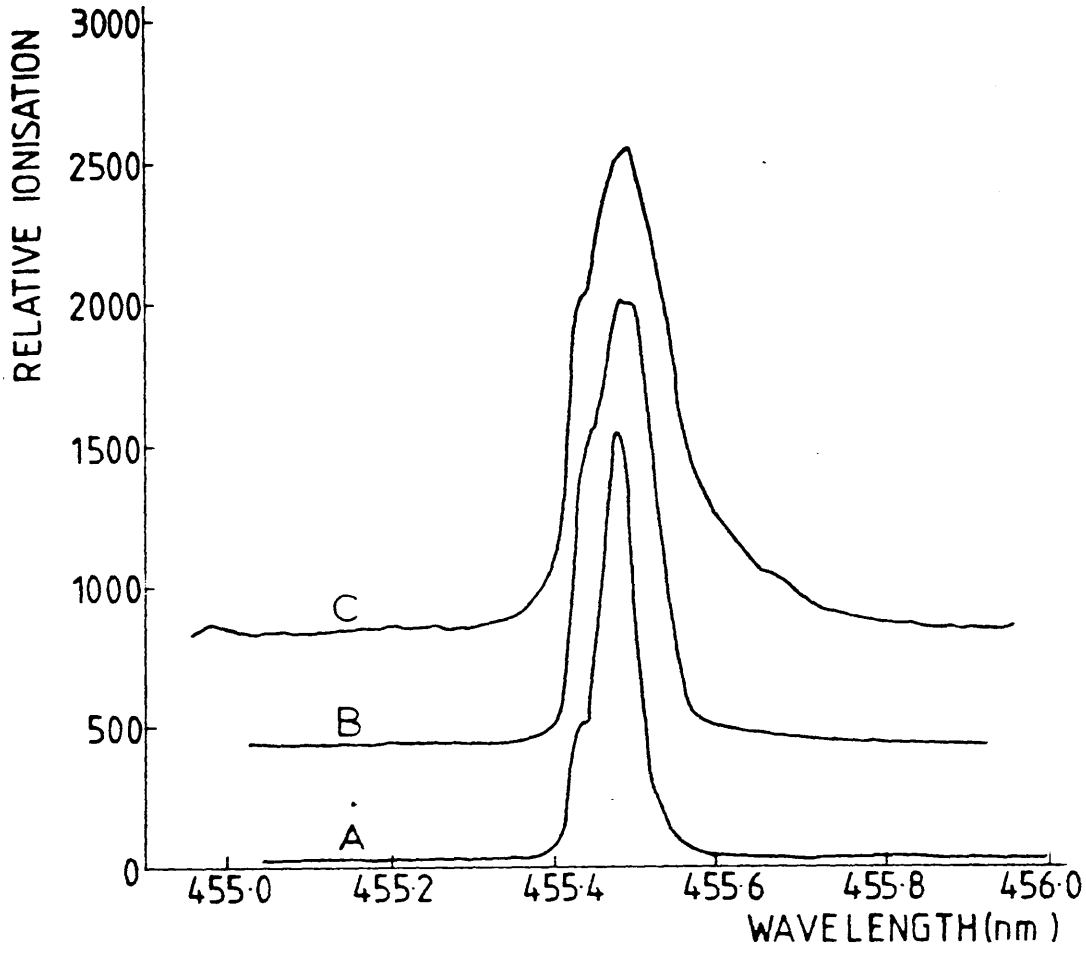

FIG. 5.39: POWER BROADENING

satellite peak resluting from distortion of the caesium 7p levels by argon atoms of the filling gas. Such effects, in the Cs-Ar system, have been studied by Nayfeh (124) who has observed structure in the blue wing of a two-photon resonant transition via the 7p level. However, the satellite reported by that author occurred at 0.4 nm from the line centre, considerably further out than the structure reported here.

V 6s - 8p Transitions

Using the laser dye BBQ, the $^2 6s_{\frac{1}{2}} \rightarrow {}^2 8p_{\frac{3}{2}}$ and $^2 6s_{\frac{1}{2}} \rightarrow {}^2 8p_{\frac{1}{2}}$ transitions were observed at the expected wavelengths of 387.7 and 388.9 nm (122). Figure 5.310 shows a spectrum recorded at a laser fluence of 23.8 $\mu J/mm^2$. The number of ion pairs contributing to the ionisation at 387.7 nm was $\sim 10^4$. The S/N ratio of the 387.7 nm transition was 8:1 and that of the 388.9 nm peak 3:1. The ratio of the peak heights is 4:1. Since, to the knowledge of the author, values of the ionisation cross sections from the caesium 8p levels have not been reported, this ratio could not be ratified by comparison with the literature.

Figure 5.311 is a spectrum recorded at close to saturation fluence. It was found impossible to produce sufficient power from the BBQ dye to actually saturate the two-photon transitions. The laser fluence used was 7 mJ/mm^2, at which considerable power broadening is apparent. In order to obtain the data shown in Figure 5.311 without saturating the ADC (whose maximum acceptable signal is 2V), the gain of the proportional counter had to be reduced, making accurate/

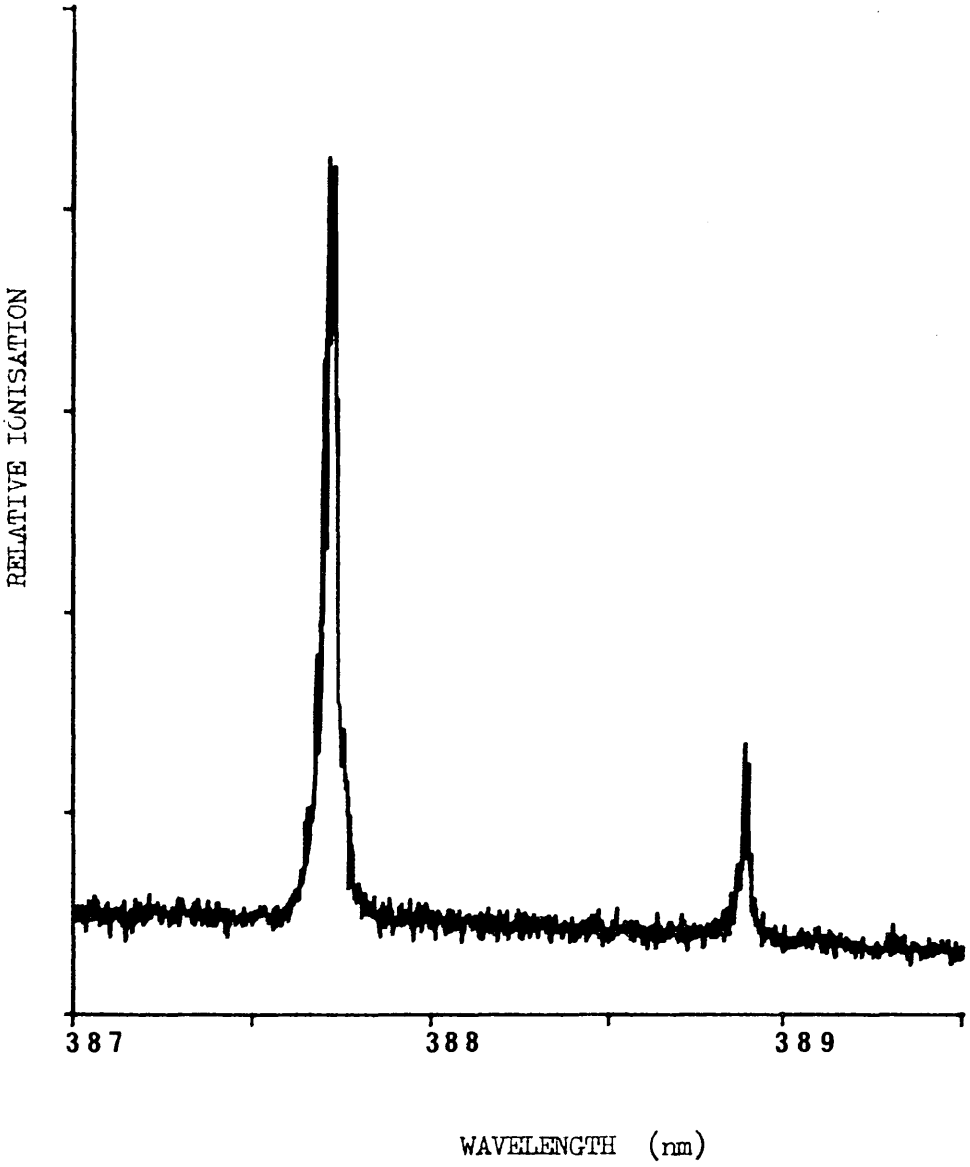

FIG. 5.310: 6s - 8p TRANSITIONS AT A FLUENCE OF 23.8 $\mu J/mm^2$

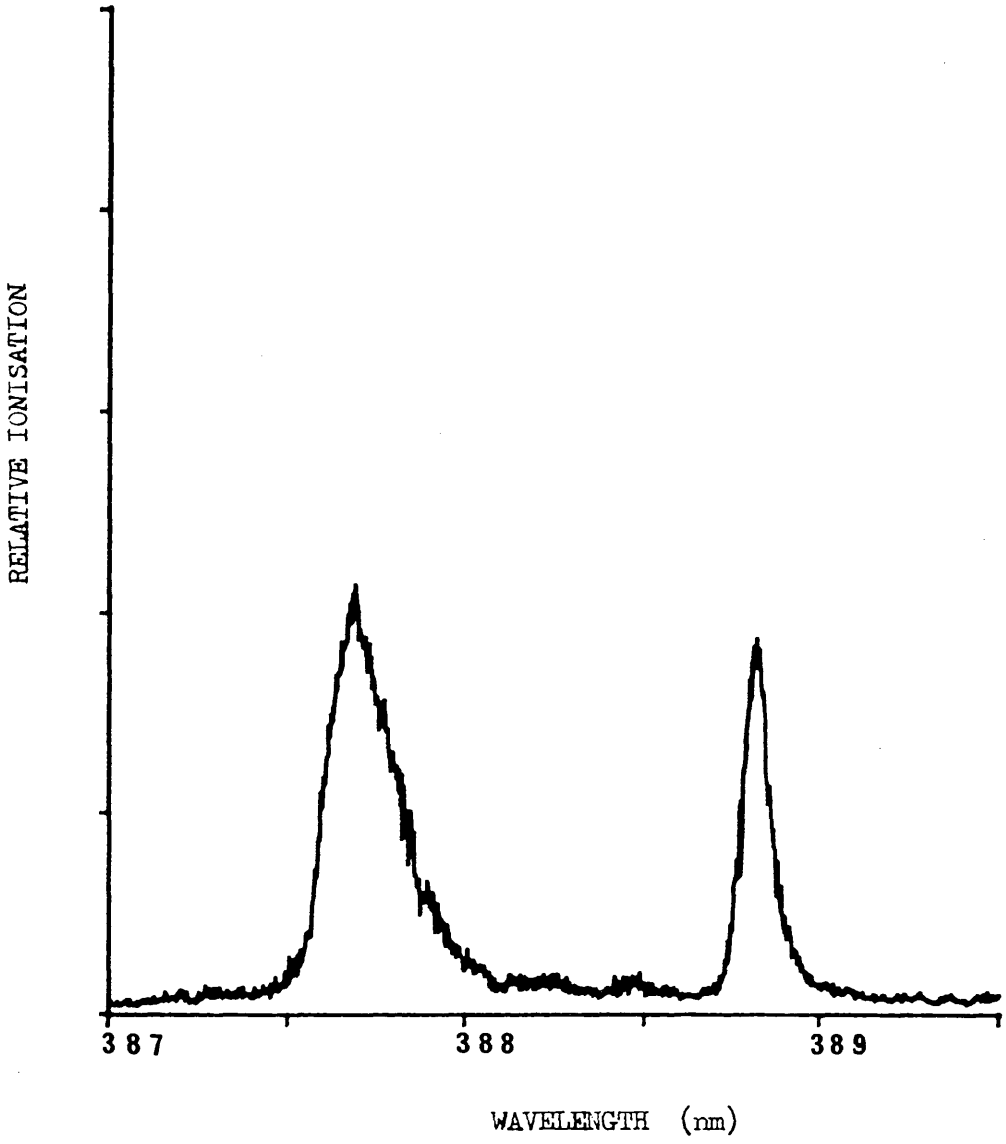

FIG. 5.311: 6s - 8p TRANSITIONS AT A FLUENCE OF 7 mJ/mm^2

accurate observation of the ^{55}Fe calibration pulses impossible. In order to calibrate the (near) saturation spectrum, the ionisation from a constant fluence laser was recorded with a variety of voltages applied to the central wire of the counter. The resulting gas gain curve was used to extrapolate measured values of ^{55}Fe pulse height to lower voltage settings. By this means, it was calculated that 4×10^4 caesium atoms within the focused laser volume contributed to ionisation at 387.7 nm in Figure 5.311. This value is slightly less than that obtained from the saturation spectrum at 455.5 nm, reflecting the fact that insufficient fluence could be obtained from the laser to fully saturate the 6s → 8p transitions.

Power dependence curves were obtained which showed that ionisation at 387.7 nm was quadratically dependent on fluence at low power, i.e. below ~ 6 $\mu J/mm^2$, where deviation from quadratic behaviour became apparent. See Figure 5.312. At the maximum power available (7 mJ/mm^2) the power dependence curve - shown in Figure 5.313 - is sub-linear but does not quite flatten off. This is to be expected since the transition is not saturated (although, for the reasons discussed in section IV of this Chapter, even once saturation is achieved, background or laser profile effects may prevent observed ionisation from becoming fluence independent). Background at 386 nm is at most fluences of linear power dependence, as shown in Figure 5.314. Unlike the situation at 455 nm, however, there is some slight indication that the background does not arise from photoelectrons: at low fluence, a greater than linear power dependence is apparent (suggesting a two-photon process, partially saturated, is operating).

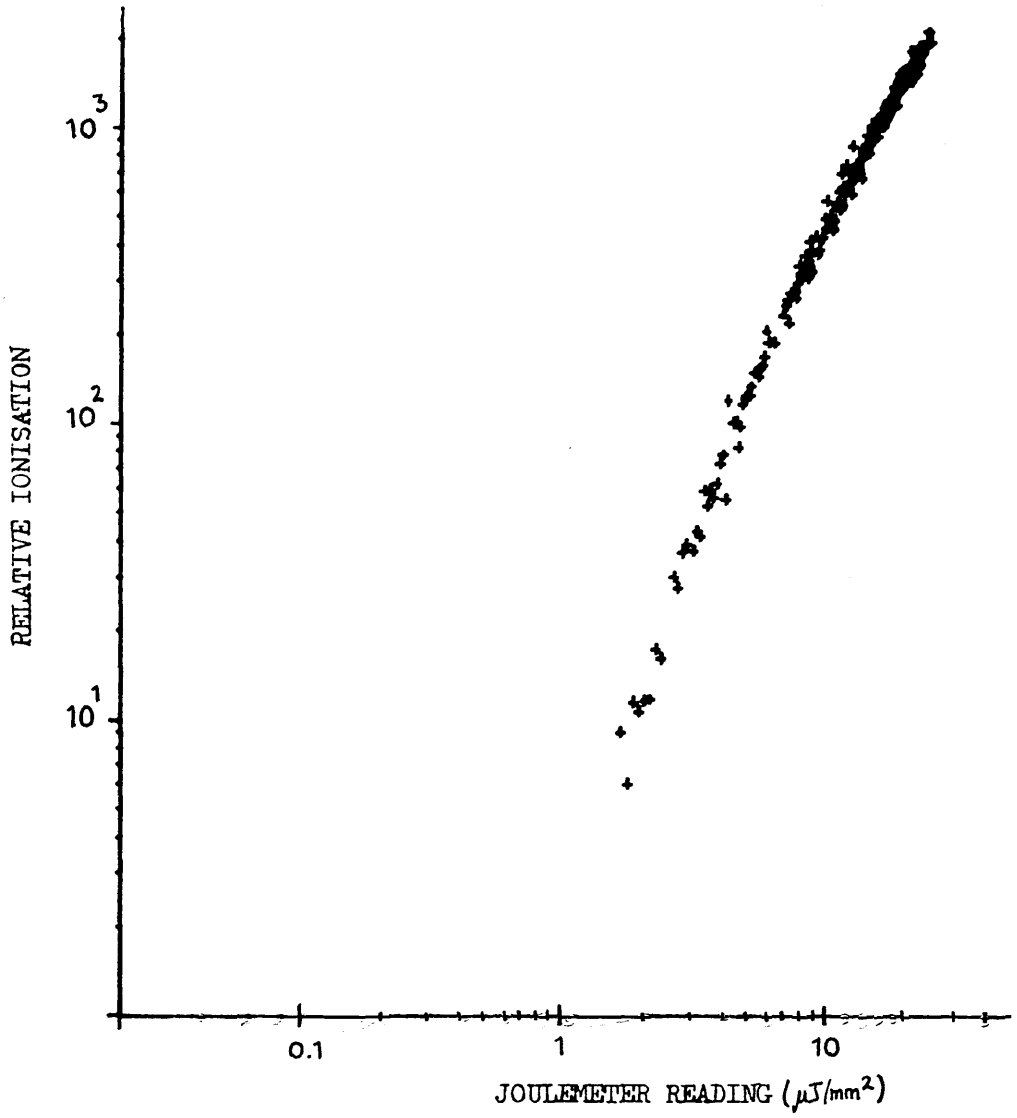

FIG. 5.312: POWER DEPENDENCE GRAPH AT LOW FLUENCE,

387.7 nm

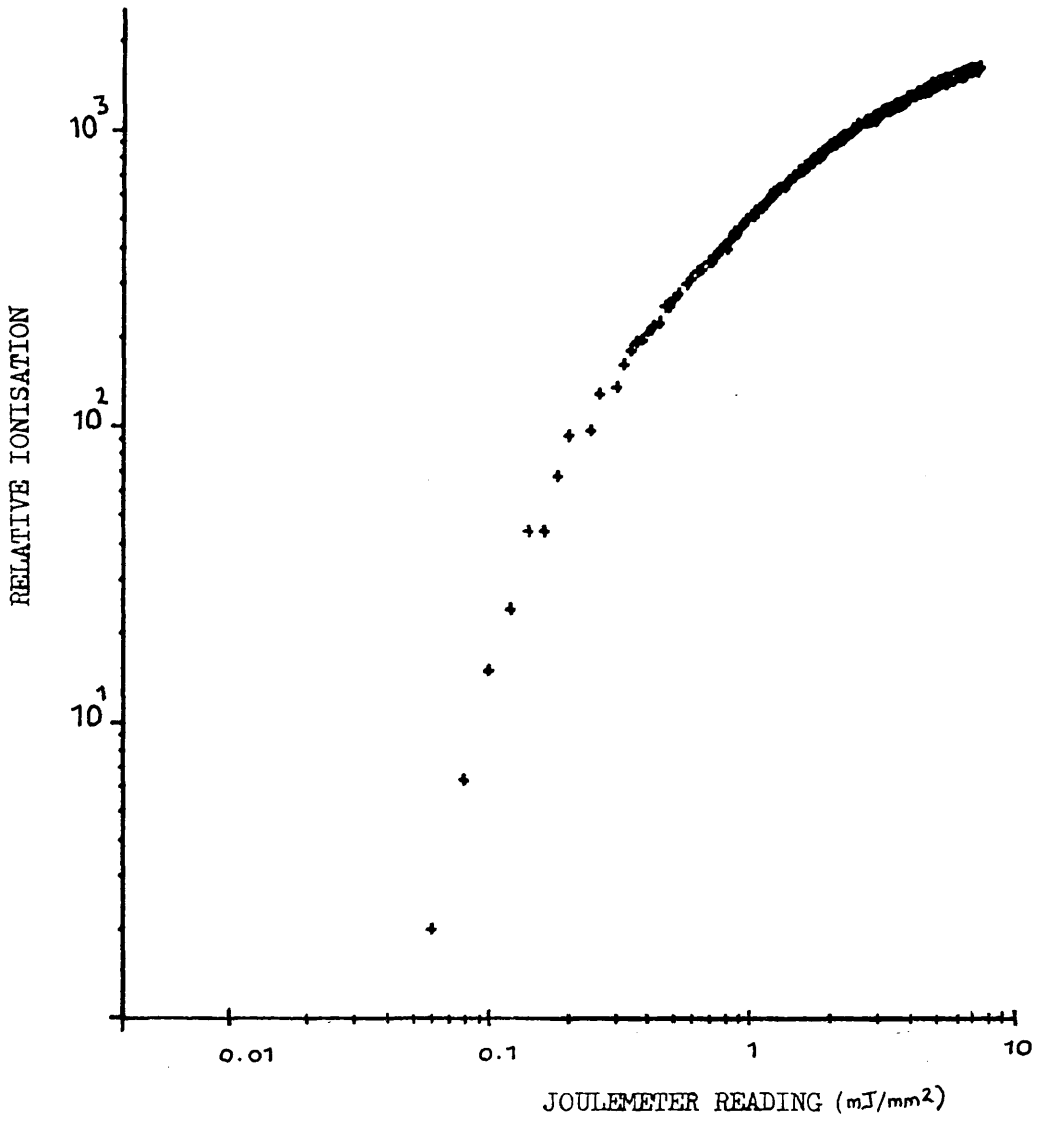

FIG. 5.313: POWER DEPENDENCE GRAPH APPROACHING SATURATION,

387.7 nm

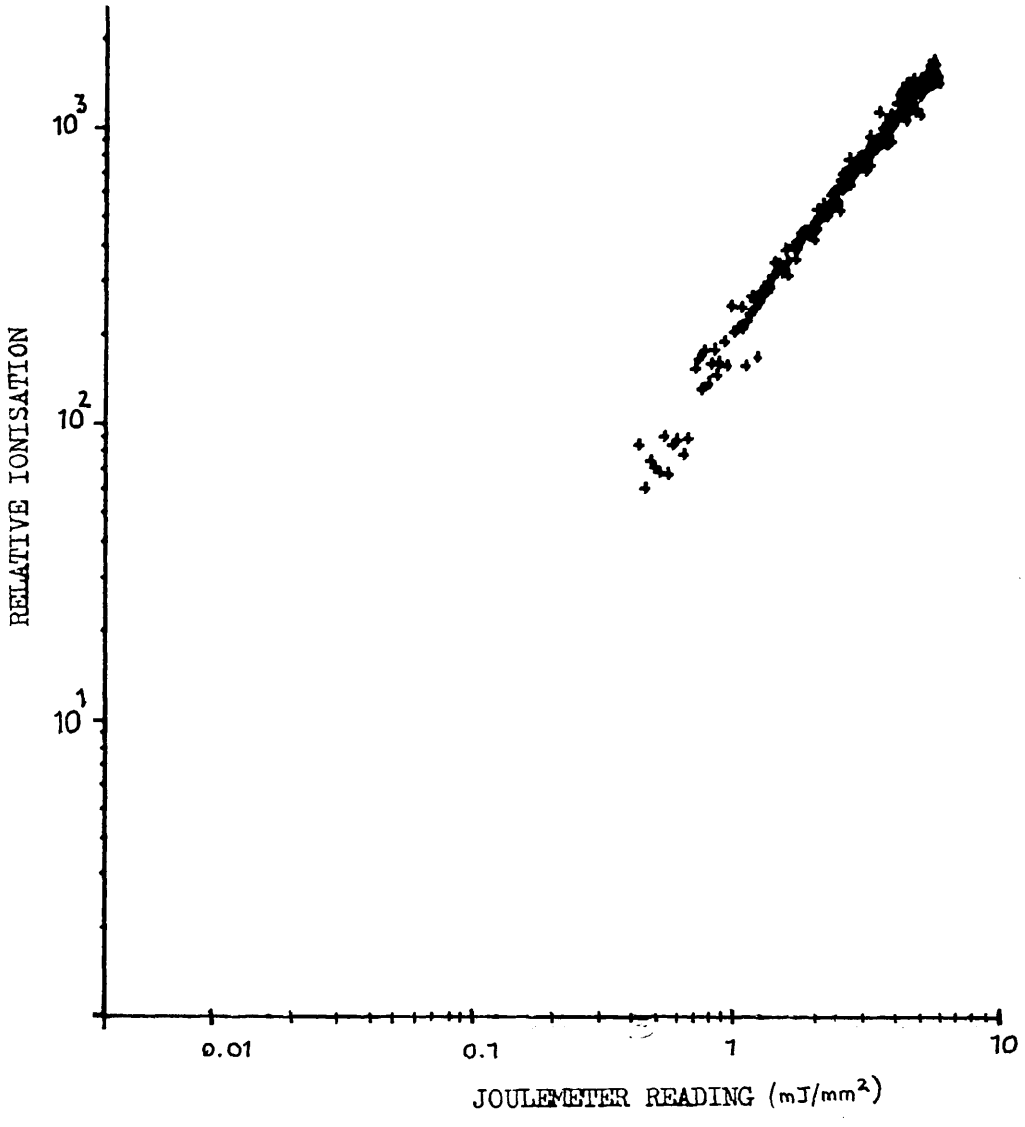

FIG. 5.314: POWER DEPENDENCE GRAPH, BACKGROUND, 386.0 nm

Figure 5.315 shows a spectrum recorded at low laser fluence (1.19 $\mu J/mm^2$), where around 130 ion pairs contribute to the $6s_{\frac{1}{2}} - 8p_{\frac{3}{2}}$ peak intensity. The 387.7 nm transition has a S/N ratio of 3:1 whereas the 388.9 nm peak can scarcely be distinguished from the background.

VI 6s - 9p Transitions

Using the laser dye PBD, the $^2 6s_{\frac{1}{2}} \rightarrow {}^2 9p_{\frac{3}{2}}$ and $^2 6s_{\frac{1}{2}} \rightarrow {}^2 9p_{\frac{1}{2}}$ transitions were observed at 361.2 and 361.9 nm, close to their generally accepted wavelengths (122), within the error of the dye laser wavelength readout. Figure 5.316 shows a spectrum obtained at a laser fluence of 155 $\mu J/mm^2$. Around 3.6×10^4 atoms within the unfocused laser volume contributed to the 361.2 nm peak ionisation. Due to the low gas gain of the counter used to record the data, most background wavelength settings gave ionisation too small to be registered by the computer data acquisition system. The peak ratio 361.2:361.9 nm is around 3.4:1. Again, to the knowledge of the author, comparable literature values are not available.

With the PBD dye, insufficient laser fluence could be obtained to approach saturation of the 6s → 9p transitions. A spectrum recorded at the maximum fluence attained - 8.5 mJ/mm^2 - is shown in Figure 5.317. The peak ratio is approximately 5:4. The number of ion pairs contributing to the 361.2 nm ionisation is calculated to be 2.72×10^4, more than a factor of two away from the saturation value derived from the $6s_{\frac{1}{2}} - 7p_{\frac{3}{2}}$ transition.

Power/

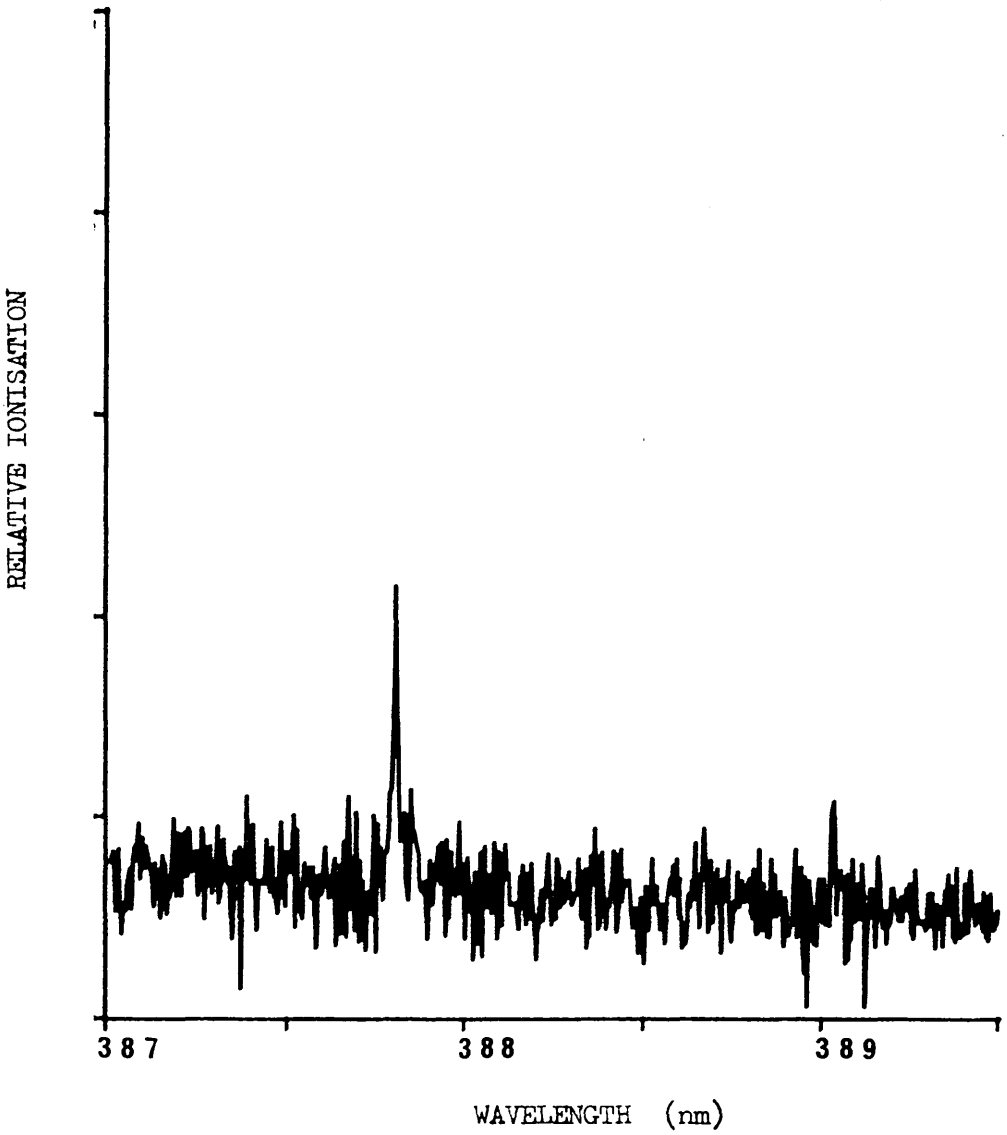

FIG. 5.315: 6s - 8p TRANSITIONS AT A FLUENCE OF 1.19 $\mu J/mm^2$

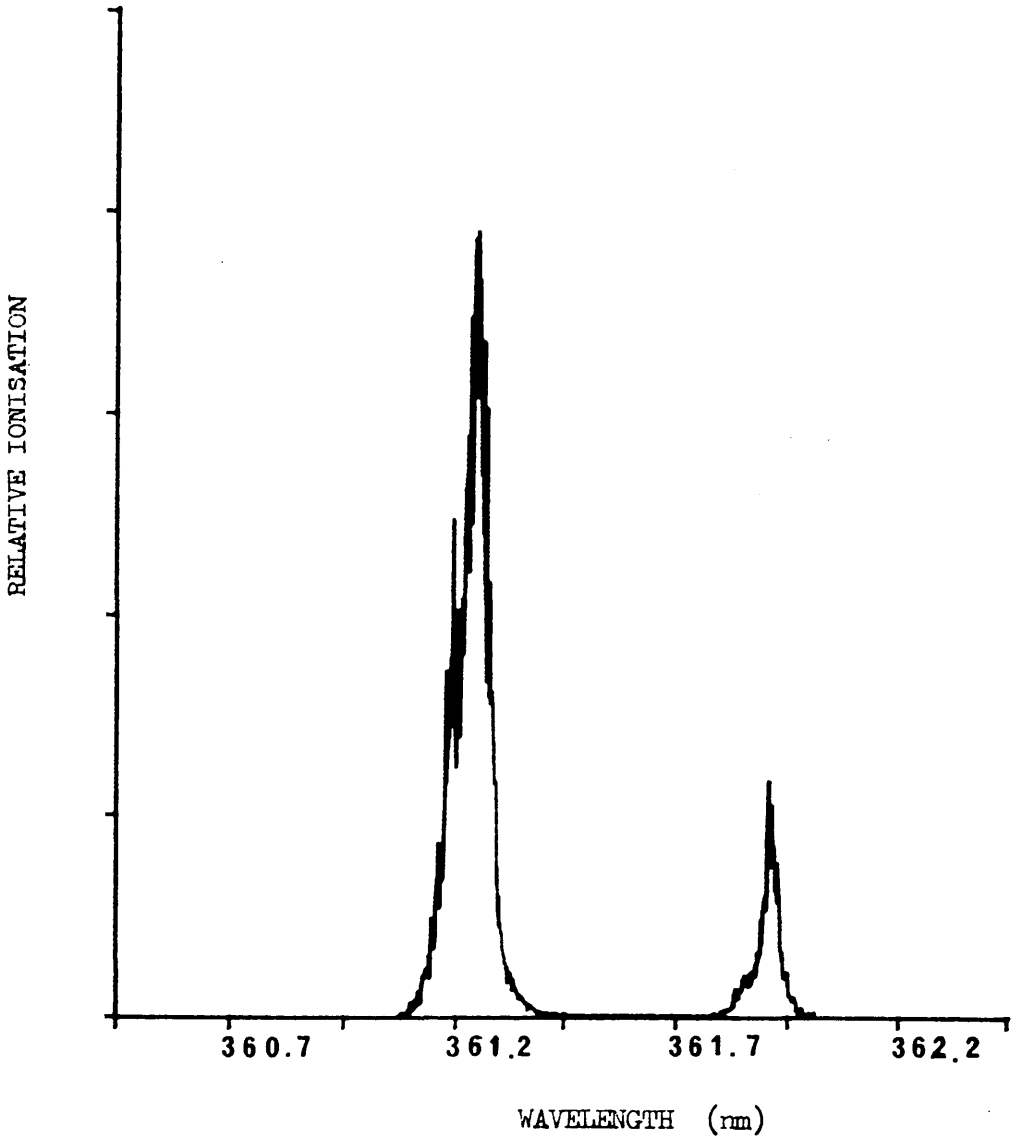

FIG. 5.316: 6s - 9p TRANSITIONS AT A FLUENCE OF 155 $\mu J/mm^2$

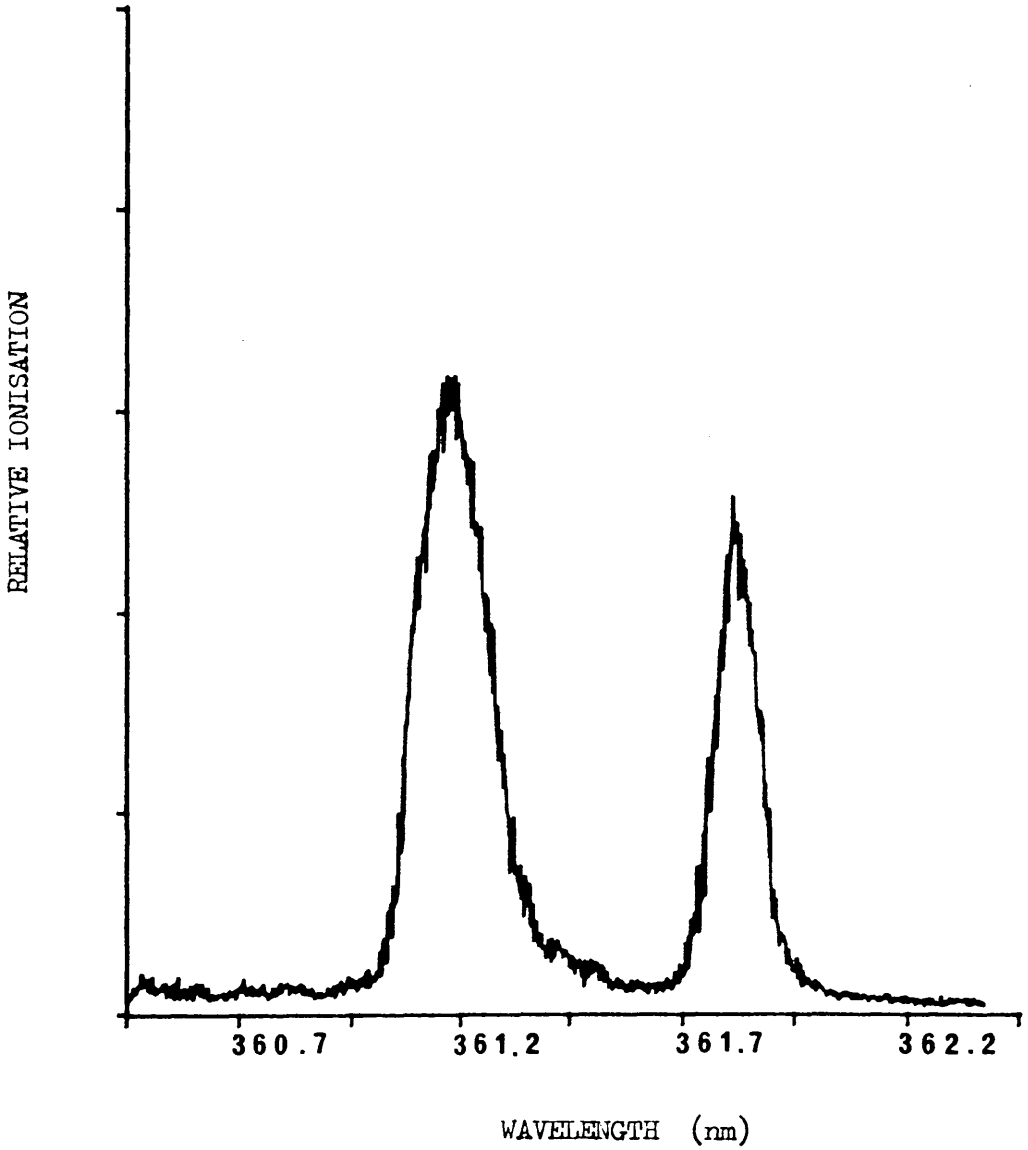

FIG. 5.317: 6s - 9p TRANSITIONS AT A FLUENCE OF 8.5 mJ/mm^2

Power dependence curves were obtained which showed that the ionisation was a quadratic function of laser fluence at 361.2 nm up to around 10 $\mu J/mm^2$. The dependence was then linear to $\sim$ 5.6 mJ/mm^2, after which it became sub-linear indicating some saturation of the upper step of the two-photon resonance ionisation process. Figure 5.318 illustrates the power dependence of the $6s_{\frac{1}{2}} \rightarrow 9p_{\frac{3}{2}}$ transition.

The power dependence of the background at 360 nm is shown in Figure 5.319. The plot is linear to around 2 mJ/mm^2 when it becomes sub-linear, indicating the occurrence of saturation effects. Data shown in the background power dependence graph were obtained at higher gas gain than those shown in the resonant plot (Figure 5.318).

Comparing two-photon resonance ionisation via the 7p, 8p and 9p levels, it was found that greater incident laser fluence was required to saturate the process the higher the p level principal quantum number. Saturation of the first step of the two-photon process showed a similar np dependence, with power dependence graphs at 455.5, 387.7 and 361.2 nm becoming sub-quadratic at $\sim$ 1, 6 and 10 $\mu J/mm^2$ respectively. This indicates that the single photon absorption cross section is smaller the higher the p level to which the atom is raised. Since absorption cross section and transition probability are directly proportional, the above conclusion is concordant with the published transition probabilities for the 6s - 7p, 8p and 9p absorptions of 1.8×10^6, 0.38×10^6 and 0.15×10^6 s^{-1} respectively (128).

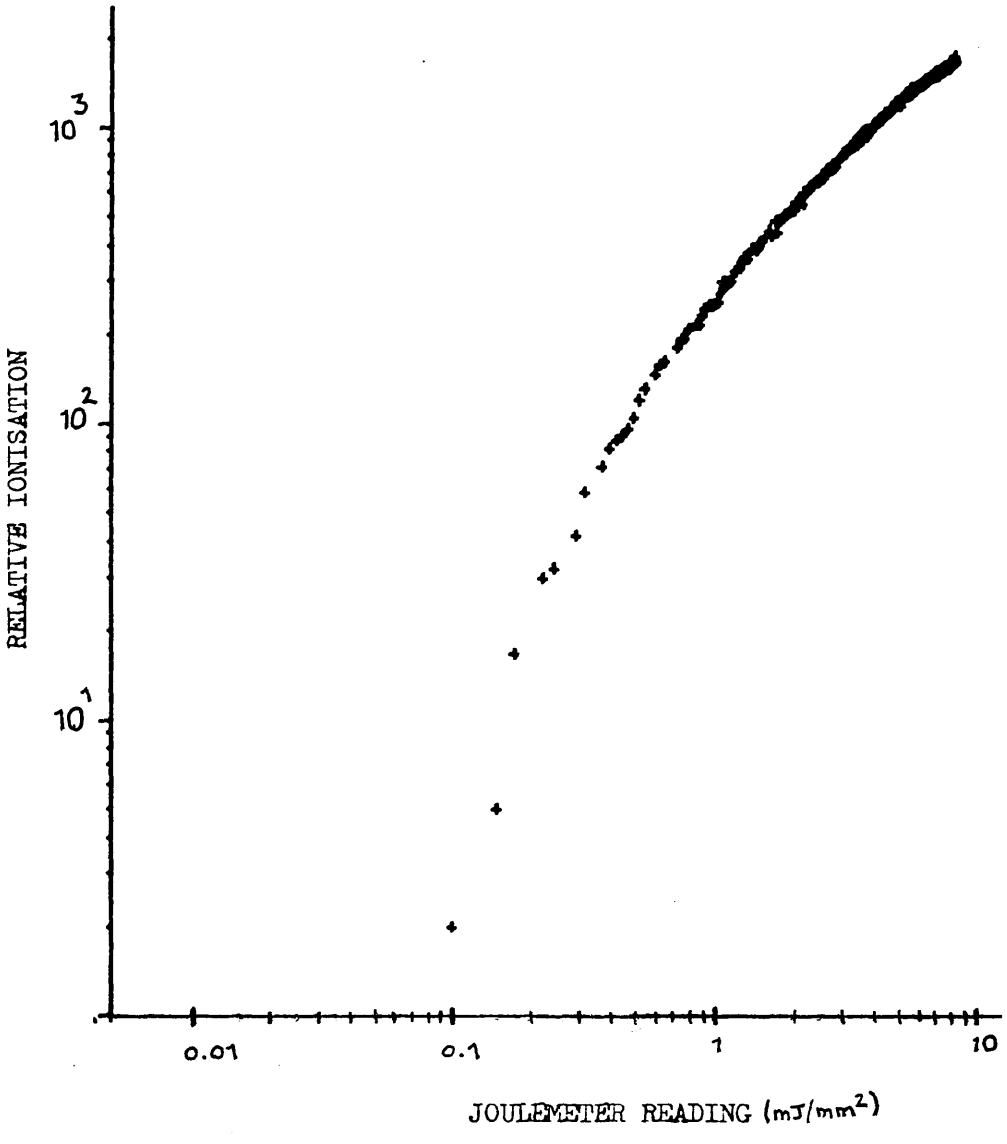

FIG. 5.318: POWER DEPENDENCE GRAPH, 361.2 nm

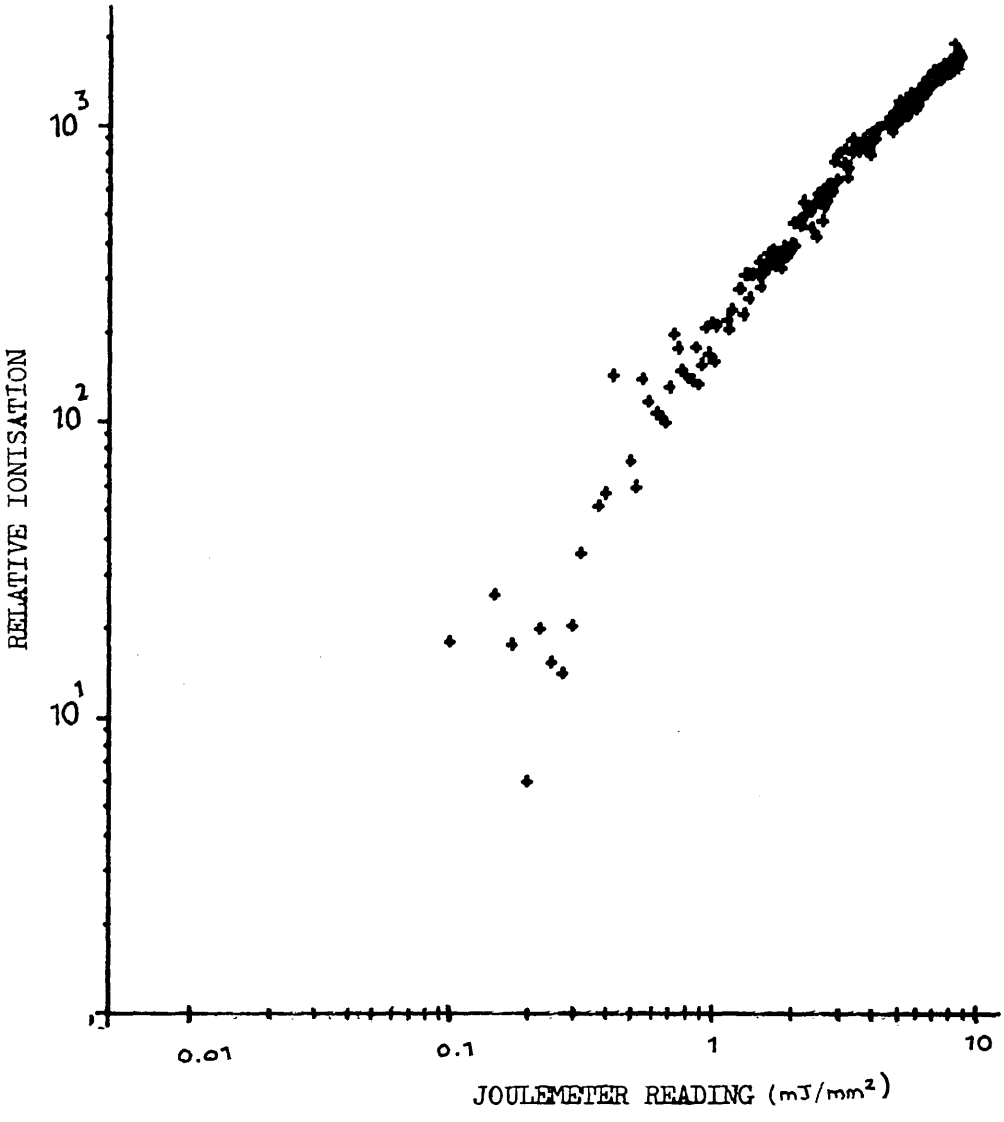

FIG. 5.319: POWER DEPENDENCE GRAPH, BACKGROUND, 360.0 nm

Although not the original purpose of the experimental work on caesium, it is interesting, from the data obtained, to calculate approximate two-photon resonant ionisation cross sections for the 455.5 and 459.3 nm transitions. The two photon ionisation cross section σ_2 is given by:

$$\sigma_2 = \sigma_1 \sigma_I \tau \qquad \text{---- 35}$$

where the symbols are as defined in Chapter 1

The values of τ are taken from the literature (2) and the quantity $\sigma_1 \sigma_I$ is obtained experimentally from equation 32 which, rearranged, gives:

$$\sigma_1 \sigma_I = \frac{2N_I}{N_0 \phi^2} \qquad \text{---- 36}$$

To ensure that the ionisation was indeed produced by a two photon process at the fluence used to calculate σ_2, power dependence curves were obtained. Data used in the calculation were collected at 0.3 $\mu J/mm^2$, in the quadratic regions of the power dependence curves, and were then normalised to 1 $\mu J/mm^2$. Results are presented in Table 14.

It is immediately apparent that the measured cross sections are considerably smaller than the 10^{-36} - 10^{-38} $cm^4 s$ which would be expected from the typical values of σ_1, σ_I and τ given in Chapter 1, although they are considerably larger than the published non-resonant two photon ionisation cross section of caesium which is $6.7 \pm 1.9 \times 10^{-50}$ $cm^4 s$ (129).

TABLE 14

Two-photon ionisation cross sections for the 6s - 7p resonant transitions

wavelength (nm)	N_I (at 1 $\mu J/mm^2$)	N_0 (atoms)	$\sigma_1 \sigma_I$ (cm^4)	τ (2) (ns)	σ_2 ($cm^4 s$)
455.5	234 ion pairs	7.1×10^6	1.27×10^{-33}	130	1.65×10^{-40}
459.3	103 ion pairs	7.1×10^6	5.58×10^{-34}	150	8.37×10^{-41}

Values of σ_2, for comparison with the above, can be inferred from the early literature on RIS. Hurst quotes values of σ_I, at 455.5 and 459.3 nm respectively, of 8.8×10^{-18} and 6.2×10^{-18} cm^2, and gives values of the transition probabilities (also called transition rates) for the $6s_{\frac{1}{2}} \rightarrow 7p_{\frac{3}{2}}$ and $6s_{\frac{1}{2}} \rightarrow 7p_{\frac{1}{2}}$ processes, of 1.67×10^6 and 0.694×10^6 s^{-1} respectively. From the given transition probabilities, σ_1 may be deduced from the relationship

$$W = \sigma_1 \Phi \qquad \text{---- 37}$$

where W is the transition probability.

Using the flux appropriate to the present experiment (100 J/mm^2s), the results presented in Table 15 were obtained.

TABLE 15

Two-photon ionisation cross-sections (after Hurst (2,12))

wavelength (nm)	σ_I (cm^2)	σ_1 (cm^2)	τ (ns)	σ_2 (cm^4s)
455.5	8.8×10^{-18}	7.33×10^{-17}	130	8.39×10^{-41}
459.3	6.2×10^{-18}	3.04×10^{-17}	150	2.83×10^{-41}

Thus Hurst's values too lead to two photon ionisation cross sections considerably smaller than expected.

Errors in the present experiment arise from lack of precision in measuring/

measuring the parameters N_I, N_0 and ϕ . The random (statistical) error (associated with accuracy in reading joulemeter and ^{55}Fe pulse heights from the oscilloscope) is estimated at $\sim$ 20% and the systematic error (arising from uncertainties in reproducibility of laser beam quality from day to day and from variations in caesium partial pressure within the counter) at approximately a factor of two.

The low value of σ_2 obtained from the experiment is attributed to the relative line widths of the caesium transitions and the laser pulse. Calculations have shown that the collision and Doppler broadened 455.5 nm caesium transition has linewidth of $\sim 5 \times 10^{-4}$ nm whereas the laser linewidth is $\sim 5 \times 10^{-2}$ nm. Thus most of the photons contributing to the fluence measured by the joulemeter are not, in fact, resonant with the caesium transition, and the value of the denominator in equation 36 (used to calculate σ_2) is therefore exaggerated.

It is difficult to determine, without precise knowledge of the energy profiles of the transition and of the laser, the exact degree of overlap between the two. However, if it is assumed that 1 - 10% of photons are resonant, cross sections within the range predicted in Chapter 1 may be obtained.

If RIS experiments of the above type are to be used specifically to determine two photon resonant ionisation cross sections it will be necessary either to carry out detailed mathematical analyses to determine the energy overlap between the photons in the laser beam and/

and the resonant state, or to reduce the laser bandwidth to ensure that most incident photons are on resonance. A first step towards this type of study in Glasgow would be the installation of the prism beam expander within the dye laser cavity to reduce bandwidth to 0.003 nm.

VII 6s - Rydberg State Transitions

By frequency doubling the output of the DCM dye and scanning in the ultraviolet region of the spectrum using the modified INRAD harmonic generator, a large number of sharp resonances close to the caesium single photon absorption edge at 318.4 nm (130) could be observed. These are attributed to two photon ionisation via Rydberg states.

Rydberg levels are high energy, s-like orbitals close to the continuum. Both excitation and photoionisation cross sections of Rydberg levels decrease rapidly with increased principal quantum number: the excitation cross section being proportional to $^1/_n{}^3$ and the photoionisation cross section to $^1/_n{}^5$ (130). The $^1/_n{}^3$ dependence of σ_1 can be confirmed by either a) plotting a graph of published transition probabilities (6s-p) (128) versus $^1/_n{}^3$ and confirming that it is linear for $n > 16$; or b) plotting transition probability versus n on log-log graph paper and confirming that the gradient of the resulting line is close to -3. From equation 35, the two photon ionisation cross sections for resonant transitions via Rydberg states is therefore expected to be a function of $^1/_n{}^8$ (in the absence of saturation). Since Rydberg levels are long lived and Rydberg orbits large (131), atoms/

atoms in Rydberg levels are prone to collisional processes and it is this phenomenon that is thought responsible for the observed enhancement in resonance ionisation from levels close to the continuum. See Figure 5.320.

An increase in the density of the observed resonant transitions as the wavelength is varied from 323 - 319 nm is apparent, which reflects the increased density of atomic levels as the continuum is approached. The intensities of the transitions increase from 323 - 319.7 nm and then decrease to the continuum. By comparison of the wavelength separation between adjacent peaks with literature values of the separation between p levels (122) it was possible to allocate the peaks to particular transitions; to determine that the maximum ionisation (2.95×10^4 ion pairs) occurs at 32p, and to calibrate the dye laser readout (giving the lower scale on the figure). An expansion of part of Figure 5.320 is shown in Figure 5.321, illustrating the fact that Rydberg levels up to n = 48 can be resolved.

As stated above, the enhancement of ionisation between 323 nm and the continuum is attributed to collisional ionisation of caesium Rydberg levels. Collisional ionisation is only feasible when collisions can transfer enough energy to the caesium atoms to raise them above E_c. As the energy separation between the resonantly populated Rydberg level and the continuum decreases (i.e. as n increases) a larger fraction of the atoms in the Maxwell-Boltzmann distribution of room temperature kinetic energies can transfer the required amount of energy to excited caesium atoms for ionisation to take place, i.e. a larger fraction of the collisions lead to ion pair formation.

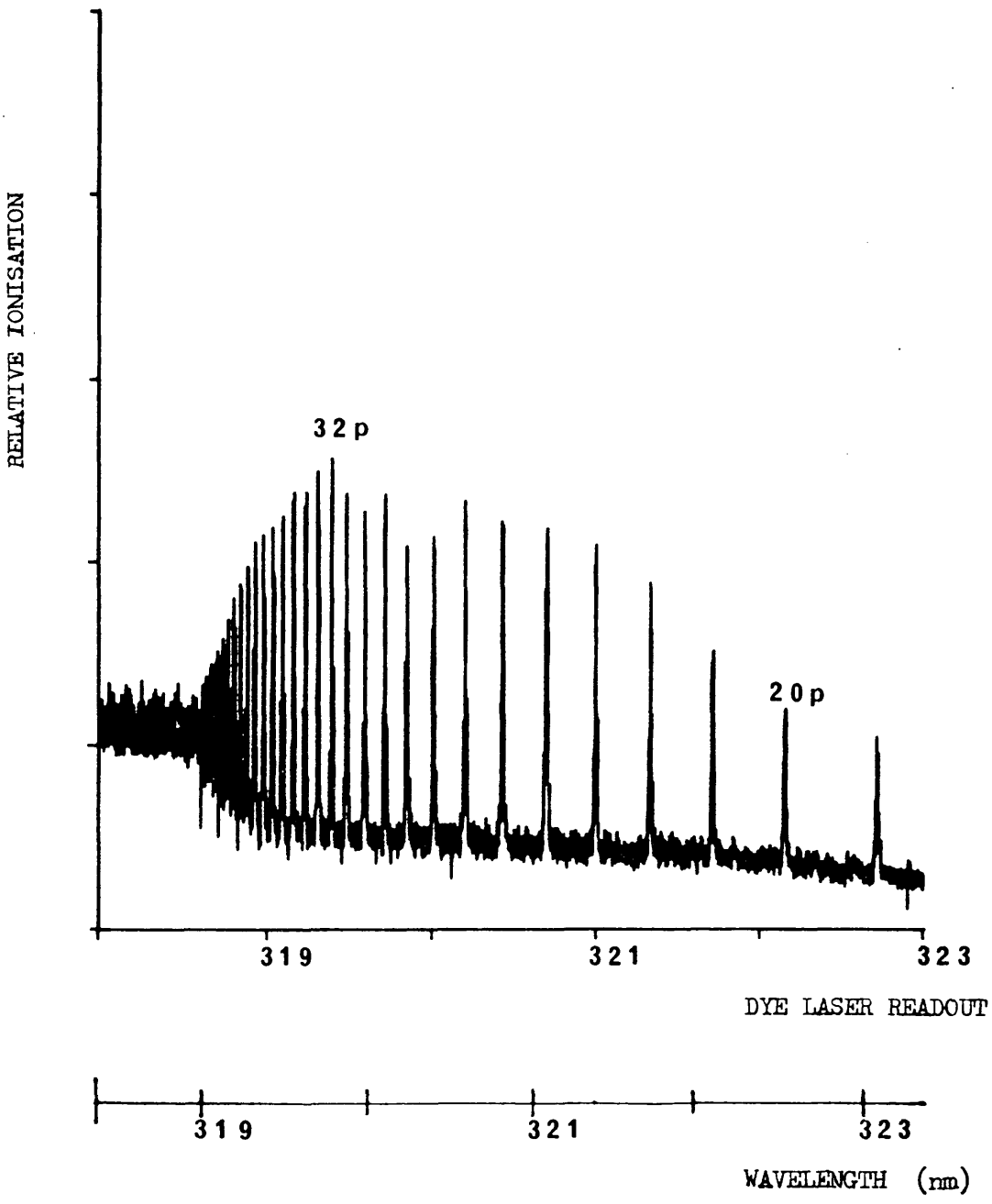

FIG. 5.320: 6s - Rydberg TRANSITIONS 318 - 323 nm

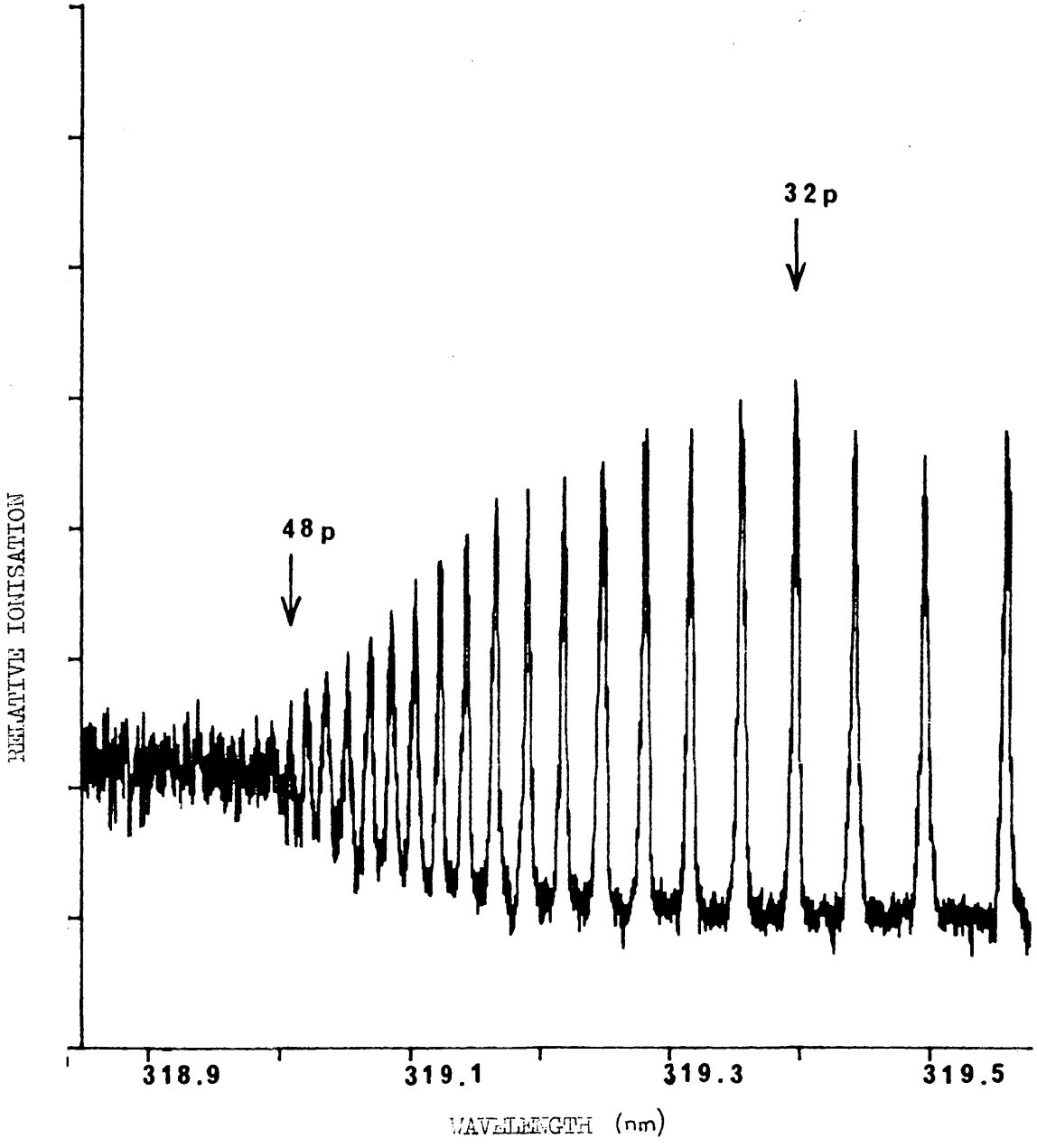

FIG. 5.321: 6s - HIGH RYDBERG TRANSITIONS

Thus, ionisation increases with n. Eventually a condition is reached where every atom reaching the Rydberg level is collisonally ionised. This is termed collisional saturation. After this point, the limiting factor in ion pair production is the rate at which the Rydberg level is populated from the ground state. From theory, this is expected to decrease as $^1/_{n^3}$ (131).

A plot of peak height (read from Figure 5.321) versus $^1/_{n^3}$ was found to be linear for $n \geq 38$, confirming the theoretical prediction. A log-log plot of peak height versus n was of gradient -3.2 for $n \geq 38$ and of gradient -1.5 for $32 < n < 38$. The smaller gradient obtained for the lower Rydberg levels (n=32 - 37) is interpreted as arising from a saturation effect. The laser is of sufficient fluence to partially saturate the excitation to the lower Rydberg levels, whereas the higher Rydberg levels cannot be saturated and thus the intensity of the resonant transitions via the higher levels only decreases in accordance with theory.

A relatively large variation in the background ionisation is apparent in Figures 5.320 and 5.321. At first this was thought to be due to etaloning - a process which had previously been observed in the caesium counter - but, on closer inspection, the variation was found to be irregular and was attributed to variations in the fluence of the frequency doubled laser.

Collisional enhancement of ionisation during multiphoton ionisation experiments/

experiments has previously been observed by Bushaw and Whitaker whilst studying Rubidium - and similar spectra to Figure 5.320 have been obtained for that element (23). In their work, the above authors used three-photon resonance ionisation with the lower transition ($s \rightarrow p$) strongly saturated. The remaining two photon ionisation process from the $^2 5p_{\frac{3}{2}}$ level, via the high d levels to the continuum is analogous to the two-photon scheme, via high p levels, of the present work. Bushaw and Whitaker attributed the collisional enhancement which they observed to Rb-Kr interactions, by analogy with which, Cs-Ar interactions are thought responsible for the effect reported here. A possible contribution from Cs(Rydberg level) - Cs(ground state) collisions cannot be excluded but it is thought that such events would be much less probable than Cs-Ar collisions since the partial pressure of argon in the counter is $> 10^9$ times that of caesium. It is interesting to note that the decrease in ionisation towards the continuum observed for rubidium (23) was also a function of $^1/_{n^3}$ (as is reported here for caesium). A log-log plot of peak height versus n (for d levels in the range $20 < n < 29$), using values taken from reference 23, is of gradient -2.83.

Were it possible to remove the 6s-Rydberg structure from Figure 5.320, the remaining plot would show clearly the caesium single photon edge at 319.1 nm. This appears at longer wavelength than the nominal value of 318.4 nm which would be calculated from the ionisation potential, due to the fact that the experiment was conducted in the presence of an electric field which could, itself, ionise the highest of the Rydberg levels. The Stark effect was also apparent in the resonant/

resonant caesium transitions, i.e. shifts in wavelength of the peaks with different voltages applied to the counter. An ionisation edge at longer wavelength than that observed under field free conditions has previously been observed for both caesium (130) and rubidium (23), during laser ionisation experiments conducted in the presence of electric fields.

Figure 5.322 is a second scan obtained in the 323 - 319 nm region of the spectrum but differs from Figure 5.320 in that the incident laser fluence was greater and that the red, fundamental, output of the dye laser was allowed to pass through the counter along with the ultraviolet. The fluence used was 6.3 mJ/mm^2 of ultraviolet plus 18.3 mJ/mm^2 of red cf. ~ 1 mJ/mm^2 of ultraviolet used to obtain Figure 5.320. The increased fluence has increased the intensity of the 19p and 20p resonant transitions to close to the same value as that of the collisionally enhanced transitions around 32p. Ionisation intensity is similar from 32p to 38p before dropping towards the continuum (again with approximately $^1/_n 3$ dependence) whereas, in Figure 5.320, an immediate decrease in intensity at $n > 32$ is apparent. This may be due to saturation of the single photon excitation leading to the Rydberg state, up to $\sim$ 38p, in the higher fluence spectrum.

The single photon absorption edge of caesium is visible in Figure 5.322. From the distance labelled X, the single photon ionisation cross section may be calculated using the relation:

$$\sigma_1 = \frac{N_I}{N_0 \phi} \qquad \text{---- 38}$$

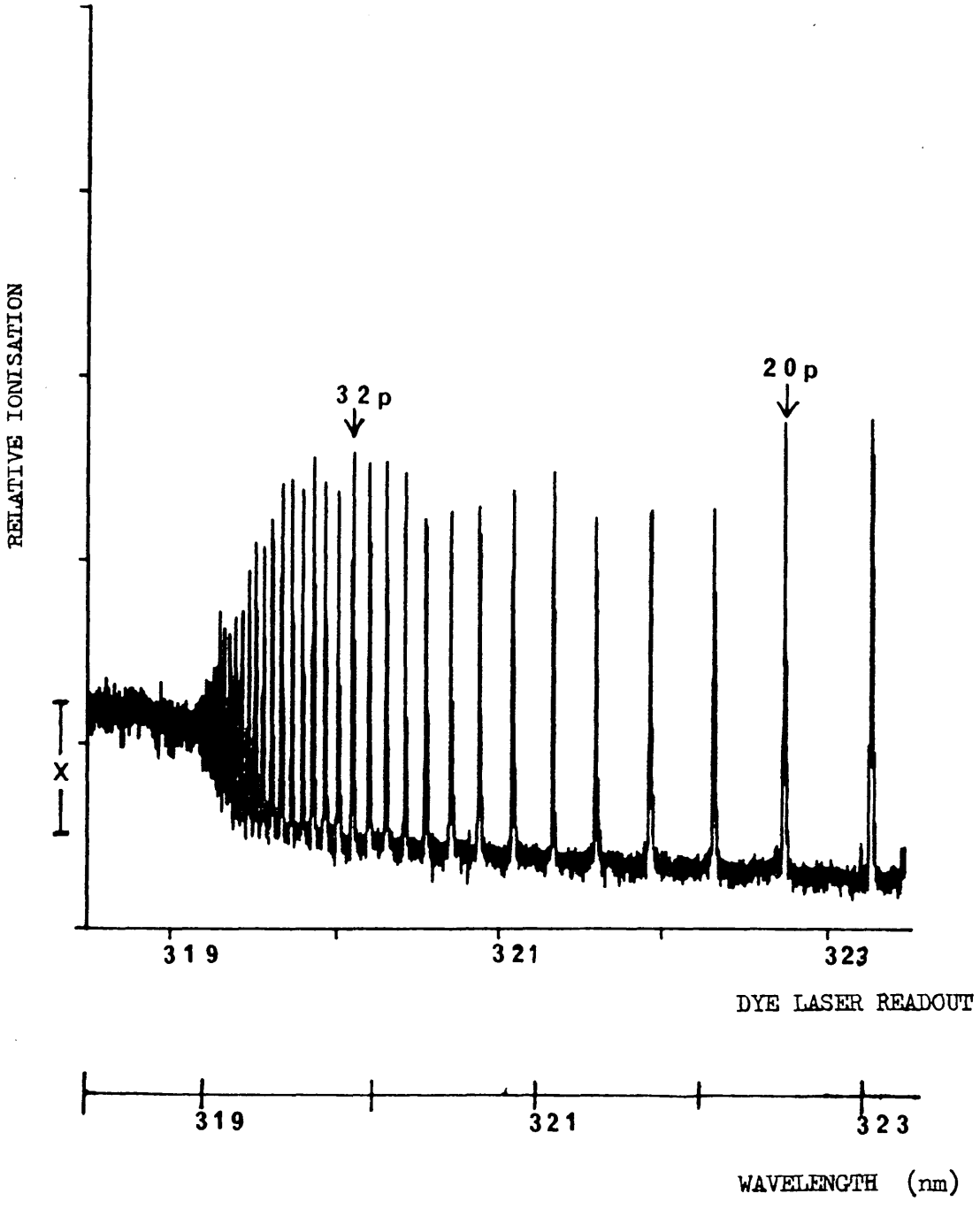

FIG. 5.322: 6s - Rydberg TRANSITIONS 318 - 323 nm

The data of Figure 5.322 were chosen over those of Figure 5.320 for this calculation since the fluence was known with greater precision in the latter spectrum. At a fluence of 6.3 mJ/mm^2 (1.01×10^{18} photons/cm^2), and knowing from the ^{55}Fe calibration of the figure that $N_I = 7.01 \times 10^3$ atoms ionised in the focused laser beam, $\sigma_1 = 1.16 \times 10^{-19}$ cm^2. This value is, within the systematic error of the experiment, in good agreement with the generally accepted value of 2×10^{-19} cm^2 (132).

Figure 5.323 is an expansion of part of Figure 5.322, allowing the higher Rydberg transitions to be more clearly distinguished. Resonant transitions via Rydberg levels up to $\sim$ 51p can be resolved.

Figure 5.324 continues the wavelength range of Figure 5.320 and 5.322 to longer wavelength. It was obtained with 2.8 mJ/mm^2 of ultraviolet and 12.7 mJ/mm^2 of red light passing through the counter. Although there has been variation in the laser fluence around 324 nm it is still clear from the figure that, having reached a minimum at 17, 18 or 19p, the intensity of the peaks then increases with decreasing principal quantum number of the resonant Rydberg state, as would be expected in the absence of collisional effects.

Thus collisional processes appear only to be effective in enhancing ionisation from levels within $\sim$ 2.3 kT of the continuum, i.e. at wavelengths shorter than 324 nm.

There is evidence in both Figures 5.322 and 5.324 of low intensity fine/

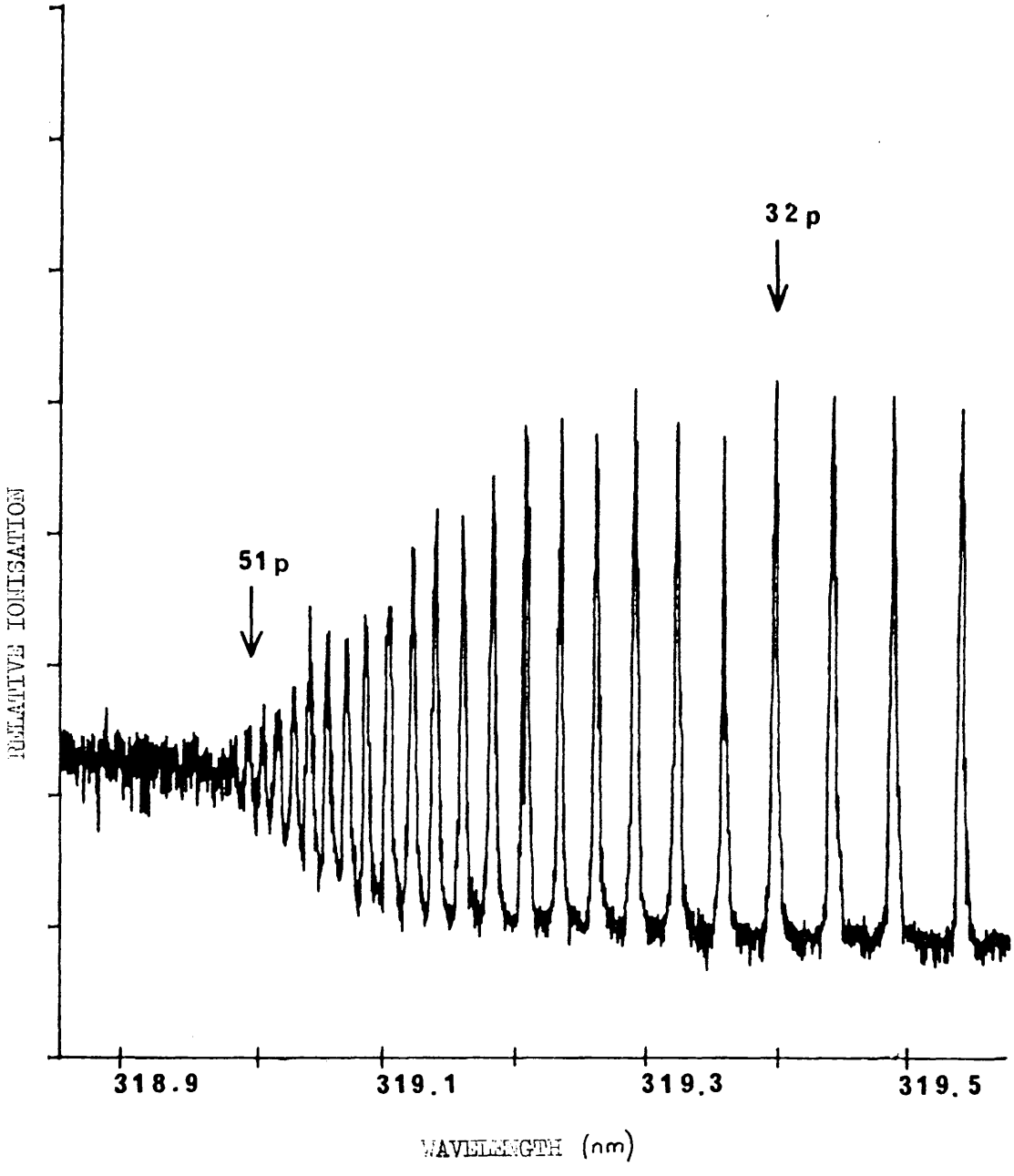

FIG. 5.323: 6s - HIGH RYDBERG TRANSITIONS

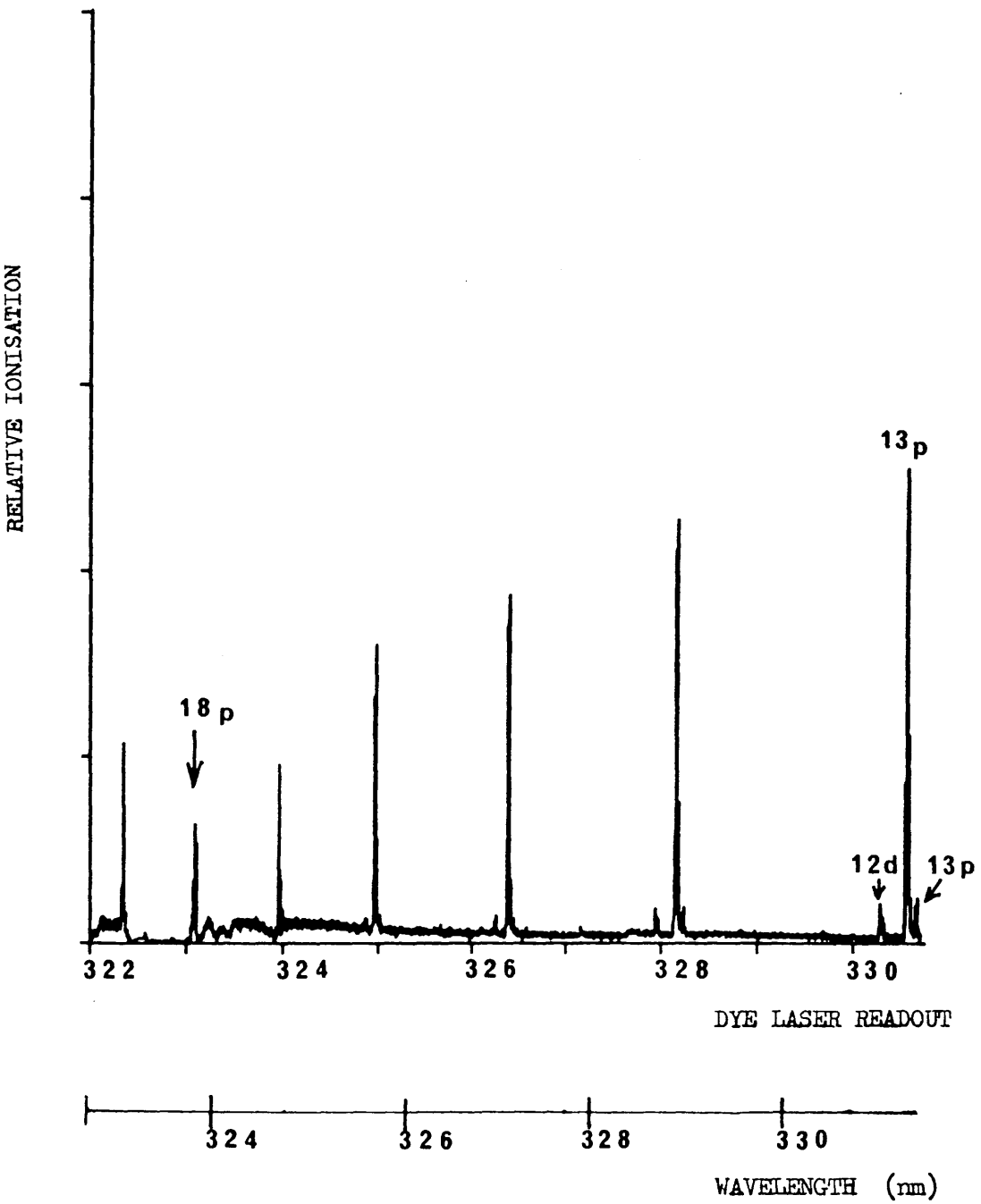

FIG. 5.324: 6s - p TRANSITIONS 322.5 - 331.5 nm

fine structure close to the base of the large peaks. This is attributed to two photon resonant (via a virtual state) s → d transitions induced by red photons from the fundamental laser beam. An expansion of the area around 331.3 nm in Figure 5.324 is shown in Figure 5.325. The 13p doublet, which can only just be resolved in Figure 5.324, is well defined with measured peak separation of 0.095 nm (literature value 0.09 nm (122)). The intensity ratio of the $6s \rightarrow 13p_{\frac{3}{2}}$: $6s \rightarrow 13p_{\frac{1}{2}}$ transitions is 11:1. The structure on the blue side of the 13p transitions has also been resolved as a doublet. From the separation of the peaks of the doublet (0.027 nm) and from its separation from 13p, this structure was identified as arising from ionisation via the 12d atomic levels of caesium. The small peaks visible to the blue side of the 14p, 15p, 16p and 19p transitions in Figures 5.322 and 5.324 are thought to arise via two-photon excitation of the 13d, 14d, 15d and 18d states respectively.

To obtain some estimate of the degree of collisional enhancement in ionisation taking place comparison can be made between the intensity ratio (20p/32p) observed in the experiment and that which would be derived theoretically. The ratio of the peaks, at constant fluence (assuming the validity of the $^1/_n{}^8$ intensity dependence) is $32^8/20^8$ = 43. However, in Figure 5.322 the ratio is ~ 1, and in Figure 5.320 it is 0.48. Thus in Figure 5.320 collisional processes have enhanced the ionisation yield from the 32p level by approaching two orders of magnitude.

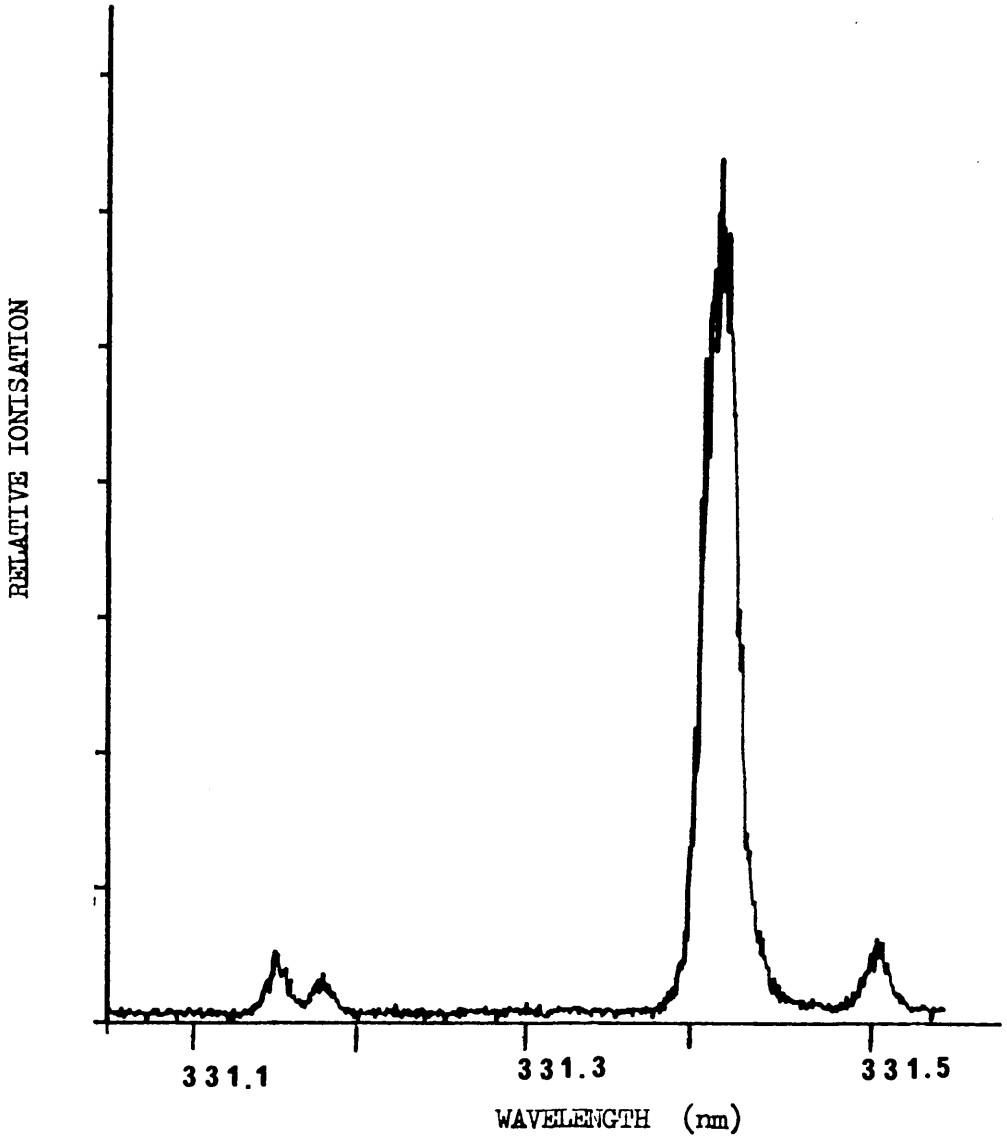

FIG. 5.325: EXPANSION OF A SECTION OF FIGURE 5.324

VIII 6s - Higher s and 6s-d Transitions

Although transitions from the 6s ground state of caesium to higher s or to d levels are l-forbidden via single photon excitation, they are allowed if the excitation is induced by a two photon process. As discussed above, two photon excitation, three photon resonant transitions were evident in Figures 5.322 and 5.324. In order to study these transitions in more detail, the harmonic generator was removed from the caesium experimental line and the red, fundamental, output of the dye laser alone allowed through the counter.

Of the five basic RIS schemes (2), scheme 5 resonance ionisation requires the highest fluence for saturation due to the short lifetime of the virtual intermediate state. In order to observe any resonances at all in the 635 - 665 nm region it was found necessary to use a focused laser beam.

A typical spectrum in this wavelength range is shown in Figure 5.326. A fluence of 52.8 mJ/mm^2 was used and 2.8×10^4 ion pairs contributed to the peak labelled 13d. The figure shows two series of sharp peaks, one approximately six times more intense than the other, both of which decrease in intensity towards the caesium two-photon ionisation edge. The peak at 662 nm (12d transition) has been depressed by the decrease in fluence at the edge of the dye's power output spectrum. Broad structures are also visible at 642.34, 647.66, 654.68 and 658.51 nm. These are not intrinsic components of the background in the counter since they could not be observed prior to the release of caesium from the ampoule, and are much too broad to represent atomic transitions.

It/

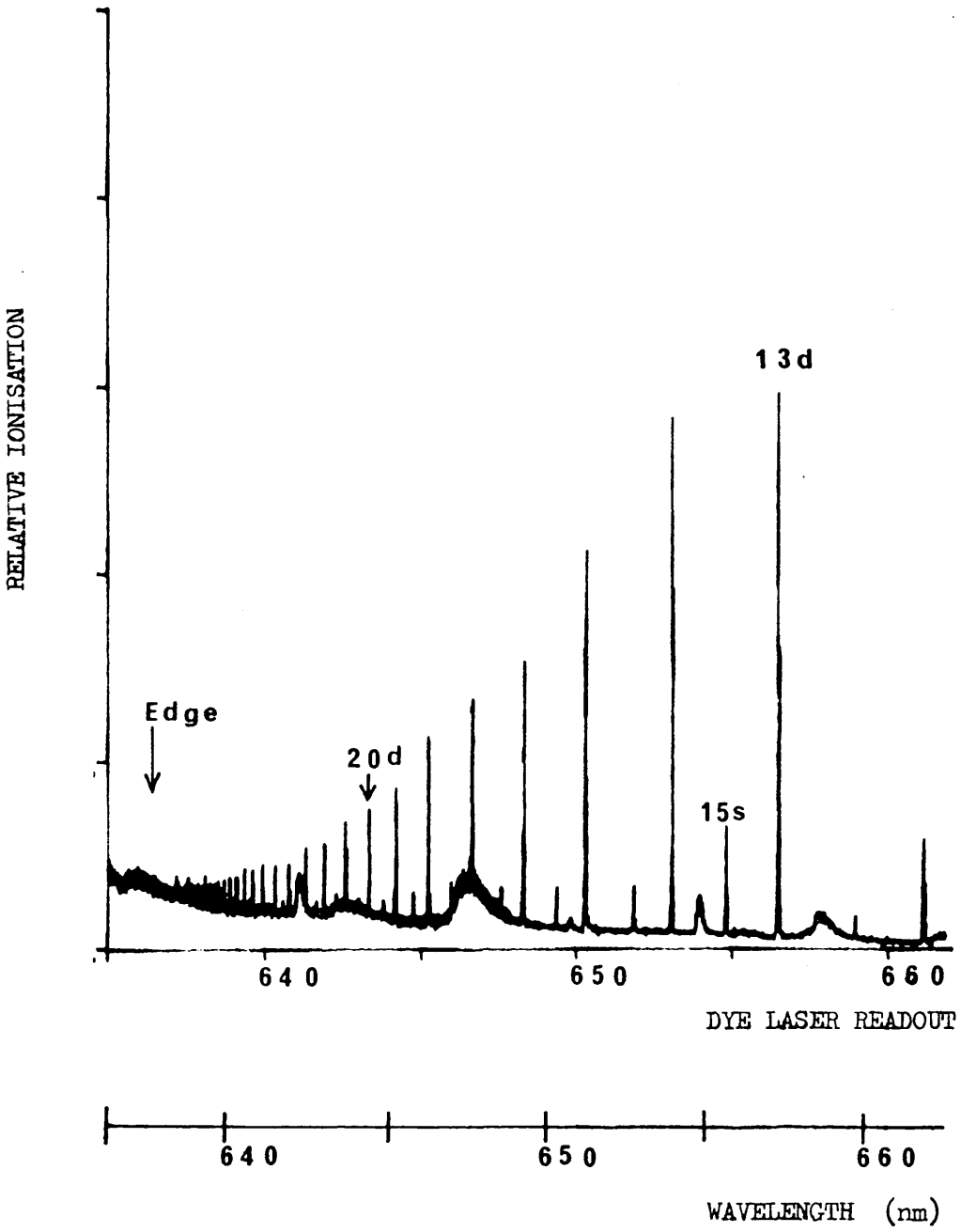

FIG. 5.326: 6s - s / 6s - d TRANSITIONS ~635 - 660 nm

It is tentatively suggested that they may originate in polyatomic caesium species, e.g. dimers.

The more intense of the two sets of sharp peaks is attributed to resonance ionisation via d levels, for the following reasons: firstly, the wavelength spacing between the transitions match with literature values of d level spacings (122) and, secondly, fine scans reveal resolvable doublet structure on the 654.0 and 657.2 nm peaks, which is to be expected for d atomic levels. A scan over the 13d doublet is shown in Figure 5.327. The spacing between the peaks is 0.022 nm, close to the literature value of 0.020 nm (122). In fact there is evidence of doublet structure on all of the larger intensity series of peak up to ~ the transition labelled 17d, but it is poorly resolved except for the lowest values of principal quantum number, i.e. 13d and 14d.

The less intense series of transitions is attributed to resonance ionisation via s levels. Fine scans of e.g. the 656 nm transition show no resolvable structure, i.e. those peaks are singlets (at least to within the resolution capability of the laser system) as would be expected for s atomic levels.

The reason the s-d transitions exceed the s-s transitions in intensity is unclear - although the effect has been observed previously by Compton and co-workers (130) who attributed the different intensities to dissimilar photoionisation cross sections from d and s levels of similar energy. A possible, and very simplistic, explanation of this is/

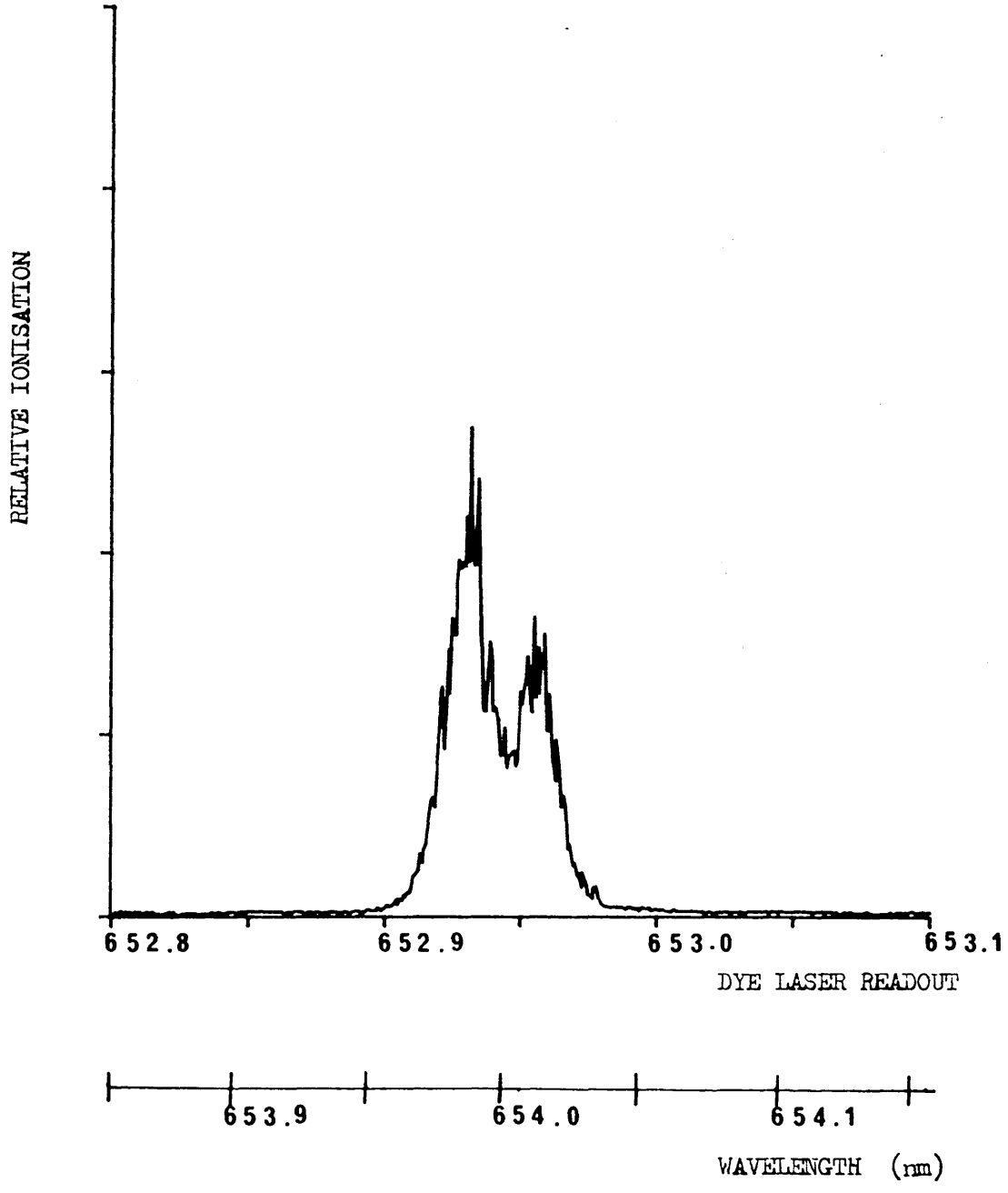

FIG. 5.327: EXPANSION OF A SECTION OF FIGURE 5.326

is that the potential overlap between the plane wave of a free electron and a d-type orbital wavefunction is greater than that between the free electron and the s-type (spherical) orbital wavefunction, increasing the photoionisation cross section of the d level over that of the s.

Power dependence graphs have been obtained on resonance with both d and s levels. A typical result, obtained with the laser tuned to resonance with the 14d levels, is shown in Figure 5.328. A cubic dependence of ionisation on incident fluence is apparent, indicating that, at the laser power available, little or no saturation of the three photon ionisation process is possible.

The caesium two photon ionisation edge is not well defined in Figure 5.326. There is some evidence for collisional enhancement of ionisation from states close to the continuuum in that the 24d to 28d peaks are of similar intensity and do not follow the smooth downward trend of ionisation apparent between 13d and the two photon continuum. (This is illustrated more clearly in Figure 5.329 which is an expansion of the wavelength region close to the two photon ionisation edge of Figure 5.326.) However, no dramatic increase in ionisation due to collisions is expected using scheme 5 resonance ionisation (2) since, even if collisional saturation is achieved, the observed ionisation intensity is severely limited by the rate at which the Rydberg levels can be populated by two photon excitation from the ground state.

In summary, three photon resonance ionisation, due to its small cross section and to the unattainably high fluence levels required for saturation,/

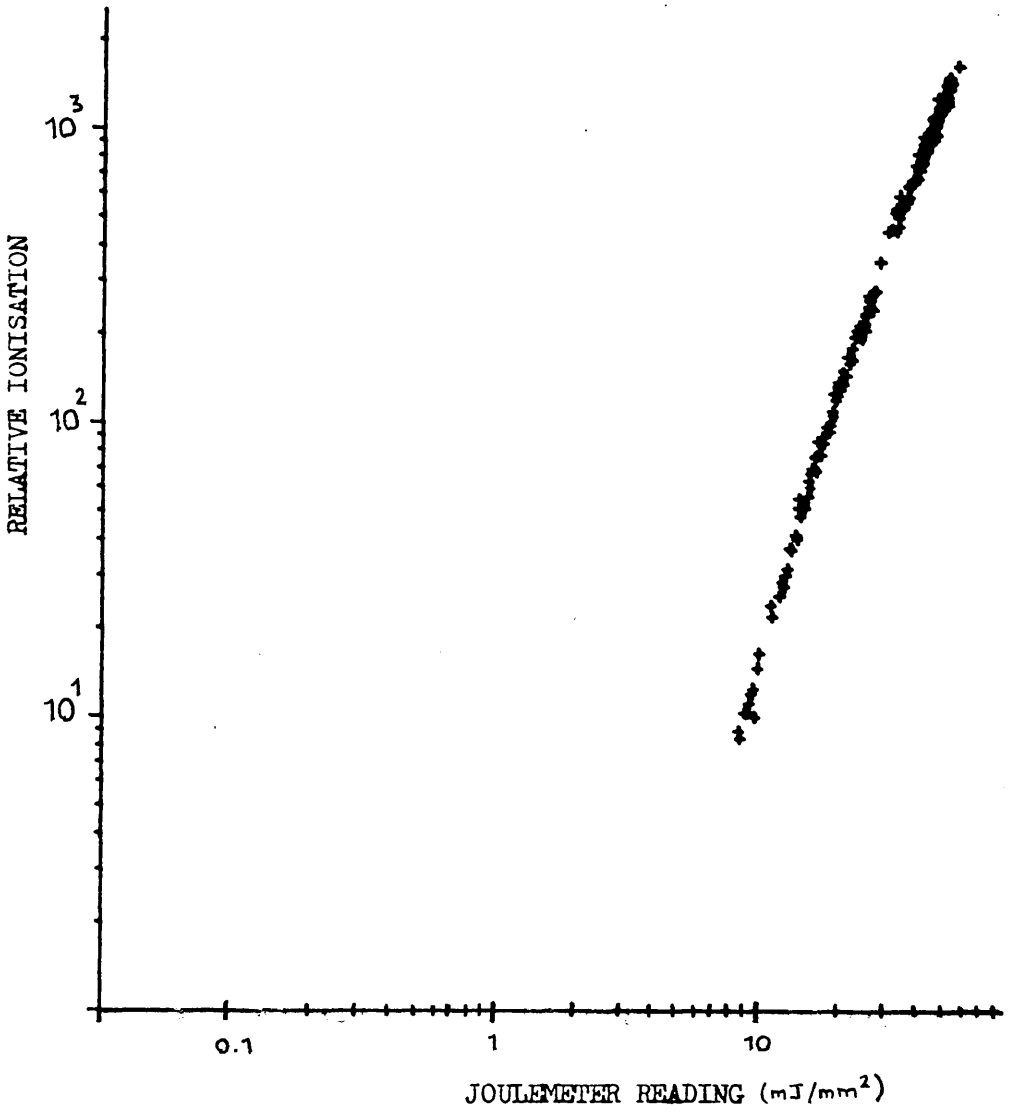

FIG. 5.328: POWER DEPENDENCE GRAPH, 654 nm

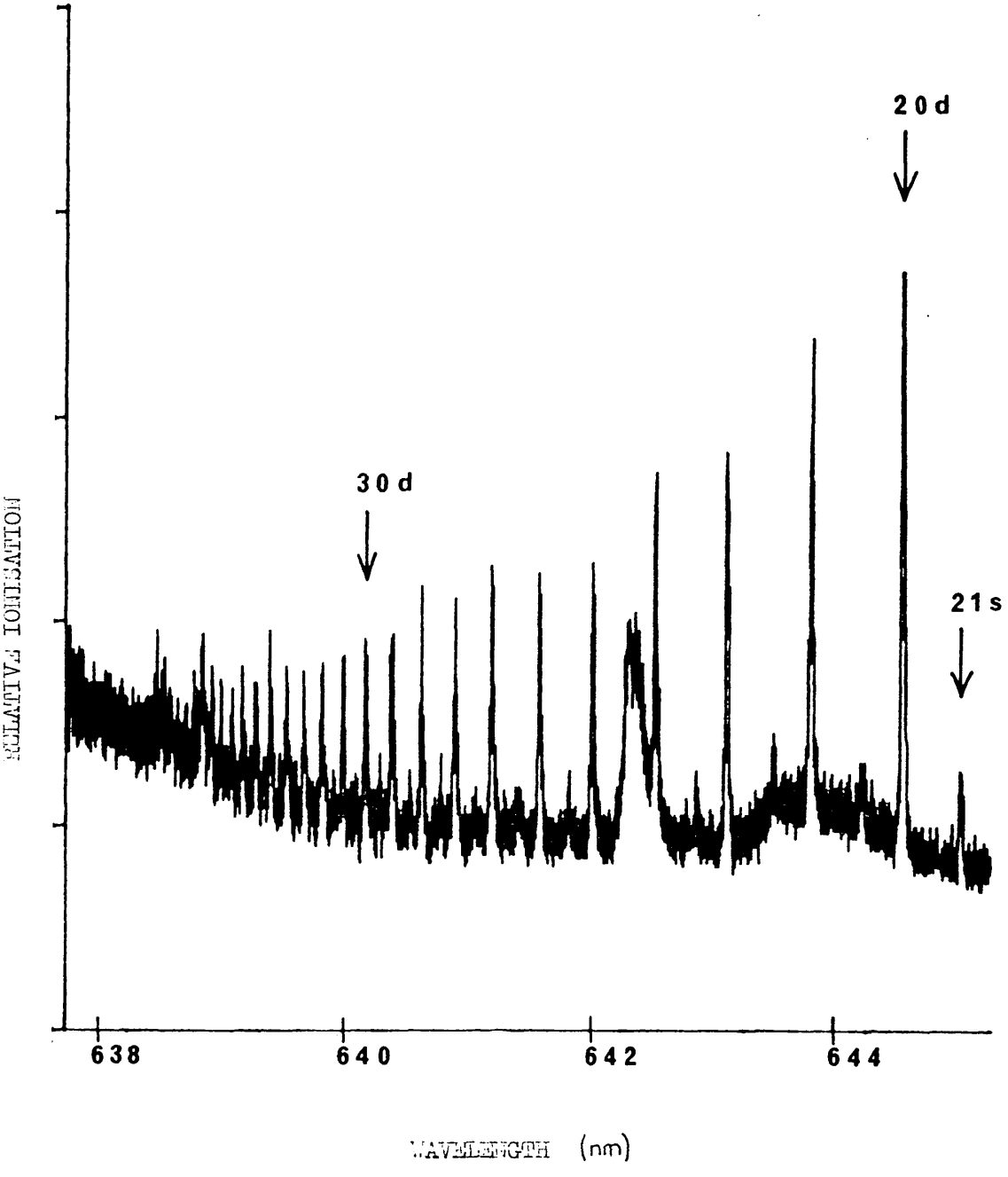

FIG. 5.329: EXPANSION OF A SECTION OF FIGURE 5.326

saturation, would seem (of the ionisation modes attempted) to be the least effective for the detection of caesium even though it has the advantage of low background. Two photon resonance ionisation requires less fluence and saturation is feasible, at least for the 6s→7p transitions, with the current laser system. Better still, however, is the combination of resonance excitation and collisional ionisation shown in Figure 5.320. Although ultraviolet wavelengths are required to populate the resonant Rydberg states, fluence need not be high since only the excitation (i.e. not the ionisation) step requires photons. Thus reduced flux compensates for the potential increase in background associated with the use of shorter wavelength light.

CHAPTER 6 FUTURE PROGRAMME AND CONCLUSIONS

6-1 Future Programme

I Introduction

Future work in Resonance Ionisation Spectroscopy at Glasgow will centre around the development of laser mass spectrometer systems for analytical applications of the technique. High Energy Physics laser-related studies will decline as effort within the Glasgow portion of the ALEPH TPC project is switched to the manufacture and testing of hardware.

Three main areas of application are currently envisaged for these resonance ionisation mass spectrometer systems. The suitability of RIMS for nuclear waste monitoring has already been described in Chapter 2 and is discussed further later in this chapter. It is likely that an early use for one of the Glasgow-built RIMS devices will be in the demonstration of isotopically-selective detection of caesium, an experiment which follows naturally from the work presented in this thesis. However, the need for ultrasensitive analysis also exists in the electronics industry and in medicine, and applications in these fields are also prospected.

As the current drive for miniaturisation of semiconductor devices continues, more sensitive techniques for trace analysis of impurities are required and it is hoped that RIMS will fulfill this need. The capacity to profile semiconductor materials, i.e. to analyse the material/

material (hopefully a monolayer at a time) to depth, in order to elucidate information on bulk as well as surface impurities is also potentially present in the RIMS technique.

In medicine, the ability to accurately assess the amounts of trace elements present in different body fluids and tissues may lead to significant advances in the understanding of the role and importance of these elements to living systems. It may also be possible to improve, by RIMS, both the routine health monitoring of workers occupationally exposed to toxic chemicals or radiation, and the accuracy and speed of accident assessment in the event of exposure of members of the general public to such hazards. Atom Sciences Inc. have already begun to explore such an application of RIMS in their study of uranium levels in human urine (133).

Proportional counter systems such as that used for caesium detection may still be useful to determine the most appropriate ionisation schemes and wavelengths for elements to be studied in the laser mass spectrometers.

With the above applications in view, two distinct resonance ionisation time-of-flight mass spectrometers are currently under construction or test at Glasgow.

II Resonance Ionisation Mass Spectrometers

Both resonance ionisation mass spectrometers were based on the design illustrated in Figure 6.11 although the Mark I device lacked some/

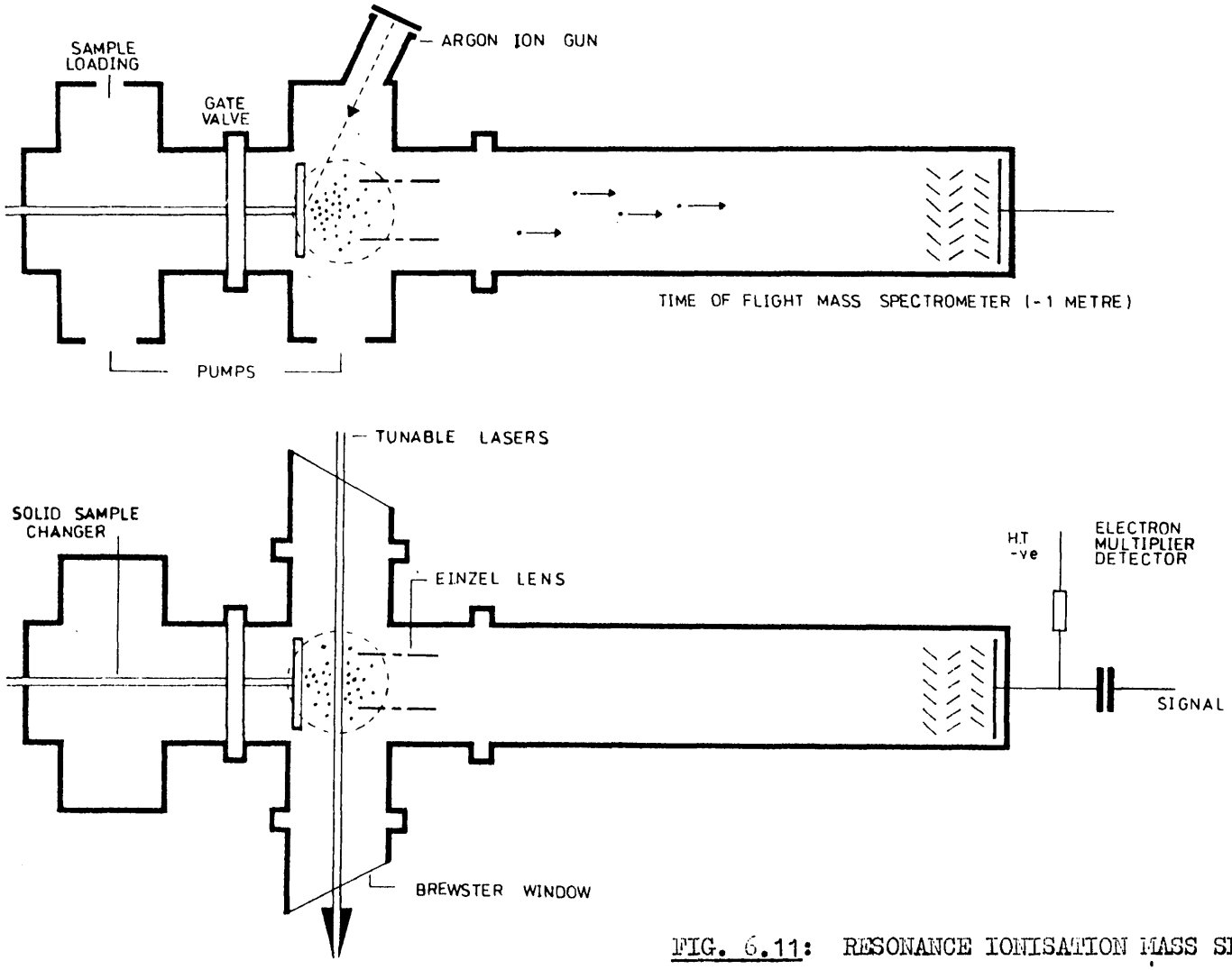

FIG. 6.11: RESONANCE IONISATION MASS SPECTROMETER

some of the features of the Mark II shown, i.e. the sample loading stage and associated vacuum pumps.

In the first system built, atoms may be vaporised from a fixed target maintained at 1-2 kV positive potential by the incident beam from a N_2 laser. Laser ablation was envisaged rather than ion ablation because an ion gun was not available at the time the Mark I spectrometer was constructed. (Ion ablation would, however, be preferable since the lower temperature process would reduce the rate of spreading of the sputtered plume of atoms and hence improve the geometrical overlap between the ionising laser and the plume.) The released atoms are then interrogated by the tunable output from a Nd:YAG pumped dye laser [SPECTRON LASER SYSTEMS LTD.], of pulse-length 14-17 ns, maximum repetition rate 20 Hz and pump laser maximum power 75 mJ (at 265 nm). Resonantly ionised atoms are focused with an Einzel lens (i.e. a system of three cylindrical electrodes) into the 1 m long field free drift region of a time-of-flight (TOF) mass spectrometer. In this region, ions of different mass travel with different velocities, thus, when they reach the electron multiplier at the end of the tube, they are separated temporally according to their time of flight through the drift region.

In the second system, a recently obtained Ar ion gun was installed for surface ablation. The gun is shown in Figure 6.12. It has the ability to raster the surface, allowing depth profiling studies to be carried out. Such an experiment is illustrated schematically in Figure 6.13./

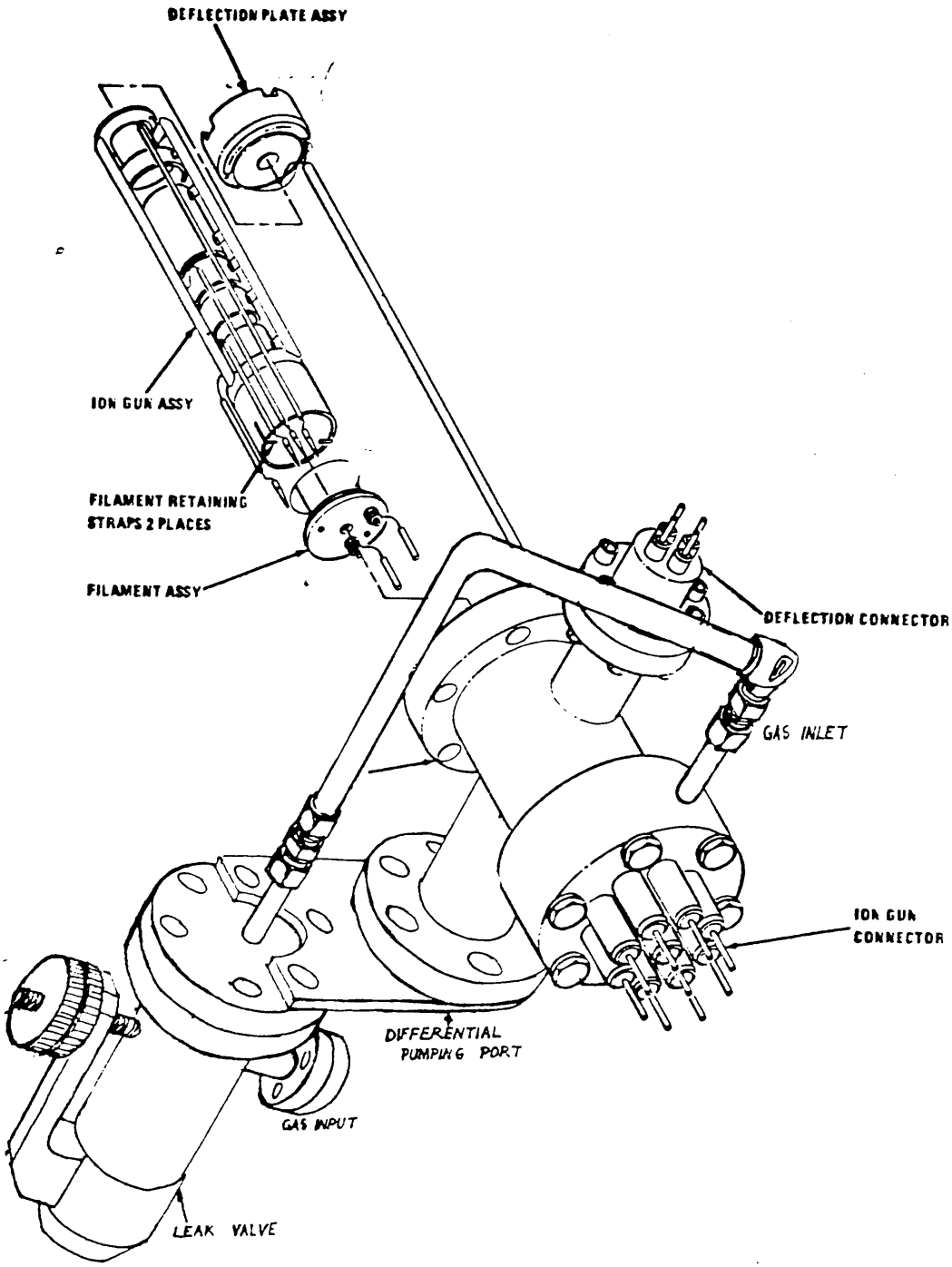

FIG. 6.12: Ar^+ ION GUN

Figure 6.13. A rectangular pit is created using the Ar ion gun and the region in the centre of the pit ablated to create a plume of sputtered atoms. The laser is tuned to resonance with only one type of atom in the plume (the white atoms), and only these pass through the Einzel lens and are detected. The target material in the Mark II spectrometer is variable i.e. it can be changed without having to open the entire system to the atmosphere as was necessary in the Mark I instrument. Resonance ionisation of species of interest is again brought about by the Nd:YAG pumped dye laser and the ions are detected by an electron multiplier at the end of a time-of-flight system. Data collection is controlled by an IBM personal computer. It is hoped soon to obtain a second dye laser which can be used in parallel with the presently installed one, allowing more complex resonance ionisation schemes to be attempted and more elements to be detected. The envisaged laser system is shown in Figure 6.14, along with a schematic representation of the mass spectrometer.

III Prospected Sensitivity

The prospected sensitivity of the laser mass spectrometers under construction in Glasgow is of the order of parts per billion (10^9). Indeed it is unlikely that any RIMS system will exceed this sensitivity by more than $\sim$ a factor of ten if it is constructed from technology which is currently readily available (and in the absence of chemical pre-enrichment of the sample). This limit is comparable with the best results obtained by SIMS but, due to the drastically reduced matrix dependence of RIMS, it is likely that RIMS will routinely achieve ppb sensitivity, whereas SIMS can only attain/

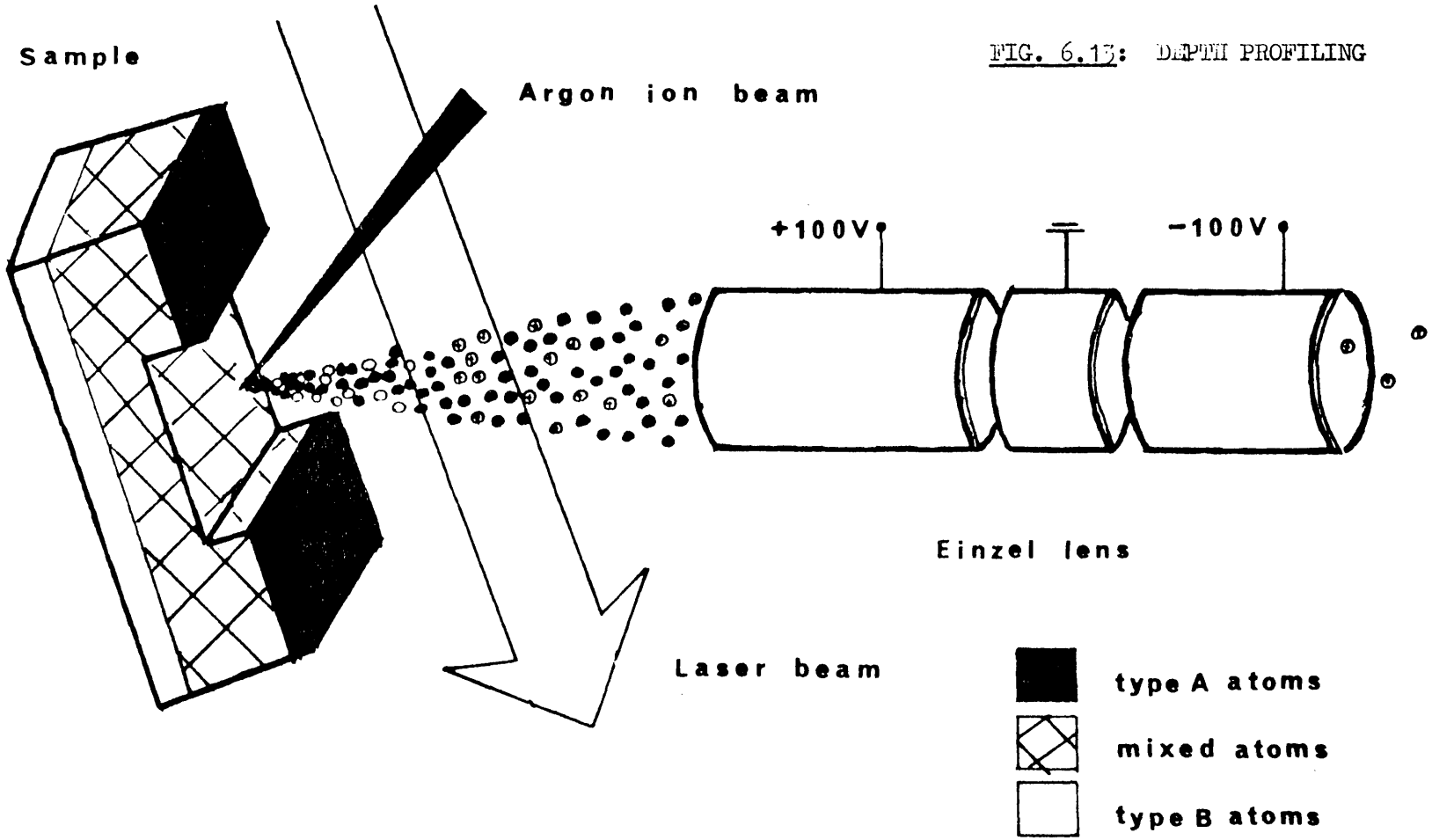

FIG. 6.13: DEPTH PROFILING

RESONANT IONISATION MASS SPECTROMETER

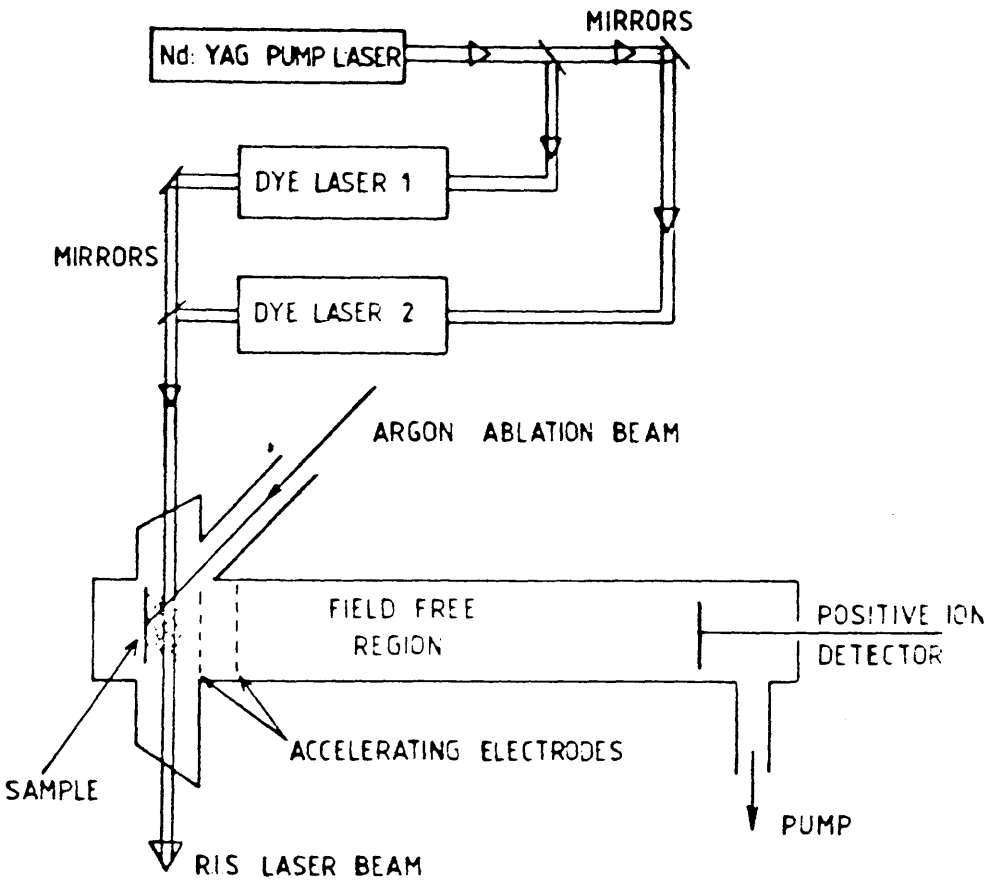

FIG. 6.14: LASER SYSTEM

attain these levels in certain favourable cases (59).

The major limit on the number of atoms which can be analysed per second by RIMS is the low duty cycle of high powered, short pulse lasers such as the excimer and Nd:YAG. Since the laser only emits photons for a small part of each second (e.g. $<$ 1 millionth), d.c. operation of the ablating ion gun would be very wasteful in terms of sample material and it too, therefore, must be pulsed. Sputter yield (i.e. number of atoms ablated per incoming ion) of neutral species must be optimised and timing and geometrical effects considered to maximise the overlap between the sputtered plume and the ionising laser. The dilemma between a large diameter, lower fluence laser beam (to maximise geometrical overlap) and a small, higher fluence beam (to ensure saturation) must be resolved.

Finally, detection efficiency must be made as high as possible. A low resolution, high transmission mass spectrometer, e.g. a time-of-flight system, is more suited to RIMS than a high resolution, low transmission instrument for the following reasons: a) TOF systems detect ions of all masses created at each laser pulse, whereas quadrupole or magnetic sector systems are gated to detect atoms of one mass only per laser pulse; b) since the ionisation process is element-specific, high resolution is not necessary. Indeed, were a high resolution instrument used, the associated transmission of 10^{-1} - 10^{-4} (59) would seriously reduce analytical sensitivity.

Resolution in conventional TOF mass spectrometers is limited by the temporal,/

temporal, spatial and kinetic energy distributions of the ions which are to be analysed (134 , 135). Using laser ionisation, the temporal distribution of the ions is narrow since they are all produced within the duration of the laser pulse (which is short compared with their time-of-flight through the drift region). The spatial distribution is a function of the ionising laser beam diameter and thus, as beam area is increased to maximise sputtered plume/laser interaction volume, space resolution may be lost. A typical kinetic energy distribution of sputtered species (produced from a sample of gold at 30°C by an incident 20 keV Ar ion beam) is shown in Figure 6.15 (136). This distribution is also appropriate to the kinetic energy of resonantly ionised atoms in a RIMS instrument of the type envisaged, since these atoms are produced by sputtering. The spread of kinetic energies is broad, extending to thousands of eV, but is fairly sharply peaked at a value of a few eV.

Various time-of-flight mass spectrometer systems have been developed which have better energy resolution than conventional instruments. Two such systems, the reflectron and the Poschenrieder (137) are described below.

A reflectron type TOF mass spectrometer is shown in Figure 6.16. In this instrument (138 , 139), ions produced by a laser travel down the drift tube and are reflected by a system of electrodes back into the detector. Voltages are applied to the reflectron such that faster ions which penetrate further into the field than slower ions of the same mass are delayed, by so doing, for exactly the time necessary for/

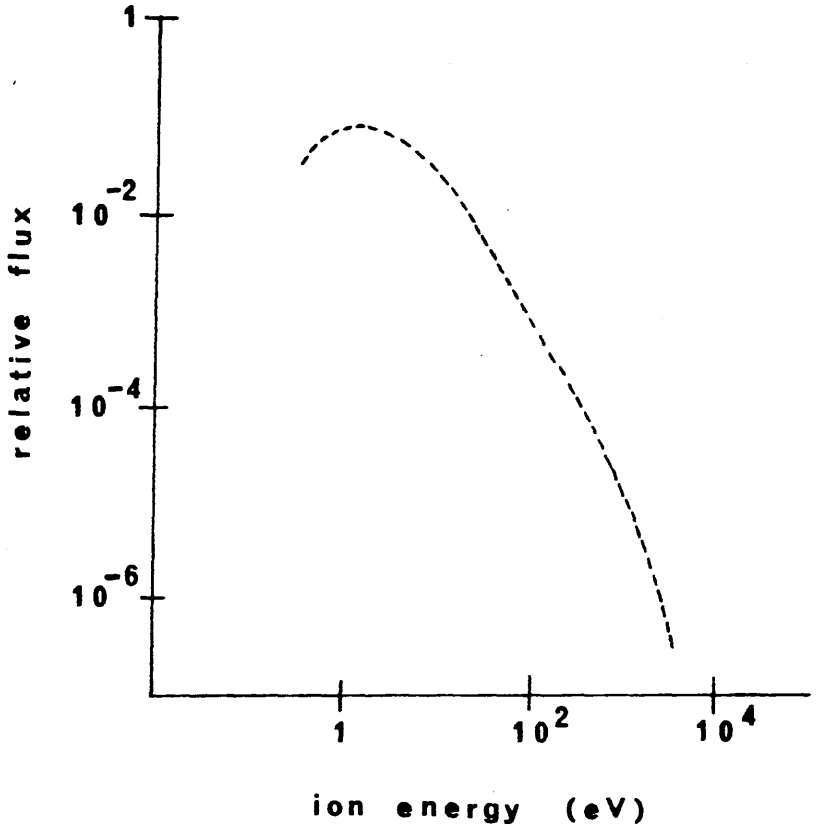

FIG. 6.15: KINETIC ENERGY DISTRIBUTION OF SPUTTERED SPECIES

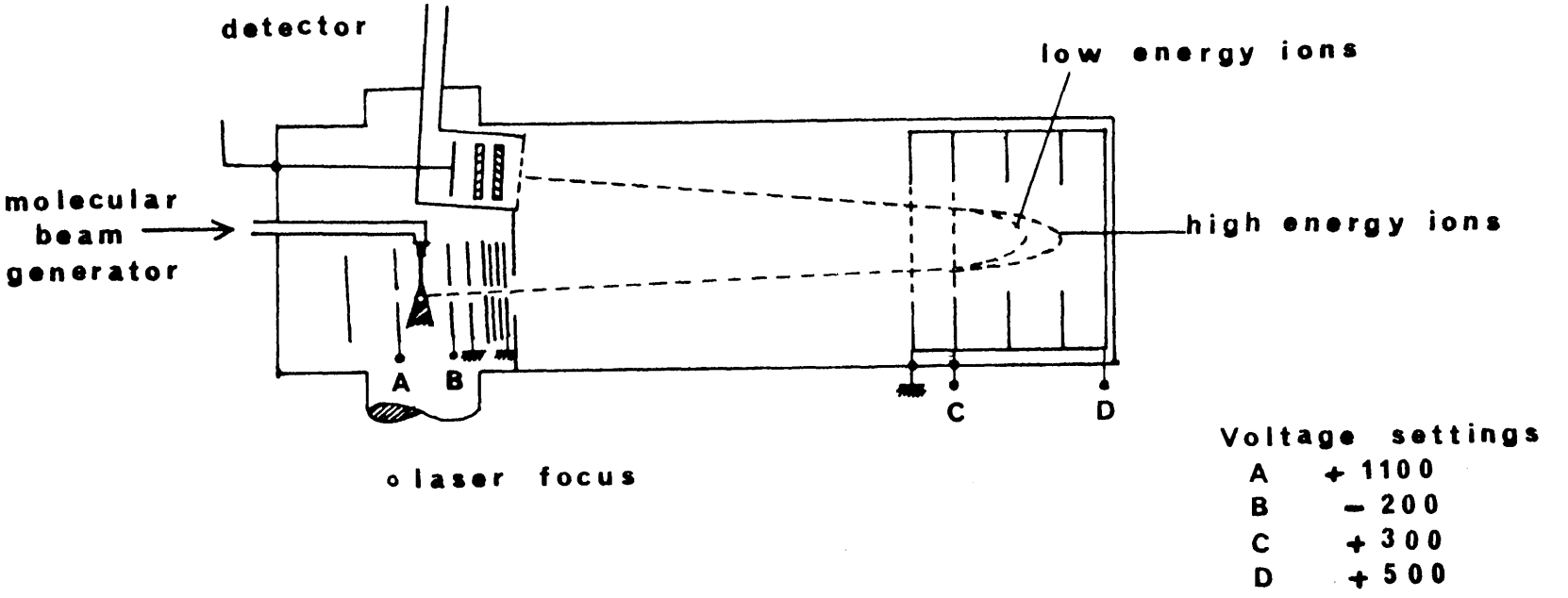

FIG. 6.16: REFLECTRON TOF MASS SPECTROMETER

for the slower ions to "catch up". Effectively, therefore, the reflectron focuses ions of the same mass but different initial kinetic energies. This instrument has been used in the detection of metastable species formed by ion fragmentation within the drift region of the spectrometer; species which cannot normally be distinguished from their parent ion by conventional TOF mass spectrometry (138).

A Poschenrieder type (137) TOF mass spectrometer is shown in Figure 6.17. (The illustration actually shows a commercial SIMS instrument, but this could readily be modified to accommodate a tunable laser for RIMS studies.) Again the intial kinetic energy spread of the ions is compensated for by increasing the distance travelled by higher energy ions relative to lower energy ions of the same mass. However, instead of a system of parallel plate electrodes, curved electrostatic sectors generate a toroidal electric field for energy focusing of the ions.

Although the resonance ionisation mass spectrometers currently under development at Glasgow are of the conventional type it is possible that, in the future, reflectron or Poschenrieder type systems may be used.

The ppb detection limit claimed above for a typical RIMS system is derived from the following considerations:

a) Sputtering

The sputter yield from the surface depends on a number of factors. The/

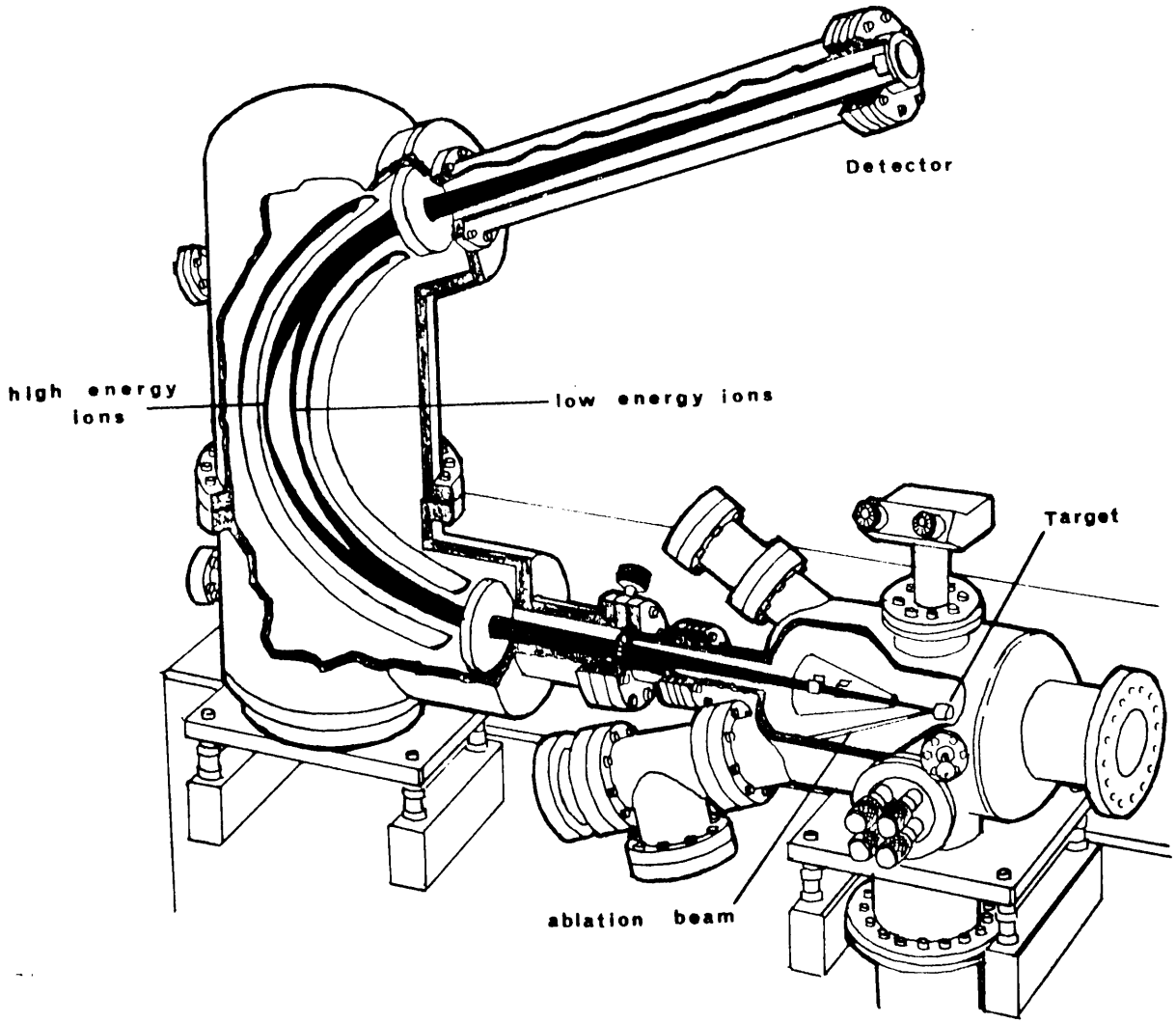

FIG. 6.17: POSCHENRIEDER TYPE TOF MASS SPECTROMETER

The angle of incidence of the bombarding ions normally gives optimal yield at between 45 and 60° from the normal to the surface (59). The variation of yield with primary ion energy is shown in Figure 6.18 (136). Although the maximum in this curve is ~ 20 keV it is, in practice, better to keep to lower energies (~ 5 keV) to avoid autoimplantation i.e. embedding of Ar into the target. The identity of the primary ions can also affect both the sputter yield and neutral:ion ratio of the atoms leaving the surface. Oxygen ion beams have been shown to enhance positive ion formation whilst caesium ion beams enhance negative ion formation. Noble gas primary ion beams normally produce a predominance of neutral species. The variation of sputter yield with type of noble gas used as primary ions is shown in Figure 6.19 (136). At ~ 5 keV energy the yield for all the noble gases except He and Ne is 4 or 5.

A typical primary ion current is 15 μA (9.4×10^{17} Ar^+/sec) and a typical primary ion gun pulselength 3 μs. These values are derived from the need to remove as much material from the sample, for analysis, at each ion pulse as possible, without exceeding the volume of the interrogating laser beam. Pulselengths longer than a few μs result in sputter plumes too large to be ionised, i.e. much of the sputtered material is lost before it is probed by the laser. Increasing the amount of material sputtered per 3 μs ion gun pulse would necessitate increasing primary ion gun current - a process which is difficult due to space-charge effects (59).

Assuming the above typical values, plus a sputter yield of 5 and a pulse rate/

FIG. 6.18: VARIATION OF SPUTTER YIELD WITH PRIMARY ION ENERGY

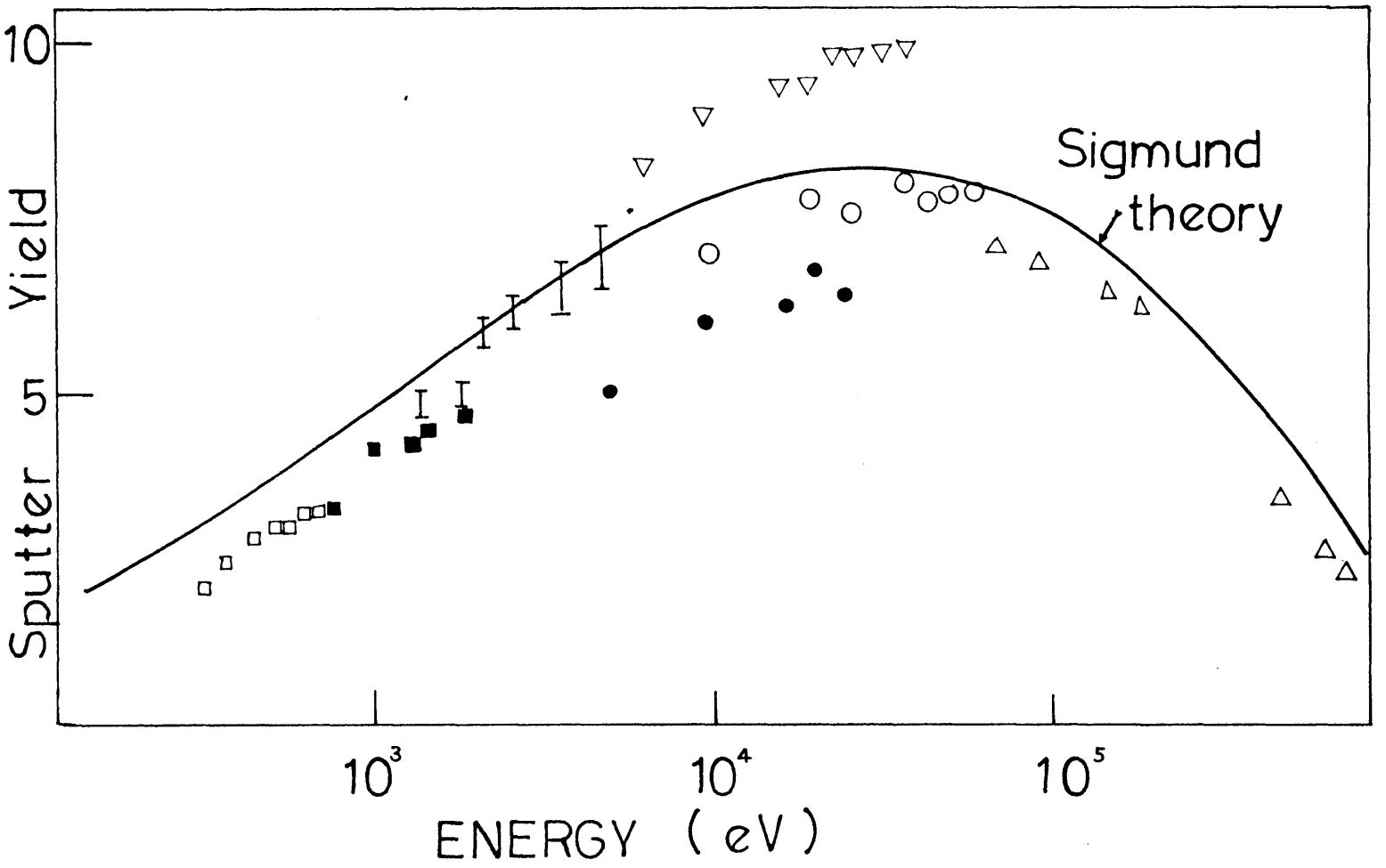

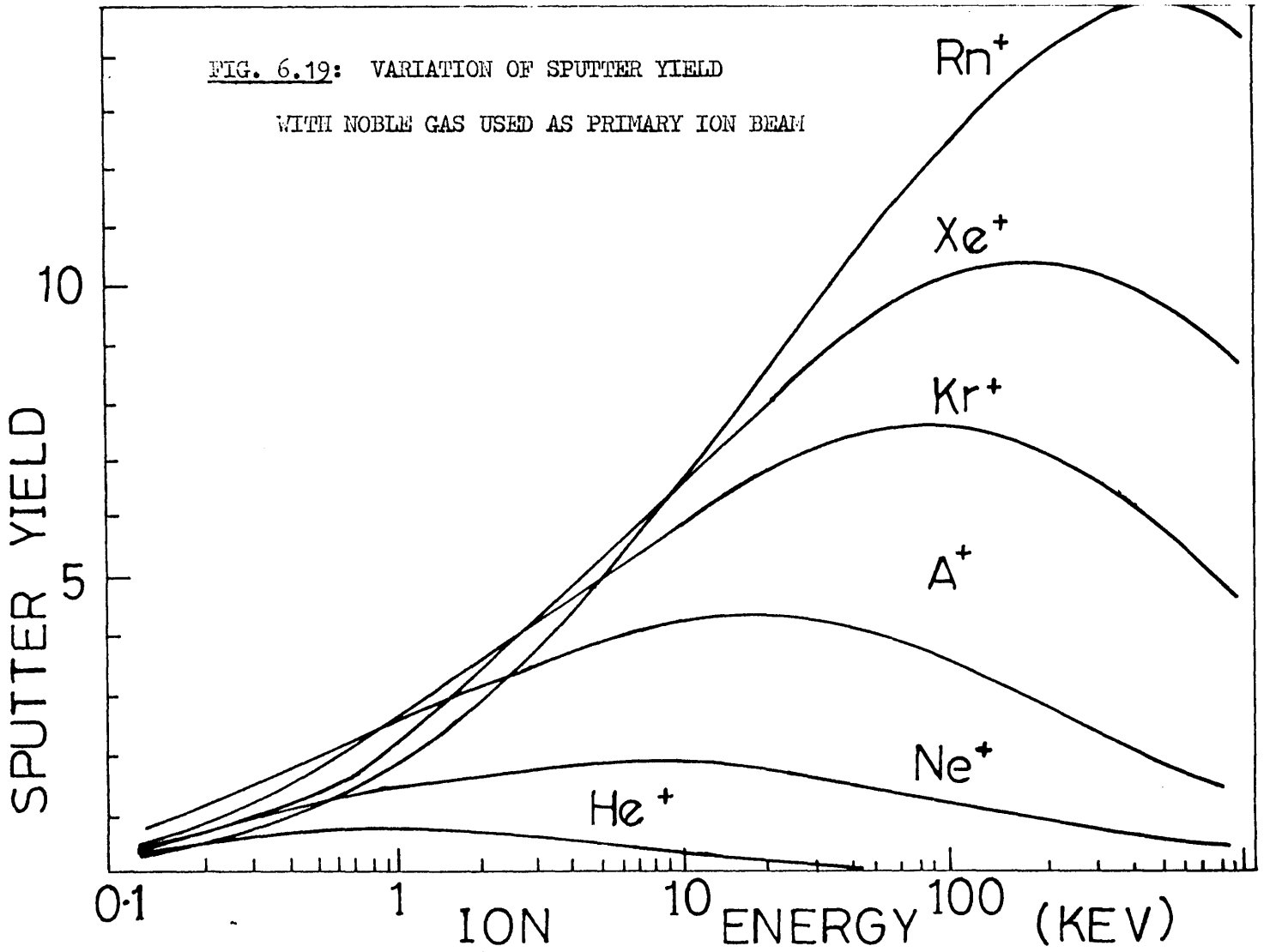

FIG. 6.19: VARIATION OF SPUTTER YIELD WITH NOBLE GAS USED AS PRIMARY ION BEAM

pulse rate of 20 Hz, the number of atoms which can be reomved from the surface is 2.82 x 10^{10}/sec.

b) Ionisation

Not all the atoms leaving the surface will necessarily be in the correct electronic configuration to be resonantly ionised. By use of noble gas primary ions the fraction leaving as ions may be small (1 in 10^2 - 10^4 (62)) but there is also the possibility of formation of excited species by interaction between the primary ion beam and the surface. These will, in general, not be amenable to resonance ionisation at the same wavelengths as the ground state. Estimating this effect as reducing the number of atoms amenable to ionisation by a factor of two - a value determined by Winograd (59) for a highly oxidised In surface and quoted by Peuser et al. for Pu evaporated from a heated filament (74), 1.41 x 10^{10} atoms/sec are produced in the correct state to be resonantly ionised.

Further the geometrical overlap between the plume and the laser is unlikely to approach 100% if laser fluence suitable for saturation is required. Within the 3 μs Ar ion beam pulse the sputtered plume will develop to extend some 6 mm from the surface. Saturation fluence over a diameter of 6 mm cannot readily be obtained from the present Nd:YAG pumped dye system. Estimating that ∿ 30% of the plume may be ionised with high efficiency by the current laser system, 4.23 x 10^9 ion pairs/sec are produced. It should be stressed at this point that the factor of 30% may be an overestimate by at least an order of magnitude and will vary considerably depending on the ionisation scheme used and the saturation requirements (59).

c) Detection/

c) Detection

Since elemental selectivity is inherent in the ionisation stage of RIMS, a low resolution mass spectrometer, with high transmission, i.e. a time-of-flight system is adequate for detection of the ionised atoms. Typically 50% transmission is readily achievable in such systems and, with careful construction, 100% transmission may be approached (59). Assuming 50% transmission 2.12×10^9 ions/sec are detected by the RIMS system. In other words an impurity present in the target medium at a concentration of 1 ppb will give 2 events/sec. Background in the system is expected to be small provided care is taken in the selection of resonance ionisation scheme. As has been discussed in Chapter 4, background in proportional counters and therefore, by extrapolation, in RIMS systems, arises chiefly from outgassing of materials which have become absorbed onto surfaces within the apparatus. Organic compounds, typically with mass approaching 100 amu and ionisation potentials of around 9 eV (plus, possibly, their fragmentation products) are expected to be principally responsible for background ionisation. Thus, the RIMS analysis of high atomic mass elements may suffer less from background interference than experiments on low atomic mass elements.

From the study of the wavelength dependence of ionisation, it is clear that, to minimise background, resonance ionisation schemes employing visible laser light should be used in preference to those involving higher energy photons. Incident laser fluence should also be kept as low as practicable and, if possible, processes which do not involve photons should be employed to bring about bound-continuum transitions/

transitions, i.e. resonant excitation followed by electric field or collisional ionisation, as recommended by Letokhov (7,8), should be used.

The background in the RIMS system, provided the above considerations are taken into account, is expected to be, at most, 1 event/sec (59). Indeed, a broadly similar RIMS system constructed at the University of Mainz and used for the three photon ionisation of plutonium had a vanishingly low background (74).

From the above considerations, an impurity present at 1 ppb represents the limit of the detection sensitivity of current resonance ionisation mass spectrometers.

Improved sensitivity is possible but requires the use of innovative (and expensive) technology. Duoplasmatron primary ion current sources may be able to increase the incident primary ion beam current by 10^2, increasing the density of the sputtered plume by a similar amount. Since the major limitation on RIMS sensiitivity was the laser duty cycle, recent developments such as the availability of copper vapour pumped dye lasers with repetition rates of up to 10 kHz and excimer lasers with 1 kHz repetition rates may lead to significant improvements, particularly if they can be combined with non-photon ionisation processes to reduce saturation fluence requirements. By such means RIMS sensitivity in the parts per 10^{12} region could be attained. Alternatively, as mentioned earlier, sensitivity may be improved by chemical preparation of the sample prior to analysis to enhance/

enhance the concentration of the species of interest.

6-2 Conclusions

If routine analytical sensitivity in the ppb region can be attained by resonance ionisation mass spectrometry, the technique has a highly promising future in many fields. In the particular application concerned in this study - the monitoring of (in particular low-energy) components of nuclear waste, β^- emitting isotopes with half lives greater than 10^5 - 10^6 years (see Chapter 2, Table 4), which cannot be monitored by conventional radiometry, could be assayed in environmental materials and reliable information both on the amounts of these nuclides discharged and on their geochemistry could be obtained. In view of the current fears amongst the general public over, in particular, the more insidious effects of long term exposure to "low" levels of radioactivity (i.e. levels which are difficult to accurately measure by counting techniques) the importance of a method which has the potential to quantify and monitor extremely small amounts of radionuclides cannot be overstated.

In the work presented here, significant progress has been made towards the ultimate aim of the routine monitoring of components of nuclear waste difficult to detect by radiometry, by RIS. Firstly, from a literature based assessment, isotopes of greatest environmental importance have been selected and those most difficult to detect by counting techniques identified. Particular emphasis has been given to/

to $^{135}_{55}Cs$ since it has a long half life and a low energy β^- decay mode; since it is amenable to RIMS detection in the environment in concentrations (1 pCi/g) where conventional radiometry fails and since, by analogy with other isotopes of caesium (which constitute a large portion of all nuclear waste materials currently discharged into the sea around the British Isles) it is likely to be released (currently virtually undetected) in considerable amounts. Calculations on the detection capability of current RIMS apparatus for radionuclides also served to define a sensitivity limit of around ppb for substances present in environmental (solid or liquid) samples. Thus, although $^{135}_{55}Cs$ is detectable at pCi/gram of sample concentrations in the environment, isotopes with shorter half lives (or pollutants at lower than ppb concentrations) will not, in general, be suitable for RIMS monitoring unless some chemical separation of the sample is carried out before it is introduced to the spectrometer. It is likely, however, that even if pre-enrichment of the sample must be undertaken, the chemical separation required will be neither as extensive nor as time consuming as is often necessary in conventional counting.

Apparatus has been designed in which element-specific detection of relatively small numbers of caesium atoms (10^2 - 10^3) have been demonstrated. Various difficulties associated with the development of resonant ionisation for analytical work have been overcome: in particular, ways to reduce background have been discovered through an improved understanding of its causes. From the study of wavelength dependence of ionisation it has been shown that background

can/

can be greatly reduced by excluding organic materials from experimental chambers and by judicious choice of resonant ionisation scheme i.e. the use of visible laser radiation.

Spectroscopic study of multiphoton transitions of caesium has allowed the selection of efficient means to ionise caesium atoms and revealed the possibility of using collisions to induce bound-continuum transitions in the element at lower incident fluence than would be required were photoionisation employed. The possibility of saturation at reduced flux is appealing for a number of reasons. As stated in Chapter 4, lower fluence leads to lower background and less fragmentation of molecular samples which may, in turn, increase sensitivity. Further, in RIMS systems such as those discussed earlier in this chapter, less stringent fluence requirements may lead to the possibility of increasing the geometrical overlap between sputter plume and laser, also increasing sensitivity. Collisional enhancement of ionisation in RIMS apparatus could readily be brought about by the incorporation of a valve and nozzle through which gas e.g. Ar could be introduced to the interaction region between plume and laser, in temporal synchronisation with the laser pulse. Indeed, it is possible that such a modification will be unnecessary and that the Ar^+ ions from the ion gun will themselves serve to bring about collisional ionisation.

A further alternative ionisation method which, although it does employ photoionisation requires less fluence than would normally be required is the use of autoionisation levels. These are energy states/

states above the ionisation potential of an atom (see Figure 6.20) which actually result from configurational changes within the valence electrons lowering the atomic ground state energy so that bound-bound transitions from the ground state occur at higher energy than would be observed in the unperturbed system. If such transitions are of sufficient energy that they would normally promote ground state electrons to the continuum, they are deemed to be autoionising transitions. Transitions to autoionisation states are characterised by high cross sections (relative to bound-continuum cross sections of $\sigma_I = 10^{-17} - 10^{-18}$ cm^2) of around $\sigma = 10^{-15}$ cm^2. Thus two to three orders of magnitude lower fluence will saturate an autoionisation process than will be required to saturate a photoionisation process. Autoionisation levels are, in general, not well known but may be identified by scanning the photoionising laser wavelength (in a multiphoton ionisation experiment) whilst keeping the excitation laser(s) at fixed wavelength until resonances are encountered. Autoionisation levels of plutonium have recently been observed (74) and Letokhov and co-workers have studied gadolinium (140) and ytterbium (141) autoionisation. Since low energy autoionisation levels occur only in elements with two or more valence electrons, it is not possible to study autoionisation in caesium. However, it is thought likely that, once autoionisation levels of more suitable elements have been characterised, they will be used extensively in RIS.

In conclusion, considerable amounts of evidence exist which suggests that current nuclear waste management philosophy is inadequate and that improvements in the understanding of the behaviour of such wastes/

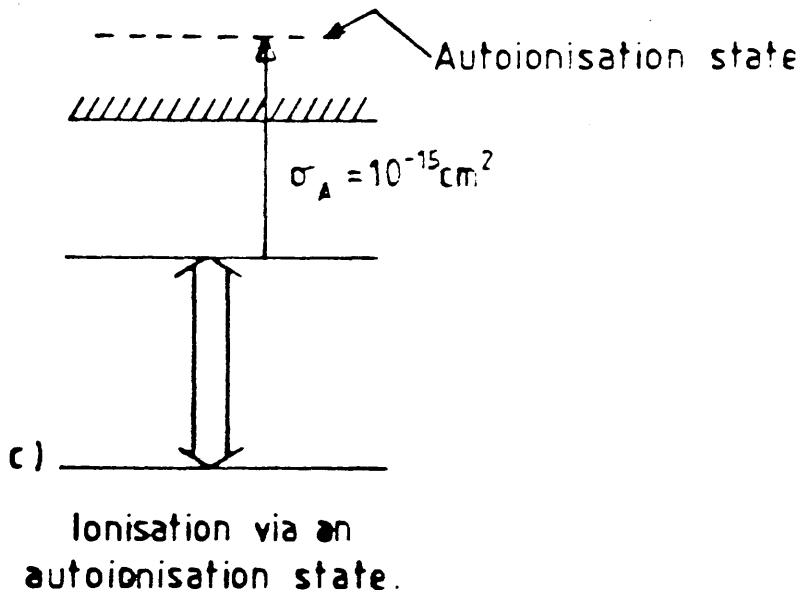

FIG. 6.20: AUTOIONISATION

wastes in the environment are essential (81). In particular, little is known about the movement of low energy waste products through the biosphere as they are difficult to detect by conventional radiometry, particularly at the concentrations at which they occur in environmental materials. The concept that "because these nuclides are present at conventionally undetectable levels they constitute no radiological hazard" is an extremely dangerous one, and opposed to the basic philosophy of the International Commission on Radiological Protection who emphasise that no level of radiation exposure can be deemed to carry zero risk.

To accurately measure low energy nuclides released to the environment a technique capable of ultrasensitive analysis is necessary and, to the knowledge of the author, no analytical method currently established or under development can rival RIS for sensitivity or range of application. Detection limits of at least ppb are prospected from RIMS systems in routine analysis for almost any of the elements (except He or Ne) using samples in any physical form. Isotopic selectivity, at the same sensitivity level, is also achievable. Thus RIS is ideally suited to the analysis of small amounts of radionuclides in environmental substances.

At the present time no demonstration of RIS detection of environmental radionuclides has been performed. However, trace amounts of stable nuclides have been detected, with elemental specificity, from environmental materials e.g. aluminium in seawater, and ruthenium in sediment and bones have been detected at ppb sensitivity or better (21,22).

It/

It is the view of the author that detection of specific isotopes in environmental materials will follow in the near future.

At Glasgow, the RIMS systems under development will soon be operational and isotope selective experimental work will be undertaken. The transition from analysis of laboratory-prepared to environmental samples will follow in due course.

Currently, energy demands are increasing on a global scale whilst fossil fuel resources diminish. The role of resonance ionisation spectroscopy in monitoring the activities of an expanding nuclear power industry is of vital importance since no other analytical technique is capable of the sensitivity required to ensure that nuclear power installations, both present and future, serve the public need for energy without constituting a serious environmental, radiological hazard.

APPENDIX - AN APPLICATION OF RIS TO HIGH ENERGY PHYSICS

A-1 Introduction

Laser induced ionisation has received much attention recently from high energy physicists since the use of lasers to simulate particle tracks has been shown to be an expedient method for calibration of large, multiwire drift chambers, e.g. the ALEPH TPC at CERN (142) shown in Figure A.11. Lasers are suited to such an application, as they can produce narrow, spatially and temporally well defined beams which are not affected by the presence of magnetic fields.

Anderhub and co-workers first demonstrated the generation of ions by a N_2 laser, in a drift chamber (143). Ionisation in counter gas doped with small quantities of nickelocene was studied in 1979 (143), and the results of doping with various organic molecules and ionising with a tunable, dye laser, were reported in 1980 (144). In the chamber used, no background laser induced ionisation (i.e. ions generated in counter gas free of doping material) was ever detected.

Freuholz, conducting experiments on naphthalene detection by two-photon resonance ionisation, also reported zero background ionisation between 280 and 650 nm in a proportional counter system filled with P-10 gas (145).

Around the same time, Bourotte and Sadoulet, using both N_2 and Nd:YAG/

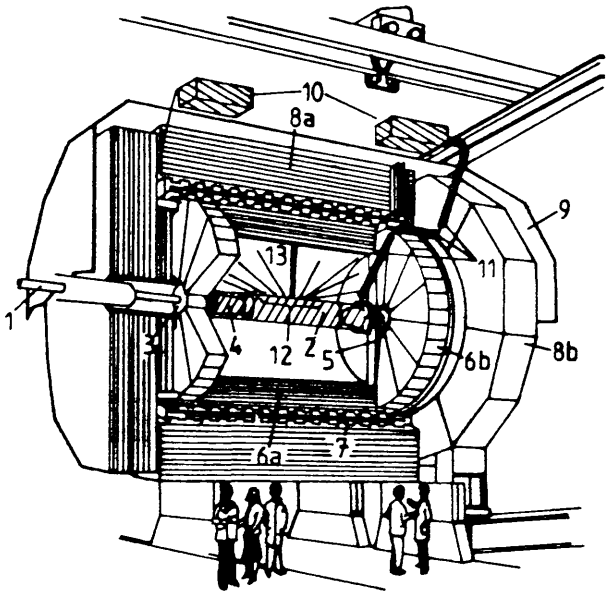

1. BEAM PIPE
2. INNER TRACKING CHAMBER
3. LUMINOSITY MONITOR
4. BEAM PIPE CONE
5. TPC
6a. e-γ CALORIMETER (BARREL)
6b. e-γ CALORIMETER (END CAP)
7. SUPERCONDUCTING SOLENOID
8a. HADRON CALORIMETER (BARREL)
8b. HADRON CALORIMETER (END CAP)
9. MUON CHAMBERS
10. YAG LASER (265nm)
11. MIRRORS
12. PRISMS ATTACHED TO INNER FIELD CAGE.
13. LASER TRACKS INSIDE THE TPC VOLUME

FIG. A.11: THE TIME PROJECTION CHAMBER (TPC)

Nd:YAG lasers did observe a background in their drift chambers, of roughly 200 ion pairs/cm/μJ of laser fluence (146). At the N_2 wavelength (337 nm), the ionisation showed a quadratic power dependence whereas at the quadrupled Nd:YAG wavelength (265 nm) a linear dependence was apparent. This was thought to indicate that ionisation at 265 nm was occurring via a two photon process with a real intermediate level, and that the first (i.e. excitation) step was saturating. Hilke observed a background signal, at the N_2 wavelength, of 2×10^3 ion pairs/cm (147). This background was of linear power dependence at low powers but became exponential as the fluence was increased. Desalvo and Desalvo, also using a N_2 laser, confirmed a quadratic dependence of background ionisation on laser fluence at low power, and observed this to become linear at a fluence of 20 $\mu J/mm^2$ (148). The background ionisation level was 38 ion pairs/μJ of incident light (148). Guo *et al.* observed 5×10^4 ion pairs/cm at a high N_2 laser fluence of 40 MW/mm^2, although this was measured in a drift chamber which had been doped with N,N-diethylamine, an additive known to increase ionisation by a factor of 10 or 20 (149).

Thus highly variable amounts of background ionisation were encountered by different workers and in different chambers. It became clear that some method of standardisation, so that the same laser fluence always gave approximately the same amount of ionisation (at any constant wavelength), was required. A suitable method is seeding - the introduction to the counter gas of small quantities of an ionisable molecular species which will give reproducible/

reproducible and controllable, above background, levels of ionisation without in any way degrading the performance of the chamber itself.

Within the framework of the CERN collaboration, work has been undertaken at Glasgow to test a variety of compounds potentially useful as seeding agents, and to recommend the most suitable for use in the ALEPH TPC.

A-2 Seeding Agents

The substances tested for their suitability as seeding agents are shown in Figure A.21. They are triethylamine (TEA), tetrakis-(dimethylamino)ethylene (TMAE), N,N-dimethylaniline (DMA), N,N-diethylaniline (DEA), and trimethylamine (TMA) (107,150). Some properties of the compounds are shown in Table 16.

Phenol and toluene, the principal components of background in the proportional counters constructed at Glasgow, have also been considered for the role of seeding agents.

The study of ionisation induced in counter gas seeded with the above compounds was carried out using types 1, 2 and 3 counters described in Chapter 4. Any increase in laser induced ionisation resulting from seeding which is observed in a small, single-wire proportional counter may be expected to be apparent also in a large, multi-wire chamber. Two different techniques were used to introduce the/

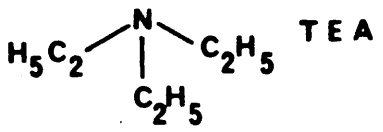

TEA

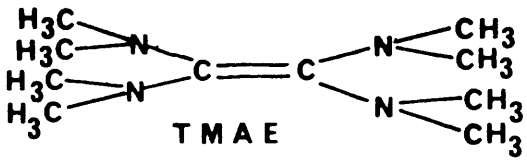

TMAE

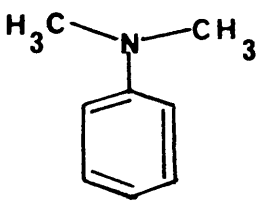

DMA

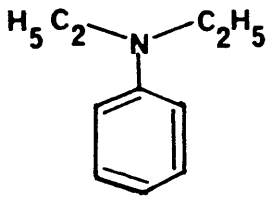

DEA

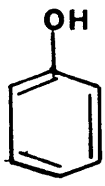

Phenol

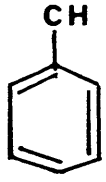

Toluene

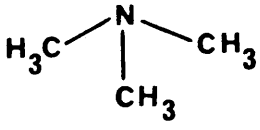

TMA

FIG. A.21: SEEDING COMPOUNDS

TABLE 16

Properties of Seeding Agents Described

NAME	CHEMICAL FORMULA	MOL.WT. (AMU)	M.Pt. (^{o}C)	B.Pt. (^{o}C)	IONISATION POTENTIAL (eV)
TEA	$C_6H_{15}N$	101.19	-114.7	89.3	7.5 (151)
DMA	$C_8H_{11}N$	121.18	2.45	194.15	7.14 (151)
DEA	$C_{10}H_{15}N$	149.24	-38.8	216.27	6.99 (151)
TMAE	$C_{10}H_{24}N_4$	200.23	-12 -10	59 *	5.36 (152)
TMA	C_3H_9N	59.11	-117.0	2.9	7.82 (116) 8.5 (153)

* at 0.9 mm Hg

the seeding agents to the counter - the static filling method and the flowing method.

In the static mode of operation, both the counter and a resealable vial containing the seed were connected to a vacuum system. A MKS Baratron - a device for recording differential pressure across a membrane - was also attached to the sytem. The Baratron had previously been carefully calibrated using distilled water samples. After the system had been evacuated (using a rotary and an/

an oil diffusion pump) the sample vial was opened to the counter and the seeding pressure read from the Baratron. To vary the seed pressure, the seed sample temperature could be altered by immersing the vial in a freezing, crushed ice and salt mixture (for temperatures below $0^{o}C$) or in a controlled temperature water bath (for higher temperatures). After the seed had been introduced, the counter was filled to 760 torr with standard P-10 counter gas (10% CH_4 in Ar) and closed off.

The apparatus used for flowing mode operation is shown in Figure A-22. This device, made of pyrex glass and incorporating ground glass taps lubricated with silicon grease, was placed in the gas inlet line of the counter and Ar/CH_4 mixture was flowed through. The counter gas could be made either to bypass or to flow over the seed reservoir. Control of the seed vapour pressure was again brought about by varying the temperature of the sample with a water bath or with a freezing mixture contained in an insulated dewar vessel. A flowmeter was also included in the counter outlet pipe.

Since, in both seeding techniques, the amount of seed introduced to the counter was governed by the temperature dependence of its vapour pressure, accurate knowledge of this relationship was vital. Unfortunately, however, there were no published reports available of the saturated vapour pressures of most of the seeding agents at sub-zero temperatures. Therefore the MKS Baratron and vacuum system used for static mode operation was also used to measure saturated/

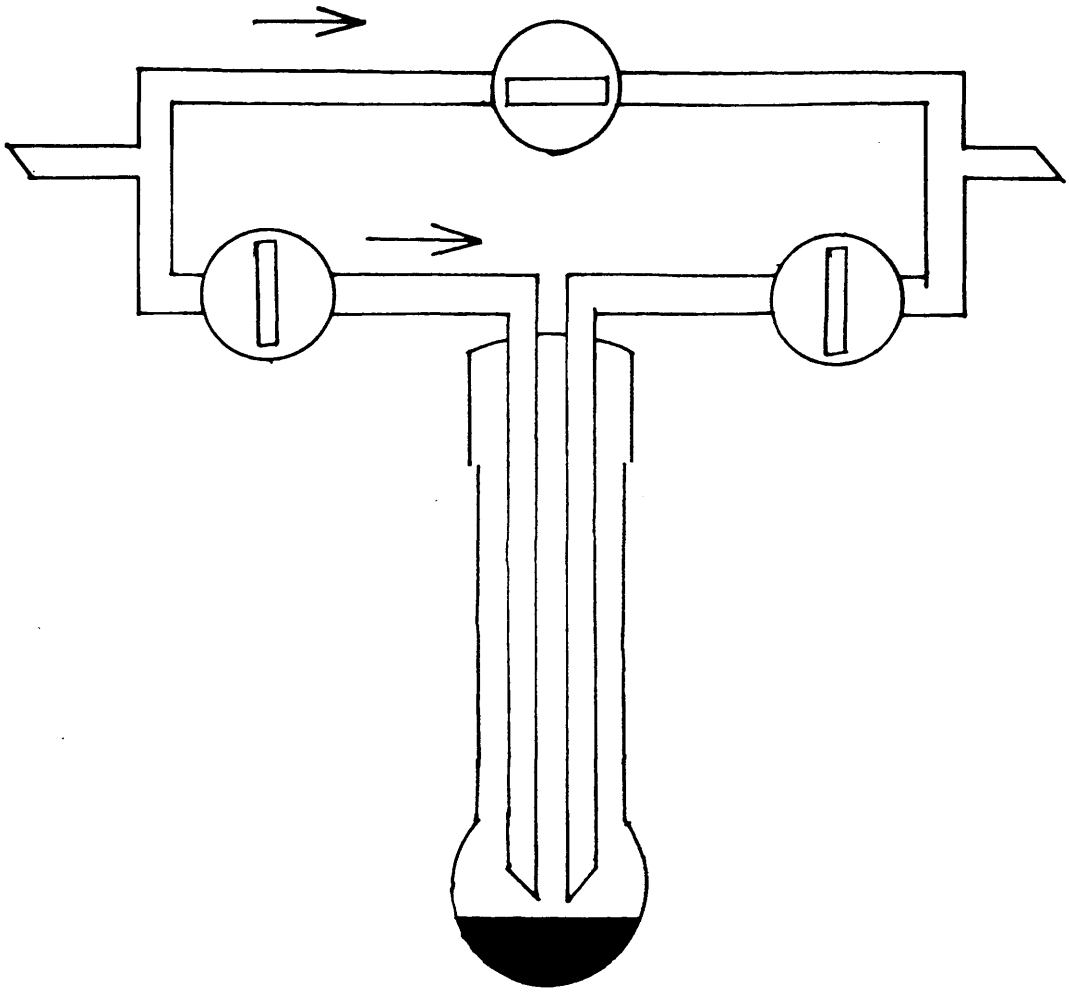

FIG. A.22: SEEDING APPARATUS

saturated vapour pressure data for DMA, DEA, and TMAE. For TEA, which has a higher vapour pressure, a mercury filled glass manometer replaced the Baratron.

Vapour pressure data was obtained as follows. A sample of the prospected seeding agent was pipetted into a resealable vial. Since most of the compounds studied are toxic, this procedure was carried out in a fume cupboard. The vial was connected to the vacuum system, pumped on for ~ 30 seconds to remove air, and resealed. It was surrounded with freezing mixture or water and left to stand for a few minutes to allow the saturated vapour pressure appropriate to that temperature to be achieved. Meanwhile the vacuum system was evacuated. Presently, the vapour was released from the vial into the system (with the vacuum pumps closed off). The rise in pressure after opening of the sample vial and closing off of the pumps was monitored for several minutes. It was found to consist of two components, one of which was rapid and was attributed to the build-up in seed vapour pressure within the system, and the other of which remained constant with time and was attributed to outgassing of impurities from the vacuum system itself. Saturated vapour pressure values reported are the result of plotting pressure versus temperature graphs and extrapolating the pressure increase attributable to leaks back to the origin, to obtain the pressure increase associated with the seed sample. Three measurements were taken at each temperature and averaged to give a final result. Errors are estimated as $\pm$ 10%. Whenever the temperature of the sample was changed the sample vial was pumped on for/

for 30 seconds to remove any excess vapour associated with previous measurements.

I TEA

The saturated vapour pressure of TEA as a function of temperature is shown in Figure A.23. The straight line has been drawn to guide the eye only and the inclusion of two points at certain temperatures is to indicate the reproducibility of the results. The present measurements in the -20 - 11°C region are a reasonable extrapolation of the higher temperature work reported in the literature (154).

TEA was introduced to a type 1 counter in flowing mode, at various pressures. The output of the LUMONICS TE-861-3M, operated as a N_2 laser (i.e. filled with N_2 rather than with a conventional excimer filling mixture, and fitted with unstable resonator optics) was directed through the counter at a fluence of 14 $\mu J/mm^2$. At 337 nm, TEA gave little or no ionisation above background (40 - 60 ion pairs/cm in the counter used). This is to be expected since two photons at 337 nm (3.68 eV) are of insufficient energy to bring about ionisation of the TEA molecule (I.P. 7.5 eV).

Using the excimer pumped dye laser system, however, ionisation considerably greater than background was observable with TEA, but only at wavelengths below 280 nm. This is shown in Figure A.24, which also, for comparison, shows the background in the counter prior to seeding. The data shown was recorded in a type 2 counter to/

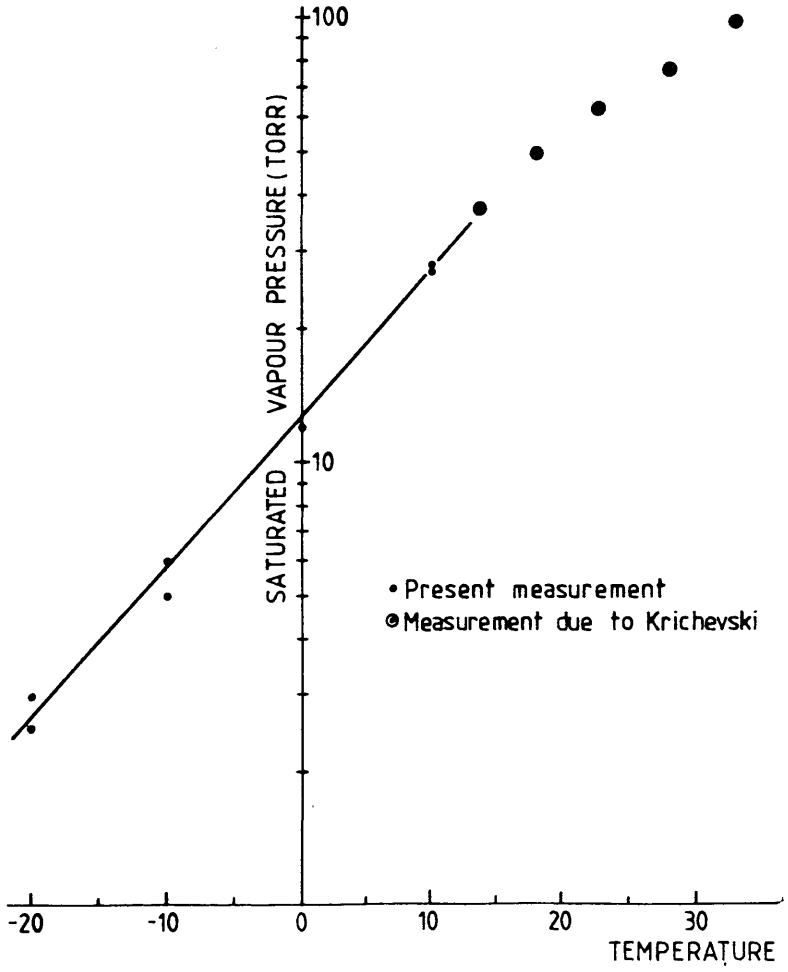

FIG. A.23: SATURATED VAPOUR PRESSURE OF TEA AS A FUNCTION OF TEMPERATURE

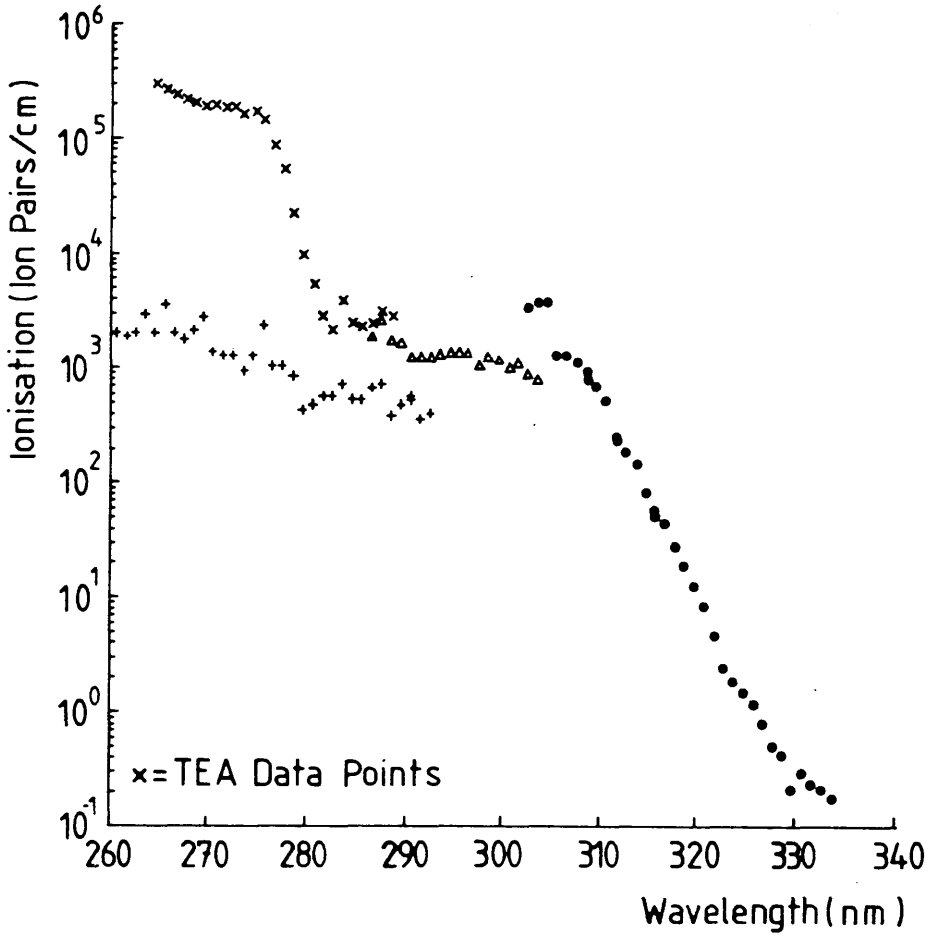

FIG. A.24: WAVELENGTH DEPENDENCE OF A COUNTER SEEDED WITH TEA. (The different symbols (+, Δ and o) indicate different laser dyes.)

to which TEA was introduced by flowing Ar/CH_4 over a sample held at $-20^{\circ}C$ (equivalent to a saturated vapour pressure of 2.5 torr). Figure A.24 shows results normalised quadratically to a laser fluence of 1 $\mu J/mm^2$. The actual fluence was 8.1 $\mu J/mm^2$. A quadratic dependence of ionisation on laser fluence was observed throughout the range of the wavelength scan. At the quadrupled Nd:YAG laser wavelength of 266 nm - important since Nd:YAG lasers have now superseded N_2 lasers as candidates for calibration work at CERN - TEA gives an ionisation level more than two orders of magnitude greater than background.

A problem, apparent in work with TEA in both types of counter, was that it profoundly affected the gas gain, increasing it by as much as a factor of six (as determined from the ^{55}Fe calibration source pulse height). This may be due to the relatively high pressure of TEA in the counter ($\sim 0.3\%$ of the gas fill). Care is required, when seeding with TEA, that the change in gas gain is not interpreted as an increase in ionisation.

II DEA

The saturated vapour pressure of DEA as a function of temperature is shown in Figure A.25, along with literature results (155). Some discrepancy is evident between the accepted and measured value which may be due to condensation of DEA within the vacuum system.

DEA was seeded into a type 1 counter by the flowing method. The N_2 laser/

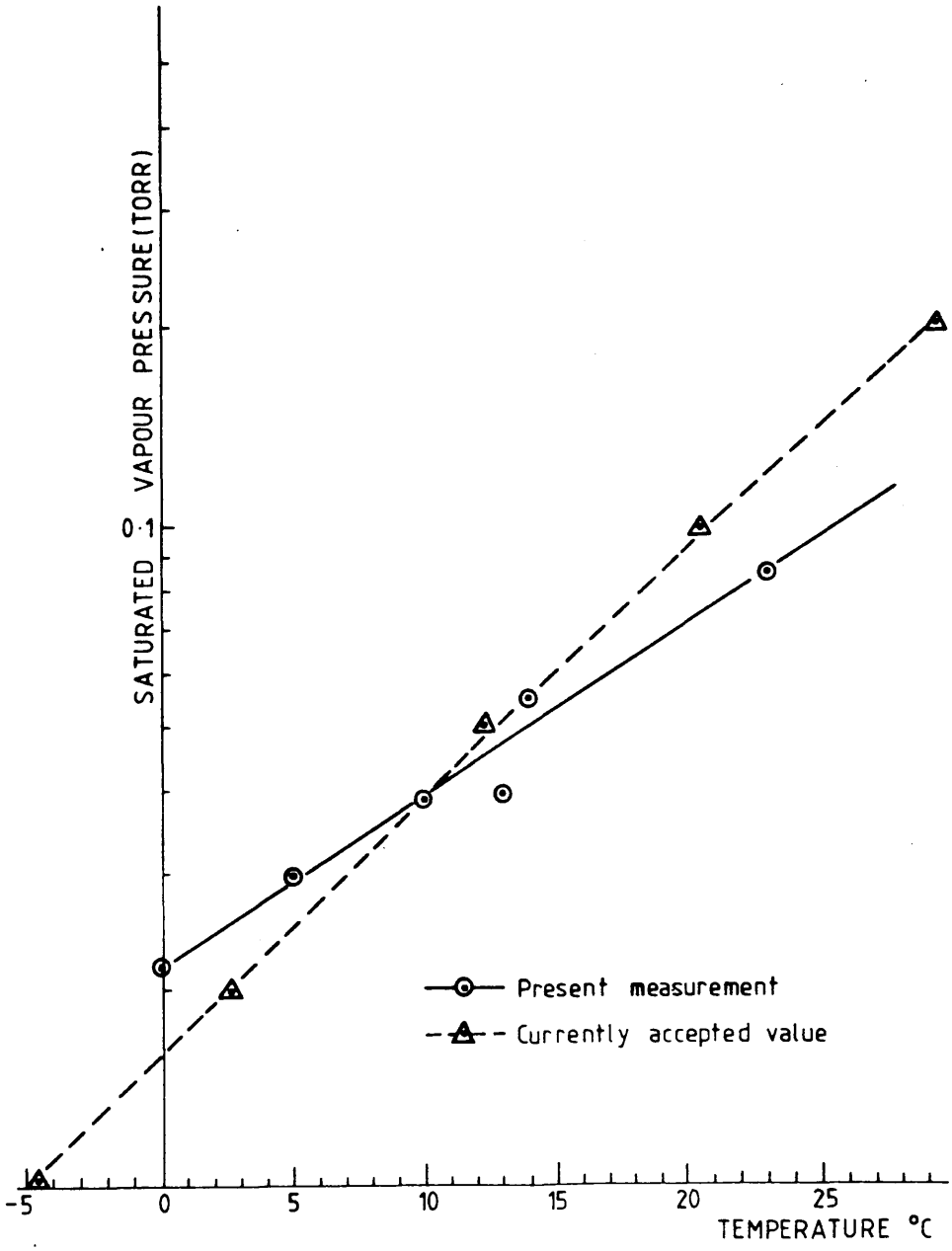

FIG. A.25: SATURATED VAPOUR PRESSURE OF DEA AS A FUNCTION OF TEMPERATURE

laser was used (fluence 14 $\mu J/mm^2$). Results for DEA samples at a variety of different temperatures are shown in Figure A.26. For the first few minutes of data collection, the DEA sample was bypassed. When the Ar/CH_4 was switched to flowing over the seed reservoir, ionisation increased smoothly to a constant level determined by the seed sample temperature. The maximum ionisation attained was found to be independent of Ar/CH_4 flowrate in the range 50 -- 250 ml/min, although the slower the flowrate the longer it took for the maximum level of ionisation to be achieved. When the DEA sample was bypassed, ionisation returned to background levels. This typically took somewhat longer than the ionisation increase when DEA was switched on, i.e. about twice as long; the time taken to reach background being a function of Ar/CH_4 flowrate. It was also observed that flowing Ar/CH_4 very fast through the counter (i.e. $\gg$ 250 ml/min) depressed the ionisation and that it rose again when the flowrate was reduced. This was tenuously attributed to the speed of the counter gas molecules reducing the gas gain although no ^{55}Fe data was taken at very fast flowrates to substantiate the possibility.

Since the currently reported and literature values of DEA saturated vapour pressure were discrepant, an alternative method of measuring DEA vapour pressure was used. This measurement was also useful in that it tested whether or not saturated vapour pressures of seed were generated in flowing mode operation. After de-gassing the ground glass joint, the DEA sample and reservoir were weighed to four decimal places on an accurate balance [UNIMATIC Model GL1] .

Ar/CH_4 /

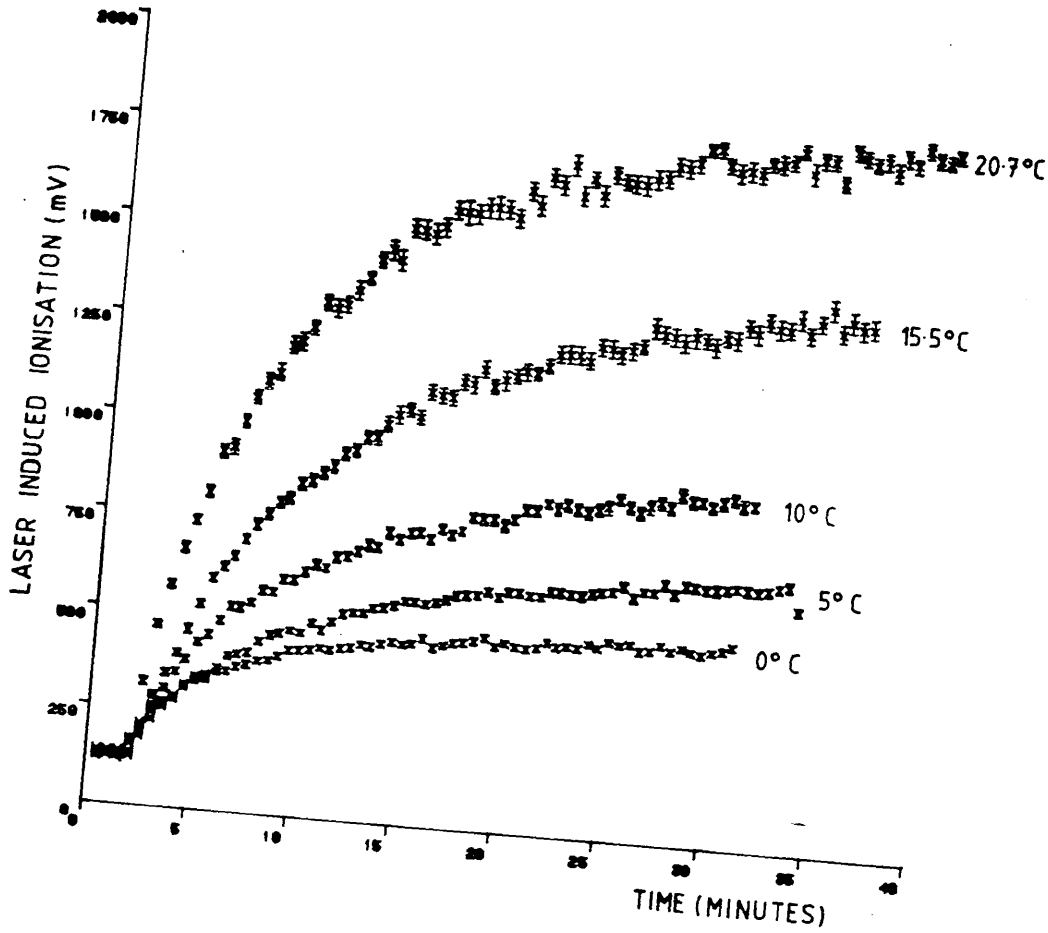

FIG. A.26: DEA SEEDING EXPERIMENTS

Ar/CH_4 gas was flowed over the sample, at a constant flowrate, for several hours, after which the sample and reservoir were reweighed. From the rate of mass loss and the flowrate, a value of the DEA vapour pressure actually maintained in the gas stream was calculated. At 20°C for example, where the saturated vapour pressure measured in static mode is 0.075 torr, a value of 0.025 torr was found. For DEA, the vapour pressure generated in flowing mode operation is therefore approximately $\frac{1}{3}$ of the saturated vapour pressure value appropriate to the sample temperature. With the above amount of DEA in the Type 1 counter (and at the N_2 wavelength) an ionisation level of around 35 times background was measured.

It became apparent, in static mode operation of the DEA seeded counter, that the substance was sticking to the inner walls. Even after considerable periods of pumping using rotary and diffusion pumps ionisation did not return to background levels although, as stated above, DEA could be flushed out of the counter. It is therefore unlikely that DEA would be a suitable seeding agent for large chambers since the amounts of Ar/CH_4 required to flush out such volumes would be prohibitive (as would the fire risk associated with the vented counter gas).

III DMA

The saturated vapour pressure of DMA as a function of temperature is shown in Figure A.27. The present measurement is only slightly lower than the literature value (155).

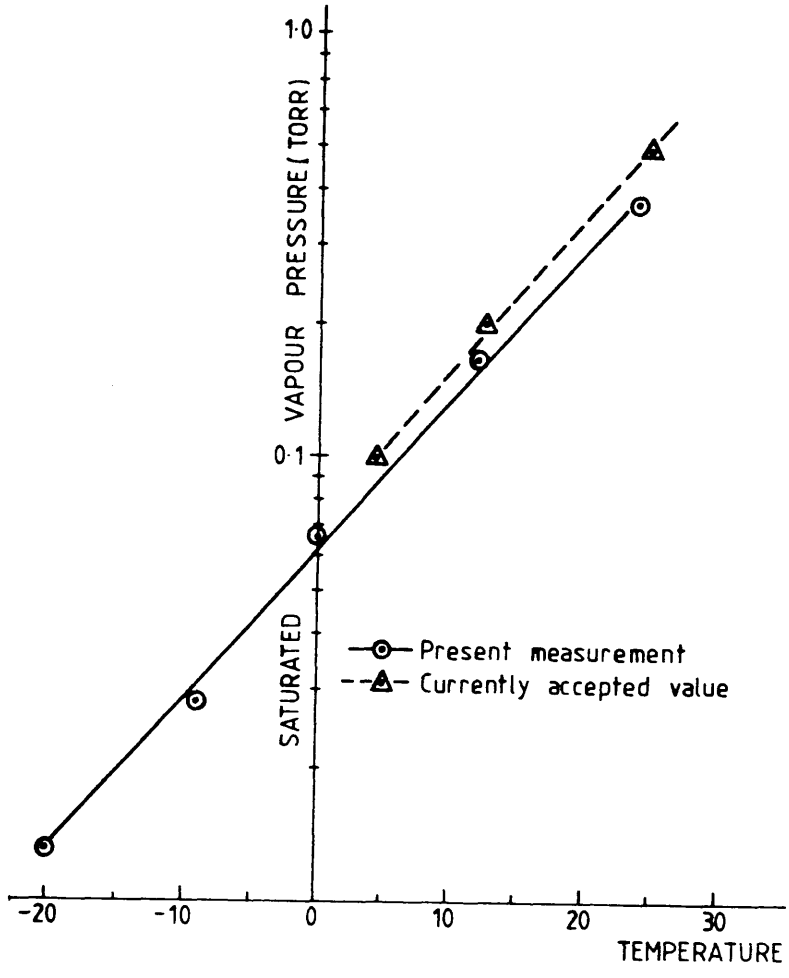

FIG. A.27: SATURATED VAPOUR PRESSURE OF DMA AS A FUNCTION OF TEMPERATURE

DMA was introduced to a type 1 counter by static operation at partial pressures between 0.04 and 0.3 torr. The total pressure in the counter was 760 torr, the remainder of the fill being Ar/CH_4. Again using the N_2 laser (fluence 14 $\mu J/mm^2$) the ionisation in the counter was a linear function of seeding pressure in the 0.04 — 0.3 torr range as is shown in Figure A.28. Results in this figure have been normalised, quadratically, to 14 $\mu J/mm^2$ as the laser output was varying by around 30% during data collection. Quadratic normalisation is valid since previous experiments had shown DMA ionisation to be quadratically dependent on laser fluence at 337 nm. At 0.3 torr seeding pressure the DMA ionisation was around 40 times background.

Pressures of DMA greater than 0.3 torr were found to degrade the counter performance, i.e. the ^{55}Fe spectrum resolution deteriorated. However, when the counter was seeded to $\leq$ 0.3 torr with DMA the gas fill could be left for several days without the ^{55}Fe resolution (26 - 27%) being affected, although ionisation decreased by $\sim \frac{1}{3}$ over a period of one week.

In flowing mode operation at 337 nm, plots similar to Figure A.26 were obtained for DMA. The wavelength dependence of DMA, also introduced by flowing but this time into a type 2 counter is shown in Figure A.29. Again, background is shown for comparison. The DMA ionisation shows similar variation with wavelength as does the background, but at a higher number of ion pairs/cm. In the spectrum shown, DMA was seeded into the counter at 0°C, equivalent to a saturated vapour pressure of 0.06 torr. At 266 nm, the ionisation

from /

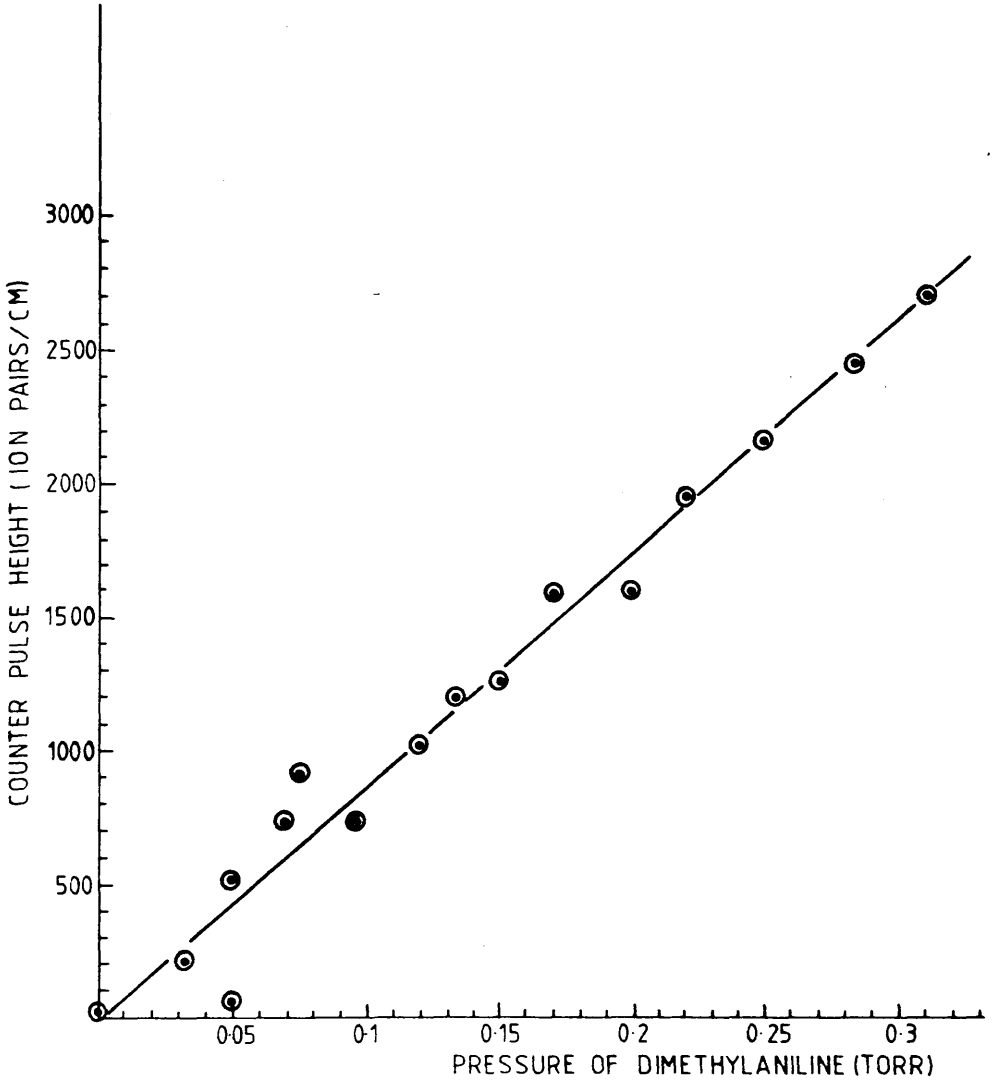

FIG. A.28: VARIATION OF LASER INDUCED IONISATION WITH PRESSURE OF DMA INTRODUCED IN THE STATIC MODE

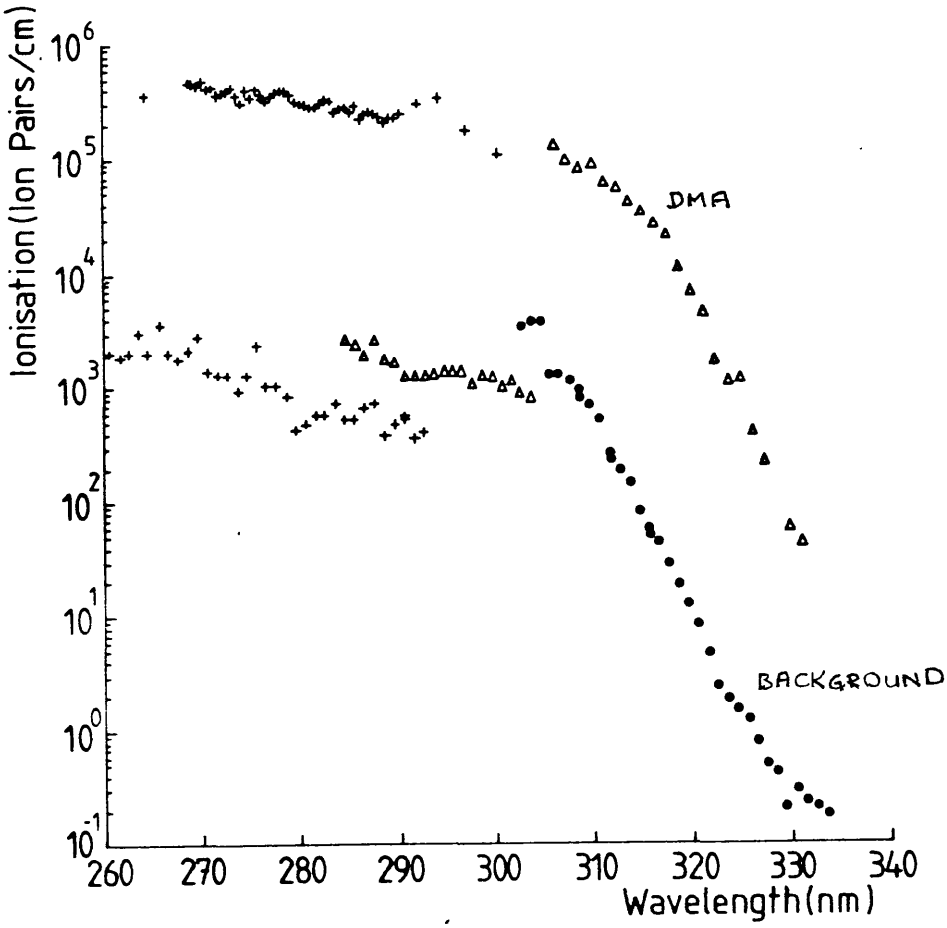

FIG. A.29: WAVELENGTH DEPENDENCE OF COUNTER SEEDED WITH DMA

from the counter seeded with DMA at $0^{o}C$ is around two orders of magnitude greater than background.

The actual vapour pressure of DMA introdcued to the counter in flowing operation was calculated in an analogous way to that of DEA. At $0^{o}C$, a value of 0.036 ± 0.004 torr was calculated, i.e. 60% of the saturated vapour pressure.

As described previously, DEA had been found to stick to the inner surfaces of the counter. Similar behaviour had not been observed for DMA, i.e. it seemed to be easily pumped out of the counter. To test whether there was any "stickiness", however slight, in DMA the following was carried out. The type 2 counter was seeded with a small pressure of DMA, in static mode. The pressure was measured on the MKS Baratron. Next the counter was filled to a total pressure of 760 torr with Ar/CH_4, and the ionisation was measured. The counter was pumped out to 380 torr, topped-up to 760 torr with Ar/CH_4, and the ionisation again measured. The procedure was repeated several times and laser induced ionisation plotted against nominal DMA pressure (assuming that this halved on each refill). The resulting graph - Figure A.210 - is non-linear indicating that DMA is not as easy to pump from the counter as Ar/CH_4, i.e. some DMA is retained. However, if the counter was fully opened to the rotary pump and evacuated before refilling with Ar/CH_4, background levels of ionisation could be restored. Even the small amount of "stickiness" observed in DMA may ultimately preclude its use in large drift chambers.

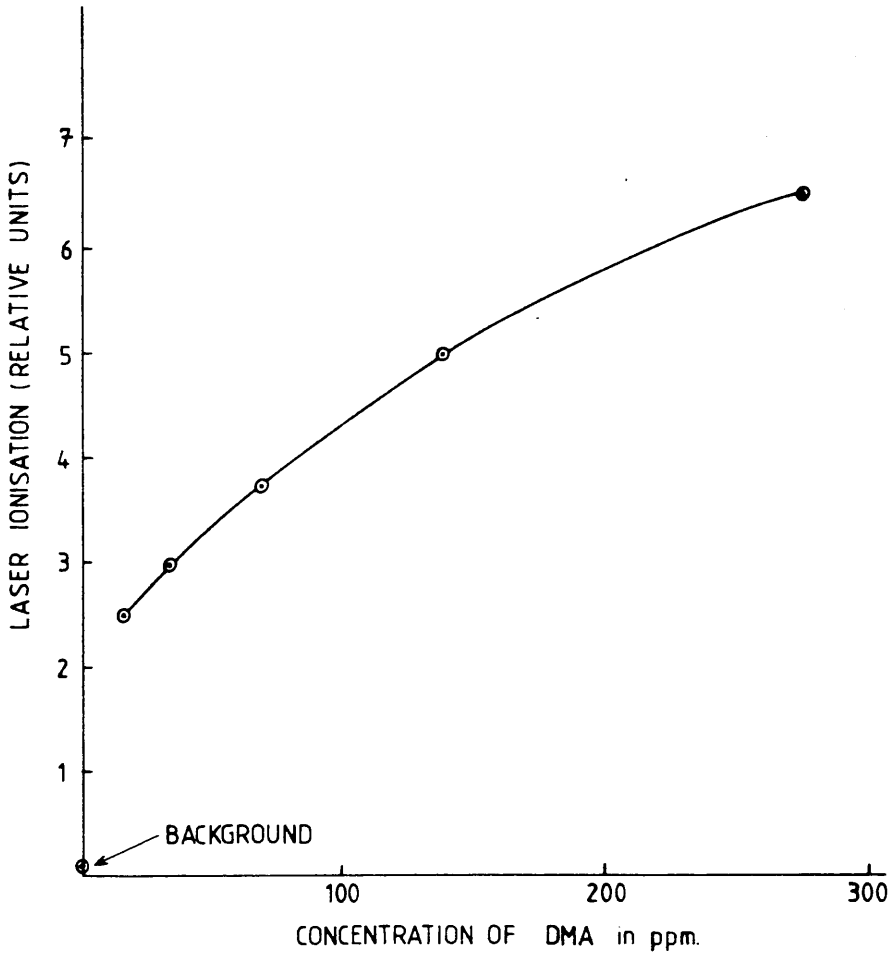

FIG. A.210: TEST OF "STICKINESS" OF DMA IN A TYPE 2 COUNTER

IV TMAE

The saturated vapour pressure of TMAE as a function of temperature is shown in Figure A.211. Reasonable agreement is found between the present work and recent results published by Anderson (156).

TMAE was first introduced to a type 1 counter, in static mode, at $-17^{o}C$, at which the saturated vapour pressure, by linear extrapolation of Figure A.211, is less than 0.02 torr. Very large amounts of ionisation were generated at the N_2 laser wavelength, saturating the electronics even at the lowest gas gain and laser fluence available. Attempts were made to pump the TMAE from the counter and reseed at lower temperature.

Removal of TMAE by pumping proved extremely difficult however. Anderson reported that TMAE introduced to an evacuated metal chamber would not only condense on to all available surfaces within seconds but would, thereafter, require many hours of pumping to remove it (157). This was also apparent at Glasgow, where many hours of pumping on an oil diffusion pump were required to return ionisation in a TMAE seeded counter to background levels.

Using the flowing mode and a solid TMAE sample at around $-40^{o}C$, ionisation in the type 1 counter was around 5×10^{3} ion pairs/cm at 337 nm. The saturated vapour pressure of TMAE at this temperature was estimated as $\sim 10^{-3}$ torr, although the actual pressure in the counter gas stream may be lower, as was observed for DEA and DMA in flowing modes. However ionisation was found to vary with time and

was/

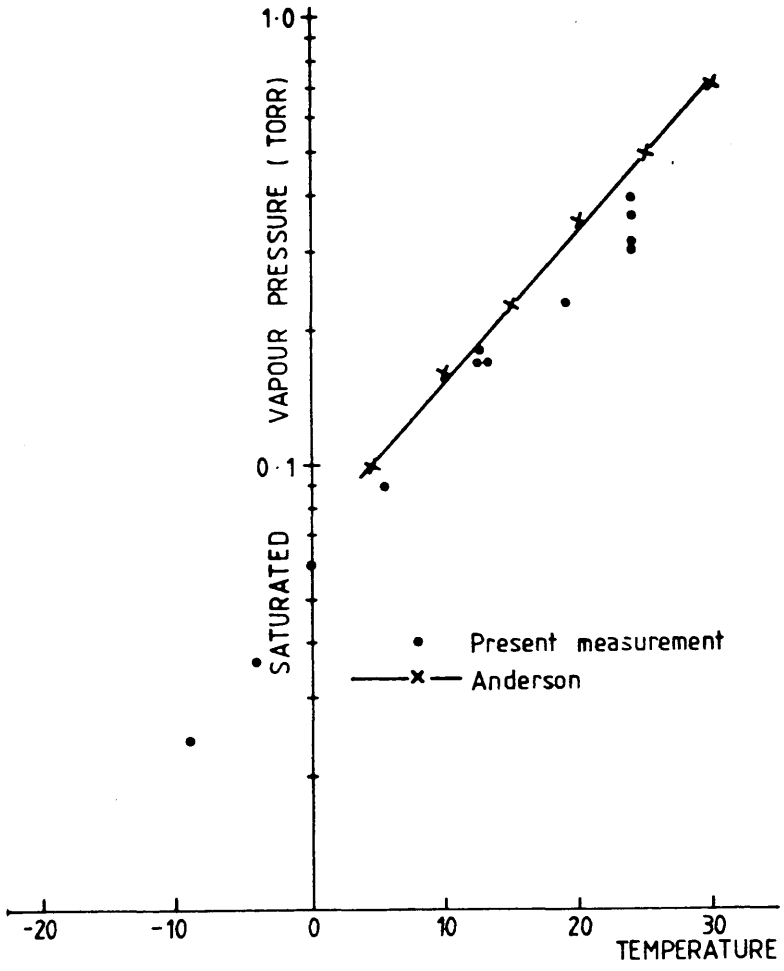

FIG. A.211: SATURATED VAPOUR PRESSURE OF TMAE AS A FUNCTION OF TEMPERATURE

was not reproducible in subsequent seeding experiments at identical temperatures. The "sticky" nature of TMAE was apparent even in flowing operation: it was necessary to flow Ar/CH_4 through the co counter for at least 12 — 16 hours to remove the seeding agent.

Due to difficulties in controlling the level of ionisation produced and to its extreme "stickiness", TMAE seemed the least suitable potential seeding agent for large drift chambers.

V TMA

TMA was introduced to a type 3 counter, in static mode, at a pressure of 10 torr as measured by the MKS Baratron. The counter was then filled to 760 torr with Ar/CH_4 and the wavelength dependence of the ionisation recorded in the range 266 - 320 nm. See Figure A.212. The ionisation from TMA exceeds background at 295 nm, and continues to rise, without indication of levelling-off, to 270 nm. At 266 nm and 1 $\mu J/mm^2$ laser fluence, TMA ionisation is 5.7×10^5 ion pairs/cm, i.e. around two orders of magnitude greater than background (n.b. TMA pressure = 10 torr). Extrapolating this result linearly to a much lower TMA pressure of 3 ppm a value of 130 ion pairs/cm at 1 $\mu J/mm^2$ fluence is obtained, comparable with the result of Hubricht et al. (112) of 160 ion pairs/cm.

To investigate the "stickiness" of TMA, an analogous experiment to that carried out for DMA was undertaken, i.e. the counter was filled with a small pressure of the seeding vapour then to 760 torr with Ar/CH_4. /

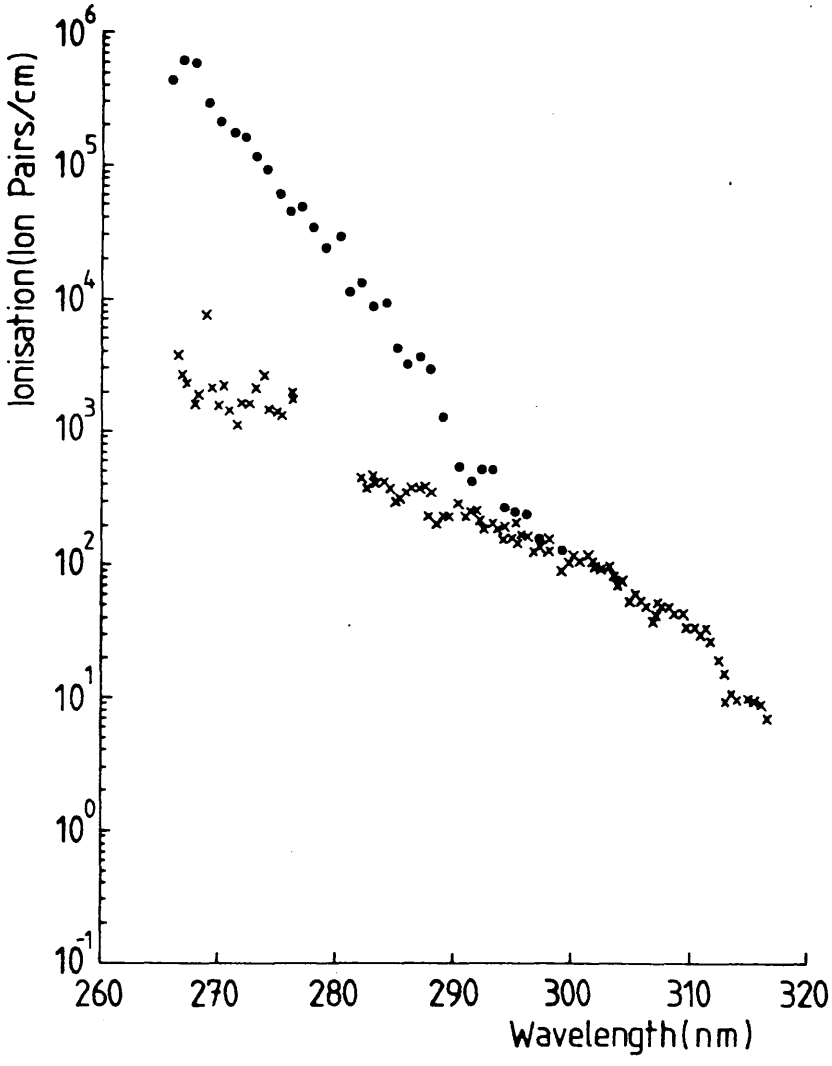

FIG. A.212: WAVELENGTH DEPENDENCE OF A COUNTER SEEDED WITH TMA

Ar/CH_4. The pressure was repeatedly halved, topping up to 760 torr with Ar/CH_4 and measuring the ionisation at each point. A plot of ionisation versus nominal TMA pressure is shown in Figure A.213. After background subtraction, a fairly linear relationship emerges showing TMA has little tendency to adhere to surfaces within the counter.

The resolution of the ^{55}Fe spectrum in a counter seeded with TMA was stable over more than 2 weeks (the duration of the experiment), although ionisation fell by a factor of 4 during this period.

Although TEA seems the most promising seeding agents tested, it has one major disadvantage. This is its characteristic and highly unpleasant smell (of rotting fish) even at ppb concentrations. Since the ALEPH TPC is unlikely to be totally leak-tight, this may become an important consideration.

VI Synopsis

The results for the five potential multiwire chamber seeding agents are summarised in Table 17.

DEA is too "sticky" to be useful in large chambers and TMAE too difficult to control. The gas gain problem associated with TEA renders it unsuitable also in the absence of some external method of calibration, e.g. X-ray sources. TMA and DMA are the most suitable substances tested although neither is ideal. The slightly "sticky"/

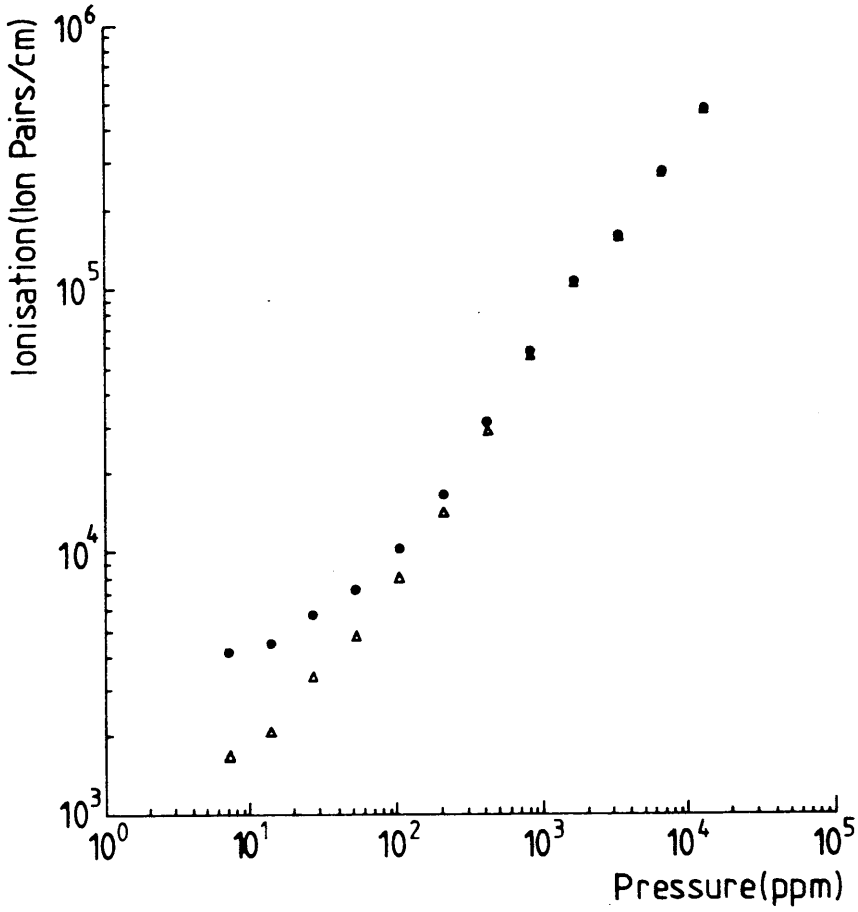

FIG. A.213: TEST OF "STICKINESS" OF TMA IN A TYPE 3 COUNTER

TABLE 17

Summary of Seeding Experimental Results

SUBSTANCE	IONISATION AT 337nm in ion pairs/cm FLUENCE = 14 $\mu J/mm^2$ (VAPOUR PRESSURE)	IONISATION AT 266nm in ion pairs/cm FLUENCE = 1 $\mu J/mm^2$ (VAPOUR PRESSURE)	NOTES
TEA - Static	NM	NM	gas gain affected
Flow	None	2.6×10^5 (2.5 torr)	
DEA - Static	NM	NM	"sticky"
Flow	1.8×10^3 * (0.025 torr)	NM	
DMA - Static	2.0×10^3 (0.3 torr)	NM	slightly "sticky"
Flow	1.2×10^3 * (0.18 torr)	4×10^5 * (0.036 torr)	
TMAE - Static	large (0.02 torr)	NM	uncontrollable
Flow	5×10^{-3} (10^{-3} torr)	NM	very "sticky"
TMA - Static	NM	5.7×10^5 (10 torr)	odour
Flow	NM	NM	

NM = not measured * = calculated from mass loss and flowrate measurements

"sticky" nature of DMA may constitute a problem and the combination of TMA's unpleasant odour and the relatively high partial pressures at which it must be used (i.e. 10 torr to produce $\sim 10^5$ ion pairs as compared with the 0.036 torr of DMA) may render it unusable.

Rudimentary experiments on a number of other chemicals to determine their suitability as seeding agents were undertaken. Methanol and ethanol (I.P. 10.85 and 10.47 eV respectively (116)) gave negligible ionisation in a type 1 counter at 290 nm and a laser fluence of 100 $\mu J/mm^2$, which is expected since the ionisation potentials are high. Naphthalene (I.P. 8.13 eV (116)), and N,N,N',N'-tetramethyl-phenylenediamine (TMPD) (I.P. 6.18 eV (112)) introduced to a type 3 counter were difficult to control or "sticky". Hubricht et al. also seeded a chamber with TMPD (112) and naphthalene (158) but required a sophisticated gas purification system to return ionisation levels in the chamber to background after seeding.

VII Phenol and Toluene

As was discussed in Chapter 4, phenol and toluene are the main constituents of background ionisation in Glasgow-built proportional counters. Since they are, manifestly, ionisable at around 266 nm, do not seem to adversely affect counter performance and give large amounts of ionisation at low concentrations they may be very suitable as seeds. The properties of the two compounds, both chemical and as seeding agents, are shown in Tables 18 and 19.

Phenol/

TABLE 18

Properties of Phenol and Toluene (115)

NAME	CHEMICAL FORMULA	MOL.WT. (AMU)	M.Pt. (^{o}C)	B.Pt. (^{o}C)	IONISATION POTENTIAL (eV) (116)
Phenol	C_6H_6O	94.11	43	181.7	8.5
Toluene	C_7H_8	92.14	-95	110.6	8.82

TABLE 19

Seeding Properties of Phenol and Toluene

NAME	IONISATION AT 266nm (ion pairs/cm) FLUENCE = 1 $\mu J/mm^2$	VAPOUR PRESSURE	NOTES
Phenol	3.5×10^4	$\sim$ ppm	"sticky"
Toluene	3.7×10^3	$\sim$ ppb	

Phenol proved very difficult to remove from counters after seeding. It could only be removed by dismantling the counter and baking and cleaning the component parts. Toluene, by contrast, was easily removed from a counter by flushing with clean Ar/CH_4. It is of low toxicity and has a slight but not unpleasant odour. Thus it seems that/

that toluene may be the most suitable seeding agent so far studied, provided that it is introduced at high enough concentrations that any contribution to ionisation from "background" toluene be negligible.

Fragmentation of toluene (and phenol) when subjected to laser radiation is important for two reasons. Firstly, if they are to be used as seeding agents, care must be taken not to produce radicals or reactive hydrocarbon fragments which could impair counter operation and, secondly, in analytical techniques such as RIMS, the products from laser fragmentation of background impurities may give rise to isobaric interference. To investigate the fragmentation patterns arising from irradiation of toluene and phenol with laser light a small, quadrupole mass spectrometer was used [VSW].

Phenol or toluene was introduced to the mass spectrometer at a base pressure of 10^{-6} torr, in a stream of Ar/CH_4, through a needle valve. The 266 nm output of the dye laser was focussed into the region of the mass spectrometer where ionisation had formerly been brought about by an electron beam. Ions produced by the laser passed through the quadrupole filter just as electron beam induced ions would, and were detected using a Faraday plate or secondary ion multiplier.

At a fluence of 3 mJ/mm^2 considerable fragmentation of the molecules was apparent as is shown in Figure A.214 (159). However at lower fluence, $< \sim 1$ mJ/mm^2, it was possible to obtain mass spectra containing only the parent ion peaks (M^+). In both analytical and HEP applications/

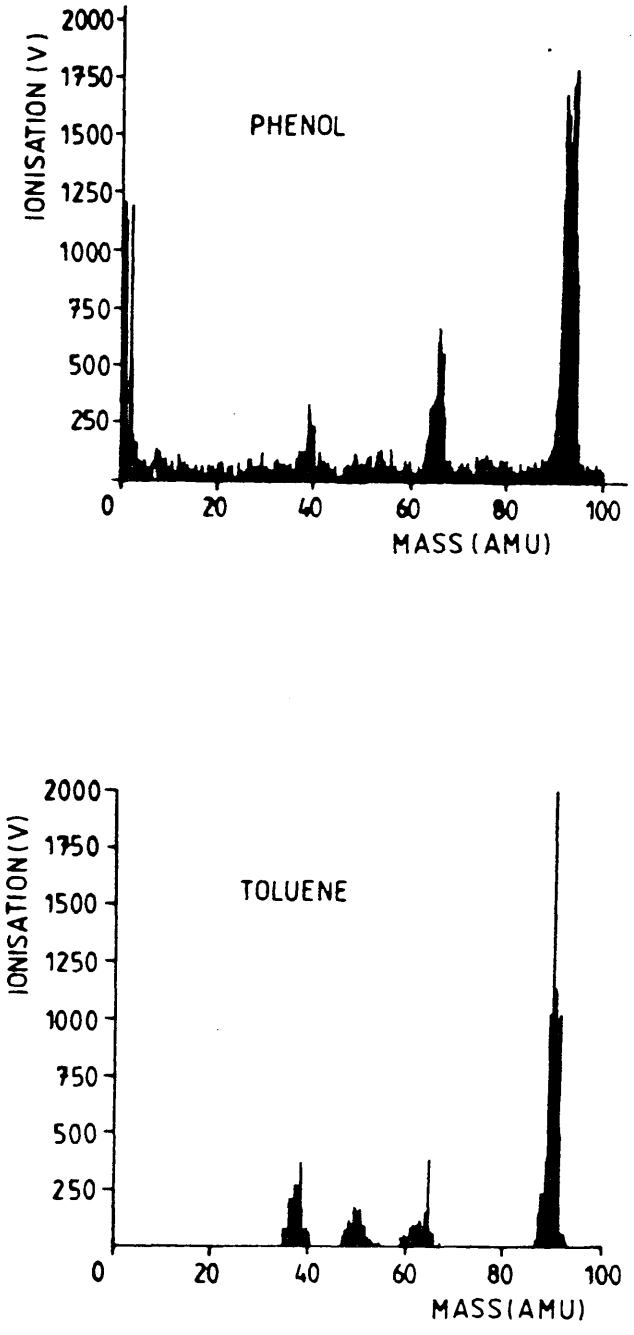

FIG. A.214: THE LASER-INDUCED FRAGMENTATION OF PHENOL AND TOLUENE

applications of laser induced ionisation it may therefore be important to work at low laser fluence in order to reduce unwanted laser induced fragmentation effects.

REFERENCES

(1) Resonance Ionisation Spectroscopy
Analytical Chemistry 51, 1050A (1979)
J. P. Young, G. S. Hurst, S. D. Kramer and M. G. Payne

(2) Resonance Ionisation Spectroscopy and one-atom detection
Reviews of Modern Physics 51, 767 (1979)
G. S. Hurst, M. G. Payne, S. D. Kramer and J. P. Young

(3) Resonance Ionisation Spectroscopy of Atoms and Molecules
Optical Engineering 19, 57 (1980)
M. H. Nayfeh

(4) Counting the Atoms
Physics Today 33, 24 (1980)
G. S. Hurst, M. G. Payne, S. D. Kramer and C. H. Chen

(5) Resonance Ionisation Spectroscopy
Analytical Chemistry 53, 1448A (1981)
G. S. Hurst

(6) Counting the Atoms: Some Applications in Chemistry
Journal of Chemical Education 59, 895 (1982)
G. S. Hurst

(7) Laser resonant photo-ionization spectroscopy for trace analysis
Trends in Analytical Chemistry 2, 252 (1983)
G. I. Bekov and V. S. Letokhov

(8) Laser Atomic Photoionisation Spectral Analysis of Element Traces
Applied Physics B 30, 161 (1983)
G. I. Bekov and V. S. Letokhov

(9) Saturated Two-Photon Resonance Ionisation of He($2\,^1s$)
Physical Review Letters 35, 82 (1975)
G. S. Hurst, M. G. Payne, M. H. Nayfeh, J. P. Judish and E. B. Wagner

(10) Kinetics of He($2\,^1s$) Using Resonance Ionisation Spectroscopy
Physical Review Letters 35, 1154 (1975)
M. G. Payne, G. S. Hurst, M. H. Nayfeh, J. P. Judish, C. H. Chen, E. B. Wagner and J. P. Young

(11) A Demonstration of one-atom detection
Applied Physics Letters 30, 229 (1977)
G. S. Hurst, M. H. Nayfeh and J. P. Young

(12) One-atom detection using resonance ionisation spectroscopy
Physical Review A 15, 2283 (1977)
G. S. Hurst, M. H. Nayfeh and J. P. Young

(13) Selective single atom detection in a 10^{19} atom background

Springer Series in Optical Science 7 (Laser Spectroscopy 3) 44 (1977)

G. S. Hurst, M. H. Nayfeh, J. P. Young, M. G. Payne and L. W. Grossman

(14) Single-atom detection of ytterbium by selective laser excitation and field ionisation from Rydberg states

Optics Letters 3, 159 (1978)

G. I. Bekov, V. S. Letokhov, O. I. Matveev and V. I. Mishin

(15) Saturated photodissociation of CsI

Chemical Physics Letters 50, 70 (1977)

L. W. Grossman, G. S. Hurst, M. G. Payne and S. L. Allman

(16) A Sensitive, absolute and time-resolved method for the study of reactive atoms

Chemical Physics Letters 50, 207 (1977)

L. W. Grossman, G. S. Hurst, S. D. Kramer, M. G. Payne and J. P. Young

(17) Precision measurements of the diffusion of reactive atoms

Chemical Physics Letters 60, 150 (1978)

G. S. Hurst, S. L. Allman, M. G. Payne and T. J. Whitaker

(18) One-atom detection in individual ionisation tracks

Optics Letters 3, 16 (1978)

S. D. Kramer, C. E. Bemis Jr., J. P. Young and G. S. Hurst

(19) Resonance Ionisation Spectroscopy with Amplification
Chemical Physics Letters 63, 1 (1979)
G. S. Hurst, M. G. Payne, S. D. Kramer and J. P. Young

(20) Resonance Ionisation Spectroscopy of Lithium
Optics Communications 30, 47 (1979)
S. D. Kramer, J. P. Young, G. S. Hurst and M. G. Payne

(21) Direct determination of aluminium in natural waters by laser stepwise photoionisation
Nature 301, 410 (1983)
G. I. Bekov, A. S. Egorov, V. S. Letokhov and V. N. Radayev

(22) Laser photoionisation spectroscopy of ruthenium traces at the level of 1 part in 10^{12}
Journal of the Optical Society of America B 2, 1554 (1985)
G. I. Bekov, V. S. Letokhov and V. N. Radayev

(23) Collisionally induced ionisation of rubidium atoms in Rydberg states
Chemical Physics Letters 79, 506 (1981)
T. J. Whitaker and B. A. Bushaw

(24) Doppler-cancelled, two-photon resonant ionisation spectroscopy
Journal of Chemical Physics 74, 6519 (1981)
B. A. Bushaw and T. J. Whitaker

(25) Double Resonance Multiphoton Ionisation Determination of Mercury Vapour
Analytical Chemistry 57, 2397 (1985)
B. A. Bushaw

(26) The Detection of Bromine Atoms by Resonant Multiphoton Ionisation
Chemical Physics Letters 117, 64 (1985)
S. Arepalli, N. Presser, D. Robie and R. J. Gordon

(27) Detection of Cl atoms and HCl molecules by Resonantly Enhanced Multiphoton Ionisation
Chemical Physics Letters 118, 88 (1985)
S. Arepalli, N. Presser, D. Robie and R. J. Gordon

(28) Multiphoton Ionisation Spectroscopy of Atomic Fluorine
Chemical Physics Letters 120, 337 (1985)
W. K. Bischel and L. E. Jusinski

(29) Laser two-photon ionisation spectroscopy: a new method for real-time monitoring of atmospheric pollutants
Optics Letters 4, 337 (1979)
J. H. Brophy and C. T. Rettner

(30) Laser Multiphoton Ionisation-Dissociation Mass Spectroscopy
Chemical Reviews 85, 529 (1985)
D. A. Gobeli, J. J. Yang and M. A. El-Sayed

(31) Laser two-photon ionisation of organic molecules in dielectric liquids

Chemical Physics Letters 80, 504 (1981)

K. Siomos, G. Kourouklis and L. G. Christophorou

(32) Laser Two-Photon Ionisation for Determination of Aromatic Molecules in Solution

Analytical Chemistry 55, 1914 (1983)

S. Yamada, A. Hino, K. Kano and T. Ogawa

(33) Applications of Resonance Ionisation Spectroscopy to Ultralow-level Counting and Mass Spectroscopy

Radiocarbon 22, 428 (1980)

S. D. Kramer, G. S. Hurst, J. P. Young, M. G. Payne, M. K. Kopp, T. A. Callcott, F. T. Arakawa and D. W. Beekman

(34) Laser Resonance Ionisation Mass Spectrometry

Science 230, 262 (1985)

J. D. Fassett, L. J. Moore, J. C. Travis and J. R. DeVoe

(35) Resonance Ionisation Source for Mass Spectroscopy

International Journal of Mass Spectrometry and Ion Physics 34, 89 (1980)

D. K. Beekman, T. A. Callcott, S. D. Kramer, E. T. Arakawa, G. S. Hurst and E. Nussbaum

(36) Direct counting of Xe atoms

Chemical Physics Letters 75, 473 (1980)

C. H. Chen, G. S. Hurst and M. G. Payne

(37) Selective counting of krypton atoms using resonance ionisation spectroscopy

Applied Physics Letters 44, 640 (1984)

C. H. Chen, S. D. Kramer, S. L. Allman and G. S. Hurst

(38) Noble Gas Detection Using Resonance Ionisation Spectroscopy and a Quadrupole Mass Spectrometer

Proceedings SPIE - International Society for Optical Engineering (Laser-based Ultrasensitive Spectroscopic Detection 5) 426, 2 (1983)

C. H. Chen and G. S. Hurst

(39) Determination of Rare-Earth Isotope Ratios by Resonance Ionisation Mass Spectrometry

International Journal of Mass Spectrometry and Ion Physics 43, 293 (1982)

D. L. Donohue, J. P. Young and D. H. Smith

(40) Ionisation Spectra of Neodymium and Samarium by Resonance Ionisation Mass Spectrometry

Analytical Chemistry 55, 88 (1983)

J. P. Young and D. L. Donohue

(41) Detection of Plutonium by Resonance Ionisation Mass Spectrometry

Analytical Chemistry 55, 378 (1983)

D. L. Donohue and J. P. Young

(42) Isotopic Analysis of Uranium and Plutonium Mixtures by Resonance Ionisation Mass Spectrometry

Analytical Chemistry 56, 379 (1984)

D. L. Donohue, D. H. Smith, J. P. Young, H. S. McKown and C. A. Pritchard

(43) Spectral Studies of Actinide Elements by Resonance Ionisation Mass Spectrometry

Applied Spectroscopy 39, 93 (1985)

D. L. Donohue, J. P. Young and D. H. Smith

(44) Multiphoton ionisation of azulene and naphthalene

Journal of Chemical Physics 72, 3034 (1980)

D. M. Lubman, R. Naaman and R. N. Zare

(45) Use of Resonant Two-Photon Ionisation with Supersonic Beam Mass Spectrometry in the Discrimination of Cresol Isomers

Analytical Chemistry 56, 1962 (1984)

R. Tembreull and D. M. Lubman

(46) Resonant Two-Photon Ionisation Spectroscopy in Supersonic Beams for Discrimination of Disubstituted Benzenes in Mass Spectrometry

Analytical Chemistry 56, 2776 (1984)

C. H. Sin, R. Tembreull and D. M. Lubman

(47) Isotopically Selective Resonant Two-Photon Ionisation in Supersonic Beams

Analytical Chemistry 57, 1084 (1985)

D. M. Lubman, R. Tembreull and C. H. Sin

(48) Atomic Ion Formation and Measurement with Resonant Ionisation Mass Spectrometry

Analytical Chemistry 55, 765 (1983)

J. D. Fassett, J. C. Travis, L. J. Moore and F. E. Lytle

(49) Systematics of Multielement Determination with Resonance Ionisation Mass Spectrometry

Analytical Chemistry 56, 2770 (1984)

L. J. Moore, J. D. Fassett and J. C. Travis

(50) Determination of Iron in Serum and Water by Resonance Ionisation Isotope Dilution Mass Spectrometry

Analytical Chemistry 56, 2228 (1984)

J. D. Fassett, L. J. Powell and L. J. Moore

(51) Pulsed Thermal Atom Source for Resonance Ionisation Mass Spectrometry

Analytical Chemistry 56, 203 (1984)

J. D. Fassett, L. J. Moore, R. W. Shideler and J. C. Travis

(52) Resonance-Ionisation Mass Spectrometry of Carbon

Journal of the Optical Society of America B 9, 1561 (1985)

L. J. Moore, J. D. Fassett, J. C. Travis, T. B. Lucatorto and C. W. Clark

(53) Selective Laser Photoionisation for Mass Spectrometry

Analytical Chemistry 54, 2377 (1982)

C. M. Miller, N. S. Nogar, A. J. Gancarz and W. R. Shields

(54) Multiple Photon Processes in Tantalum Resonance Ionisation Mass Spectrometry

Analytical Chemistry 57, 1144 (1985)

N. S. Nogar, S. W. Downey and C. M. Miller

(55) Continuous Wave Lasers for Resonance Ionisation Mass Spectrometry

Analytical Chemistry 55, 1607 (1983)

C. M. Miller and N. S. Nogar

(56) Continuous-wave Double-Resonance Ionisation Mass Spectrometry of Barium

Journal of the Optical Society of America B 2, 1542 (1985)

B. D. Cannon, B. A. Bushaw and T. J. Whitaker

(57) Time-Interval Distribution and Photon-Burst Correlation Spectroscopy of a Strontium Atomic Beam
Journal of the Optical Society of America B 2, 1547 (1985)
B. A. Bushaw, T. J. Whitaker, B. D. Cannon and R. A. Warner

(58) Isotopically Selective Laser Measurements
Lasers and Applications p. 67 (August 1986)
T. Whitaker

(59) Solids Analysis Using Energetic Ion Bombardment and Multiphoton Resonance Ionisation with Time-of-Flight Detection
Analytical Chemistry 56, 2782 (1984)
F. M. Kimock, J. P. Baxter, D. L. Pappas, P. H. Kobrin and N. Winograd

(60) Multiphoton Resonance Ionisation of Sputtered Neutrals: a Novel Approach to Materials Characterization
Chemical Physics Letters 88, 581 (1982)
N. Winograd, J. P. Baxter and F. M. Kimock

(61) Sputter-initiated Resonance Ionisation Spectroscopy
Thin Solid Films 108, 69 (1983)
J. E. Parks, H. W. Schmitt, G. S. Hurst and W. M. Fairbank, Jr.

(62) Ultrasensitive Elemental Analysis of Solids by Sputter-Initiated Resonance Ionisation Spectroscopy
Proceedings SPIE - International Society for Optical Engineering (Laser-based Ultrasensitive Spectroscopic Detection 5) 426, 32 (1983)
J. E. Parks, H. W. Schmitt, G. S. Hurst and W. M. Fairbank, Jr.

(63) Sputter Initiated Resonance Ionisation Spectroscopy for Trace Element Analysis
Analytical Chemistry Symposia Series 19, 149 (1984)
J. E. Parks, H. W. Schmitt, G. S. Hurst and W. M. Fairbank, Jr.

(64) Ion and Neutral Yields from Ion Bombarded Metal Surfaces During Chemisorption Using Low Dose SIMS and Multi-photon Resonance Ionisation
Surface Science 124, L41 (1983)
F. M. Kimock, J. P. Baxter and N. Winograd

(65) Laser Ablation and Resonance Ionisation Spectrometry for Trace Analysis of Solids
Analytical Chemistry 54, 553 (1982)
S. Mayo, T. B. Lucatorto and G. G. Luther

(66) Detection of Trace Elements with Resonance Ionisation and Time-of-Flight Mass Spectrometry
Analytical Chemistry 56, 1348 (1984)
M. W. Williams, D. W. Beekman, J. B. Swan and E. T. Arakawa

(67) Ion Microprobe Mass Spectrometry Using Sputtering Atomisation and Resonance Ionisation
Analytical Chemistry 57, 1193 (1985)
D. L. Donohue, W. H. Christie, D. E. Goeringer and H. S. McKown

(68) Pulsed Laser Desorption with Resonant Two-Photon Ionisation Detection in Supersonic Beam Mass Spectrometry
Analytical Chemistry 58, 1299 (1986)
R. Tembreull and D. M. Lubman

(69) Pulsed Laser Desorption for Resonance Ionisation Mass Spectrometry
Analytical Chemistry 57, 2441 (1985)
N. S. Nogar, R. C. Estler and C. M. Miller

(70) Surface Analysis by Nonresonant Multiphoton Ionisation of Desorbed or Sputtered Species
Analytical Chemistry 56, 1671 (1984)
C. H. Becker and K. T. Gillen

(71) Selective Two-Step Ionisation of Rubidium by Laser Radiation
Soviet Physics JETP 43, 866 (1976)
P. V. Ambartsumyan et al.

(72) Resonance Ionisation Mass Spectrometry of Uranium with Intracavity Laser Ionisation
Analytical Chemistry 56, 827 (1984)
S. W. Downey, N. S. Nogar and C. M. Miller

(73) Laser Resonant Ionisation of Plutonium
Applied Physics B38, 65 (1985)
U. Kronert, J. Bonn, H.-J. Kluge, W. Ruster, K. Wallmeroth, P. Peuser and N. Trautmann

(74) Trace Detection of Plutonium by Three-Step Photoionisation with a Laser System Pumped by a Copper Vapour Laser
Applied Physics B38, 249 (1985)
P. Peuser et al.

(75) A Generalisation of One-Atom Detection
IEEE Transactions on Nuclear Science NS-26, 133 (1979)
G. S. Hurst, S. D. Kramer, M. G. Payne and J. P. Young

(76) The Interaction of Light with Light
Scientific American 210, 38 (1984)
J. A. Giordmaine

(77) Nuclear Power Technology Vol. 1 Reactor Technology
W. Marshall (ed.) Clarendon Press, Oxford (1983)

(78) Fission Product Yields from Neutron Induced Fission
Nucleonics 18 (11), 201 (1960)
S. Katcoff

(79) Nuclear Power Technology Vol. 2 Fuel Cycle
W. Marshall (ed.) Clarendon Press, Oxford (1983)

(80) Nuclear and Radiochemistry 3rd ed.
G. Friedlander, J. W. Kennedy, E. S. Macias and J. M. Miller
Wiley International, New York (1981)

(81) The Disposal of High-Activity Nuclear Waste in the Oceans
Marine Pollution Bulletin 14 (4), 126 (1983)
M. S. Baxter

(82) Limits for Intakes of Radionuclides by Workers
International Commission on Radiological Protection
Publication 30 (1979)

(83) Radioactivity in Surface and Coastal Waters of the British
Isles, 1981
G. J. Hunt Directorate of Fisheries Research, Ministry
of Agriculture, Fisheries & Food, Lowestoft (1983)

(84) Hanford Radioactive Waste Management

in Industrial Radioactive Waste Disposal Hearings before the Joint Committee on Atomic Energy (J. C. A. E. vol. 1)

H. M. Parker U. S. Government Printing Office, Washington (1959)

(85) Annual Report on Radioactive Discharges and Monitoring of the Environment

British Nuclear Fuels Ltd., Health & Safety Directorate, Risley, Warrington, U. K. (1982)

(86) Gross Beta Counting of Environmental Materials

J. W. R. Dutton Fisheries Radiobiological Laboratory. Ministry of Agriculture, Fisheries & Food, Lowestoft (1968)

(87) ^{241}Am from the decay of ^{241}Pu in the Irish Sea

Nature 292, 43 (1981)

J. P. Day and J. E. Cross

(88) Sources of radioactivity and their characteristics

in Radioactivity in the Marine Environment, pp. 6-41

A. B. Joseph et al. National Resarch Council, National Academy of Sciences, Washington (1971)

(89) Evaluation of Human Radiation exposure

in Radioactivity in the Marine Environment,

pp. 240-260

R. F. Foster, I. L. Ophel and A. Preston National

Research Council, National Academy of Sciences,

Washington (1971)

(90) Nuclear Power Technology Vol. 3 Nuclear Radiation

W. Marshall (ed.) Clarendon Press, Oxford (1983)

(91) A Review of Applications of Mass Spectrometry to Low-Level

Radionuclide Metrology

Nuclear Instruments and Methods 223, 349 (1984)

J. E. Halverson

(92) The Potential of Resonance Ionisation Mass Spectroscopy for

Detecting Environmentally Important Radioactive

Nuclides

Proceedings of the 3rd International Symposium on Resonance

Ionisation Spectroscopy and its Applications,

Swansea, 1986 (to be published)

M. H. C. Smyth, S. L. T. Drysdale, R. Jennings,

K. W. D. Ledingham, D. T. Stewart, M. Towrie,

C. M. Houston, M. S. Baxter and R. D. Scott.

(93) Applications of Microwave Oven Sample Dissolution in Analysis

Analytical Chemistry 56, 2233 (1984)

R. A. Nadkarni

(94) Application of Resonance Ionisation Spectroscopy to Transuranic Waste Assay
Nuclear Instruments and Methods 173, 317 (1980)
L. A. Franks et al.

(95) Resonance Ionisation Spectroscopy for Low-Level Counting
ACS Symposium Series (Nuclear Chemical Dating Techniques) 176, 149 (1982)
G. S. Hurst, S. D. Kramer and B. E. Lehman

(96) Atomic and Nuclear Data Tables 19, 417 (1977)
E. A. C. Crouch

(97) Handbook of Chemistry and Physics 64th ed.
R. C. Weast (ed.) CRC Press, Boca Raton, Florida (1984)

(98) Neutron Activation Tables
G. Erdtmann Verlag Chemie, Weinheim (1976)

(99) An Introduction to Lasers and their Applications
D. C. O'Shea, W. R. Callen and W. T. Rhodes
Addison-Wesley, Reading, Mass. (1978)

(100) Atomic Physics of Lasers
D. Eastman Taylor and Francis, London (1986)

(101) Stimulated Emission Observed from an Organic Dye, Chloro-aluminium Phthalocyanine
IBM Journal of Research and Development 10, 162 (1966)
P. P. Sorokin and J. R. Lankard

(102) Laser Dyes: Properties of Organic Compounds for Dye Lasers
M. Maeda Academic Press, New York (1984)

(103) Repetitively Pulsed Tunable Dye Laser for High Resolution Spectroscopy
Applied Optics 11, 895 (1972)
T. W. Hansch

(104) Observation of Optical Harmonics
Physical Review Letters 7, 118 (1961)
P. A. Franken, A. E. Hill, C. W. Peters and G. Weinreich

(105) Optical Harmonics and Nonlinear Phenomena
Reviews of Modern Physics 35, 23 (1963)
P. A. Franken and J. F. Ward

(106) Observation of Continuous Optical Harmonic Generation with Gas Masers
Physical Review Letters 11, 14 (1963)
A. Ashkin, G. D. Boyd and J. M. Dziedzic

(107) Wavelength Dependence of Laser Induced Ionisation in Proportional Counters
Nuclear Instruments and Methods A241, 441 (1985)
K. W. D. Ledingham, C. Raine, K. M. Smith, M. H. C. Smyth, D. T. Stewart, M. Towrie and C. M. Houston

(108) Vapour Pressure Data for the Solid and Liquid Elements
RCA Review 30, 285 (1969)
R. E. Honig and D. A. Kramer

(109) Laser Induced Ionisation in Proportional Counters
Nuclear Instruments and Methods 217, 305 (1983)
C. Raine, K. W. D. Ledingham and K. M. Smith

(110) Detection of phenol in proportional counter gas by two-photon ionisation spectroscopy
CERN-EP/85-198 (Dec. 1985)
J. W. Cahill, C. M. Houston, K. W. D. Ledingham, C. Raine, K. M. Smith, M. H. C. Smyth, D. T. Stewart and M. Towrie

(111) Detection of phenol in proportional counter gas by two-photon ionisation spectroscopy
Journal of Physics B: Atomic and Molecular Physics 19, 1989 (1986)
M. Towrie, J. W. Cahill, K. W. D. Ledingham, C. Raine, K. M. Smith, M. H. C. Smyth, D. T. Stewart and C. M. Houston

(112) Ionisation of counting gas and ionisable gaseous additives in proportional chambers by UV light
Nuclear Instruments and Methods 228, 327 (1985)
G. Hubricht, K. Kleinknecht, E. Muller, D. Pollman and E. Teupe

(113) Laser two-photon ionisation of aniline in a molecular beam and the bulk gas phase
Chemical Physics Letters 67, 351 (1979)
J. H. Brophy and C. T. Rettner

(114) UV Atlas of Organic Compounds
Ed.: Photoelectric Spectrometry Group, London, and Institut fur Spektrochemie und angewandte Spektroscopie, Dortmund. 1966 (London: Butterworths; Weinheim: Verlag Chemie)

(115) Handbook of Chemistry and Physics 1986 67th edition
Ed.: R. C. Weast (CRC Press)

(116) Energetics of Gaseous Ions
Journal of Physical and Chemical Reference Data 6, Suppl. no. 1 (1977)
H. M. Rosenstock, K. Draxl, B. W. Steiner and J. T. Heron

(117) Detection of toluene in proportional counter gas by resonant two photon ionisation spectroscopy

CERN-EP/86-28 (Feb. 1986)

S. L. T. Drysdale, C. M. Houston, K. W. D. Ledingham, C. Raine, K. M. Smith, M. H. C. Smyth, D. T. Stewart and M. Towrie

(118) Detection of toluene in a proportional counter gas by resonant two photon ionisation spectroscopy

Nuclear Instruments and Methods (to be published)

S. L. T. Drysdale, K. W. D. Ledingham, C. Raine, K. M. Smith, M. H. C. Smyth, D. T. Stewart, M. Towrie and C. M. Houston

(119) Handbook of Chemistry and Physics 53rd ed. (1973)
R. C. Weast (ed.) The Chemical Rubber Publishing Co.

(120) private communication - H. Boerner (1985)

(121) Investigation of the effects of gas purification on the background laser ionisation in proportional counters
ALEPH 86-30 (distr. TPCCAL) (1986)
S. L. T. Drysdale, A. P. Land, K. W. D. Ledingham, C. Raine, K. M. Smith, M. H. C. Smyth, D. T. Stewart, M. Towrie and C. M. Houston

(122) NBS Publication 467 "Atomic Energy Levels"
C. E. Moore U. S. Gov. Printing Office, Washington (1952)

(123) Laser Spectroscopy (Springer series in chemical physics;5)
W. Demtroder Springer-Verlag, Berlin (1982)

(124) Observation of New Satellites in the Cs-Ar system using Resonance Ionisation Spectroscopy
Physical Review Letters 41, 302 (1978)
M. H. Nayfeh, G. S. Hurst, M. G. Payne and J. P. Young

(125) Handbook of Chemistry and Physics 53rd ed. (1973)
R. C. Weast (ed.) The Chemical Rubber Publishing Co.
page F-174.

(126) The detection of Cs atoms by two-photon resonance ionisation spectroscopy
Proc. SPIE - International Society of Optical Engineering ("Laser Applications in Chemistry and Biophysics") 620 (1986)
K. W. D. Ledingham, C. Raine, K. M. Smith, M. H. C. Smyth, D. T. Stewart, M. Towrie and C. M. Houston

(127) The derivation of dependence of ionisation on laser pulse energy
K. W. D. Ledingham (unpublished work)

(128) NBS Publication 68 "Wavelengths and Transition Probabilities for Atoms and Atomic Ions"
U. S. Government Printing Office, Washington (1980)

(129) Absolute Determination of two- and four-photon ionisation cross sections of caesium atoms
Journal of Physics B: Atomic and Molecular Physics 13, 1551 (1980)
D. Normand and J. Morellec

(130) Multiphoton Ionisation of Caesium
in Laser Techniques in the Extreme Ultraviolet, American Institute of Physics Conference Proceedings (1984)
R. W. Crompton, C. E. Klots, J. A. D. Stockdale and C. D. Cooper

(131) Nonlinear Laser Chemistry
(Springer Series in Chemical Physics; 22)
V. S. Letokhov Springer-Verlag, Berlin (1983)

(132) Photoionisation processes in gases
G. Marr Academic Press, New York (1967)

(133) personal communication - Atom Sciences Inc. (1986)

(134) Time-of-Flight Mass Spectrometer with Improved Resolution
Review of Scientific Instruments 26, 1150 (1955)
W. C. Wiley and I. H. McLaren

(135) Energy Resolution of the Conventional Time-of-Flight Mass Spectrometer
Review of Scientific Instruments 41, 741 (1970)
G. Sanzone

(136) Ion Implantation, Sputtering and their applications
P. D. Townsend, J. C. Kelly and N. E. W. Hartley
Academic Press, London (1976)

(137) New Directional and Energy Focusing in Time-of-Flight Mass Spectrometers for Special Tasks in Vacuum and Surface Physics
Journal of Vacuum Science and Technology 9, 212 (1971)
W. P. Poschenrieder and G. H. Oetjen

(138) Multiphoton mass spectrometry of metastables: Direct observation of decay in a high-resolution time-of-flight instrument
Journal of Physical Chemistry 86, 4857 (1982)
U. Boesl, H. J. Neusser, R. Weinkauf and E. W. Schlag

(139) Multiphoton Mass Spectrometry
Accounts of Chemical Research 16, 355 (1983)
E. W. Schlag and H. J. Neusser

(140) Observation of a long-lived autoionisation state in the spectrum of the gadolinium atom
JETP Letters 28, 283 (1978)
G. I. Bekov, V. S. Letokhov, O. I. Matveev and V. I. Mishin

(141) Laser Spectroscopy of narrow doubly excited autoionising states of ytterbium atoms
Soviet Physics JETP 53, 441 (1981)
G. I. Bekov, E. P. Vidolova-Angelova, L. N. Ivanov, V. S. Letokhov and V. I. Mishin

(142) An application of resonant ionisation spectroscopy to accelerator based high energy physics
Proceeding of the 3rd International Symposium on RIS and its Applications, Swansea, 1986
K. W. D. Ledingham, J. W. Cahill, S. L. T. Drysdale, C. Raine, K. M. Smith, M. H. C. Smyth, D. T. Stewart, M. Towrie and C. M. Houston
(to be published)

(143) On a new method of testing and calibrating ionising particle detectors
Nuclear Instruments and Methods 166, 581 (1979)
H. Anderhub, M. J. Devereux and P. G. Seiler

(144) On a new method for testing and calibrating wire chambers
Nuclear Instruments and Methods 176, 323 (1980)
H. Anderhub, M. Devereux and P. G. Seiler

(145) Resonance Enhanced Two-Photon Photoionisation Spectroscopy Applied to Detection of Naphthalene Vapour
Analytical Chemistry 52, 281 (1980)
R. Frueholz, J. Wessel and E. Wheatley

(146) Ionisation of multiwire proportional chamber gas by double photon absorption
Nuclear Instruments and Methods 173, 463 (1980)
J. Bourotte and B. Sadoulet

(147) On the formation and application of laser induced ionisation tracks in gases
Nuclear Instruments and Methods 174, 145 (1980)
E. J. Hilke

(148) Measurement of Laser Induced Ionisation in an argon-ethane gas mixture
Nuclear Instruments and Methods 201, 357 (1982)
M. Desalvo and R. Desalvo

(149) The use of laser induced electron clusters for drift chamber tests
Nuclear Instruments and Methods 204, 77 (1982)
J. C. Guo, F. G. Hartjes and J. Konijn

(150) Laser induced ionisation in proportional counters seeded with low ionisation potential vapours
Nuclear Instruments and Methods 225, 319 (1984)
K. W. D. Ledingham, C. Raine, K. M. Smith, A. M. Campbell, M. Towrie, C. Trager and C. M. Houston

(151) Ionisation Potentials, Appearance Potentials, and Heats of Formation of Gaseous Positive Ions
NBS Publication 26 (June 1969)
J. L. Franklin, J. G. Dillard, H. M. Rosenstock, J. T. Herron, K. Draxl and F. H. Field
U. S. Government Publication Office, Washington

(152) Experimental determination of ionisation potentials of organic amines, β-carotene and chlorophyll a
Bulletin of the Chemical Society of Japan 47, 3001 (1974)
Y. Makato, T. Chiyoda and H. Tsubomura

(153) Two-photon-ionisation coefficients of propane, 1-butene, and methylamines
Journal of Applied Physics 53, 203 (1982)
L. C. Lee and W. K. Bischel

(154) Total vapour pressure over triethylamine-water mixtures in the critical region
Russian Journal of Physical Chemistry 34, 1027 (1960)
I. R. Krichevskii, N. E. Khazanova, G. M. Svetlova and R. S. Panina

(155) Vapour pressures and critical points of liquids, vol. 12: aromatic nitrogen compounds
Engineering Sciences Data Unit Item No. 78011
Institute of Chemical Engineers, London (1981)

(156) A photoionisation detector for the detection of xenon light
IEEE Transactions on Nuclear Science NS-28, 842 (1981)
D. F. Anderson

(157) Coupling of a BaF_2 scintillator to a TMAE photocathode and a low-pressure wire chamber
Nuclear Instruments and Methods 217, 217 (1983)
D. F. Anderson, R. Bouclier, G. Charpak, S. Majewski and G. Kneller

(158) Investigation of UV Laser Ionisation in Naphthalene and Phenol vapours added to Proportional Chamber-Gases
ALEPH Note 154 UNIDO 85/285
G. Hubricht, K. Kleinknecht, E. Muller, D. Pollmann, K. Schmitz and C. Sturzl

(159) personal communication - Michael Towrie (1986)